Apatite - Wollastonite glass ceramic scaffolds for bone tissue engineering applications

Sotiria Toumpaniari

A thesis submitted in partial fulfilment of the requirements for the degree of Doctor of Philosophy

Arthritis Research UK – Tissue Engineering Centre

School of Mechanical and Systems Engineering – SAgE

Newcastle University

March 2016

ABSTRACT

In bone tissue engineering, one of the main challenges is to fabricate scaffolds that promote and support osseous reconstruction. The research reported in this thesis considers the use of apatite-wollastonite (A-W) as a bone scaffold.

A variety of scaffold fabrication techniques, all based on initially processing powder to create a pre-form for subsequent sintering, have been developed and characterised for their ability to create microporous; and interconnected macroporous scaffolds. A range of powder processing techniques were used: pelleting, dry powder and slurry moulding, and different powder particle size ranges were assessed for the preparation of microporous scaffolds to influence their surface roughness without significantly varying the porosity.

To introduce macroporosity within the ceramic scaffolds that would be comparable in terms of scale and organisation to trabecular bone, a variety of methods were employed. Burning off negative templates such as polymeric particles, filaments and fused deposition modelling 3D constructs was investigated, together with a novel method based on thermally induced phase separation (TIPS), freeze-drying and sintering.

Selected microporous scaffolds with different surface topography and pore size; and highly interconnected scaffolds with porosity >80% were fabricated with height 2± 0.1 mm and diameter 8- 10 mm depending on the fabrication method and the particle range that was used.

The parameters that were evaluated *in vitro* were the effect of variable topographies on microporous constructs and the influence of high porosity on cell adhesion, proliferation and cell differentiation.

It is concluded that the surface area of A-W scaffolds affects their bioactivity, degradation and mechanical properties. Microporous scaffolds with smaller pores allow cell-cell interaction and promote osteogenesis. Further investigation is required to clarify the observed chondrogenesis that occurred when MSCs were cultured on microporous scaffolds with larger pores. Highly porous A-W scaffolds allow cell infiltration, migration and demonstrate signs of osteochondral lineage differentiation.

ACKNOWLEDGEMENTS

My deepest appreciations goes to Prof Kenny Dalgarno, Dr Mark Birch and Prof Andrew McCaskie who have helped me immensely throughout my PhD.

To my friends and colleagues who helped me out and supported me whenever I needed, namely Dr Ana Marina Ferreira-Duarte, Dr Matt Benning, Maria Tselepi, Dimitra Tsompani, Steven Wilkinson, Fabio D'Agostino, Sylvia Muller, Dr Najla Alburae, Natacha Rodrigues, Dr Sarah Upson, Elena Mancuso and Dr Naif Alharbi.

A big thank you to Dr Deepak Kalaskar for all the consultancy and support he provided to me when he was working with me as a postdoc and later on when he moved to a different university; and to Chris Aylott that was always very helpful. I would like to thank Dr Kathleen Wright for helping me at the beginning of my PhD.

I would like to express my appreciation for Prof Paul Genever that kindly donate to our group the h-TERT Y201 cell line and I was able to use them for my cell studies.

I would like to thank Dr David Wilkinson, Dr Isabel Arce Garcia, Adam Richardson, Maggie White, Sharon Watson and Tracey Davey for helping collect my results.

I would like to especially thank Simon Partridge, who has been next to me and helped me at every step. Above all I would like to express my gratitude to my family who has always been very supportive and provided me with everything I needed to fulfil my aspirations.

TABLE OF CONTENTS

INTRODUCTION

Currently the life expectancy has increased and the ageing population suffers from degenerative diseases, such as osteoarthritis (OA) that affects the bone and cartilage. Therefore, there is a need for scaffolds that may prevent OA at the early stage and have long-term impact on disease progression (Roberts et al., 2011).

Currently there is no treatment for osteoarthritis. Only when the disease is at the end stage and the patient is immobilised, a total joint replacement surgery takes place. The main purpose of this thesis was to develop a ceramic scaffold that would be the bony part of an osteochondral plug for early stage intervention in the pathogenesis of OA. This scaffold could potentially be used by removing the diseased area and replacing it bone to prevent progression of the disease.

A-W was used as material, because it combines biocompatibility, bioactivity, osteoconductivity and bioresorbability *in vivo* with high mechanical properties (Kokubo et al., 1986, Dyson et al., 2007) that are necessary characteristics for bone scaffolds (Will et al., 2012). Additionally, a bone scaffold needs to be highly porous and interconnected to promote fluid diffusion, cellular migration, neo-vascularisation and tissue ingrowth (Karageorgiou and Kaplan, 2005).

In this thesis different scaffold fabrication techniques were investigated to prepare microporous and highly porous interconnected scaffolds. The fabrication techniques that were used were: cast compact and loose powder, cast slurry, organic polymeric particle and filaments burnt out. Two new techniques were developed during this study.

- FFF negative templates were used as cores in a mould and A-W was poured. After sintering a macroporous interconnected scaffold remained.
- Polymeric scaffolds fabricated with thermally induced phase separation (TIPS) followed by freeze drying have been reported to be highly porous with channels that indicate interconnectivity (Yang et al., 2006). During TIPS method, a polymer dissolved in a solvent system to promote phase separation. In this occasion, poly (lactic acid) was dissolved in dioxane or dioxane: water solution. To fabricate hard, mechanically robust scaffolds for

bone tissue engineering applications, A-W microparticles were incorporated into the polymeric solution and after the slurry was frozen and freeze dried; it was sintered to burn out the polymeric phase and leave behind a hard, rough ceramic scaffold.

The main technique that was common for all the A-W scaffolds was sintering to provide a ceramic scaffold with mechanically robust structure.

One of the main goals of this thesis was to develop and characterise ceramic fabrication techniques using A-W ceramic powder that would result in microporous scaffolds; and highly porous and interconnected scaffolds.

One type of microporous and one of macroporous scaffolds were selected to further investigate. The structural integrity was the main criterion to select the scaffolds to be used for further examination. Scaffolds were assessed *in vitro* before and after they were immersed in SBF solution to examine their bioactivity, bioresorbability and mechanical properties.

In addition, the immortalised human telomerase reverse transcriptase mesenchymal stem cell line (h-TERT MSCs) Y201 was seeded on the microporous and macroporous highly interconnected scaffolds to study their influence on cell fate. The Y201 cells were selected, because they are clonal cells from a donor patient that underwent total hip replacement, have the ability to differentiate to the three lineages (osteogenic, chondrogenic and adipogenic) (James et al. 2015) and can obtain a high cell number to test all the scaffolds for different assays.

Using different particle ranges the surface area of the microporous was altered aiming to study how the different surface areas of the sintered A-W ceramic influenced the resorption and bioactivity of the material. Additionally, Y201 cells were cultured on the top of these microporous scaffolds since their pore sizes were prohibitive for cell infiltration (2D cell culture). The cells cultured on these scaffolds were aimed to investigate how the different surface areas could influence the cell fate of human mesenchymal stem cells.

It is generally accepted that the 3D cell culture is more representative of the native tissue (Pampaloni et al. 2007). The interconnected highly porous scaffolds A-W scaffolds were intentioned to be used in order to evaluate how the high porosity in combination with interconnectivity could influence A-W bioactivity and bioresorption

and whether they could promote *in vitro* osteogenesis to the hTERT cell line (3D cell culture).

This thesis is structured as follows:

Chapter 1 presents a literature survey covering musculoskeletal biology and tissue engineering approaches to bone and cartilage.

Chapter 2 shows standardised methodologies used through the thesis.

Chapter 3 displays results from the development and selection of a number of A-W scaffold fabrication techniques.

Chapter 4 demonstrates results from the *in vitro* assessment of cast slurry scaffolds, investigating surface topography, bioresorbability and hMSC behaviour.

Chapter 5 illustrates results from the *in vitro* assessment of A-W TIPS scaffolds, investigating mass change and the influence on hMSC behaviour.

Chapter 6 discusses the details of chapters 4-6 with a focus on specific challenges and how they conform to current scientific understanding.

Chapter 1 LITERATURE SURVEY

1.1 Osteoarthritis

Osteoarthritis (OA) is a slow degenerative and highly prevalent chronic disease that is estimated to affect approximately 8.5 million people in the U.K. alone (Roberts et al. 2011). The disease is an outcome of unbalanced equilibrium in normal homeostasis causing increased catabolism relative to anabolism of joint tissues (Hunter 2011).OA is distinctively characterised by chronic cartilage degeneration that leads to subchondral bone alterations causing sclerosis (Guilak 2011; Hunter 2011). The remodelling mechanisms in the arthritic joint often are overactive, but they produce abnormal bone and cartilage in the form of osteophytes (Roberts et al. 2011) . OA is categorised as non-inflammatory, however synovial inflammation (synovitis) can sometimes be present and can influence the progression of cartilage degradation (Bonnet & Walsh 2005). The aetiopathogenesis of OA appears to be the outcome of a complex interplay between systemic and local biomechanical risk factors. Systemic factors related to OA are genetic susceptibility, age, sex, race, bone density, oestrogen levels and nutrition (Benito et al. 2005) . At final stages - joint stiffness and gradually loss of joint function leading to mobility disability and loss of quality of life. Consequently, the need for symptomatic relief increases the demand for improved therapies (Suri & Walsh 2012).

Nonpharmacology measures include exercise and manual therapy, weight loss, electrotherapy, appropriate footwear, assistive devices. Pharmacological measures comprise oral analgesic, such as paracetamol and topical nonsteroidal anti-inflammatory drugs. Joint replacement (arthroplasty) is the last alternative for patients that have been offered non-invasive treatments. On the one hand, arthroplasty can alleviate the pain and restore the functionality of the joint. On the other hand, the implants have a limited lifespan and are likely to loosen and form wear particles. Additionally, it has been reported that the failure rates of implants are higher for young patients compared with older patients. Further surgery is inevitable following implant failure and makes the procedure more complex and painful for the patient (Roberts et al. 2011).

To date the therapies for OA target pain relief, motion improvement and partial regeneration. Consequently, the current treatments aim to alleviate the symptoms of

OA, but not the disease itself. There is, therefore a need for innovative treatment strategies that bridge the gap between conventional symptomatic treatment and joint replacement. It is believed that cell based therapies and tissue engineering can develop early stage repair strategies that may prevent OA and have long-term impact on disease prevalence and progression (Luyten & Vanlauwe 2012).

1.2 Tissue Engineering

Tissue engineering (TE) as a rapidly developing area of regenerative medicine and contains a plethora of interdisciplinary interfaces between engineering, materials science, biology and clinical medicine. It strives to repair, maintain or enhance, diseased or damaged tissues and organs without the formation of scar tissue restoring their function and physiology (Langer & Vacanti 1993; Luyten & Vanlauwe 2012).

Cell therapies provide the potential for early stage treatment of osteochondral defects. One approach is marrow stimulation techniques, such as microfracture, which is based on the penetration of the defected area into the bone marrow cavity causing the outflow of marrow blood that contains mesenchymal stem cells (MSCs). MSCs are multipotent stem cells that have the ability to differentiate towards bone and cartilage amongst other tissues (Barry & Murphy 2004; Ren et al. 2012). The MSCs are stabilised in the defected area by clot formation due to the clotting (coagulation) factors. The MSCs number and their differentiation rate depend on the patient's age (Steinwachs et al. 2008).

Autologous (patient's) cell transplantation is another promising cellular approach. Osteoblasts – bone progenitor cells, chondrocytes – cartilage progenitor cells and/or MSCs can be isolated from the patient's tissues, expanded *in vitro* and introduced in the patient via injection or seeded in a biocompatible 3D construct or scaffold (Hutmacher 2000). MSCs can be harvested in adequate number, have good proliferation capacity and can differentiate into chondrocytes and osteoblasts, as has been referred above, promoting the regeneration of both cartilage and bone (Nejadnik et al. 2010). MSCs can be isolated from various tissues such bone marrow, synovium, umbilical cord, adipose tissue. Sakaguchi et al. (2005) demonstrated that synovium- derived MSCs (SMSCs) and bone marrow- derived MSCs (BMSCs) have more advanced chondrogenic and osteogenic potentials than MSCs derived from periosteum, adipose and muscle. SMSCs have been reported to have superior

chondrogenic and osteogenic potential from BMSCs (Sakaguchi et al. 2005); however, SMSCs not only they have not been used in clinical practise, but also the harvesting method for these cells necessitate arthroscopy that is more invasive than bone marrow biopsy for BMSCs (Nejadnik et al. 2010).

An alternative tissue engineering strategy is the implantation of a three dimensional (3D) biomaterial construct – scaffold – alone or in combination with autologous cells in the defected area (Langer & Vacanti 1993). Mechanical, architectural and topographical properties of scaffolds stimulate cell fate (Guilak et al. 2009) and therefore have the potential to be exploited as mechanisms to control the biological response to implanted material. This report will focus on bone scaffolds for the application to the tissue engineering field. To recapitulate human tissues we must first consider the normal tissue physiology.

1.3 Bone

1.3.1 *Biological and biomechanical properties*

It is of primary significance to understand the biological and biomechanical properties of the physiological bone in order to suggest possible materials and techniques that can participate in the regeneration of the disrupted tissue.

The adult human skeleton consists of 213 bones without encountering the sesamoid bones (Clarke 2008). Bone tissue is composed of 60% hydroxyapatite (HA), 10% water and 30% collagen; and is organized into cortical (compact) bone and trabecular (cancellous or spongy bone) (Weiner & Wagner 1998) . Cortical bone is very dense – only 10% porous- and surrounds cancellous bone. Cancellous bone has high porosity- 50-90% porous- and consists of a honeycomb-like network of trabecular rods and plates in the bone marrow compartment enclosing large voids (macropores) (Clarke 2008; Salgado et al. 2004).

Bone plays an important role in the vertebrate body, since it provides the acquired rigidity for locomotion and protection of vital internal organs and structures - viscera, as well as it contributes to numerous physiological functions as haematopoiesis, acid-base balance, mineral homeostasis -regulation of calcium and phosphorus- and growth factors and cytokines storage (Clarke 2008; Bayliss et al. 2012; Liao et al. 2011).

Bone is an active, highly vascularised and innervated connective tissue with the capacity to remodel and renovate continuously without scar tissue formation either as response to injury or as normal process throughout adult life(Salgado et al. 2004; Dimitriou et al. 2011). The bone structure constantly undergoes restoration by maintaining the dynamic equilibrium between bone resorption and bone remodelling processes to maintain its architecture and mechanical strength (Clarke 2008). Bone resorption and remodelling are processes that are determined by two cell types: osteoclasts and osteoblasts.

Osteoclasts are polarised cells of hematopoietic origin with a ruffled boundary area of the cell membrane that is enclosed in an organelle-free region and are adhered to the bone via integrins (specialised surface receptors that mediate the cellular adhesion on tissues). Osteoclasts are the cells responsible for the bone resorption. Consequently, bone resorption occurs beneath the ruffled border of the osteoclasts initiating with mineral dissolution that leads to organic phase degradation and is dependant by secretion of lysosomal enzymes (proteases) and acid (Robling et al. 2006).

Osteoblasts are bone cells of mesenchymal origin located on the bone tissue that secrete osteoid, which is unmineralised bone matrix that is later mineralised to form mature bone (Robling et al. 2006). Therefore, osteoblasts direct the formation and organisation of the extracellular matrix (ECM) of the bone and its mineralisation. Mature osteoblasts produce type I collagen, which consists the 90% of the proteins in bone, proteoglycans, alkaline phosphatase, bone specific vitamin-K dependent proteins, osteocalcin and matrix Gla protein, phosphorylated glycoproteins including bone sialoproteins I and II, osteopontin and osteonectin. Some osteoblasts are trapped in the lacunae within the bone matrix and are known as osteocytes. Osteocytes can break down the bone ECM through osteocytic osteolysis to maintain calcium homeostasis (Jang et al. 2009)

The two procedures are sequential with the resorption of old, micro-fractured bones followed by the remodelling of new bones, but the regulatory events leading to these procedures are not fully. A disruption of this balance is known to be closely related with severe bone diseases, such as OA and osteoporosis (Liao et al. 2011).

Bone formation (ossification) takes place with two diverse mechanisms: intramembranous and endochondral bone formation. Intramembranous bone

formation occurs by direct osteoblastic differentiation of the MSCs that forms only in the absence of a cartilaginous model. Examples of bones that develop through the intramembranous ossification are the flat bones of the skull, sternum, and scapula. During endochondral bone formation MSCs differentiate into chondrocytes that become hypertrophic and die releasing growth factors to induce differentiation of migrating MSCs into osteoblasts and promote angiogenesis in the dying hyaline cartilaginous template (Szpalski, Barbaro, et al. 2012; Scotti et al. 2010). Ribs and the long bones of the limbs are the bones that develop through endochondral ossification.

Intramembranous ossification is considered to be a simpler procedure to recapitulate and it is the bone formation method that has been mainly targeted by scientists for bone TE. However, recent publications have proved that endochondral ossification can be mimicked by bioceramic scaffolds (Teixeira et al. 2006) and even both bone formation mechanisms respectively (Scotti et al. 2010). Hence, bone formation is dependent on the substratum, which provides the appropriate environment for cellular adherence, proliferation, migration and differentiation (Logeart-Avramoglou et al. 2005). This is inspired from the biology as the majority of cells that manage to survive in 3D are attached onto a network of ECM, which TE aspires to imitate via scaffolds (Rodrigues & Jr. 2011).

Growth factors are proteins secreted by cells in an autocrine (self-acting), paracrine (locally-acting) and endocrine (systemically-acting) fashion. These proteins act as molecular signalling agents and govern proliferation, ECM production and differentiation.

Bone morphogen proteins (BMP) also known as CBFA1 are a family of growth factors responsible for the organisation of growth factors responsible for bone patterning and formation a transcriptional activator of osteoblast differentiation.

Runx 2 has two major isoforms type 1 (T1) and type 2 (T2). T1 Runx2 is expressed in early precursors of osteoblasts and chondrocytes and stimulates BMP2. Consequently, this enhances T2 Runx2 to stimulate osteoblast differentiation and maturation(Yang et al. 2011).

In intramembranous ossification MSCs are exposed to BMP which promotes osteogenesis through the expression of Runx2, collagen II and IX. Runx2 is downregulated and OPN is upregulated at the later stages of osteogenesis.

During endochondral ossification condensation and proliferation of cartilage cells appears to be regulated by the expression of Sox9, which is also responsible for the production of cartilage ECM; collagen II and aggrecan. Runx2 organises the transformation of cartilage into hypertrophic cartilage cells.

In vitro and *in vivo* models of osteogenesis have demonstrated that blood vessel formation is essential for bone regeneration (Brandi and Collin, 2006), since cells, nutrients, oxygen and soluble factors diffuse in the bone tissue through the vasculature. Different growth factors participate in angiogenesis, such as Vascular Endothelial Growth Factor (VEGF), Fibroblast Growth Factor-2 (FGF-2), and members of the Transforming Growth Factor beta (TGF-β) family (Madeddu 2005). Combination of angiogenic with osteogenic factors can enhance bone regeneration (Geiger et al. 2005). Subsequently, a system with various releases of growth factors like VEGF and BMP (Bone Morphogenetic Protein) at different rates might mimic the natural bone repair conditions promoting early vascularisation followed by neo-tissue formation (Jang et al. 2009).

1.4 Bone structure

Bone is consists of ECM and cells. The former is composed of inorganic phase - minerals, mainly hydroxyapatite (HAp); organic matrix (osteoid) that is consisted of collagen type I (90%) and non-collagenous proteins and other macromolecules (10%) and water (Ferreira et al. 2012) The elementary subunit of the natural bone is mineralised assembly of collagen type I nanofibrils that are organised in parallel. HAp nanocrystals are precipitated on the surface of these fibrils with the crystallographic c-axes aligned with the fibril long axis (Alves et al. 2010; Ferreira et al. 2012).

1.4.1 *Collagen*

Collagen type I is a predominant protein in the human body and the main organic component of the bone ECM. Three coiled tropocollagen macromolecules, approximately 300nm long, consist of a heterometrimeric triple helix that self-assembled into collagen fibrils that exhibit a characteristic banding pattern and following they associate into bundles forming collagen fibres. Collagen combines with non-collagenous proteins, proteoglycans and other bone ECM components.

Moreover, HAp mineralises collagen fibres strengthening the organic matrix (Ferreira et al. 2012)

1.4.2 *Hydroxyapatite*

HAp consists the two third of the dry substances of the natural bone and is the major inorganic bone component. It is composed of calcium phosphate (CP) (85-90%), calcium carbonate (8-10%), magnesium phosphate (1.5%) and calcium fluoride (0.5%) (Kolk et al. 2012) Biomineralisation of HAp *in vivo* take place in matrix vesicles (MVs) that are extracellular particles released by osteoblasts, chondrocytes, odontoblasts and tenocytes located in regions where initial matrix calcification occurs. The activity of MV phosphatases in combination with calcium –binding molecules that are concentrated within or near the MV membrane leads to the formation of the first mineral crystals. Following, the biological mineralisation initiates with the mineral release from the MVs into the extracellular fluid, which includes sufficient Ca^{2+} and PO_4^{3-} to stimulate crystal proliferation (Anderson 2003).

HAp crystals have hexagonal crystallographic symmetry and are precipitated outside or within the collagen fibres affecting defining the bone resistance and hardness (Weiner & Traub 1992; Kolk et al. 2012).

1.5 Bone tissue engineered scaffolds

A fundamental constituent for an efficient TE strategy is a 3D scaffold. Scaffolds aim to recapitulate the ECM of the defected tissue in order to support the new neo-tissue formation by being the template for cellular adhesion, proliferation, differentiation and organisation of the new formed tissue as the scaffold biodegrades. Also, the integration with the host tissue is essential. A bone scaffold can be characterised successful, if it has promoted and supported the tissue remodelling through all the stages. An ideal bone TE scaffold has specific requirements that should fulfil and are presented in Table 1-1.

Requirements for bone TE scaffolds	
Biocompatibility	The implanted material should be accepted by the organism and not be rejected due to immune reaction.
Bioactivity	Development of a direct strong bonding with the bone tissue that leads to cellular adhesion and differentiation.
Biodegradation	The rate of resorption is balanced with the natural bone regeneration rate preventing implant collapse or rejection (Hannink and Arts, 2011).

Table 1-1: Requirements for a bone scaffold

<table>
<tr><th colspan="2">Requirements for bone TE scaffolds</th></tr>
<tr><td>Bioresorption</td><td>The material can be broken down in the body by dissolution or cell mediated without being mechanically removed. Cells that are responsible for the resorption are multinuclear cells and osteoclasts (Guarino & Ambrosio 2010; Hutmacher 2000).</td></tr>
<tr><td>Osteoconductivity</td><td>Ability of a material to promote bone formation along its surface. A strong bond is formed between scaffold and host tissue without the presence of osteogenic factors and the formation of encapsulating is eliminated (Rezwan et al. 2006; Hutmacher 2000).</td></tr>
<tr><td>Osteoinduction</td><td>The stimulation of cell differentiation for bone modelling (Albrektsson & Johansson 2001).</td></tr>
<tr><td>Porosity</td><td>High porosity promotes nutrients and waste diffusion, bioactivity, bioresorption, osteoconductivity and osseointegration (Hannink & Arts 2011). The porosity of the human cortical bone is around 5-15 % (Mirzaali et al. 2015) and the cancellous bone 50- 90% (Wang et al. 2016).</td></tr>
<tr><td>Surface roughness</td><td>Surface roughness stimulates cell adhesion, proliferation and differentiation of dependent bone forming cells (LeGeros et al. 2008). High microporosity increases surface roughness.</td></tr>
<tr><td>Interconnectivity</td><td>High interconnectivity influences nutrient and waste diffusion, cellular migration, vascularisation, tissue ingrowth.</td></tr>
<tr><td>Pore Size</td><td>Each bone on the human body has a large variety of pore sizes depending on the area, the age and the individual. Based on experiments that have been performed with scaffolds, the pore size that is required from scaffolds in tissue engineering has been divided into the following categories:
<table>
<tr><td>Microporosity <50µm (Perez & Mestres 2015)</td><td>Promotes of protein and cell adhesion, cellular migration and osseointergration. Small pore size favours hypoxic conditions that result in chondrogenesis and endochondral ossification.</td></tr>
<tr><td>Macroporosity >50µm (Perez & Mestres 2015)</td><td>Enhances vascularisation, tissue ingrowth and intramembranous ossification</td></tr>
</table></td></tr>
<tr><td>Mechanical properties</td><td>The biomaterial properties in combination with the porosity of the scaffold determine the mechanical properties of the scaffold. The scaffold should be able to support the cells and withstand load-bearing forces.
<table>
<tr><th>Material properties</th><th>Trabecular bone</th><th>Cortical bone</th></tr>
<tr><td>Compressive strength (MPa)</td><td>0.1- 16</td><td>130- 200</td></tr>
<tr><td>Compressive modulus (GPa)</td><td>0.12- 1.1</td><td>11.5- 17</td></tr>
<tr><td>Young’s modulus (GPa)</td><td>0.05- 0.5</td><td>7- 30</td></tr>
</table>
(Gerhardt & Boccaccini 2010)</td></tr>
</table>

Table 1-1: Requirements for a bone scaffold

1.6 Bone grafts and bone graft substitutes for TE applications

Critical size bone defects require surgical intervention and implantation of bone substitute or artificial material – scaffold at the site of the injured or diseased tissue (Marklein & Burdick 2010). In traditional orthopaedic surgery, autografts (patient's tissue) or allografts (donor's tissue) have been widely used as bone substitute material .

1.7 Harvested bone grafts

1.7.1 *Autologous bone grafts*

Autologous bone grafts (autografts or autogenous transplants) are considered as the "gold standard" in remodelling damaged bone due to their efficacy and extremely low risk of disease transmission. They have inherited biocompatibility, since they derive from the same patient, so they cause the minimum immunological reaction. They have excellent osteoconductive, osteoinductive and osteogenic properties, which can be compared with every other graft. They contain surviving cells and growth factors that promote cell differentiation and vascularisation. Moreover, autografts include matrix proteins and have natural architecture; therefore they are mechanically efficient and can support bone growth sufficiently (Dinopoulos et al. 2012). Bone autografts can be classified into three groups: cancellous, cortical and free-vascularised grafts (Finkemeier 2002).

Autologous cancellous grafts are good fillers for the defected area, but they do not support the structure immediately as autologous cortical bone grafts, because their mechanical properties are not very robust due to their advanced porosity. However, they integrate fast and attain mechanical properties comparable to the cortical grafts within one year. It has been reported that autologous cancellous grafts are more osteogenic than cortical. A noteworthy advantage of the cancellous grafts is that they contain endosteal cells and osteoblasts on their surface, so the latter has the potential to be transferred to the defected area and participate to the regeneration accelerating the osteogenesis. They are osteoconductive since the high porosity and interconnectivity of these grafts stimulate the neo-vascularisation and new MSCs and MSC-origin cells infiltration. They are osteoinductive due to the growth factors they naturally contain and release during their resorption promoting osteogenic differentiation. During the resorptive procedure of the graft, cytokines are also released that may contribute in the bone healing (Dinopoulos et al. 2012).

Autologous cortical grafts have osteoconductive, little or no osteoinductive and osteogenic properties, due to the viable osteoblasts that are contained (Finkemeier, 2002; Dell et al., 2000). Non-vascularised autologous cortical grafts can support the bone structure instantly. However, due to the lack of vasculature, there is resorption of necrotic osteons before the neo-tissue formation. On the one hand, this results in the revascularisation and remodelling of the tissue; but on the other hand, the bone porosity increases, so the graft becomes weaker. In practise, non-vascularised cortical bone grafts have lower mechanical properties than the vascularised within six weeks after the implantation (Dinopoulos et al. 2012).Additionally, the number of cells in the autologous cortical graft is lower than the cancellous, so the bone repair is considerably slower. Vascularised cortical bone can accelerate the procedure of bone healing and their restoration is analogous to the normal bone. Even though, autologous cortical grafts have enhanced mechanical properties in relation to cancellous, internal or external fixation is required to avoid the potential of fracture (Sen & Miclau 2007).

Regardless all the advantages of the autografts and the high success rate, there are important drawbacks including limited availability; need for second operation to harvest the graft resulting in prolonged morbidity of the patient and increased blood loss; long operating time and poor aesthetic result; risk of infection and fracture; issues with the resorption (Kolk et al. 2012).

1.7.2 *Allografts*

An alternative to autografts are allografts (allogenic bone graft) obtained from either living donors after arthroplasty or cadaveric bone tissue eliminate the limitation of the autografts. Bone allografts are available in various preparations, as demineralised bone matrix (DBM), cortico-cancellous or cortical grafts, osteochondral and various bone parts, morcellised and cancellous chips (Dinopoulos et al. 2012)

They are osteoconductive and reduced osteoinductive, but do not have osteogenic properties due to the absence of living cells, since they have been irradiated of freeze-dried (Finkemeier 2002). A further advantage of allografts is that there is no need for donor-site morbidity and sacrifice host tissue. However, significant disadvantages of the allografts are the risk of transmission of infectious agents, toxins, malignancies; rejection and limited supply.

Allografts are available in market and they differ according to the manufacturing procedure and type of bone tissue. Examples of the already existent in market are Maxgraft® (botissdental GmbH, Berlin, Germany) and ICB™ (Rocky Maintain Tissue Bank, Colorando, USA) are allogenic bone replacement materials from living donors. Donors have to give their consent and then are screened for potential infectious diseases. Donor bones are chemically cleaned without affecting the mineralised tissue and sterilised via irradiation (Kolk et al. 2012).

1.8 Anorganic bone grafts

During the last years, a variety of biomaterials have been produced to be used as bone scaffolds including metals, biopolymers, bioceramics and composites. Each developed material has specific properties associated with biocompatibility, bioactivity, bioresorption, osteoconduction, osteoinduction and mechanical properties that affect the fate of the cells that are cultured on them and consequently the probability to form new tissue. Bioceramics are the materials that have been extensively investigated and used due to their effectiveness and common characteristics with the HA of the bone (Stevens 2008).

1.8.1 *Metals*

Metals, such as titanium and stainless steel, are biocompatible with high mechanical properties. However, they are not biodegradable, the released particles from the wear debris of the metals can be dangerous, and their high stiffness promotes stress shielding, so the native tissue is prevented from mechanical stimulation (Barone, et al., 2011). As it has been demonstrated from the literature, mechanical stimulation promotes osteogenic differentiation (Mauney et al. 2004) Additionally, metals are bioinert, which means that they cannot interact with the adjacent tissues resulting in not bonding with the tissue and finally failure of the implant –scaffold.

Recently novel biodegradable metal scaffolds have been invented that overcome some of the innate drawbacks of the metals. Magnesium alloys have appropriate degradation rate (Witte et al. 2007) and increased osteoinductive properties probably due to the corrosion product magnesium hydroxide which can temporarily increase osteoblastic activity and decrease the number of osteoclasts (Janning et al. 2010). Also, they have strong bone-implant interface and the degradation products neither induce an inflammatory reaction nor affect cellular blood composition (Castellani et al. 2011).

1.8.2 *Bioactive Ceramics*

The most common materials used for bone scaffold fabrication are calcium phosphate (CaP) ceramics and in particular, HAp and tricalcium phosphates (TCP). A wide variety of different chemical compositions (Ca: P) and morphology has been formulated. CaP ceramics are considered to have excellent biocompatibility, bioactivity and biodegradability and do not cause immune response or cytotoxicity after implantation. They are osteoconductive, but they do not express osteoinductive or osteogenic properties (Lichte et al. 2011).

CaPs are polycrystalline ceramics that are fabricated usually by sintering different compositions of apatite under specific pressure and temperatures. Their chemical structure is similar to the mineral phase of natural bone, so they promote release of phosphate and calcium ions inducing scaffold-host tissue (bone) strong bonding.

An important drawback of ceramics for clinical applications is their brittleness and poor mechanical properties (Lichte et al. 2011).

1.8.2.1 Synthetic HAp

A large range of HAp - $Ca_{10}(PO_4)_6(OH)_2$ scaffolds have been formulated and advocated for bone TE applications, because the inorganic constituent of the ECM of the native bone is formed by precipitated HAp crystals (Szpalski, Wetterau, et al. 2012).The component ratio Ca:P is high importance for the bioactivity of the material with the optimum to be 1.67.The biocompatibility of the material depends on its chemical and mineralogical composition. In general, HAp is brittle and has slow rate of resorption; however, it has been demonstrated that sintered HAp has no or extremely slow biodegradation rate compared to the raw- precipitated (The biodegradation is also affected from the crystallite size, where the nano-size (bone-like) has higher solubility (Kolk et al. 2012). Nano- HAp has trivial level of cytotoxicity *in vitro* and shows good cellular attachment and proliferation HA scaffolds are extremely osteoconductive , but not as osteogenic (Patel et al. 2010)However, the material becomes more osteogenic when osteogenic cells have been seeded on it (patel, et al., 2010).

Some of the commercial materials that contain HAp are: Actifuse (ApaTech, UK), Apaceram (Pentax, Japan), ApaPore (ApaTech, UK), Bioroc (Depuy-Bioland, France), Bonefil (Pentax, Japan), Bonetite (Pentax, Japan), Boneceram (Sumitomo Osaka Cement, Japan), BoneSource (Stryker Orthopaedics, NJ, USA), Calcitite

(Zimmer, IN, USA), Cerapatite (Ceraver, France), Neobone (Toshiba Ceramics, Japan), Ostegraf (Ceramed, CO, USA), Ostim (Heraeus Kulzer, Germany), Synatite (SBM, France) (S. V Dorozhkin 2010).

1.8.2.2 Tricalcium phosphates (TCP)

TCP - $Ca_3(PO_4)_2$ ceramics are analogous to amorphous bone precursors making them promising for bone TE applications, because ossification depends on the calcium and phosphate concentration, TCP ceramics (α-TCP and β-TCP), as HAp, are highly biocompatible, osteoconductive, but TCP are have faster biodegradation rate than HAp. α- and β-TCP have the same chemical composition, but they have different physical properties, such as structure, solubility and density, which influence their biological properties and their applications (Carrodeguas & De Aza 2011). Both are used in orthopaedics, dentistry and maxillofacial surgery, but α-TCP is main component of hydraulic bone cements, whereas β-TCP is the constituent of mono or biphasic bioceramics.

1.8.3 *Alpha - Tricalcium phosphate (α-TCP)*

α-TCP is non-toxic, biocompatible, osteoconductive, *in vitro* and *in vivo*, has increased solubility than β-TCP and biodegradability than HAp, b-TCP and biphasic (HAp/b-TCP) bioceramics. It has adsorption time of up to 24 months (pure-phase α-TCP), so it can be replaced by neo-tissue formation faster than other CaPs, making it suitable for implant applications. Biomedical grade a-TCP bioceramic granules are available in market as Biobase (Germany; Implant Support Services CC, Pretoria, South Africa), a-TCP 13-1000 (InnoTERE GmbH, Dresden, Germany) and ArrowBone™ (BrainBase Corporation, Tokyo, Japan) (Carrodeguas & De Aza 2011).

1.8.4 *Beta - Tricalcium phosphate (β-TCP)*

β-TCP is biodegradable and osteoconductive without being cytotoxic. Nevertheless, it can cause immunological reaction, has poor mechanical properties due to the rapid breakdown that exceeds the bone formation rate (Kolk et al. 2012)

Commercial β-TCP are Bioresorb (Sybron Implant Solutions, Germany), Biosorb (SBM S.A., France), Calciresorb (Ceraver, France), Cerasorb (Curasan, Germany), Ceros (Thommen Medical, Switzerland), ChronOS (Synthes, PA, USA), Conduit (DePuy Spine, USA), JAX (Smith and Nephew Orthopaedics, USA), Osferion (Olympus Terumo Biomaterials, Japan), OsSatura TCP (Integra Orthobiologics, CA, USA) and Vitoss (Orthovita, PA, USA (S. V. Dorozhkin 2010)

1.8.5 *Bioglasses*

Bioglasses are amorphous, hard solid materials that are based on acid oxides, such as aluminium oxide, silicon dioxide and basic oxides, such as magnesium oxide and zinc oxide. The resorbability of the bioglasses depends on the proportions of sodium oxide, calcium oxide, and silicon-dioxide. Bioglasses are biocompatible, osteoconductive, osteoinductive and more mechanically robust in relation to most calcium phosphates. Moreover, bioglasses form strong bond with the bone forming Ca-P layer and with soft tissue, which has not been reported for other bioactive materials (Saito et al. 2005; Lichte et al. 2011)

Silicate bioglasses as 45S5 Bioglass® increase the secretion of vascular endothelial growth factor promoting *in vivo* vascularisation (Hench 2009).

1.8.6 *Bioactive glass-ceramics*

Bioactive glass ceramics are composed of two crystalline phases, an apatite and a wollastonite phase.

A/W is the most used glass ceramic in the clinic. It was developed by Kokubo et al. in 1982 (Kokubo et al. 1982). It is an FDA approved material and is one of the most clinically used glass ceramics. It contains apatite and β -wollastonite crystals, 50-100nm, embedded in a glassy phase. A/W combines biocompatibility, bioactivity, osteoconductivity and bioresorbability *in vivo* with high mechanical properties in comparison to the natural bone and other glass-ceramics (Kokubo 1990; Anon 1991; Dyson et al. 2007).

1.9 Fabrication methods for bone TE applications

Characteristics such as biocompatibility, bioactivity, resorption, osteoconductivity, osteoinduction, biodegradability, mechanical properties depend on the material that is used. However, porosity, interconnectivity, surface roughness are influenced by the scaffold fabrication technique that is used. A variety of methods for scaffold fabrication has been developed to obtain architecture similar to the natural bone. A sample of the existing scaffold fabrication techniques are described in Table 1-2.

Method	Description
Sintering	Loose glass-ceramic particles are packed into a mould or pressed into a compact and then undergo heat treatment-sintering process. The compact is called “green body” before sintering and “brown body” after sintering (Johnson & German 1996).
Organic phase burning-out	Ceramic (glass) particles are blended homogenously with organic phase granules and are packed into a mould or pressed into a compact as it happens in traditional sintering. During thermal treatment, the organic phase burns out acting as pore former and the inorganic particles sinter (Chevalier & Gremillard 2009).
Sponge replication	A porous polymeric template is impregnated in ceramic (glass) slurry that infiltrates the structure and the ceramic particles attach to the template surface. Excess of slurry must be removed to conclude to homogenously coated foam struts. The organic phase removes during heat treatment and the ceramic particles sinter. The “brown body” has similar architecture as the natural cancellous bone.
Solvent casting/particulate leaching (SCPL)	Water-soluble particles with specific granule size are added into a polymer that has been dissolved into an organic solvent. Ceramic (glass) grains can be introduced into the mixture. The final mixture is casted into a mould. After the solvent evaporation, the structure that is a compact with polymer and particles can be bathed to dissolve the water-soluble particles leaving behind a porous structure (Vitale-Brovarone et al. 2010)
H_2O_2 foaming	Ceramic (glass) granules are mixed homogenously with H_2O_2 solutions. This mixture is casted into a mould and thermal treat at 60°C in an oven to foam. The foaming procedure is followed by sintering of the ceramic structure (Navarro et al. 2004).
Starch consolidation	Ceramic (glass) powder and starch powder (corn-, rice-, potato-derived) are mixed with distilled water and continuously stirred at 70-80°C to obtain homogenous suspension. Starch swells due to the water uptake leading to gelatinous material. After consolidation, heat treatment follows to remove the organic phase and sinter the ceramic .
Coating methods	Polymeric templates are coated homogenously via slurry dipping by a layer of ceramic (glass) (Baino et al. 2009)
Microsphere sintering	Through emulsion/solvent evaporation, ceramic (glass)/ polymer composites are fabricated. These composites are casted in mould and sintered (Lu et al. 2003).
Thermally induced phase separation (TIPS)	A polymer is dissolved into a solvent and stirred to result in a homogenous solution. Ceramic (glass) powder can be introduced, while the stirring continues. The mixture is casted in moulds and phase separation is induced by lowering the temperature of the mixture. The solvent is sublimated

Table 1-2: Examples of ceramic (glass) or polymer/ceramic scaffold fabrication methods for bone TE applications and their analytical description.

Method	Description
Thermally induced phase separation (TIPS)	through freeze-drying leaving a solidified, porous polymer/glass (Guarino & Ambrosio 2010).
Freeze casting	A liquid suspension (aqueous or not) that contains ceramic powder must be dispersed in the liquid medium (the solvent) (dispersant and plasticizer can be used). The slurry is casted into a mould and stored at low temperature. Finally, the solidified phase is sublimated under reduced pressure and finally sinters (Deville 2008).
Rapid Prototyping (RP)/ Solid freeform fabrication (SFF)	A group of computer aided manufacturing (CAM) techniques that use computer aided design (CAD) programs or computer based medical imaging modalities, such as MRI and CT to generate data that can rapidly produce 3D structures (Lee & Chow 2012). A variety of RP techniques that can be used for TE applications (Figure 1-1). Many of the RP methods mainly use polymers. The constructs prepared from these methods can be used as negative templates for ceramic scaffolds or ceramic particles can be incorporated in the polymeric materials resulting in hybrid ceramic/polymer scaffolds.

Table 1-2: Examples of ceramic (glass) or polymer/ceramic scaffold fabrication methods for bone TE applications and their analytical description.

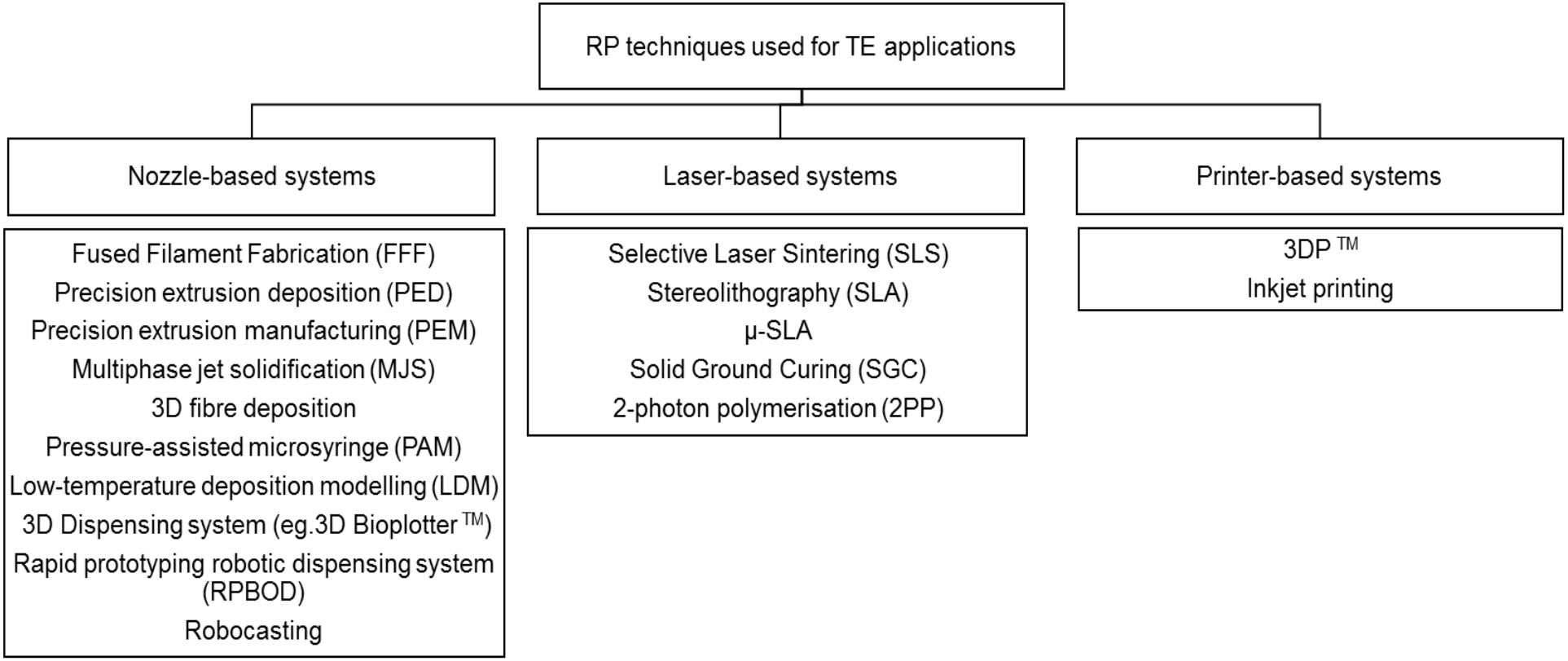

Figure 1-1: Classification of Rapid Prototyping used for Tissue Engineering applications. Figure adapted from Billiet et al. 2012.

Chapter 2 GENERAL MATERIALS AND METHODS

This chapter focuses on the experimental materials and methods utilised throughout this thesis. Many methodologies have been exploited in more than one result chapters and constitute the basis for a number of experiments that were implemented. This chapter emphases on the material fabrication, material characterisation and tissue culture practices for the various *in vitro* studies. Further description and explanation of individual experimental methodologies are explicitly mentioned in the corresponding chapters.

2.1 General Laboratory Procedure

All laboratory procedures were performed in compliance with safety regulations designated from the University of Newcastle safety policy and publications. All experimental processes were carried out subsequent to full risk assessment form and in compliance with Control of Substances Hazardous to Health (COSHH) regulations. All laboratory work was carried out in compliance with the 'University Safety Policy' and the safety policy of the various departments the experiments took place. Tissue culture was accomplished in accordance to regulations for containment of class II pathogens. Aseptic technique and supplementary antibiotics were used during tissue culture procedures to avoid bacterial contamination. Human tissues (bone marrow aspirate and femoral head fragment) were manipulated according to the Human Tissue Act (HTA). High quality deionised H_2O produced by a Purewater 300 water purification system (Purite UK). All solutions were made using water as a solvent unless specified otherwise.

2.2 Chemicals and glassware

All chemicals were purchased from Sigma Aldrich (Gillingham, Dorset, UK), glassware were obtained from VWR International (Lutterworth, Leicestershire, UK) unless stated otherwise.

2.2.1 *Consumable labware*

Tissue culture flasks (25 cm^2, 75 cm^2 and 225 cm^2), tissue-culture treated 6-well, 12-well, 24-well, 48-wellm 96-well plates and sterile plastic serological pipettes (5 ml, 10 ml, 25 ml, and 50 ml) were purchased from Costar UK Ltd., High Wycombe, UK. 100µm cell strainers, cryovials, pipette tips (1ml, 200µL, 20 µl, 10 µl), 0.22 µm filters, 13 mm diameter glass slides (Fisher Scientific, Loughborough, UK); 7 ml bijoux, 100

ml sterile plastic containers, syringes (10 ml, 20 ml, 50 ml) (Scientific Laboratory Supplies); 50 ml centrifuge tubes (Grenier Bio One, Stonehouse, UK); 1.5 ml, 0.5 ml Eppendorf tubes (Sarstedt, Leicester, UK).

2.2.2 *Apatite- Wollastonite ceramic powder*

Apatite-wollastonite (A-W) glass-ceramic was prepared by Glass Technology Services (GTS), Sheffield, UK as reported by Kokubo (Kokubo et al. 1987; Kokubo 1991). Briefly, A-W glass was produced by mixing the reagents reported in Table 2-1. The glass ceramic was melted at 1450 ˚C for 2 hours and then shock quenched into cold water. The cracked frits were ground ready for subsequent sieving.

Reagents	**MgO**	**CaO**	**SiO_2**	**P_2O_5**	**CaF_2**
wt%	4.6	44.7	34.0	16.2	0.5

Table 2-1: Composition of A-W glass

2.2.3 *Reagents for Simulated Body Fluid solution*

To prepare the SBF solution the reagents described in Table 2-2 were used in the specific order with referred quantities. Ion -exchanged and distilled water was used for the dilution of the reagents and preparation of SBF solution.

Order	**Reagent**	**Amount**	**Container**	**Purity (%)**	**Formula weight**
1	NaCl	8.035 g	Weighing paper	99.5	58.4430
2	$NaHCO_3$	0.355 g	Weighing paper	99.5	84.0068
3	KCl	0.225 g	Weighing bottle	99.5	74.5515
4	$K_2HPO_4 \cdot 3H_2O$	0.231 g	Weighing bottle	99.0	228.2220
5	$MgCl_2 \cdot 6H_2O$	0.311 g	Weighing bottle	98.0	203.3034
6	1.0M-HCl	39 ml	Graduated cylinder	—	—
7	$CaCl_2$	0.292 g	Weighing bottle	95.0	110.9848
8	Na_2SO_4	0.072 g	Weighing bottle	99.0	142.0428
9	Tris	6.118 g	Weighing paper	99.0	121.1356
10	1.0M-HCl	0–5 ml	Syringe	—	—

Table 2-2: Reagents for SBF solution. Table adapted from Kokubo & Takadama 2006.

2.2.4 *Cell culture medium*

DMEM is a basal medium that contains inorganic salts, amino acids, glucose, vitamins, sodium pyruvate and ferric nitrate. Phenol red can be included in DMEM as a pH indicator highlighting potential bacterial infection. DMEM contains no proteins or growth factors; therefore, it is supplemented with foetal bovine serum (FBS) and GlutaMax. FBS supplies the medium with water-insoluble nutrients, growth factors, hormones, proteases inhibitors, as well as binds and neutralises toxic moieties. GlutaMax is L-alanine-L-glutamine, which is a dipeptide, is more stable in solutions that L-glutamine and does not degrade spontaneously. L-glutamine is an essential amino acid for the cell energy production as well as the nucleic acid and protein synthesis. Penicillin/ Streptomycin was added to prohibit unwanted contamination.

The culture medium that was used for tissue culture of human mesenchymal stem cells contained DMEM with 10% FBS, 5ml Glutamax and 5ml Penicillin/ Streptomycin (detailed in section 2.6.3).

In this study the culture medium was mentioned as basal medium to distinguish from the osteogenic medium.

2.2.5 *Osteogenic medium*

The osteogenic medium was prepared by addition of 50 µg/ml l-ascorbic acid, 10 mM glycerophosphate and 100 nM dexamethasone in the basal medium (Kim et al. 2014; Seo et al. 2014; Langenbach & Handschel 2013).

2.3 Material preparation

2.3.1 *SBF solution preparation*

This protocol has been adapted from Kokubo & Takadama 2006.Before the preparation, a plastic bottle with 700 ml of distilled water was warmed in a beaker with water warmed at 37°C on a hot plate-magnetic stirrer.

Each reagent from NaCl to Na_2SO_4 mentioned in Table 2-2 were added each one after the complete dissolution of the previous one. Distilled water was added to reach a 900 ml volume. The pH of the solution was measured to be 2.0±1.0 Tris was added slowly whilst measuring the pH. When the pH was under 7.45, the dissolution of Tris addition was halted. Then, drop-wise the 1 M HCl was added to lower the pH to 7.42±0.01. The remaining Tris was added in the solution, or until solution reach pH

7.40. Distilled water was added to reach a final volume of 1000 ml. Solution was kept at room temperature to cool and then was stored at 4°C for 28 days maximum.

2.4 Post-processing

The development of post-processing consists of the characterisation of pre-sintered, sintered powder and fabricated scaffolds with different manufacture techniques. The purpose of this development was to attain the optimum scaffold that combined macroporosity, mechanical strength and bioactivity.

2.5 Materials and scaffolds characterisation

A range of techniques was employed to assess the influence of different parameters on the A-W powder and on the scaffolds that were fabricated. Scaffolds were evaluated after modifying the fabrication parameters and sintering temperatures morphologically; mechanically and chemically.

2.5.1 *Shrinkage in heat treatment*

The shrinkage volume that occurred during the different heat treatments (Table 3-3) was calculated by the equation:

$$\boldsymbol{Volume\ Shrinkage}\ \% = \frac{(\boldsymbol{Vg}-\boldsymbol{Vb})}{\boldsymbol{Vg}}\ \%$$

Equation 2-1: Calculation of the volumetric shrinkage of scaffolds after sintering.

Vg is the volume of the “green” part and Vb is the volume of the “brown”- sintered part. The volume of the parts was calculated by their actual radius and height using an ABSOLUTE digimatic caliper (Mutitoyo; UK).

2.5.2 *Inductively coupled plasma atomic emission spectroscopy (ICP)*

At each time-point of the SBF test (§2.5.10), after the scaffold was removed, the solution was filtered using syringe and filter 0.22μm. The elemental composition of the solutions was analysed for ions using Spectro Ciros Vision ICP-ES (Sheffield University). Results were given in μg/ml.

2.5.3 *Porosity*

The porosity of scaffolds fabricated with different techniques, particle ranges and heat treatments was assessed and is described below.

The porosity for the sintered scaffolds that were derived from drying mixing was calculated using the theoretical mass technique via the equation:

$$\boldsymbol{p = 1 - \frac{m}{\rho V}}$$

Equation 2-2: Calculation of porosity using the theoretical mass technique.

Where m represents the mass of the sintered scaffold, ρ the density of the sintered powder and V the volume of the scaffold was calculated by the linear dimensions. The mass was measured using an analytical balance (ABT; Kern) and an ABSOLUTE digimatic caliper (Mutitoyo; UK) was used for the linear measurements. The density of the sintered A-W has been reported to be 3.07g/cm^3 (Pattanayak 2009).

The porosity of scaffolds prepared from slurries was estimated from another theoretical method, the Archimedes method.

Samples were weighed using a density determination kit in an analytical balance (ABT; Kern). The dry mass was recorded, then the scaffold was submerged under water and the submerged mass was measured. After the scaffolds was taken out of the water, the wet mass was recorded. The porosity was calculated using:

$$\%\,\boldsymbol{Porosity = \frac{(wet\ mass - dry\ mass)}{(wet\ mass - submerged\ mass)} \times 100}$$

Equation 2-3: Calculation of porosity using a density determination kit based on the Archimedes method.

2.5.4 *Compression test*

The mechanical properties of the scaffolds were assessed by the means of compressive test using Tinius Olsen; Instron machine at a 1.0mm/min crosshead speed with crosshead maximum force at 5kN for porous scaffolds and 25 kN for dense scaffolds. Scaffolds that had uneven surfaces were ground and polished using a programmable grinder-polisher, EcoMer/AutoMet Pro, Buehler, Germany).

The stress was calculated from the following equation:

$$\boldsymbol{\sigma = F/A}$$

Equation 2-4: Calculation of stress using an applied force on a surface area.

where F represents the applied force, A the cross-sectional area.

$$A = \pi \cdot r^2$$

Equation 2-5: Calculation of surface area of a circle.

where r represents the radius of the cylinder or pellet.

The strain % was calculated from:

$$\varepsilon\% = (\Delta h / h0) \cdot 100$$

Equation 2-6: Calculation of strain % during mechanical testing.

where Δh is the extension an h0 is the initial height of the scaffold.

Five replicates were used for the mechanical characterisation calculating the Young's modulus from the slope that resulted in the graph stress-strain. The strain that was used for the calculations was 2%.

2.5.5 *Stereomicroscopy*

The green bodies, sintered scaffolds and top surface of scaffolds that were stained with Toluidine blue and Von Kossa staining were observed using optical stereomicroscopy Nikon SMZ1500.

2.5.6 *Scaffold fixation and dehydration prior SEM analysis*

Scaffolds that were in culture medium in combination with cells were fixed with 2.5% (v/v) gluteraldehyde in PBS overnight at 4˚C prior to gold coating. These were washed three times with PBS and dehydrated with serial dilutions of ethanol in water (25:75, 50:50, 75:25, 100: 0) followed by serial dilutions of HDMS in ethanol (25:75, 50:50, 75:25, 100: 0). All the ethanol: water washes were incubated at room temperature for 5 min and the HDMS: ethanol washes were incubated at room temperature for 10 min. Samples were left in pure HDMS overnight at room temperature under a fume cupboard until completely air-dried. This fixation and dehydration technique was used for all samples unless is stated otherwise.

2.5.7 *Scaffold mass change*

The mass of the different scaffolds was measured before they were immersed in SBF and at each time-point during the bioactivity assay after they were completely dried (§2.5.10) using an ATB Kern balance.

The degree of the mass change was calculated following the equation:

$$\mathbf{\Delta m\%} = \frac{\mathbf{m_f - m_0}}{\mathbf{m_0}} \times \mathbf{100}$$

Equation 2-7: Calculation of degree of mass change.

where m_0 was the mass of the scaffold before its immersion in the SBF solution and m_f was the mass of the scaffold after it was removed from the SBF (Pramanik et al. 2015).

2.5.8 *Scanning electron microscopy (SEM) and energy dispersive X-ray spectroscopy (EDX)*

The particle morphology of powders and the microstructure of the glass ceramic scaffolds and the cell morphology on scaffolds were studied via scanning electron microscopy.

For examination on the SEM, the glass ceramic scaffolds were cut using a precision cutter (IsoMet 5000, Buehler, Germany) with diamond-cut blade thickness 0.5 mm and/or were ground using the programmable grinder-polisher, EcoMer/AutoMet Pro, Buehler, Germany).

Samples seeded with cells were treated according to protocol mentioned at §2.5.6.

All dry samples (powder or scaffolds) were loaded on aluminium stubs with carbon-coated stickers. When porous samples were adhered on the aluminium stubs colloidal silver paste was used. These were then sputter-coated with gold to a thickness of 15 nm using a polaron SEM (Quorum Technologies, Sussex, UK) sputter coater. The gold-coated samples were transferred in three different microscopes (Cambridge instrument stereoscan 240, UK; Hitachi S2400 Scanning Electron Microscope, UK; Jeol LV) and images were captured at 10-15 kV.

To identify the existing elements on scaffolds, samples were analysed using EDX. All samples were carbon-coated using an emscope TB500. Samples were analysed using an XL30 ESEM-FEG (Environmental Scanning Electron Microscope-Field Emission Gun) using a 20 kV ebeam. The EDXWAS A Rontec system and the software was called Rontec QuanTax.

To analyse the elements that were identified during EDX analysis, the percentage of the normalised concentration was used. For the Ca/P ratio, the atomic percentage of each element was used.

2.5.9 *X-ray diffraction (XRD)*

- Sample preparation

Two samples were characterised by XRD technique at room temperature. For the XRD analysis the samples have to be in powder form. The raw material was already in powder, so there was no need for further preparation. However, the sintered sample that was sintered in pellet form was milled in Pulverisette 6 (Planetary mono mill, Fritch, Gerhardt, UK) at 350 rpm for 40 min. The crystals precipitated in the pre-sintered (raw) sample and the sintered according to the heat treatment B (Table 3-3) were analysed using XRD.

- Equipment and experimental process

The instrument used for XRD is a PANalytical X'Pert Pro MPD, powered by a Philips PW3040/60 X-ray generator and fitted with an X'Celerator detector. A copper (Cu) anode supplied with 40kV and a current of 40mA generated Cu-Kα X-ray radiation, which has a characteristic wavelength (λ) of 1.5418 Å.

Data were collected over a range of at least 5-90^{o} 2θ with a step size of 0.0334^{o} 2θ counting 150 sec per step. Fixed anti-scatter and divergence slits of 1/4^{o} were used together with a beam mask of 10mm. All scans were carried out in ‘continuous’ mode using the X’Celerator which is an ultra-fast X-ray detector that uses RTMS (Real Time Multiple Strip) technology. The X’Celerator operates as if it were an array of over a hundred detectors simultaneously collecting X-rays diffracted from a sample over a range of 2θ angles. It is therefore able to give high quality diffraction patterns in approximately 1/100 of the time an older style diffractometer would require.

Phase identification was carried out by means of the X'Pert accompanying software program PANalytical High Score Plus in conjunction with the ICDD Powder Diffraction File 2 database (1999), the American Mineralogist Crystal Structure Database (March 2010) and the Crystallography Open Database (September 2011; www.crystallography.net).

2.5.10 *Bioactivity and biodegradation assay*

SBF (§2.2.3, §2.3.1) was used to assess the bioactivity and degradation of the scaffolds.

Samples were immersed in SBF in plastic tubes and were incubated in an orbital shaker incubator at 37°C at 120 rpm (Maçon et al. 2015). In each relative chapter, it is defined how much SBF was used per sample. Samples were tested after 4 h, 8 h, 1, 3, 7, 14 and 21 days. At each time-point, samples were removed from the incubator, immersed in deionised water and then acetone to stop the reaction. Samples were left to dry at 50°C for 2 days. The solution was filtered using filter 0.22μm and was sent for ICP analysis (§2.5.2). SBF was used as control.

2.6 Tissue cell culture

All tissue culture procedures were accomplished according to the Newcastle university regulations for Class II pathogens. Tissue culture was performed using aseptic technique in a class II microbiological safety cabinet (Contained Air Solutions Ltd., Manchester, UK) fitted with high efficiency particulate air (HEPA) filters. All liquids used for cell culture were pre-warmed at 37˚C in a Clifton unstirred water bath unless otherwise stated. Cells were incubated in MCO-18AC CO_2 incubator (Sanyo, UK) that was maintaining a humidified, 37˚C, 5% carbon dioxide atmosphere.

2.6.1 *Material and liquid sterilisation*

Glass slides were sterilised under UV lamp (UPV™, UVLMS-38, EL series; Fisher Scientific, USA) at 254nm wavelength for 30 min in a class II safety cabinet. Ceramic scaffolds were sterilised prior to use in tissue culture using a 2100 classic Prestige autoclave (Progen Scientific, London, UK) with a 16-minute cycle 1.4 bar pressure and 121˚C temperature. Ceramic scaffolds, were then soaked in 70% v/v ethanol and washed thrice with phosphate buffered saline (PBS; Gibco, Life technologies Ltd., Paisley, UK) to remove any ethanol residue.

Liquids were purchased sterile and endotoxin free. In any other case, liquids were sterilised in a 2100 classic autoclave as mentioned before. Liquids that were temperature sensitive were sterilised by filtration. Liquids with volume less than 50 ml were filtered using an appropriate sterile syringe and a 0.22 μm filter adapter

(Millipore, Fisher Scientific, Loughborough, UK). Liquids with volume greater than 50 ml were filtered using a Stericup-GP sterile vacuum filtration system that combines a 0.22 µm pore size fast flow polyethersulfone filter membrane with a 250ml flask (Millipore, Fisher Scientific, Loughborough, UK).

2.6.2 *Human mesenchymal stem cells (hMSCs) - hTERT Y201 cell line*

Y201 cells are immortalised human mesenchymal stem cell line overexpressing human telomerase reverse transcriptase (hTERT) that were donated by Prof. Paul Genever, University of York (James et al. 2015).

2.6.3 *Y201 cell line culture*

Y201 cells were maintained in hMSC culture medium containing Dulbecco's Modified Eagle's Medium (DMEM) (D5523; Invitrogen, Paisley, UK) with 10% (v/v) FBS (F9665, batch 062M3397; Invitrogen-Gibco, UK), penicillin/ streptomycin 1,00U/Ml (15140; Invitrogen-Gibco, UK) and 20mM GlutaMax^{TM} (35050; Invitrogen-Gibco, UK). Old medium was aspirated and it was replenished with fresh every 2 days.

2.6.4 *Cell passaging*

Cells were allowed to proliferate in a flask until they reached ~70-80% confluency before detachment using trypsin. The medium was aspirated and the flask was washed using phosphate buffered saline (PBS). Pre-warmed 0.005% trypsin/ethylene diaminetetraacetic acid (EDTA) (Life-Technologies, UK) introduced in the flask and was incubated at 37°C in humidified atmosphere for 2 - 3 minutes ensuring the cell detachment visually under microscope. Trypsin is a serine protease that cleaves peptide bonds and disrupts cell-cell junctions and cell matrix attachments allowing the cells to dissociate from the adjacent cells and the flask. Trypsin was inactivated with hMSC culture medium and the cell suspension was centrifuged at 1200rpm for 5 min. Supernatant was aspirated and the cell pellet was resuspended in an appropriate volume of hMSC media to subculture the cells at one third (1/3) of the total cell number.

2.6.5 *Cell counting*

During the cell trypsinisation procedure that was described in 0, before the homogenised cell suspension was centrifuged, an aliquot of 20µl was used to calculate the cell population. Cells were counted using a Fuchs-Rosenthal

haemocytometer (Marienfeld, Lauda-Königshofen, Germany) with a depth of 0.200 mm (Figure 2-1) under a viewed using a Leica DMIL (Leica microsystems, Wetzlar, Germany) inverted light microscope with phase contrast filters. 5 or more 1 mm^2 areas of the haemocytometer were counted and the average was then divided by two and multiplied by the dilution volume (ml) to provide total cell number $\boldsymbol{x}$ x 10^4.

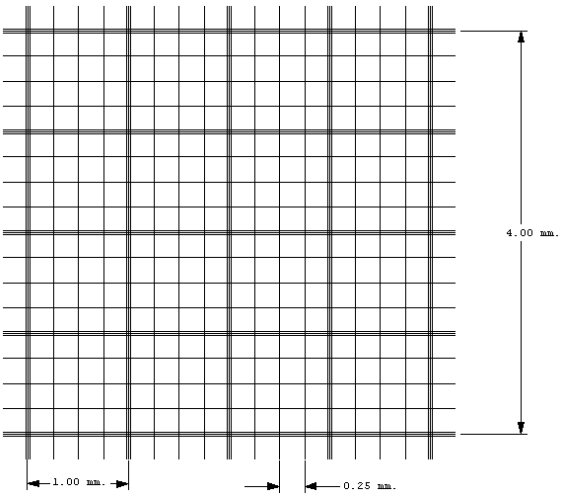

Figure 2-1: Illustration of Fuchs-Rosenthal haemocytometer.

2.6.6 *Cell cryopreservation*

Cells that were not for use were cryopreserved until they were need. Cells that reached 70-80% confluency, where trypsinised as described in §2.6.4. Briefly, they were detached from tissue culture plastic using 0.05% trypsin-EDTA and they were centrifuged at 200g.Following this step, they were resuspended in freezing medium that is composed of 10 v/v % DMSO in FBS that was kept on ice. Cell suspension was transferred into cryopreservation vials that were stored in an insulated box at -80^{o}C for 1 day. Later cryotubes were moved into a liquid-nitrogen storage unit at -196^{o}C for up to 5 years.

2.6.7 *Cell thawing*

Cells that were cryopreserved (§2.6.6) were removed from liquid nitrogen and were thawed quickly until the majority of ice had melted by immersing the cryopreservation vial in a water bath that was set at 37^{o}C. Cell suspension was diluted in pre-warmed basal medium at 37^{o}C. Cell suspension was centrifuged at x 200g. Medium with DMSO was aspirated and cell pellet was resuspended using fresh medium. Cells were seeded in a cell culture flask.

2.6.8 *Cell seeding on substrates*

Scaffolds were sterilised as described in §2.6.1 and then, were air-dried overnight in a hood before they were seeded. Cells were trypsinised (§2.6.4), counted (§2.6.5) and diluted to have the cell concentration required for each experiment. The medium where the cells resuspended was equal to 500 μL per sample.

Scaffolds were organised in 24 well plates. Cell suspension was added to sample using a pipette. Scaffolds were left in the incubator for 4 hours to allow cell adhesion. Scaffolds were then washed with PBS, transferred in a new well plate that containing 500 μL fresh medium.

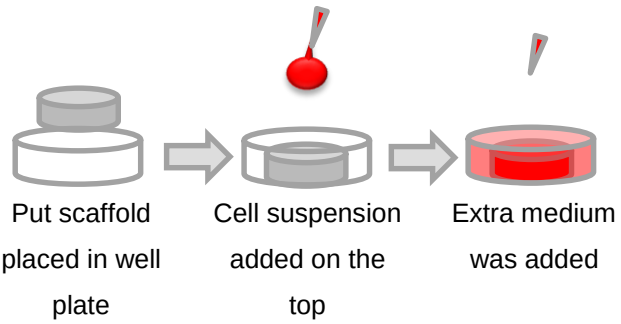

Figure 2-2: Illustration of static seeding technique

2.6.9 *Cell differentiation induction*

Cells on scaffolds that were assessed were divided into two equal groups to evaluate whether the substrate could promote osteogenesis without addition of supplements. After cell seeding (§2.6.8), cells were left in medium for 4h in an incubator at 37°C to allow cell adhesion. Then, this medium was aspirated and samples were washed with PBS. Following this step, samples were transferred in new plates and fresh medium was added. The one group had basal medium (§2.2.3) and the second group had osteogenic medium (§2.2.5). Cells were cultured in these media for 21 days in total.

2.7 Biochemical cell assessment

The viability and alkaline phosphatase activity were evaluated for scaffolds seeded on different substrates. Before each assessment, scaffolds loaded with cells, were washed with PBS and transferred into new well-plates.

2.7.1 *Cell Viability assessment*

Cellular viability was monitored using Alamar blue metabolic assay (ThermoFisher Scientific) (O'Brian,J.,Wilson,I.,Orton,T.,Pognan 2000; Hamid et al. 2004) on days 0, 1, 3, 7, 14 and 21.

At each time-point, medium was aspirated from each well and samples were washed once using PBS. 500 μL of medium was added in the samples and then 50 μl of Alamar blue was added in each well. Samples were covered with aluminium foil to prevent light exposure that would influence the fluorescence of Alamar blue. Cells were kept for 2 hours in an incubator at 37°C. Then aliquots of 100 μl from each samples were transferred in a white 96-well plate (in triplicates per sample) (Figure 2-3). The solutions fluorescence was measured using a FLUOstar Optima fluorimeter (BMG Labtech) with excitation and emission wavelengths, 540 nm and at 580 nm respectively. The cell number was calculated based on the standard curve that was prepared (Appendix- Figure 1). Cells were washed with PBS and basal or osteogenic medium – depending the experiment- was added.

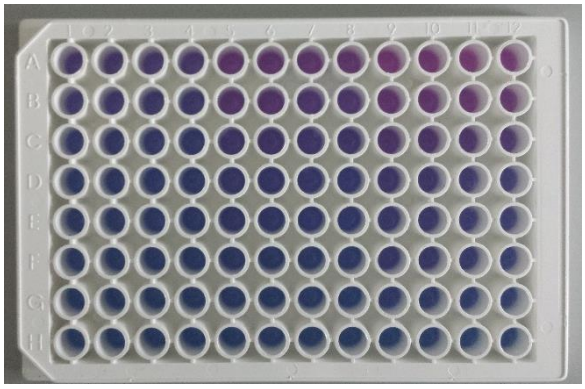

Figure 2-3: Representative image of aliquots from cells incubated with Alamar blue.

2.7.2 *Alkaline Phosphatase Activity*

Alkaline phosphatase (ALP) enzymatic activity of cells incubated on the different substrates was assessed using p-nitrophenyl phosphate (pNPP) liquid substrate system (N7653) on days 0, 1, 3, 7, 14 and 21.

At each time-point, after cells were analysed using Alamar blue (§2.7.1), medium with Alamar blue was aspirated and cells were washed using PBS. Samples were fixed with pre-warmed at 37 °C 4% paraformaldehyde in PBS for 20 minutes at room temperature. Paraformaldehyde- PBS solution was removed and after samples were

washed with PBS, they were incubated with PBS 0.1M TRIS buffer with 8.3 pH for 10 minutes. Samples were washed and 400 μL of pNPP was added per well. Samples in Chapter 4 were incubated with pNPP for 30 min and samples in Chapter 5 were incubated for 15 min.

Aliquots from the samples were plated into a transparent 96-well plate and their absorbance was measured at 405 nm wavelength using a Tecan plate reader. To determine the pNPP concentration relative to the absorbance readings and incubation time, a standard curve was used (Appendix- Figure 2). All measurements were normalised using the cell number acquired using Alamar blue method.

2.8 Cell gene expression

The expression of specific genes were assessed using Real Time Polymerase Chain Reaction at cells that were seeded on different substrates. Cells were washed with PBS at room temperature and were transferred in new plates.

2.8.1 *TRIzol® RNA Isolation*

1 ml TRIzol® reagent (15596-018, Life-Technologies, UK) was added on the samples to lyse the cell. Cells were incubated in TRIzol® for 5 min. Then, the lysates were transferred in a 1.5 ml Eppendorf tube and 200 μL of trichloromethane (C2432) was added. Samples were shaked for 15 seconds and centrifuged in a Fisher-Scientific microcentrifuge AccuSpin Micro 17 (Fisher Scientific, UK) at 13,000 rpm for 15 minutes.

Three phases were resulted in each samples after centrifugation. The top aqueous layer contained the RNA, the interface turbid layer the DNA and the last red layer was the organic phase that was compromised of proteins and lipids.

The aqueous phase was transferred into a new 1.5 ml Eppendorf tube and 500 μL of pure isopropanol was added. Samples were then incubated at room temperature for 10 min to allow RNA precipitation. 15 minute centrifugation followed at 13,000 rpm. The supernatant was removed carefully without disturbing the precipitated pellet and 1 ml of 70% ethanol solution was added in the tube. Samples were centrifuged for 15 minutes at 13,000 rpm and the supernatant was aspirated. Tubes were place in hood for 15- 25 min to air dry the precipitated pellet. The pellet was resuspended in 15 μL of RNase-free water and samples were incubated in a water bath for 10 minutes at 65^{o}C to promote the dissolution of the pellet in the water. Samples were quenched on

ice for 5 minutes to condense the RNA-water suspension and samples were briefly centrifuged (pulsed) for 5 seconds. RNA samples were stored at -80^{o}C.

2.8.2 *Complementary DNA synthesis (cDNA)*

During cDNA synthesis the mRNA converts into cDNA using reverse transcriptase and DNA polymerase enzymes.

RNA samples were thawed on ice the concentration of RNA was measured using NanoDrop spectrophotometer (Thermo Scientific) to assess their quality.

8 µl of RNA was added in 4 µl of mix 1 (Table 2-3) into a 0.2 ml RNase, DNase- free tube. Samples were incubated at 70^{o}C for 5 minutes in a PTC-200 peltier thermal cycler (MJ Research, Minnesota, USA).

Reagent	Volume/sample (µL)
20 ng/µL – Random hexamers	1
10 mM – dNTP mix	3

Table 2-3: Reagents to prepare mixture 1 used in cDNA synthesis.

Then, samples were cooled on ice for 2 minutes and centrifuged briefly. 8 µL of mix 2 (Table 2-4Table 2-4) was added to each sample and samples were incubated at 37^{o}C for 50 minutes and at 70^{o}C for 15 minutes. cDNA was stored at -20^{o}C. cDNA samples were diluted to 50 µL with RNase, DNase free water.

Reagent	Volume/sample (µL)
0.1 M – DTT	0.125
40 U/ml – RNaseOUT™	0.1
MMLV	0.5
DPEC-treated water	1.375

Table 2-4: Reagents to prepare mixture 2 used in cDNA synthesis.

2.8.3 *Real Time – Polymer Chain Reaction (RT-PCR)*

The genes that were assessed are demonstrated on Table 2-5.

Human gene	Primer sequence forward/ reverse	Reference
Internal control		
GAPDH	3'-5': CTCTGCTCCTCCTGTTCGACA	(Yang et al. 2011)
	5'-3': ACGACCAAATCCGTTGACTC	
Osteogenic markers		
T2 Runx2	3'-5': GGTTAATCTCCGCAGGTCAC	(Yang et al. 2011)
	5'-3': GTCACTGTGCTGAAGAGGCT	
ALP	3'-5': CCCAAAGGCTTCTTCTTG	

	5’-3’: CTGGTAGTTGTTGTGAGCAT	(Yang et al., 2011)
OPN	3’-5’: TTTTCTGGATCCTCCATTGC	(Yang et al. 2011)
	5’-3’: CAAAAGCCATATGCTGCTCA	

Table 2-5: Primers used for RT-PCR.

Human gene	Primer sequence forward/ reverse	Reference
Osteogenic markers		
OCN	3’-5’: GACTGTGACGAGTTGGCTGA	(Yang et al., 2011)
	5’-3’: CTGGAGAGGAGCAGAACTGG	
COL 1A1	3’-5’: ATGCCTGGTGAACGTGGT	(Sarugaser et al. 2009)
	5’-3’: AGGAGAGCCATCAGCACCT	
Chondrogenic markers		
Sox9	3’-5’: GCAGGCGGAGGCAGAGGAG	(Haleem-Smith et al., 2012)
	5’-3’: GGAGGAGGAGTGTGGCGAGTC	
Aggrecan	3’-5’: TCCCCACGGTCTCTCTTGTAG	(Haleem-Smith et al., 2012)
	5’-3’: GCCCACTTAGGTCCAGAAATCC	
COL 1A1	3’-5’: ATGCCTGGTGAACGTGGT	(Sarugaser et al. 2009)
	5’-3’: AGGAGAGCCATCAGCACCT	

Table 2-5: Primers used for RT-PCR.

All reagents and samples were left to thaw on ice and were pulse centrifuged to pool all the liquid together. The master mix for each gene was prepared using the reagents and the volume that is mentioned at Table 2-6.

Reagent	Volume/sample (µl)
Forward primer	0.4
Reverse primer	0.4
RNA, DNA free water	7.2

Table 2-6: Reagents to prepare master mix used in RT-PCR

In a 96 well clear MicroAmp® Optical 96-well reaction plate (Applied Biosystems, Life Technologies, I02N4Q) 8 µl of master mix was pipetted in every well that would be in use. Then 2 µL of cDNA of each sample and 10µL SYBR Green PCR Master Mix (Life-Technologies, 4309155) reagent per well were added. The plate was pulsed using a Megafuge40 (Heraeus™, Frankfurt, Germany) centrifuge to pool all the reagents and then it was placed in an Applied Biosystems Real-Time PCR instrument (model: 7900HT, serial: 201456), where the appropriate method was selected on SDS2 (Applied Biosystems) software.

In the RT-PCR machine, samples were incubated at 50°C for 2 minutes and 95°C for 10 minutes (holding stage). Then, samples were incubated at 95^{o}C for 15 seconds and 60°C for 1 minute. This step took place 40 times (cycling stage). At the end, the

samples were incubated at 95°C for 15 seconds, 60°C for 15 seconds and 95°C for 15 seconds (dissociation stage).

2.9 Statistical analysis

All quantitative data was presented as standard ± error of the mean (SEM). Statistical analysis of groups was performed using two tailed paired and un-paired t-test with p-values of less than 0.05 being considered significant. Statistical analysis of groups was performed with one-way and two –way analysis of variance (ANOVA) followed by Tukey and Bonferroni test respectively as Post Hoc tests. P-values less than 0.05 was considered statistically significant.

Symbol	Meaning
NS	p> 0.05
*	p> 0.01, p≤ 0.05
**	p> 0.001, p≤ 0.01
***	p> 0.0001, p≤ 0.001
****	p≤ 0.0001

Figure 2-4: Statistical significance symbols and meaning.

Chapter 3 Fabrication and Characterisation of Apatite-Wollastonite Ceramic Scaffolds for Bone Regeneration

3.1 Introduction

Bone and cartilage are the main tissues that are affected in osteoarthritic patients. The defected tissues could be removed and replaced using an osteochondral plug, when OA is detected in an early stage.

In this chapter, the fabrication of a hard scaffold that could be the bone part of the osteochondral plug was investigated. A-W has high mechanical properties (Kokubo et al. 1985) and was used for the preparation of the ceramic scaffolds that were prepared in this chapter.

There is a range of ceramic scaffold manufacturing techniques, as described in §1.9. The preliminary objective of this chapter was to characterise A-W powder of various particle ranges before and after sintering processes, prior to fabrication of scaffolds for bone tissue engineering (§0). The main aims were to identify and characterise ceramic fabrication techniques for A-W ceramic powder that would result in microporous scaffolds for 2D *in vitro* studies as well as scaffolds that were highly porous and interconnected to allow the study of cellular behaviour in 3D *in vitro* studies. The techniques which have been used were all based on the creation of a powder “green part” which was subsequently sintered. The green parts created using powder compaction (§3.4), cast loose powder (§3.5), cast slurries (§3.6) and thermally induced phase separation (TIPS) (§3.7). The techniques were chosen to allow investigation of a range of methods with the potential to create macro and microporosities within scaffolds. In order to vary the macroporosity a variety of sacrificial polymer cores have also been incorporated into the green parts.

The main criterion for the scaffolds that were further investigated as cell matrices was the lack of crack formation.

3.2 General Materials and Methods

3.2.1 *Source of Materials*

The main material for all the scaffolds that were prepared during this study was A-W powder (Figure 3-1) as already described in (§2.2.2).

Figure 3-1: Image of unprocessed A-W frit.

Specific particle ranges and combinations of these ranges were utilised (Table 3-1) according to the needs of each scaffold fabrication method in order to seek to achieve reproducible results.

		A-W:A-W (w : w)		
		<20 μm	**20- 53 μm**	**54- 90 μm**
A-W particle range	**<20 μm**	100 : 0		25 : 75 20 : 80 50 : 50 75 : 25
	20- 53 μm		100 : 0	
	54- 90 μm			100 : 0

Table 3-1: Ratio of A-W glass- ceramic particle size ranges used for ceramic scaffold fabrication.

The rest of the materials that were used for the experiments were described in Table 3-2. The use of individual materials is explained in the relative paragraph.

Material	Characteristics	Distributor
High density polyethylene (PE1)		Prof. Geoff Gibson, Mechanical and Systems Engineering; Newcastle university, Newcastle Upon-Tyne

Table 3-2: List of materials that were used in the experiments.

Material	Characteristics	Distributor
High density polyethylene (PE2)	Particle range: 101- 400µm	Goonvean fibres, UK
Polyamide powder (PA)	Particle range: 25- 92 µm	DuraForm, UK
Polymeric filament	Diameter: i) 0.5 mm ii) 1 mm	Bagnall and Kirkwood Ltd, UK
Poly(lactic) acid (PLA) (Ingeo 4032D, NatureWorks LLC)	Relative viscosity 4.0 Molecular weight: 156.651 Dalton Density: 1.24 g /cm^3	Bits from Bytes, UK
Anhydrous diethylene dioxide (1,4-dioxane)	Purity 99.8%	Sigma Aldrich
Isopropanol		Sigma Aldrich
Ethanol		Sigma Aldrich
Deionised water		

Table 3-2: List of materials that were used in the experiments.

3.2.2 *Powder Milling and Sieving*

A-W powder was milled in one of two ball mills (Pascal Engineering Co Ltd., Sussex, UK, for 6 hours; or Pulverisette 6, Planetary mono mill, Fritch, Gerhardt, UK, for 40 minutes, shown in Figure 3-2; A) to achieve a variety of particle sizes. A-W powder was then sieved on a sieve shaker (Figure 3-2; B) for about a month to separate the particle fractions of <20 µm, 20- 53 µm and 54- 90 µm. The particle ranges were selected based on the literature (Dyson et al. 2007; Xiao et al. 2008a).

A **B**

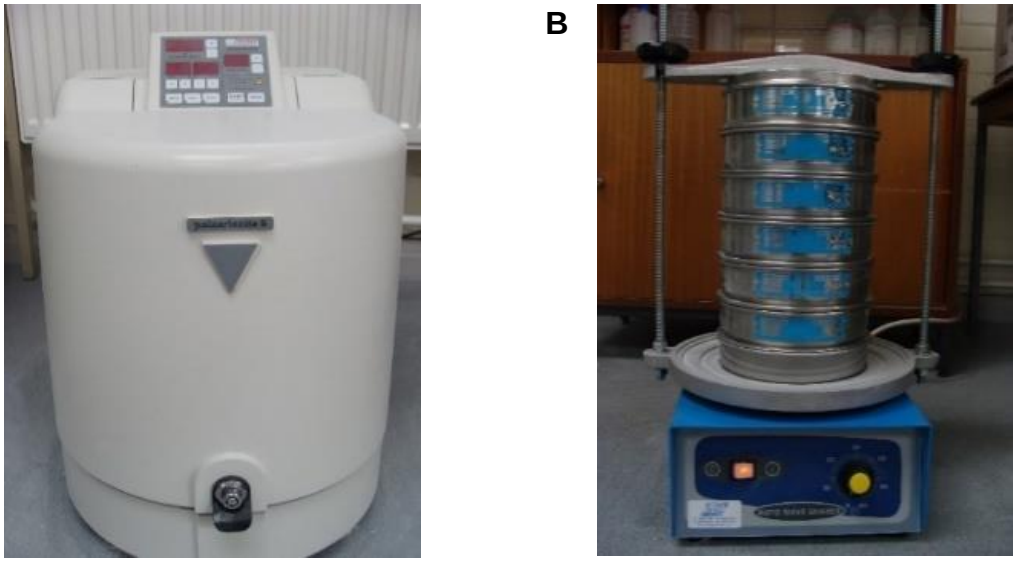

Figure 3-2: Images of milling machine (A) and sieve shaker (B) that were used for the experiments.

3.2.3 *Sintering*

Green bodies that were prepared using different fabrication techniques were placed on platinum foil that was rested on the top of a refractory brick and underwent heat

treatment in a chamber furnace (Figure 3-3) in two steps. The default heat treatment was the heat treatment A and is illustrated in Table 3-3; A. During the first step of heat treatment A, the temperature increased up to 779°C for 1 hour and then, in the second step, to 1150°C for 1 hour, before cooling back to room temperature. The heating rate that was used was 10°C/min. This heating treatment A was used by Dyson et al. 2007.

The particle range and the powder packing influence the degree of sintering of a ceramic. Some of the variables that can be changed to modify the degree of sintering are the heating rate, the maximum sintering temperature and the duration of the sintering (Kang 2005).

To find the optimal sintering temperature for each type of scaffolds, different parameters of the heat treatment A were changed. For the scaffolds with pure A-W, the parameters that were altered were: the heating rate of the first step; the maximum temperature and its duration at the second step. The alterations in these parameters occurred to improve the densification of the A-W particles. When polymers were introduced in the green part a preliminary step was added to melt the polymer (Collin et al. 2005). Depending on the polymer that was used in the different scaffolds, the temperature of step 1 in heat treatment E was decided according to their melting temperature (Tm). The sintering treatments are described in Table 3-3 and the Tm of each polymer used are in Figure 3-4.

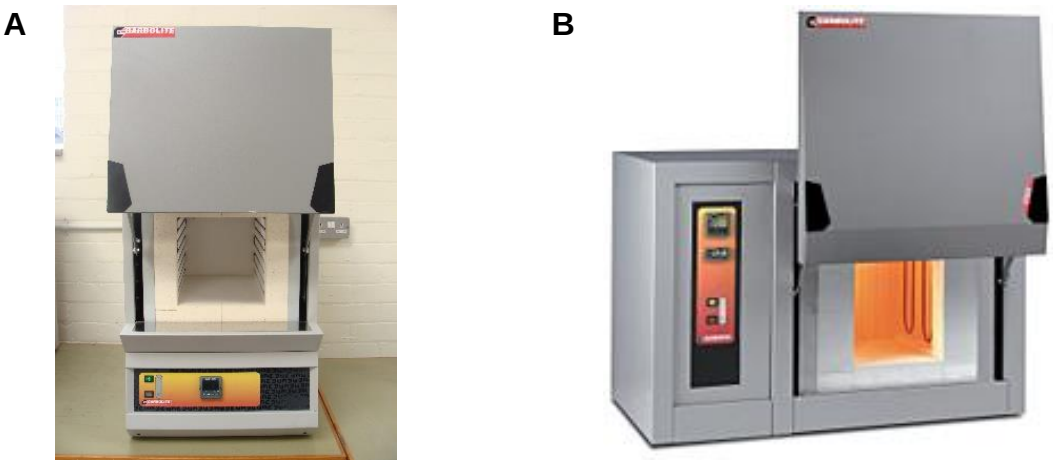

Figure 3-3: Indicative images of one the furnace used for the experiments

	Heating rate → Ramp → Swell	Heat treatment route graph
Heat treatment A	Step 1: 10˚C/min→779˚C→1h Step 2: 10˚C/min→1150˚C→1h	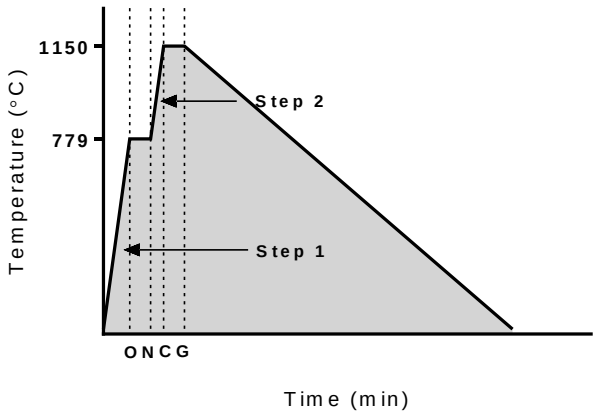
Heat treatment B	Step 1: **5**˚C/min→779˚C→1h Step 2: 10˚C/min→1150˚C→1h	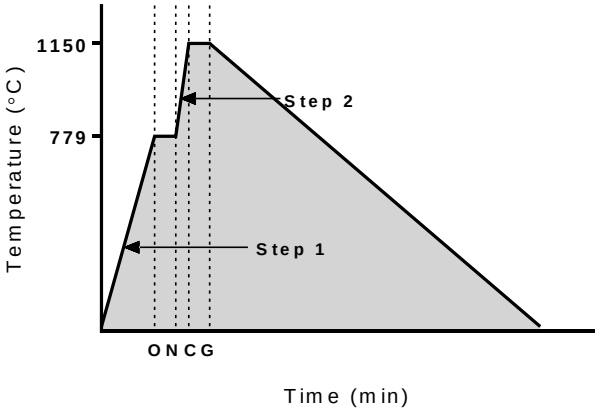
Heat treatment C	Step 1: **5**˚C/min→779˚C→1h Step 2: 10˚C/min→**1200**˚C→1h	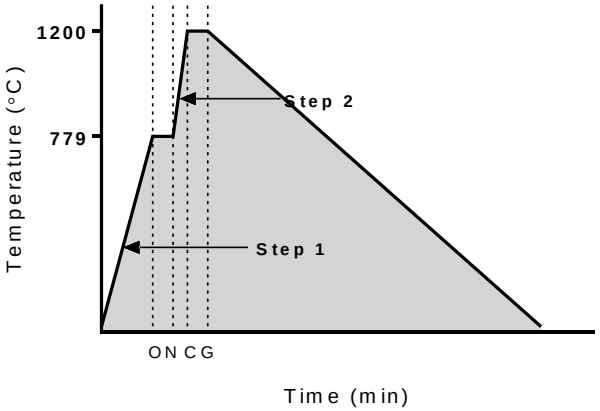

Table 3-3: Heat treatment schemes that were investigated and the correspondent graphs. (OP: optimum nucleation; CG: crystal growth; Tm: melting point of polymer that was used depending the experiment).

	Heating rate → Ramp → Swell	Heat treatment route graph
Heat treatment D	Step 1: **5**°C/min→779°C→1h Step 2: 10°C/min→**1200**°C→**2**h	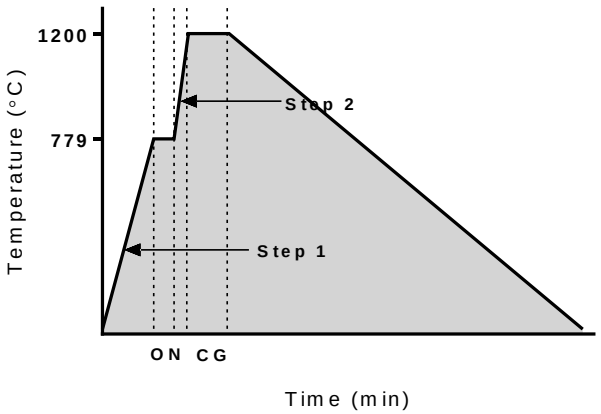
Heat treatment E	Step 1: **5°C /min→ polymer Tm→1h** Step 2: **5**°C/min→779°C→1h Step 3: 10°C/min→1150°C→1h	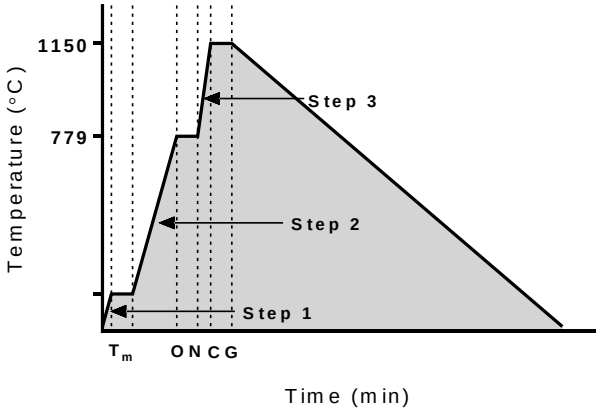
Heat treatment F	Step 1: 5°C/min→779°C→1h Step 2: 10°C/min→**1250**°C→ 1h	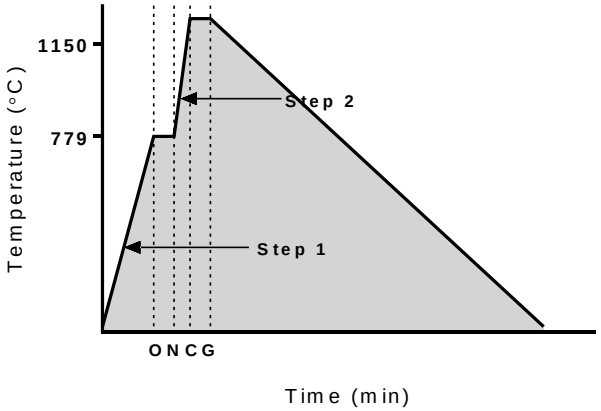

Table 3-3: Heat treatment schemes that were investigated and the correspondent graphs. (OP: optimum nucleation; CG: crystal growth; Tm: melting point of polymer that was used depending the experiment).

Polymer	Melting point (°C)
PA	184
PE	150
PLA	190

Figure 3-4: Melting point of polymers that were used as sacrificial materials.

3.2.4 *X-Ray Computed Tomography (XRCT)*

X- Ray computed tomography was performed on sintered A-W scaffolds using a XRadia Versa-410 (Zeiss, UK) with the assistance of Dr Tom Beale (Department of Physics, Durham University). Samples were fixed and dehydrated according to protocol described at §2.5.6.

Samples scanning was performed with the system running at 150 kV.

3.3 Characterisation of A-W powder particles

The raw A-W powders were characterised morphologically prior to scaffold fabrication to ensure that the correct particle ranges had been obtained after sieving. This investigation was fulfilled using SEM imaging. Figure 3-5 illustrates that the A-W particles have irregular shape and the particle size of the each group is in accordance with the sieves that were used without obvious contamination of differently sized particles.

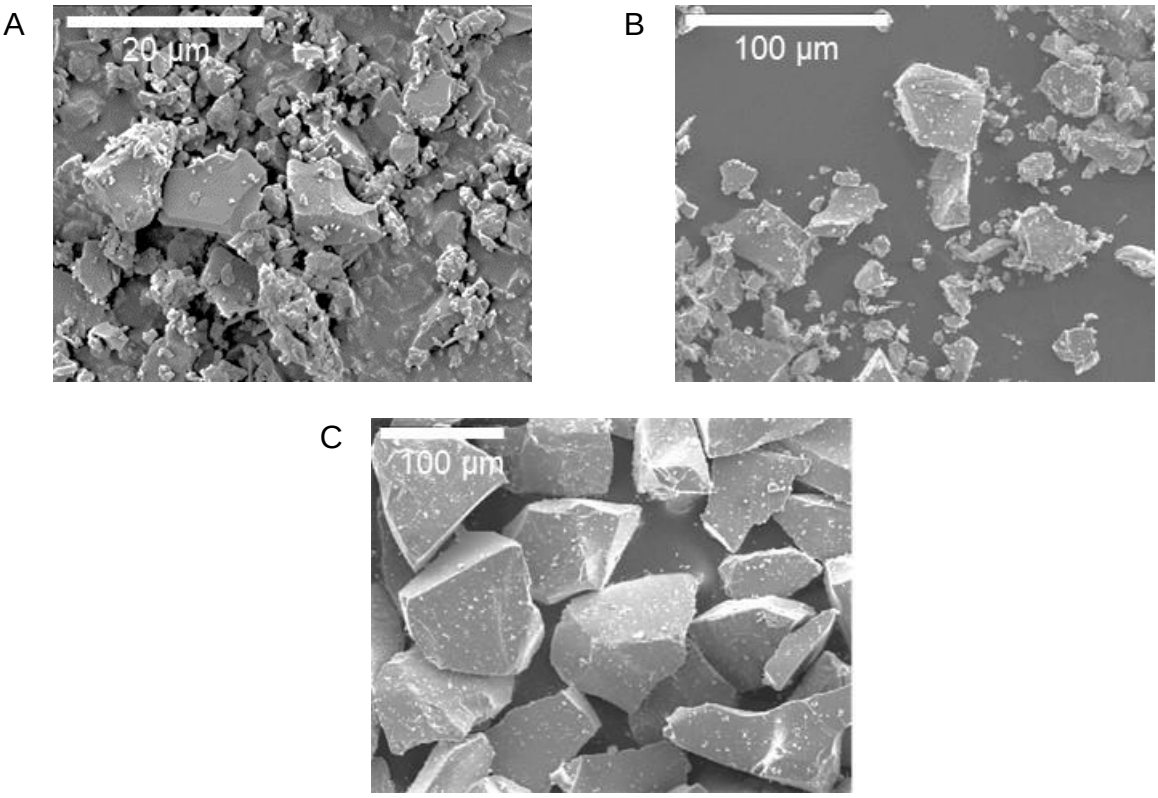

Figure 3-5: SEM micrographs of raw sieved A-W powders with particle ranges: <20 µm (A), 20- 53 µm (B), 54- 90 µm (C).

Figure 3-6 illustrated the XRD results of the raw and sintered A-W. XRD was used to observe the difference in the crystal phases before and after sintering. In Figure 3-6, it is indicated that in the raw A-W glass ceramic powder slight intensity peaks appeared; whereas after the sample was treated at 779˚C and 1150˚C (heat treatment A; Table 3-3), a large amount of high intensity peaks appeared proving that A-W after sintering is a ceramic. In addition the phase analysis results for the samples are presented in Figure 3-6. The principal crystal phase for the raw A-W (Figure 3-6; A) was hydroxyapatite (calcium phosphate hydroxide; $Ca_5(PO_4)_3(OH)$; Q: C; 01-073-1731), accompanied by smaller peaks of β- wollastonite (calcium

silicate; Ca Si O_3; Q: C; 00-027-008) and calcium magnesium hydrogen phosphate ($Ca_{19.68}$ Mg_{12} $H_{1.8}$ $(PO_4)_{13.80}$; Q.C; 01-079-2186).

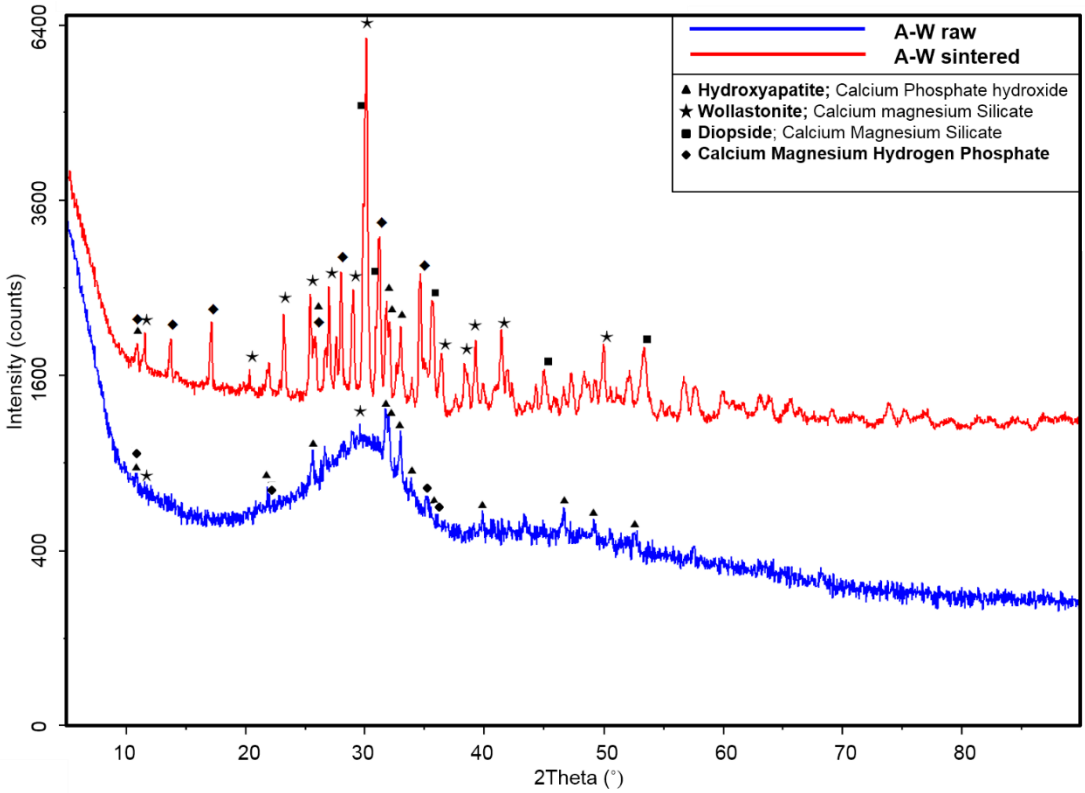

Figure 3-6: XRD spectra of A-W powders sintered according to heat treatment A (red coloured line); un-sintered – raw material (blue coloured line).

3.4 Sintering of compacted powder with and without polymer cores

A-W powder was compacted and sintered to provide pellet scaffolds. A liquid binder was used to improve the handling of the pressed powders. For this experiment, isopropanol was selected to be used as a binder prior to pellet fabrication, because it does not evaporate fast comparing to other alcohols. Water could have been used instead; however, it has been reported that scaffolds made with isopropanol have better mechanical properties that the ones made with water (Rambo et al. 2006).

The aim was to create scaffolds that were prepared using pure compacted ceramic powder creating small pores that would prohibit cell migration inside the scaffold and would promote cell proliferation only on the top surface to allow study of the influence of particle size on cell activity.

The scaffolds that were fabricated using compacted ceramic powder with polymer aimed to create a porous and interconnected scaffold that would allow cell migration and proliferation inside the 3D construct to assess the cell behaviour in a 3D environment.

Small particle range polymer was also introduced in the compacted ceramic powder to allow better powder distribution.

3.4.1 *Methods and Materials*

3.4.1.1 Preparation of pure compacted powder

Pure A-W powders were mixed in a pestle using isopropanol. The isopropanol was evaporated, the powders were put in metal mould compacted under high pressure using a hydraulic press and then were de-moulded (Brovarone et al. 2006). Due to the restrictions of the press that was used; 20 MPa was the highest pressure that was applied. Two lower pressures were assessed; 1 MPa and 10 MPa to investigate the effect of different pressures on the pellet structure.

3.4.1.2 Introduction of PA small polymeric particles

PA powder was added to the pure A-W pellet scaffolds (Figure 3-7) in ratio A-W: PA 80: 20 w/w. Pure A-W pellet scaffolds had cracks forming internally (Figure 3-15, Figure 3-16, Figure 3-18) and PA polymer particles were inserted to provide better particle distribution and cushion the impact of the forces on the pellet during de-moulding it from the metallic mould.

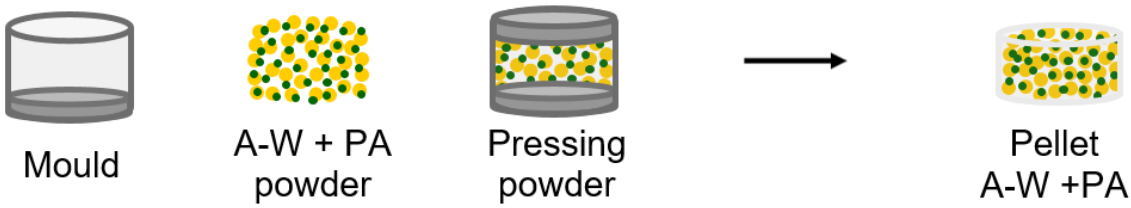

Figure 3-7: A-W compacted powder with PA particles

3.4.1.3 Introduction of large polymeric particles

PE particles were combined with pure A-W powder in ratios listed in Table 3-4 before they were pressed (Figure 3-8) to introduce macropores increasing the porosity of the scaffolds after sintering. During the primary experiments with PE, PE1 was sieved and granule range 150- 400 µm was used. PE2 was purchased to ensure the homogenous particle population.

A-W particle range (µm)	A-W: PE (w/w)
20- 53	70: 30 60: 40
54- 90	70: 30 60: 40

Table 3-4: Ratio of A-W glass ceramic powder with PE particles used.

Figure 3-8: A-W compacted powder with PE particles

3.4.1.4 Introduction of polymeric filaments

A polymeric filament either with diameter 0.5 mm or 0.7 mm was added in the centre of A-W powder before it was pressed (Figure 3-9) to form a uniform channel in the centre of the pellet. This scaffold was a pilot study to evaluate whether channels could be formed in the pellet without the crack formation that appeared in the scaffolds with the polymeric particles (Figure 3-23), so cells could migrate and promote osteogenesis *in vitro* with the potential of promoting angiogenesis *in vivo*.

Figure 3-9: A-W compacted powder with polymeric filament.

3.4.1.5 Sintering

All samples were sintered on a platinum foil inside a high temperature laboratory chamber furnace with maximum operating temperature 1800˚C (Carbolite, UK) according to the sintering regimes described in Table 3-3.

3.4.2 *Results*

3.4.2.1 Effect of different particle ranges on pure A-W sintered compacted powder scaffolds

As illustrated in Figure 3-10, in pellets, the particles were completely sintered and no individual particles were identified in the SEM micrographs A and B. The particle size that was used appeared to have an influence on the pore size in the compacted powder scaffold. Scaffolds prepared using the particle range 20- 53 µm had smaller pores with respect to the pellet fabricated with the bigger particle size range.

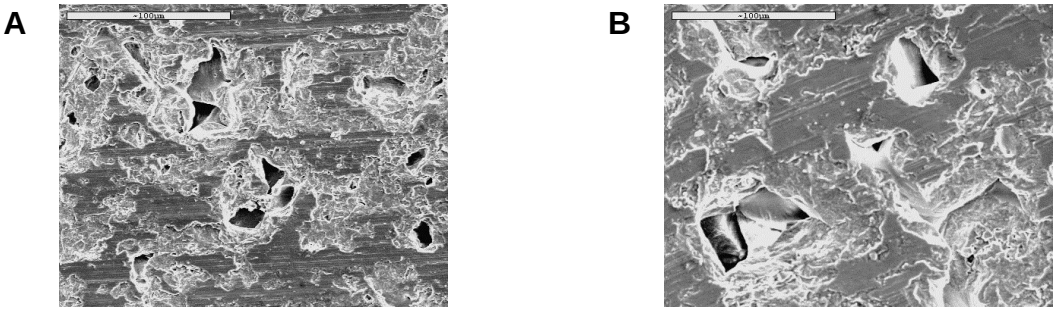

Figure 3-10: Microstructure of sintered compacted powder scaffold fabricated with pure A-W. Representative SEM photos of pellet scaffolds that were pressed using 20 MPa with particle range 20- 53 µm (A) and 54- 90 µm (B), respectively. All scaffolds were sintered according to scheme of the heat treatment A.

After analysing the data using student's t-test, samples prepared using different particle range (Figure 3-11) had no significant difference neither in shrinkage (p= 0.0839) nor in porosity (p= 0.1780).

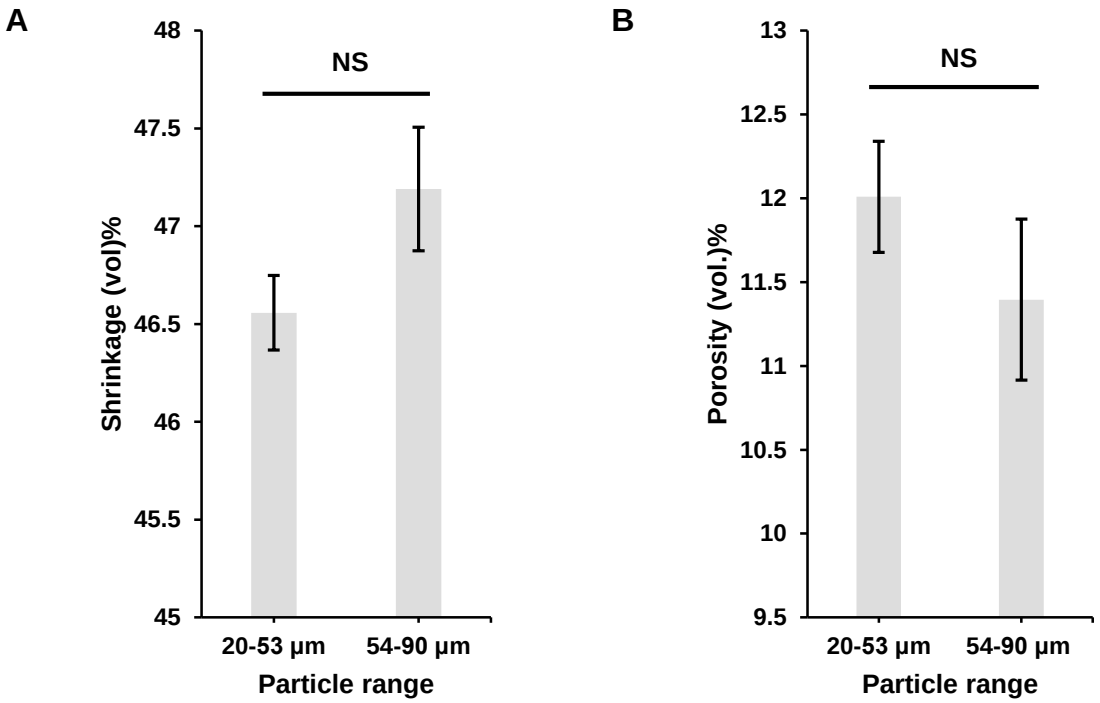

Figure 3-11: Shrinkage (A) and porosity (B) of sintered pure A-W pellet scaffolds that were prepared using 20- 53 µm and 54- 90 µm particle ranges and sintered according to heat treatment A.

3.4.2.2 Effect of different heating treatments and particle ranges on pure A-W sintered compacted powder scaffolds

Different heat treatments were explored for fabrication of compacted powder scaffolds using the two main particle ranges; 20- 53 µm and 54- 90 µm.

The shrinkage of compacted powder scaffolds is illustrated in Figure 3-12 and was analysed using two-way ANOVA. The different particle ranges had no significant effect on the shrinkage of the sintered scaffolds ($p= 0.7002$).The different heat treatment during sintering ($p <0.0001$) and the interaction of the particle range with the heat treatment ($p <0.0001$) had significant effects on the shrinkage of these scaffolds. Analysis using Bonferonni's multiple tests revealed that the differences in shrinkage produced by heat treatments B ($p= 0.0002$) and C ($p<0.0001$) on the two particle size ranges were significant.

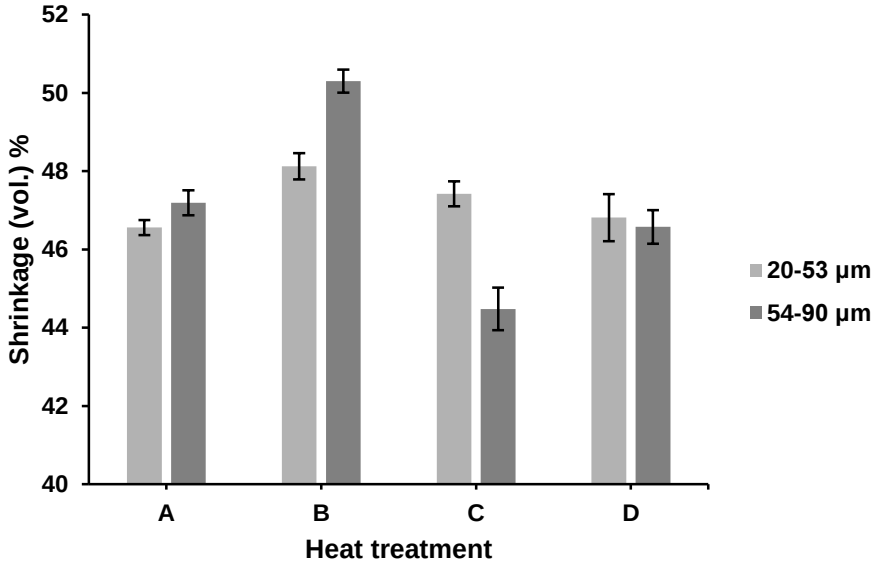

Figure 3-12: Shrinkage of pure A-W compacted powder scaffolds fabricated using particle range 20-53µm and 54-90 µm sintered according to the heat treatments A, B, C, and D.

Figure 3-13 shows the porosity of the compacted powder scaffolds. Two-way ANOVA indicated that the particle range, which was used to fabricate the scaffolds, affected significantly the porosity of the compacted powder scaffolds ($p= 0.0397$). In addition, the heat treatment had an extremely significant influence on the porosity of these scaffolds ($p<0.0001$).

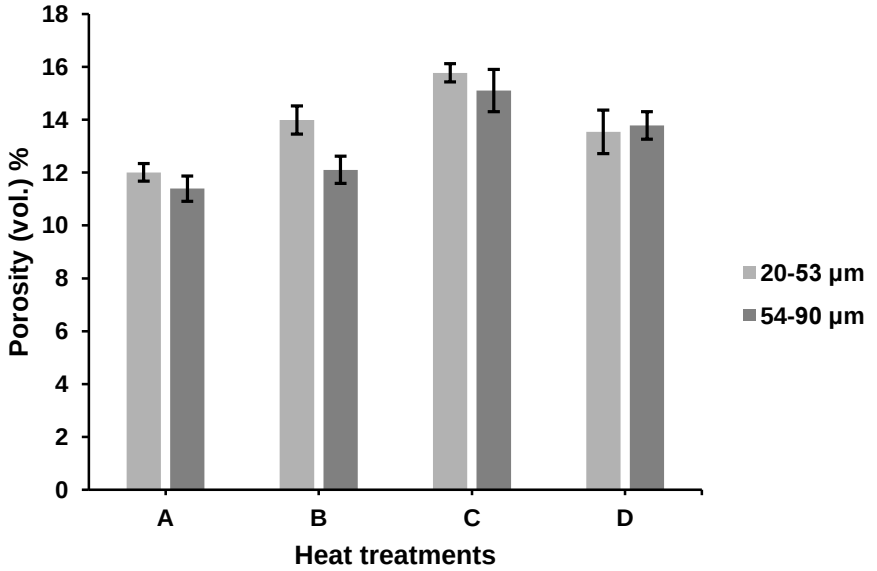

Figure 3-13: Porosity of pure A-W compacted powder scaffolds fabricated using particle range 20-53µm and 54-90 µm sintered according to the heat treatments A, B, C, and D.

In Figure 3-14, a representative sintered pellet scaffold was shown. This scaffold was fabricated with A-W 20- 53 µm and sintered according to heat treatment B. Macroscopically, pellet scaffolds had regular and smooth cylindrical shape since they were pressed in a level polished stainless steel mould under hydraulic pressure.

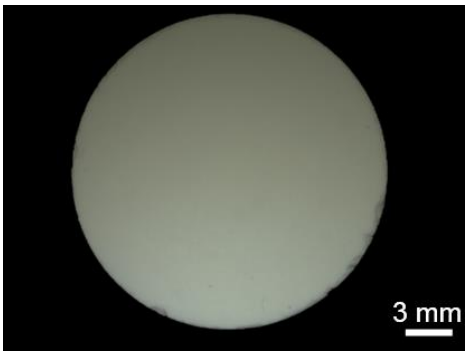

Figure 3-14: Morphology of sintered pellet scaffold fabricated with pure A-W. Representative bright field image of pellet scaffold. Scale bars, 3mm. The image A was acquired using lens 0.5 at magnification 3x.

Figure 3-15 presents sectioned scaffolds prepared with two different particle ranges- 20- 53 µm (A) and 54- 90 µm (B) that were sintered according to heat treatment B. In both scaffolds, large cracks were formed. Figure 3-15; C displays a schematic illustration of the crack that was usually created in the pellets with pure A-W powder.

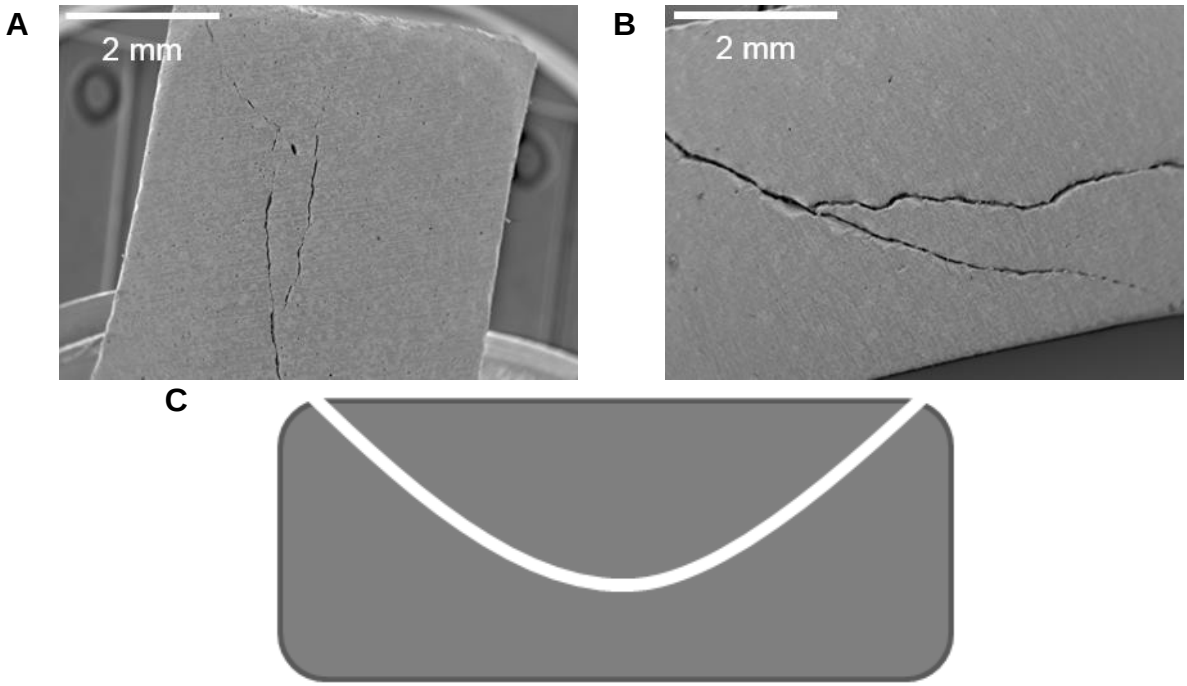

Figure 3-15: Crack formation in pellet scaffolds. SEM photos of pellet scaffolds with particle range 20- 53 µm (A) and 54- 90 µm (B). Scale bars, 2 mm. Schematic representation of observed crack formation (C).

3.4.2.3 Effect of different hydraulic pressures on pure A-W sintered compacted powder scaffolds

Different hydraulic pressures – 1 MPa, 10 MPa and 20 MPa- were investigated. In Figure 3-16 pellet scaffolds compacted under different hydraulic pressures are shown. All scaffolds had large internal cracks similar to those illustrated in Figure 3-15; C. The liquid phase increased as the levels of hydraulic pressure used for compaction were elevated the liquid phase increased. Cracks appeared in the pellet structure after different pressures were used for compacting the A-W powder. Figure 3-16; a-c, suggests that the A-W particles melted more in the scaffolds produced with increased mould pressures.

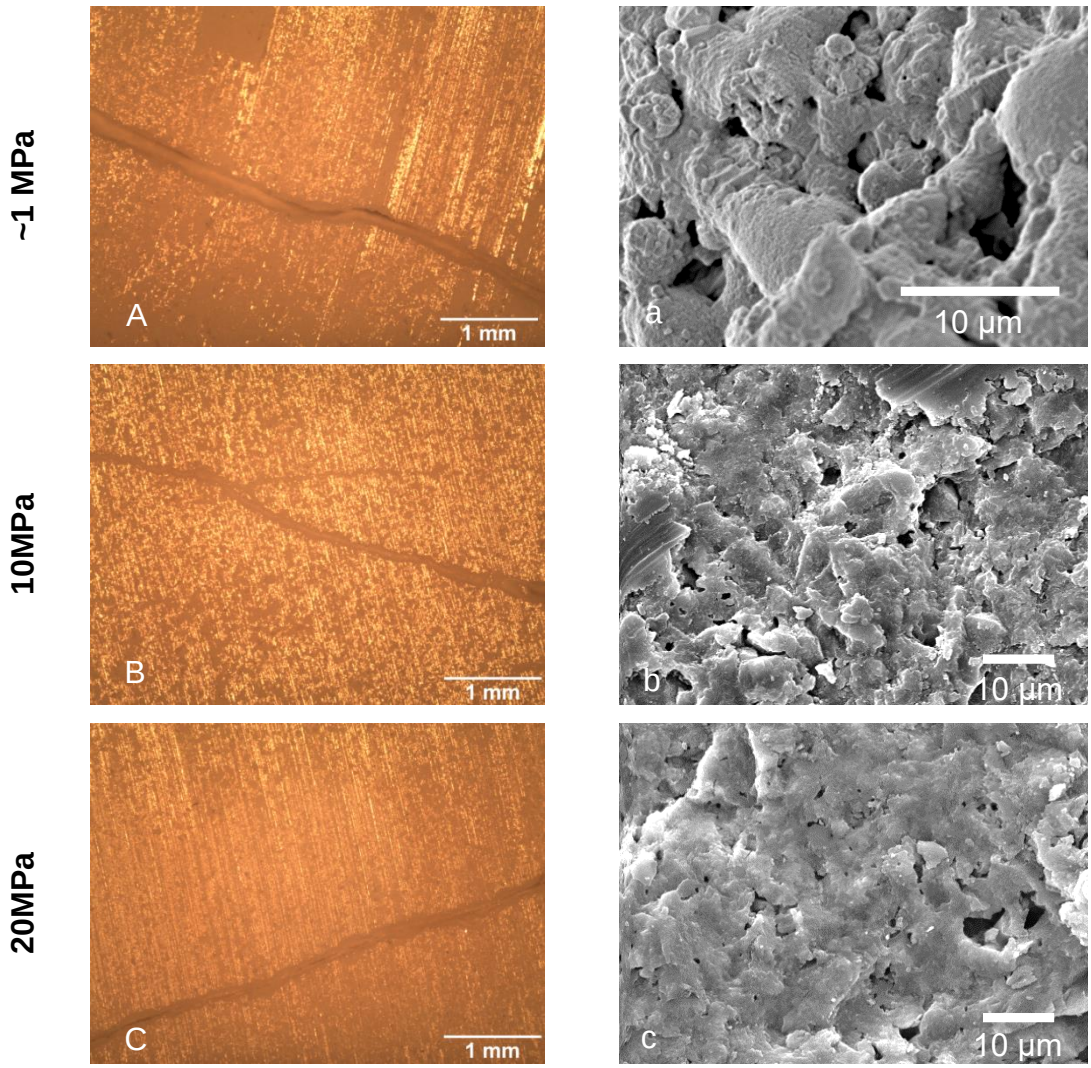

Figure 3-16: Crack formation on pellets with pure A-W (20- 53 µm) fabricated under different pressures and their microstructure. Representative bright field images of pellets (A-C) and their correspondent SEM photos (a-c). All scaffolds were fabricated with A-W 20- 53 µm and sintered according to scheme of the heat treatment B. Scale bars, 1 mm (A-C) and scale bars, 10 µm. The images were taken with lens 0.5 at magnification 1x (a) and 3x (b).

The different pressures on the green bodies of the pellet scaffolds influenced significantly ($p<0.0001$, one way ANOVA) the porosities of the sintered scaffolds (Figure 3-17). One-way ANOVA test was followed by Tukey's test indicated that the scaffolds sintered after the green body pressed under 1 MPa had very significantly increased porosity in comparison to the pellets pressed under 10 MPa ($p= 0.0011$) and 20 MPa ($p <0.0001$), but the porosity of the pellets pressed with the two latter pressures had no significant difference between them ($p= 0.2767$).

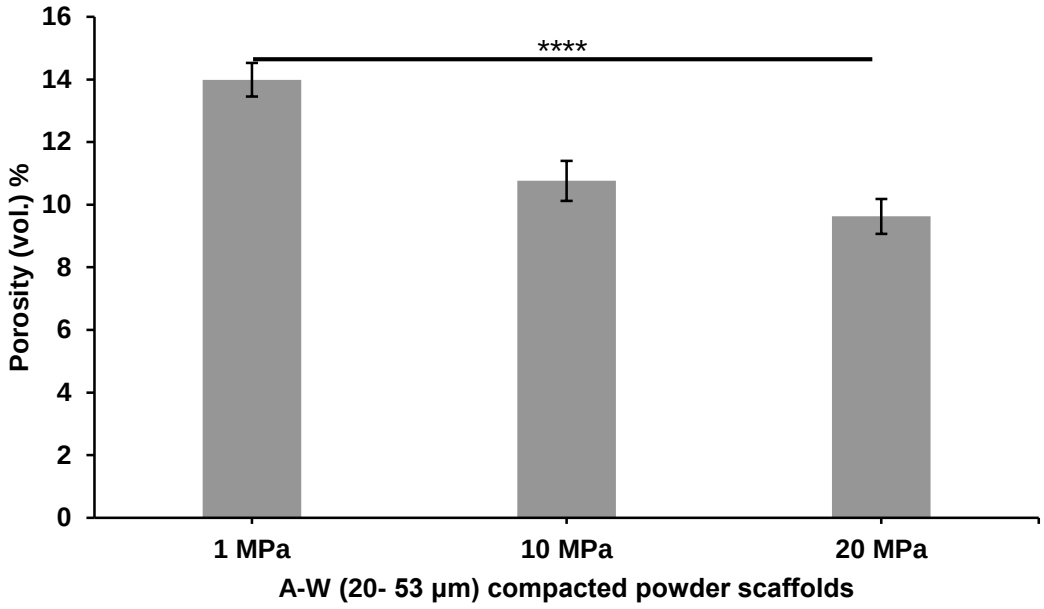

Figure 3-17: Porosity of sintered pure A-W pellet scaffolds that were pressed using different hydraulic pressures (1 MPa, 10 MPa and 20 MPa). A-W pellets were prepared using 20- 53 µm particle range and sintered according to heat treatment A.

3.4.2.4 Effect of different particle ranges on pure A-W sintered compacted powder scaffolds

A variety of granule ranges and mixtures of small and large granule ranges were used to investigate whether the cracks could be eliminated (Figure 3-18). As illustrated, the liquid phase altered depending on the granule range. The higher the particle range (54- 90 µm) content, the lower the degree of sintering (Figure 3-18; a-e). In the low magnification SEM micrographs (Figure 3-18; A-E), all samples were cracked. The cracks in the scaffolds prepared using A-W with particle ranges <20 µm: 54- 90 µm (25:75 w/w) did not appear in the image Figure 3-18; C, because it was separated before SEM and photos were taken from the remaining parts.

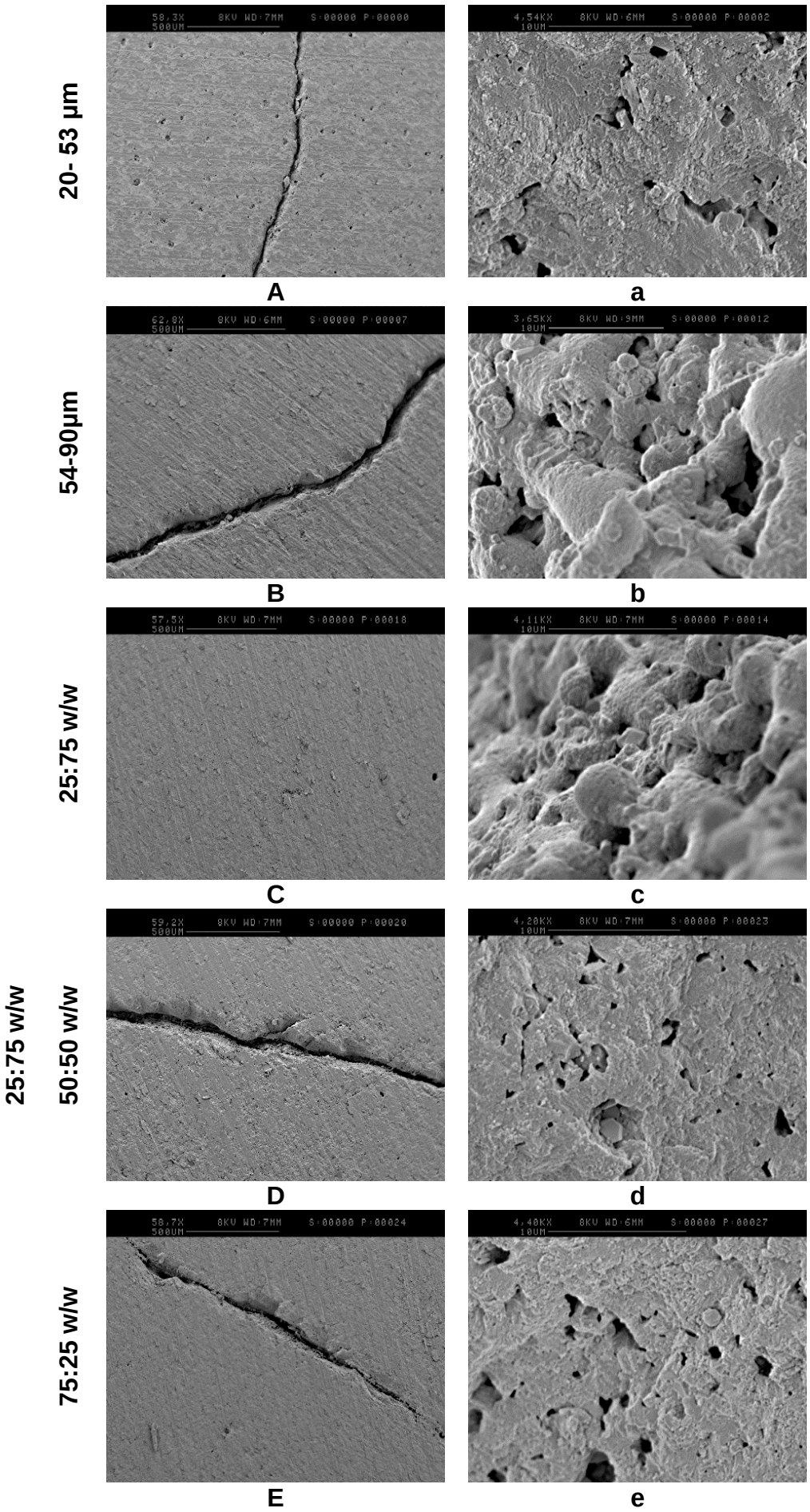

Figure 3-18: Effect of particle size range on sintering. Representative SEM photos of pellet scaffolds manufactured under ~1 MPa hydraulic pressure using A-W 20- 53 µm (A, a), A-W 54- 90 µm (B, b), A-W <20:54-90µm (25:75) (C, c), A-W <20:54-90µm (50:50) (D, d) and A-W <20:54- 90 µm (75:25) (E, e). All samples were sintered according to heat treatment B.

3.4.2.5 Effect of small polymeric particles in powder distribution on pure A-W sintered compacted powder scaffolds

Polymeric particles - PA were introduced in the scaffolds to improve the homogeneity of powder distribution. Large cracks were evident at the inner and outer surface of the pellet after sintering (Figure 3-19).

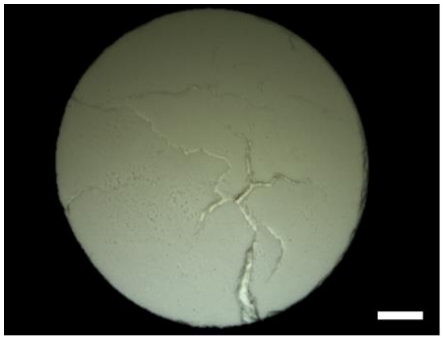

Figure 3-19: Cracks in the scaffolds after the introduction of small polymeric particles (PA) in pure A-W scaffolds. Bright-field photos of pellet scaffolds with A-W: PA (80: 20), A-W (20- 53 μm). Scale bars, 3mm. The image was taken with lens x0.5 at magnification x1.

In addition to the macro-fractures of the pellet, micro-fractures were noticeable in the pellets that were fabricated with both particle ranges 20- 53 μm and 54- 90 μm (Figure 3-20). As shown in Figure 3-20, the micro-cracks in the pellets with large particle range (54-90μm) were more and larger than the micro-fractures in the pellets with the smaller particle range (20- 53 μm).

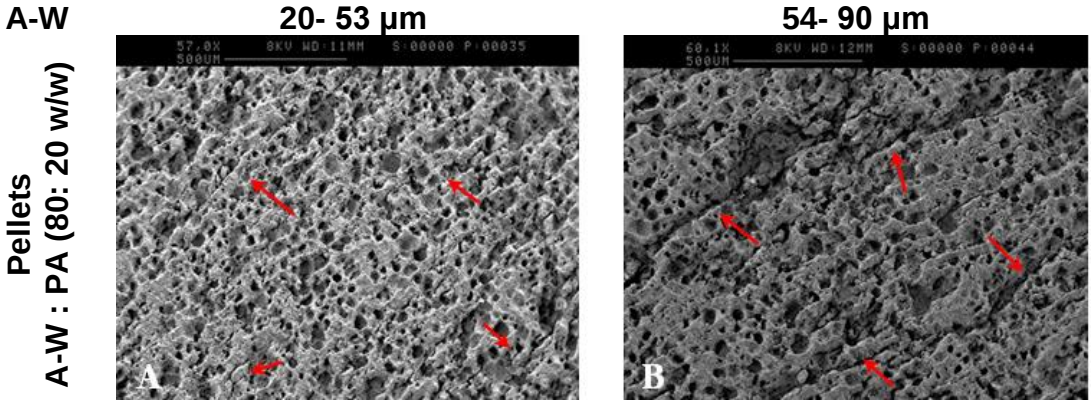

Figure 3-20: Cracks in the scaffolds after the induction of small polymeric particles (PA) in A-W scaffolds. SEM photos of pellet scaffolds with A-W: PA (80: 20), A-W (20- 53 μm) and A-W (54-90μm). Micro-fractures have been indicated with red arrows.

In Figure 3-21 the porosity of the pellets prepared with the introduction of the PA particles is compared with the pure A-W pellet scaffolds. Both groups were fabricating using two different particle ranges (20- 53 μm and 54- 90 μm). Two way

ANOVA was used to compare the influence of the PA addition to the porosity and the effect of the particle range was assessed. The addition of the PA particles had a highly significant effect on the porosity ($p < 0.0001$), whereas the particle range had no significant influence on the porosity for each group ($p = 0.4145$).

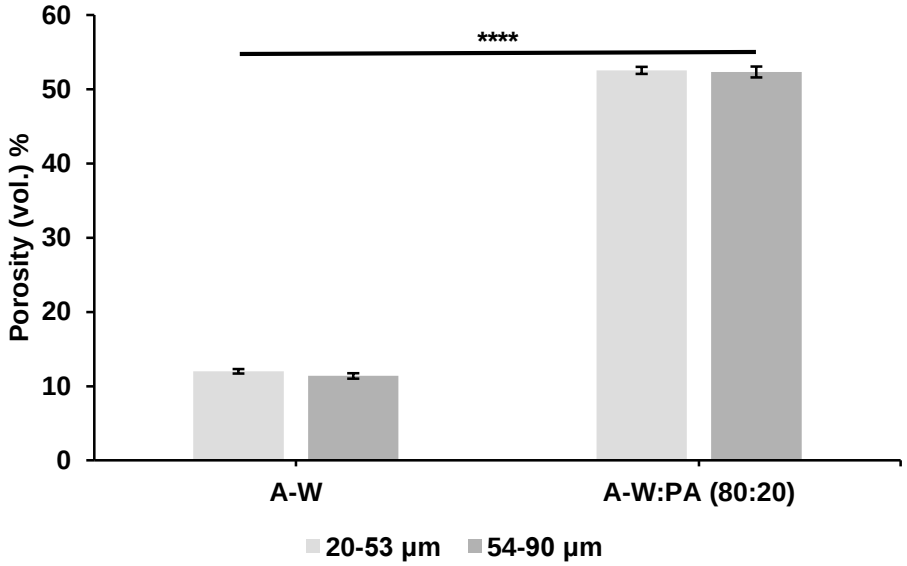

Figure 3-21: Porosity of sintered pure A-W pellet scaffolds and in combination with PA particles prepared with A-W: PA (w/w) ratio 80: 20. Samples were sintered according to heat treatment B. A-W pellets were made using 20- 53 µm and 54- 90 µm respectively.

3.4.2.6 Effect of large polymeric particles on the macrostructure and pore formation of pure A-W sintered compacted powder scaffolds

The concentration of PE particles that was mixed with A-W powder in the green body affected the macrostructure of the sintered scaffolds (Figure 3-22). Scaffolds that were sintered according to the heat treatment A collapsed, possibly because the polymeric part burnt out rapidly. A-W pellets with different ratios of A-W: PE are showed. Scaffolds with ratio 50:50 w/w (A-W: PE) with either particle range 20- 53 µm or 54-90µm collapsed (I and i respectively), while scaffolds with ratios 60: 40 w/w (II and ii) and 70: 30 w/w (III and iii) retained their shape.

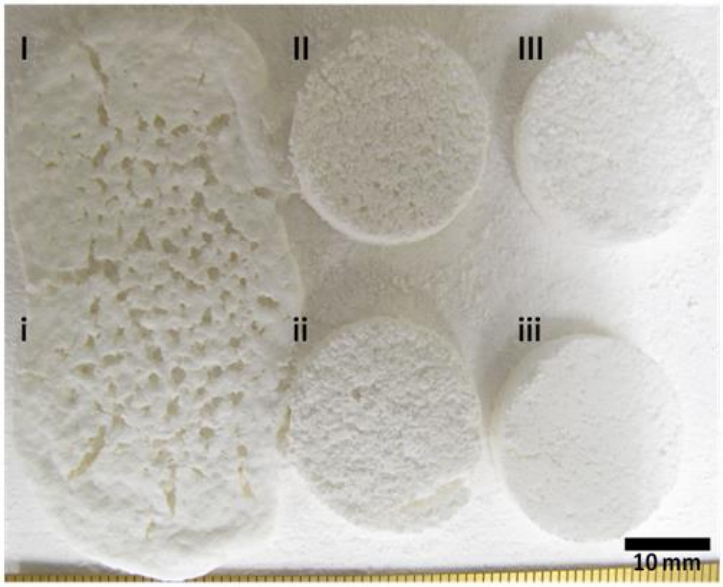

Figure 3-22: Macrostructure of porous A-W: PE scaffolds. Representative photo of pellet scaffolds with ratios 50:50 w/w (A-W: PE) (I and i), 60: 40 w/w (II and ii) and 70: 30 w/w (III and iii). Scaffolds I-III were fabricated with A-W granule range 20- 53 μm and i-iii with A-W granule range 54-90μm. All samples were sintered according to heat treatment B. Scale bars, 10 mm. The images were taken at magnification x1.

In Figure 3-23 SEM images of compacted powder scaffolds are shown. These scaffolds were fabricated using two different A-W: PE w/w. Samples imaged in A and B were sintered using the heat treatment B. In both pellet scaffolds pores have been created from the burning off of the polymer. The sample that contained lower polymeric concentration before sintering had less pores. Both scaffolds had micro-cracks throughout the structure.

The samples presented in Figure 3-23; C and D, were sintered according to heat treatment E. The distribution of the pores in these scaffolds was less homogenous than the scaffolds that were sintered according to the heat treatment B. The pore distribution in the pellets sintered according to the heat treatment E appeared to have a gradient, which is separated with a red dashed line. The one side of the scaffolds seemed to have similar pore distribution with the pellets sintered according to the heat treatment B, but these pores had smaller size. The other side had formed small channels, less pores and the pore distribution was heterogeneous. The two different ratios A-W: PE, 60: 40 and 70: 30, shows similar microstructures.

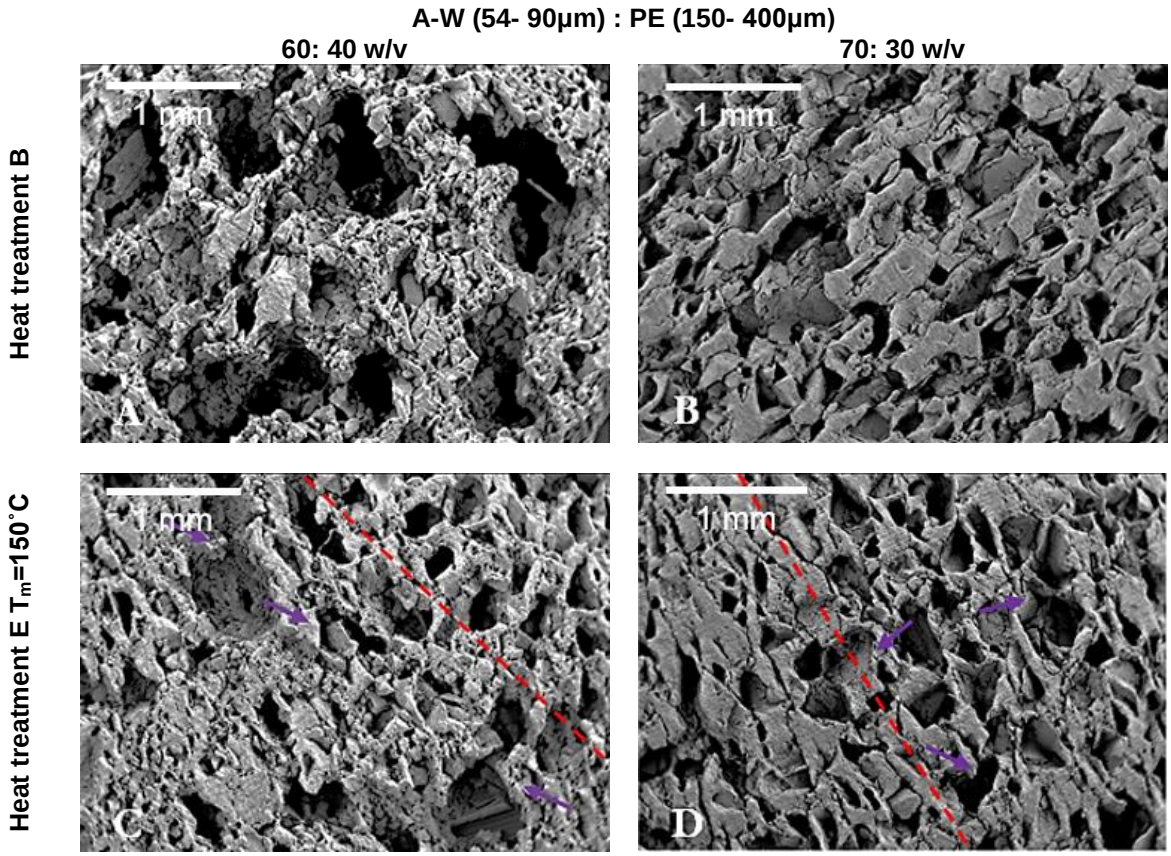

Figure 3-23: Changes in the pellet microstructure fabricated with A-W and PE2 in relation to different heat treatments. Representative SEM photos pellets that were sintered according to the heat treatment B with A-W: PE2 ratio 60: 40 (A) and 70: 30 (B). In C and D images, pellets that were sintered according to the heat treatment E (Tm=150°C) with A-W: PE2 ratio 60: 40 and 70: 30 respectively. Purple arrows highlighted channels. Red dashed line emphasised the division of two pore morphologies in the same scaffold. Scale bars, 1mm.

In Figure 3-24, the volumetric shrinkage of A-W: PE pellets that were prepared with A-W particle is illustrated. In each graph, the pellets were divided into two different groups depending on the ratio A-W: PE w/w and for each ratio the effect of the different heat treatments used was demonstrated. Statistical analysis of the shrinkage of porous A-W using two–way ANOVA indicated that the shrinkage of pelletes with A-W 20- 53 μm were significantly influenced by the PE content ($p<0.0001$) and the interaction between the polymeric content and the heat treatment ($p< 0.0001$). The shrinkage of the pellet scaffolds with A-W particle range 54- 90 μm were significantly influenced from both the polymeric content ($p<0.0001$) and the heat treatment ($p<0.0001$), but the interaction of the two factors had no significant influence in the porosity of this group ($p= 0.8868$).

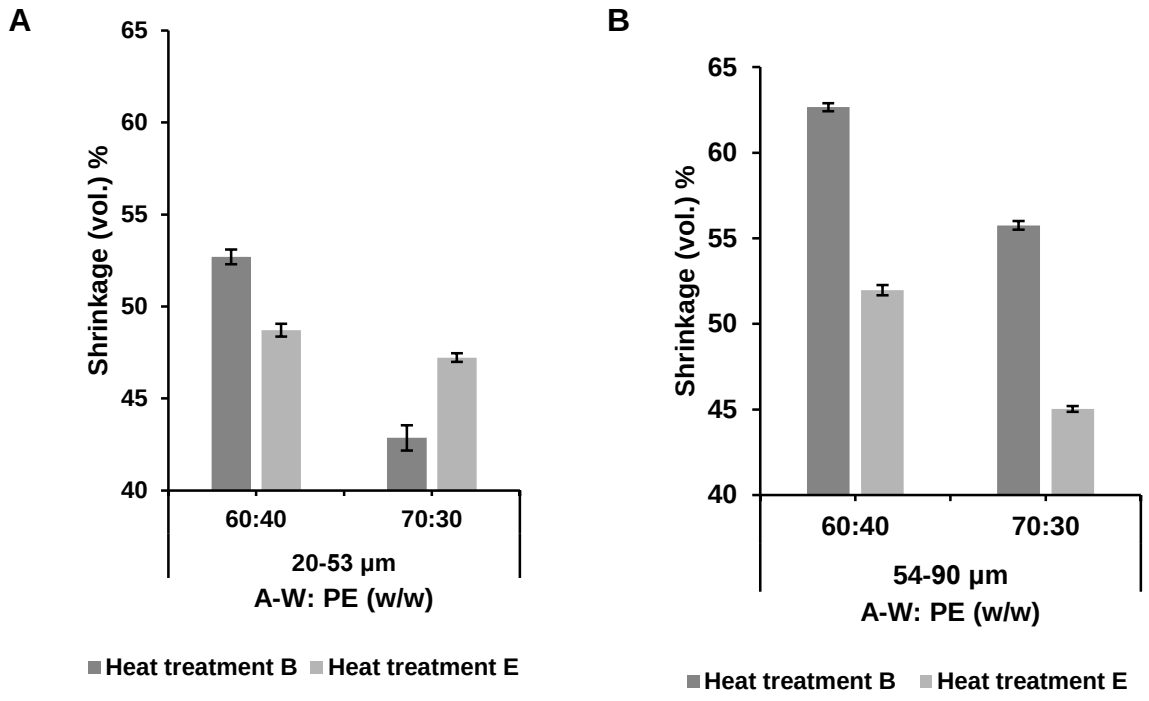

Figure 3-24: Shrinkage of pellets made of A-W: PE 70: 30 w/w or 60: 40 w/w respectively according to heat treatments B and E with Tm= 150°C.

In Figure 3-25 the porous pellets with A-W: PE were also divided into two graphical representations depending on the particle ranges that was used (A for A-W 20- 53 µm and B for A-W 54- 90 µm). In each graph the samples have been grouped depending the A-W: PE ratio and the effect heat treatments B and E. According to two-way ANOVA statistical analysis the porosity of the pellets with particle range 20-53 µm was significantly influenced by the PE concentration ($p= 0.0002$) and significantly affected by the interaction between the polymeric contant and the heat treatment that were used ($p= 0.0186$). The heat treatment as a sole factor had no significant effect on the porosity of the scaffolds with A-W particle range 20- 53 µm ($p= 0.6109$).

Using the same statistical analysis, in Figure 3-25; B, it was revealed that the porosity of the scaffolds prepared using A-W particle range 54- 90 µm was affected significantly by the heat treatment ($p= 0.0462$) and the AW:PE ratio ($p<0.0001$) and the interaction between the heat treatment and the PE content ($p= 0.0004$).

From statistical analysis of the shrinkage and porosity of the porous pellet scaffolds, there was a correlation coefficient between the two parameters.

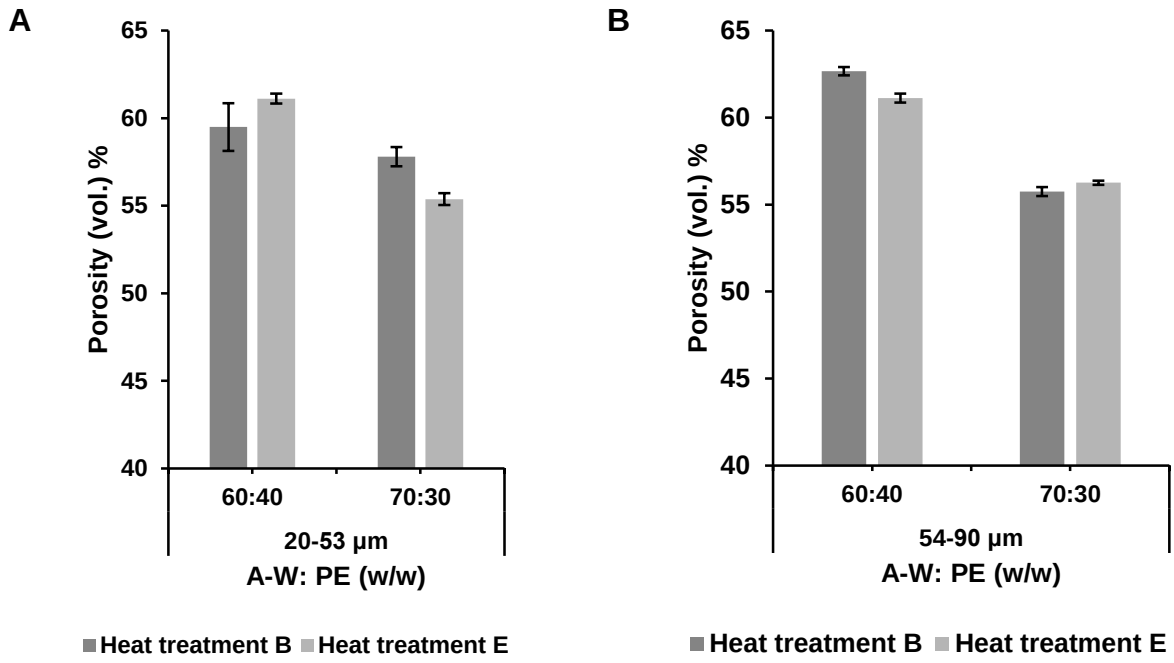

Figure 3-25: Porosity of pellets made of A-W: PE 70: 30 w/w or 60: 40 w/w respectively according to heat treatments B and E with Tm= 150°C.

3.4.2.7 Effect of polymeric filament on the macrostructure and channel formation of pure A-W sintered compacted powder scaffolds

Following the introduction of the polymeric particles, polymeric filaments were introduced in the pellet scaffolds to promote channel formation as described in Figure 3-9.

In Figure 3-26, a sample of compacted powder scaffolds with polymeric filament in the middle is presented. Large cracks were formed in the pellet after sintering that resulted in the loss of its mechanical integrity and some of its pieces broke without any other influence (Figure 3-26; A). In Figure 3-26; B, some micro-cracks were observable in the channels, but also a large crack similar to the one found in the pure A-W scaffolds (Figure 3-15) was identified. Due to this crack that was formed at its transverse plane (and was common in the pure A-W and A-W with polymer filament pellet scaffolds) the scaffolds sometimes separated into two parts (Figure 3-26; C).

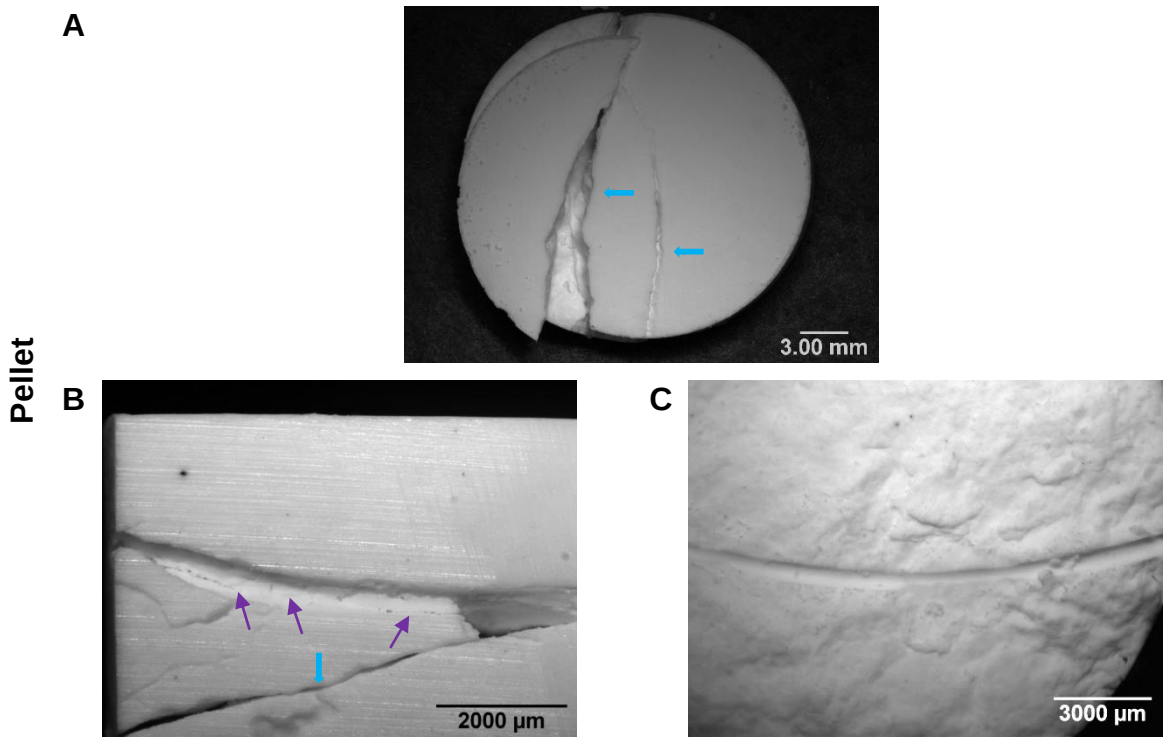

Figure 3-26: Compacted powder scaffold with polymeric fibre. Representative bright field micrographs of pellets sintered with polymeric fibre in the centre. Scaffolds were sintered according to the heat treatment B and the polymeric filament had diameter 0.7 mm. Blue arrows indicate large cracks and purple arrows micro-cracks.

Pellet scaffolds with polymeric filament that had diameters 0.7 mm and 0.5 mm were sintered using heat treatments C and E to evaluate whether the diameter of the fibre or the heat treatment affected the crack formation. No differences were observed in the fabricated scaffolds.

3.5 Sintering of Cast Loose powder With and Without Polymer Cores

A-W powder was poured into moulds to produce loose powder scaffolds. The anticipated features from manufacturing loose powder scaffolds were microporosity and topography that would be influenced by the particle range used.

Loose powder scaffolds were assessed to overcome the drawbacks which appeared during fabrication of the compacted powder scaffolds. These loose scaffolds were intended to be used as platforms to further develop highly porous and interconnected scaffolds for further characterisation studies with mammalian cells, including hMSCs.

Similarly to the pellet scaffolds, small polymeric particles were added with the A-W particles to aid powder distribution. Larger polymeric particles were mixed with the ceramic to introduce pores after burning off the polymer during sintering. Polymeric filament was added in the A-W to allow channel formation. This idea was further advanced into fabricating a PLA- FFF negative template in order to obtain a highly porous and interconnected scaffold with large pores.

3.5.1 *Methods and Materials*

3.5.1.1 Fabrication of pure A-W loose powder scaffolds

Pure A-W powder was poured in moulds (Figure 3-27; A) – either in the drilled holes of a brick (diameter 14-16 mm, height 36.7-37.1 mm) (Figure 3-27; B) or platinum tubes (25 mm height x 10 mm internal diameter) (Figure 3-27; C) closed on the one end using Parafilm® M.

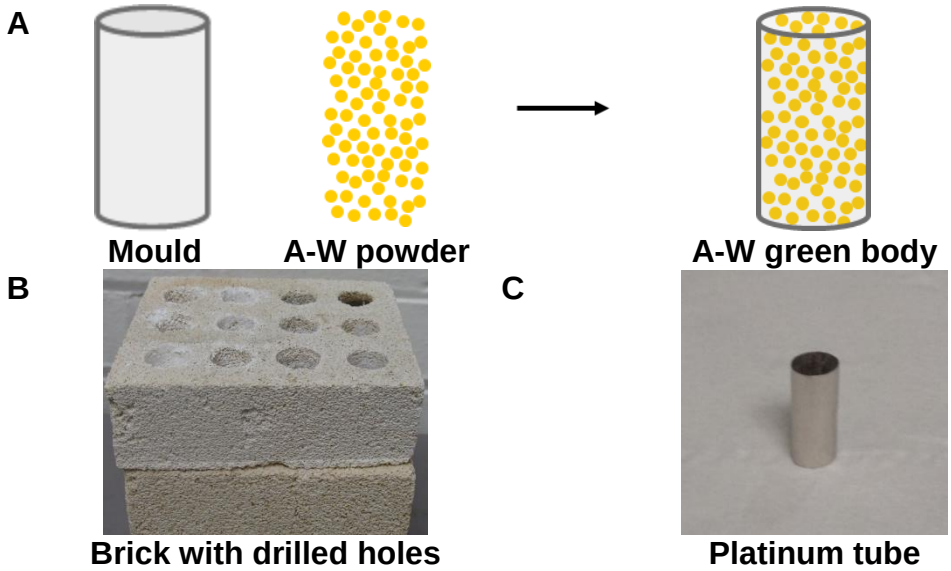

Figure 3-27: Schematic representation of pure A-W loose powder scaffolds (A) and moulds used for their fabrication (B-C).

3.5.1.2 Introduction of PA small polymeric particles

PA particles were introduced in A-W powder and mixed in A-W: PA ratio of 80: 20 w/w. Following the mixture was poured into moulds to sinter (Figure 3-28). The PA was added to promote better ceramic particle distribution.

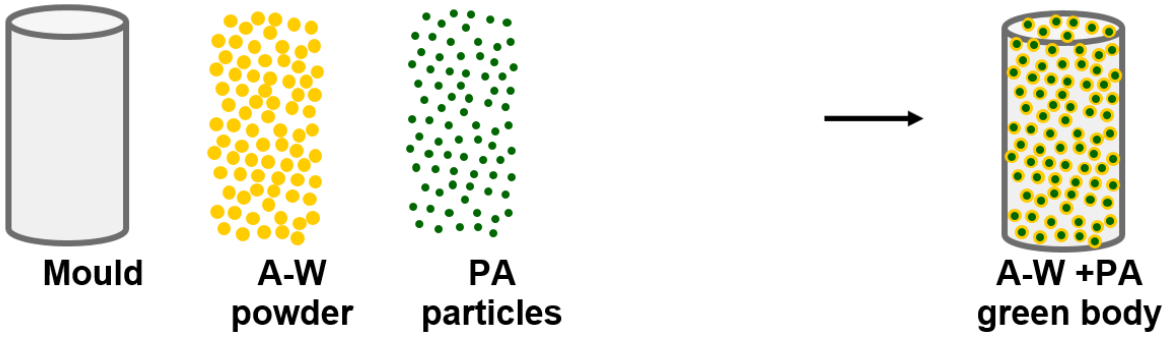

Figure 3-28: A-W loose powder with PA particles

3.5.1.3 Introduction of large polymeric particles

PE particles were mixed with A-W powder before they were poured in moulds (Figure 3-29) to form macropores improving the porosity of the scaffolds after sintering. The A-W: PE ratios that were used for the fabrication of these scaffolds were mentioned in Table 3-4.

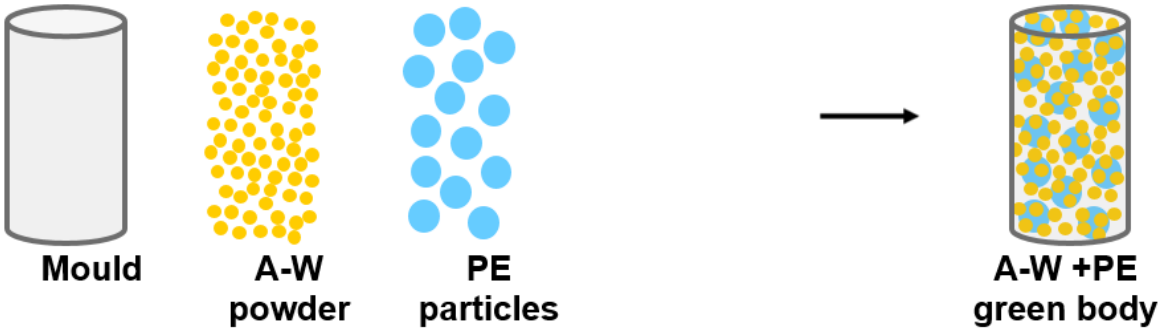

Figure 3-29: A-W loose powder with PE particles.

3.5.1.4 Introduction of polymeric filaments

One polymeric filament with diameter 0.5 mm or 0.7 mm or two FFF printed filaments (Figure 3-30) were imported in the centre of A-W powder after the powder was poured in the moulds (Figure 3-31) to create a uniform channel in the centre of the sintered scaffold. The FFF were connected on the one side to control their position in the powder keeping them a constant distance from one another. The addition of a polymeric filament aimed to investigate, if this approach ensured large channel formation in the scaffold after sintering.

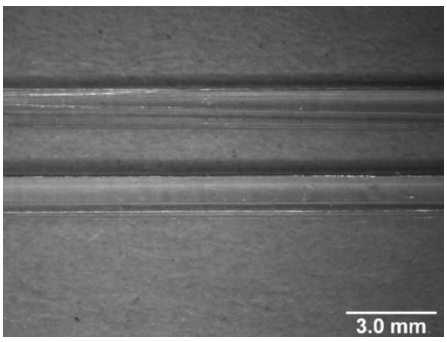

Figure 3-30: Illustration of FFF printed polymeric filament.

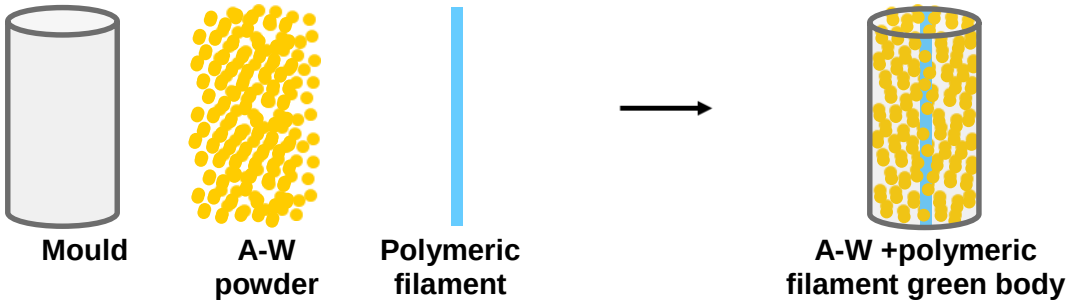

Figure 3-31: A-W loose powder with polymeric filament.

3.5.1.5 Negative template fabrication using Fused Filament Fabrication (FFF)

Negative moulds were manufactured with translucent PLA using a RapMan 3D printer (Bits from Bytes, UK) (Figure 3-32).

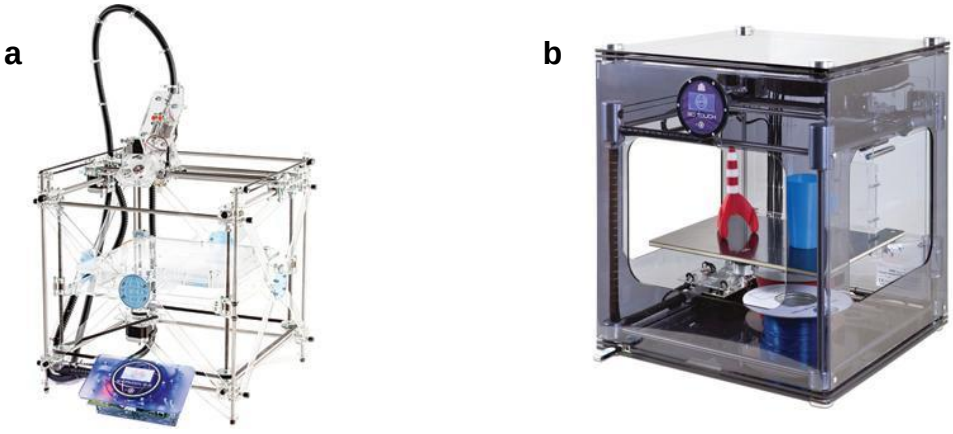

Figure 3-32 : RapMan printers: a) RapMan 3.2 3D, b) RapMan 3D Touch

The information for the parts to be printed using RapMan was contained in a G code file on an SD card. The G code was generated using Axon 2 (Axon 2.0 beta 2, Bits from Bytes, UK). The CAD program that was used for the designing of the negative moulds was Inventor 2012 (Autodesk).

Two different negative templates were designed using Autodesk Inventor. The first negative mould was a grid within circular walls with dimensions 25mm x 24 mm (diameter x height) (Figure 3-33). Each layer consisted of bars 1.5mm x 1.5mm x 20 mm and the gap between then is 3.0 mm. The next layer had the same design and dimensions, but it was rotated 90° to form a grid with pores that had diameter parallel to the bars 3.0mm and diagonal diameter 4.24 mm. Also, the structure of the mould was cylindrical and had a solid ring outside keeping the material that would be inserted inside.

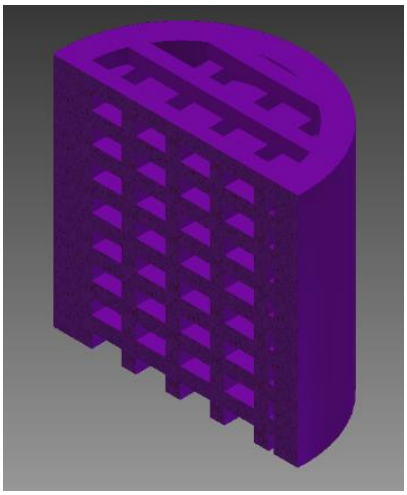

Figure 3-33: Transverse cut of the CAD design of FFF PLA negative template mould.

The second negative template was a grid that was used as the core of the ceramic scaffold (Figure 3-34). The design of the first layer was similar to the letter “S” with dimensions 1 mm height and each external side is 7 mm. The following layer was the same with the first, but rotated 90° (Figure 3-34). Depending on the height of the platinum tube that was inserted the height of the total scaffold was modified by adding extra layers.

RapMan was programmed to build the first structure with layer thickness 0.125mm and the second with 0.5 mm for both negative templates. The fill density was 100% and speed multiplier was 2x for both types of negative templates.

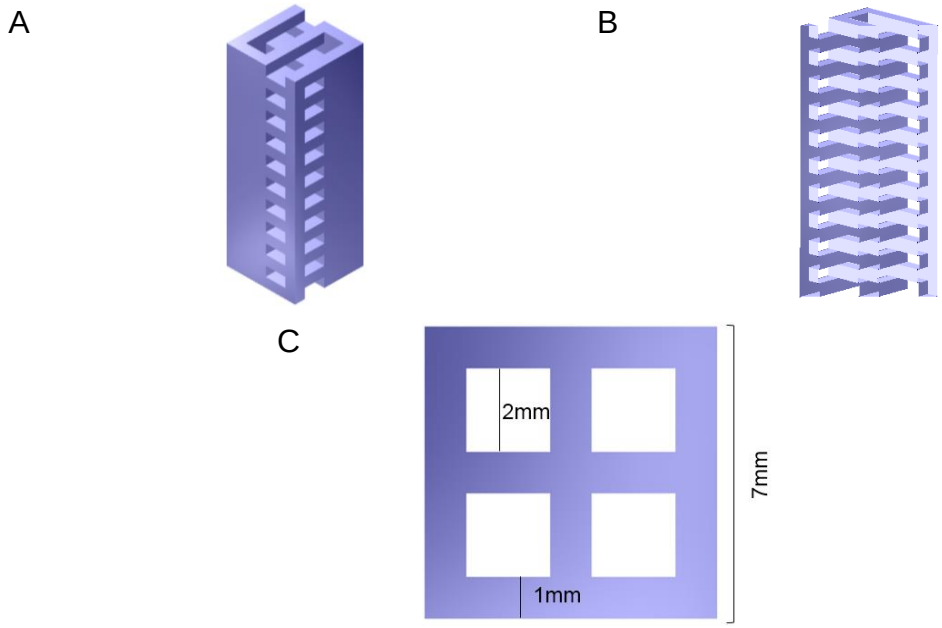

Figure 3-34: Different views of the CAD design of the FFF PLA negative template core.

3.5.1.6 A-W loose powder in FFF PLA negative template mould

A FFF PLA negative template mould (Figure 3-33) with walls was fabricated to contain the A-W powder without the need of using another mould (Figure 3-35). In addition, a grid was designed within the walls allowing the formation of interconnected channels in the scaffold after sintering the mould with the A-W powder.

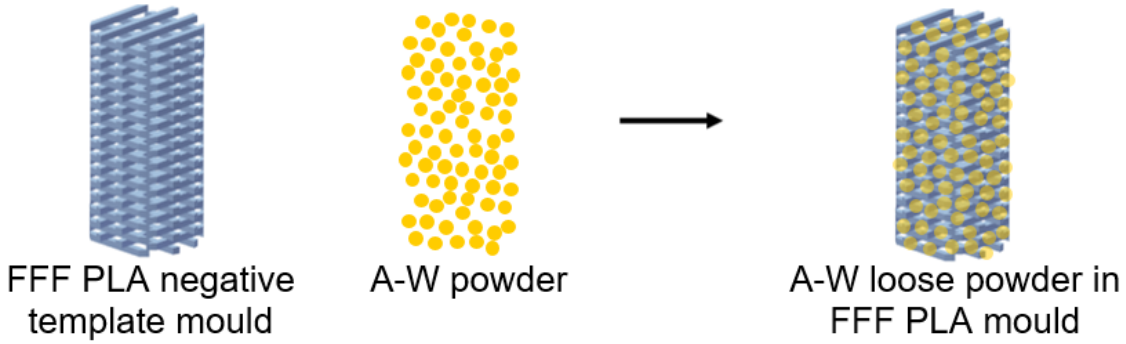

Figure 3-35: A-W loose powder in FFF PLA negative template mould

3.5.1.7 FFF PLA negative template core

A FFF PLA negative template core (Figure 3-34) with the same grid design as the FFF PLA negative template without the walls was placed into a platinum tube (Figure 3-36). The removal of the walls aimed to reduce the polymeric content in the green part and protect the integrity of the sintered scaffold.

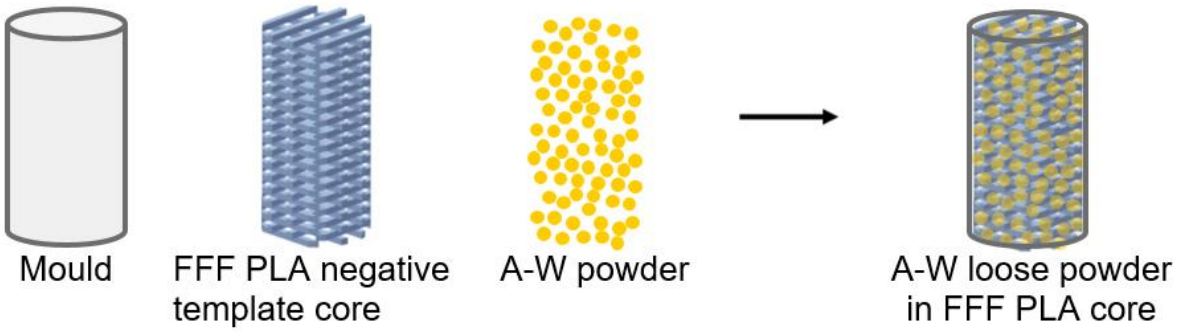

Figure 3-36: A-W loose powder poured in FFF PLA negative template core that was already placed in a mould.

3.5.1.8 Sintering

All green bodies were sintered inside a high temperature laboratory chamber furnace with maximum operating temperature 1800˚C (Carbolite, UK) after they placed on a platinum foil.

3.5.2 *Results*

3.5.2.1 Influence of different particle ranges on sintered cast loose powder scaffolds

As illustrated in Figure 3-37, the particles of the loose powder scaffolds did not fuse completely and there was neck formation between adjacent particles. In particular, the particles in loose powder scaffolds prepared using particle range 54- 90 μm had small neck formation and no fully melted particles appeared. In loose powder scaffolds made using particles 20- 53 μm apart from neck formation, some fused particles were observed, In addition, the pores in the scaffold with the smaller particle range were smoother and smaller than the corresponding scaffold with particle range 54- 90 μm.

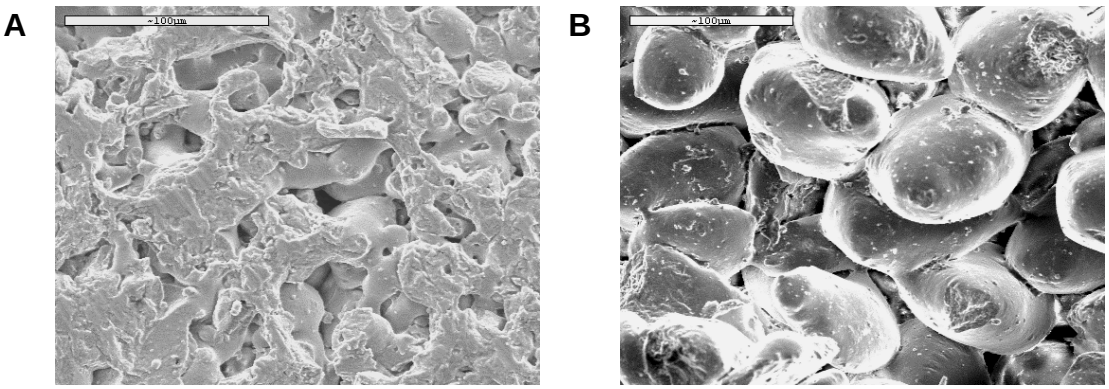

Figure 3-37: Microstructure of sintered loose powder scaffold fabricated with pure A-W. Representative SEM photos of loose powder scaffolds with particle range 20- 53 μm (A) and 54- 90 μm (B), respectively. All scaffolds were sintered according to scheme of the heat treatment A. Scale bar: 100 μm.

In Figure 3-38 the shrinkage and the porosity of loose powder scaffolds that were prepared with pure A-W using two different particle ranges were illustrated. After analysing their data using student's t-test, it was noted that the particle range had no significant effect neither on the shrinkage (p= 0.1006) nor on the porosity (p= 0. 0704) of the loose powder scaffolds.

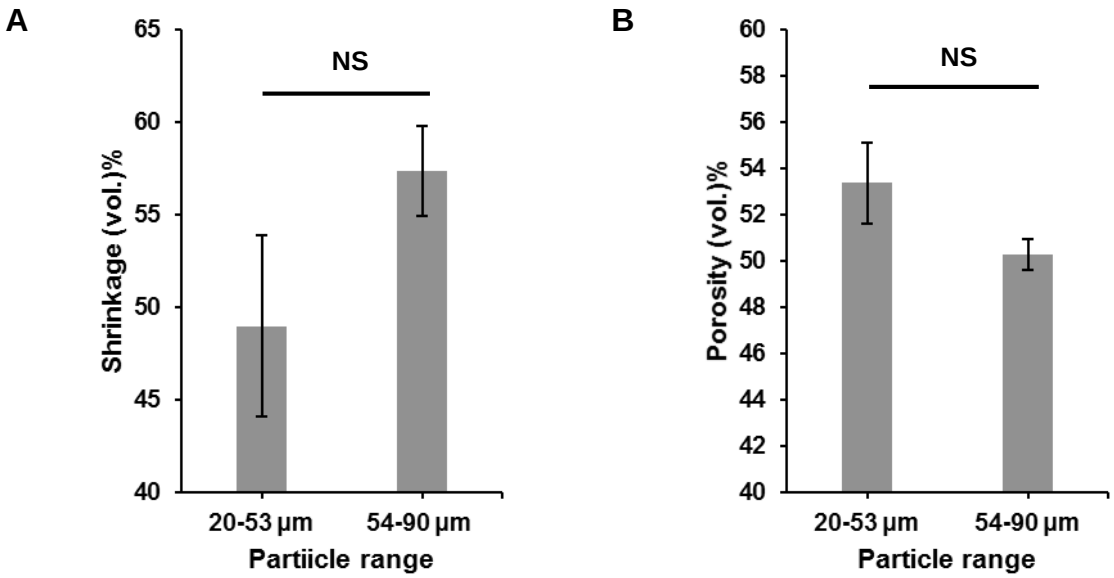

Figure 3-38: Shrinkage and porosity of sintered pure A-W loose and pellet scaffolds that were prepared using 20- 53 µm and 54- 90 µm particle ranges and sintered according to heat treatment A.

3.5.2.2 Influence of different heat treatments in combination with different particle ranges on sintered cast loose powder scaffolds

Different heat treatments were explored for fabrication of loose powder scaffolds using the two main particle ranges; 20- 53 µm and 54- 90 µm.

In Figure 3-39, the effect of the different heat treatments on sintering of the loose particle scaffolds with particle range 20- 53 µm was presented as an example. During the heat treatment A, there was neck formation and a small number of particles had fused with the neighbouring particles. The main characteristic of the scaffolds sintered according to heat treatment B was the neck formation between particle and more particles fused with adjoining ones. Sintered samples with heat treatment C and D morphologically resulted in fusion of most of the particles, densification of the scaffolds and reduction of pore size in the scaffold. It was observed that scaffolds that were fabricated according to the heat treatment D were more vitreous.

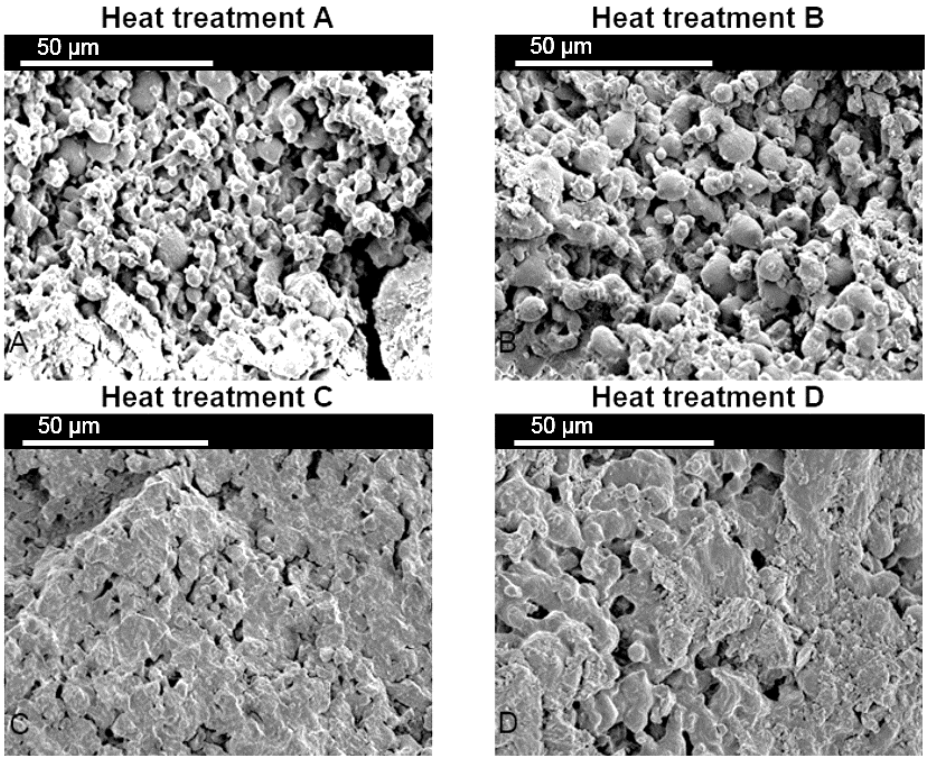

Figure 3-39: Changes in the heat treatment affect the degree of sintering of A-W. Representative SEM photos of loose powder scaffolds with A-W (20- 53 µm) sintered according to heat treatment A, heat treatment B, heat treatment C, and heat treatment D. Magnification x 1000, scale bars 50 µm.

Figure 3-40 shows that the different particle ranges (p= 0.7528) and heat treatments (p= 0.7717) had no significant influence in the shrinkage of loose powder scaffolds after analysing the data using two-way ANOVA. The interaction between the particle range and the heat treatments influenced significantly (p= 0.0195) the shrinkage of these scaffolds.

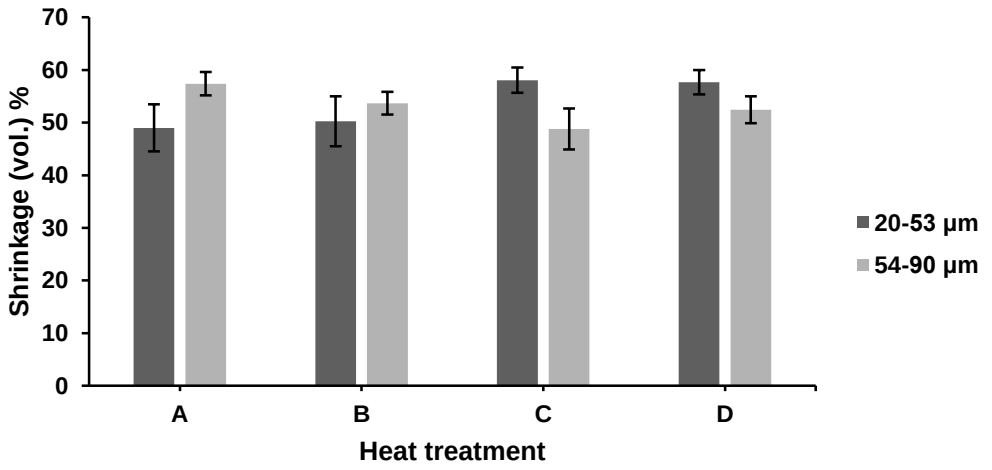

Figure 3-40: Shrinkage of pure A-W loose scaffolds fabricated using particle range 20-53 µm and 54-90 µm sintered according to the heat treatments A, B, C, and D.

Figure 3-41 shows that there was a significant difference in the porosity of the loose powder scaffolds resulting from the heat treatments (p= 0.0014) and the particle ranges (p= 0.0030) and the interaction of these two factors (p= 0.0017). The effect in porosity was predominantly only on the scaffolds with particle range 20- 53 μm and was impacted more with the alterations at the second step of the sintering programme (heat treatments C and D). Samples sintered according to heat treatment B seem to have the highest porosity.

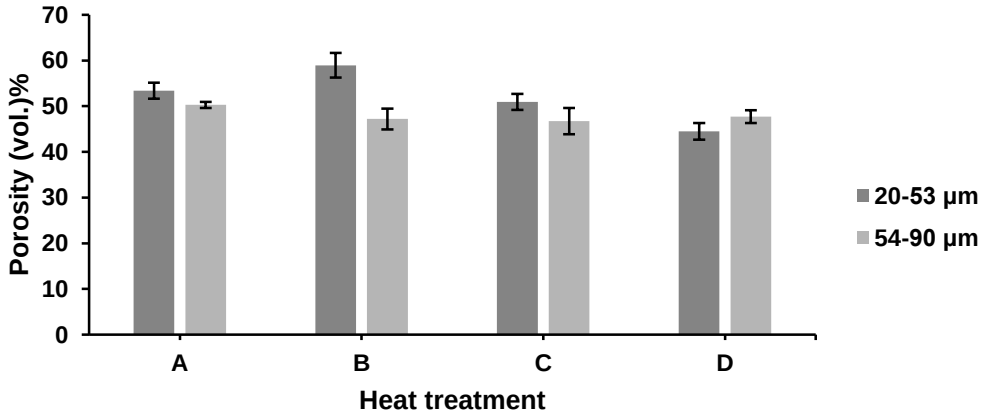

Figure 3-41: Porosity of pure A-W loose scaffolds fabricated using particle range 20-53 μm and 54-90 μm sintered according to the heat treatments A, B, C and D.

3.5.2.3 Influence of different moulds on sintered cast loose powder scaffolds

Concerning the macrostructure, the loose scaffolds that were moulded in the brick (Figure 3-42; A) had irregular shape comparing to the scaffolds that were sintered in the platinum tube (Figure 3-42; B).

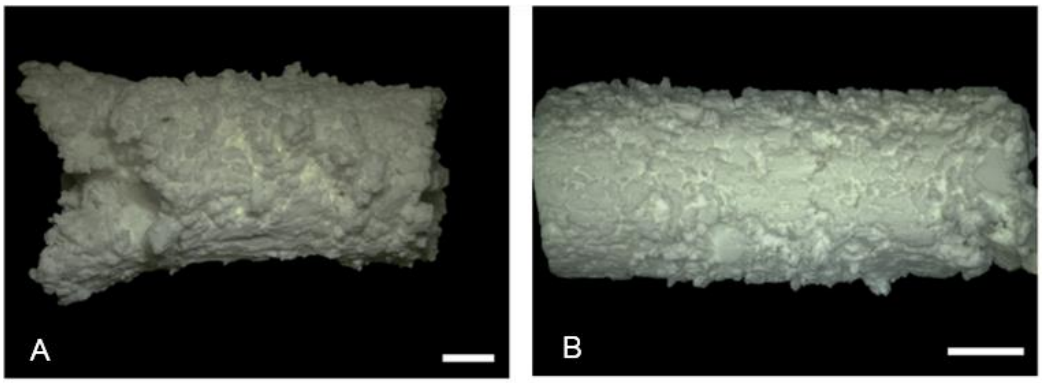

Figure 3-42: Morphology of sintered loose powder fabricated with pure A-W. Representative bright field images of dry loose powder scaffolds sintered in brick mould (a), platinum mould (b), respectively. Scaffolds were fabricated with A-W 20- 53 μm and sintered according to scheme of the heat treatment B. Scale bars, 3mm. The images were acquired using lens 0.5 at magnification 1x.

Powder was dried at 120°C overnight before use to ensure that there was no residue of humidity. No difference in powder distribution was observed between the sample that was heat treated and the raw.

3.5.2.4 Effect of small polymeric particle ranges in powder distribution and sintered cast loose powder scaffolds

Polymeric particles - PA were introduced in the loose powder scaffolds to improve the homogeneity of the powder distribution. Scaffolds collapsed during de-moulding from the brick mould after sintering.

3.5.2.5 Effect of large polymeric particle ranges in pore formation and macrostructure of sintered cast loose powder scaffolds

Loose fragments of A-W were observed in the pores of the loose powder scaffold with A-W: PE2 (60: 40) in A and B (Figure 3-43). This was considered to be due to the fact that the scaffold collapsed during sintering.

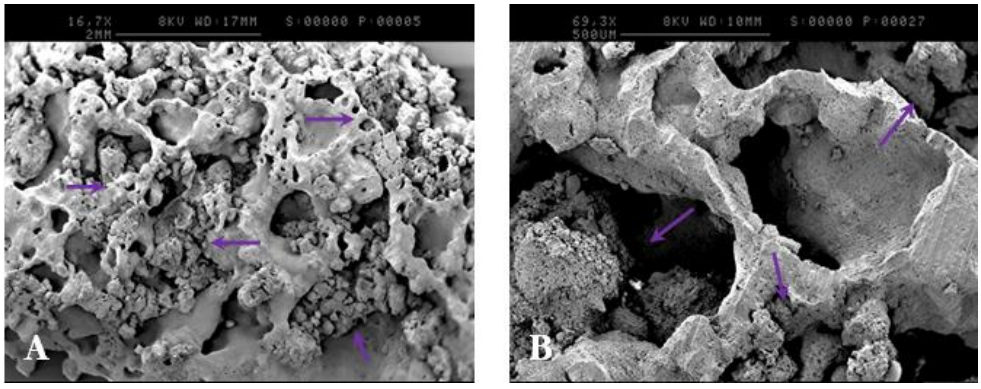

Figure 3-43: Microstructure of loose powder fabricated with PE2. Representative SEM photos of loose powder (A and B) scaffolds with A-W: PE (60: 40), and A-W particle range 54-90μm. Purple arrows highlight collapsed particles.

Heat treatments B and E were used for the fabrication of A-W: PE pellet scaffolds to stimulate the interconnectivity of the scaffolds via channel formation. The loose powder scaffolds collapsed.

3.5.2.6 Effect of polymeric lines in channel formation and macrostructure of sintered cast loose powder scaffolds

Following the introduction of the polymeric particles, polymeric filaments were introduced in loose powder scaffolds. The introduction of the one (A) and simultaneously two polymeric fibres (B- C) successfully formed channels in loose

powder scaffolds (Figure 3-44). No obvious cracks appeared in the channels after sintering.

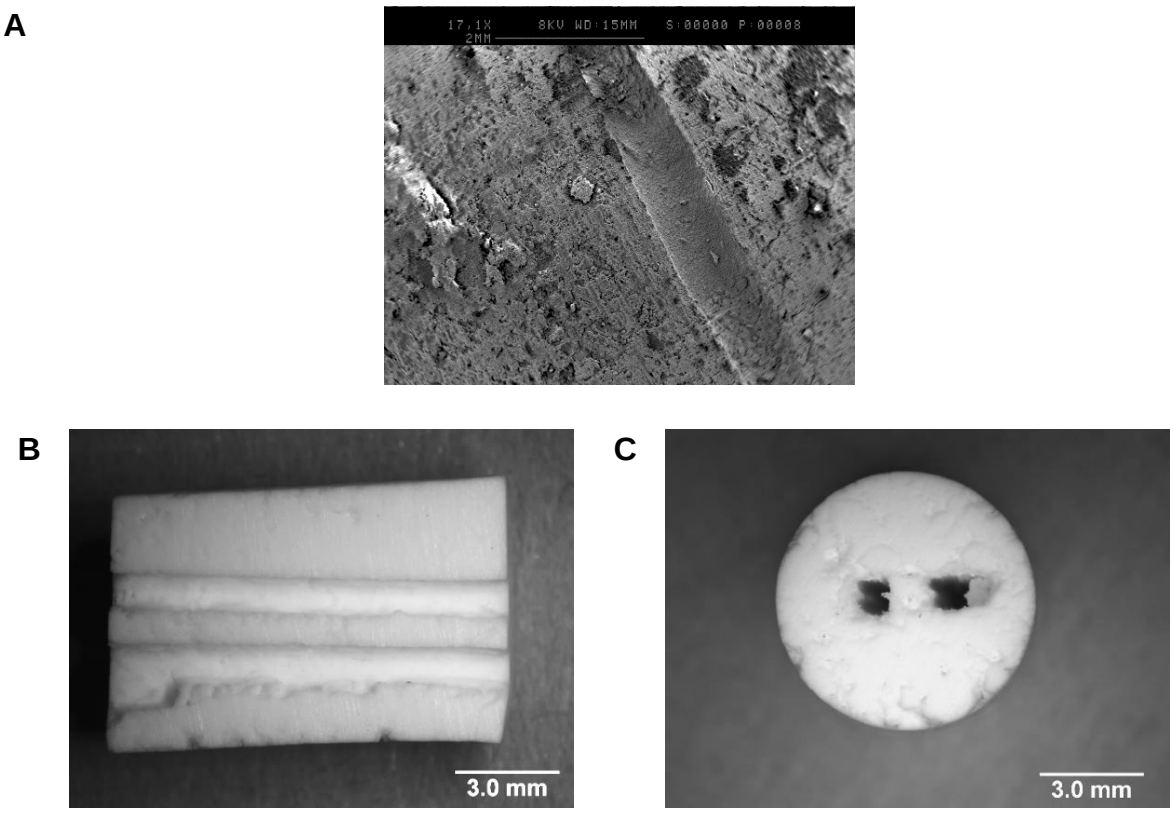

Figure 3-44: Loose powder scaffolds with polymeric fibre. Representative SEM photo of scaffolds sintered according to heat treatment B. Polymeric filament had diameter 0.7mm (A) and approximately 1mm (B-C).

3.5.2.7 Effect of negative polymeric FFF template in channel formation and macrostructure of sintered cast loose powder scaffolds

FFF printed PLA moulds were fabricated using a RapMan 3D printer and designed to be used as negative templates for the A-W scaffolds. These moulds were designed to have strut thickness of 1.5mm and gaps 3.0mm. In Figure 3-45, the first two layers (A) and a cross section (B) of the PLA negative mould are shown. In the graph Figure 3-45; C it was highlighted the difference in the printed construct in comparison to the CAD design. The printed struts were thicker than the primary design resulting in correlated smaller pores.

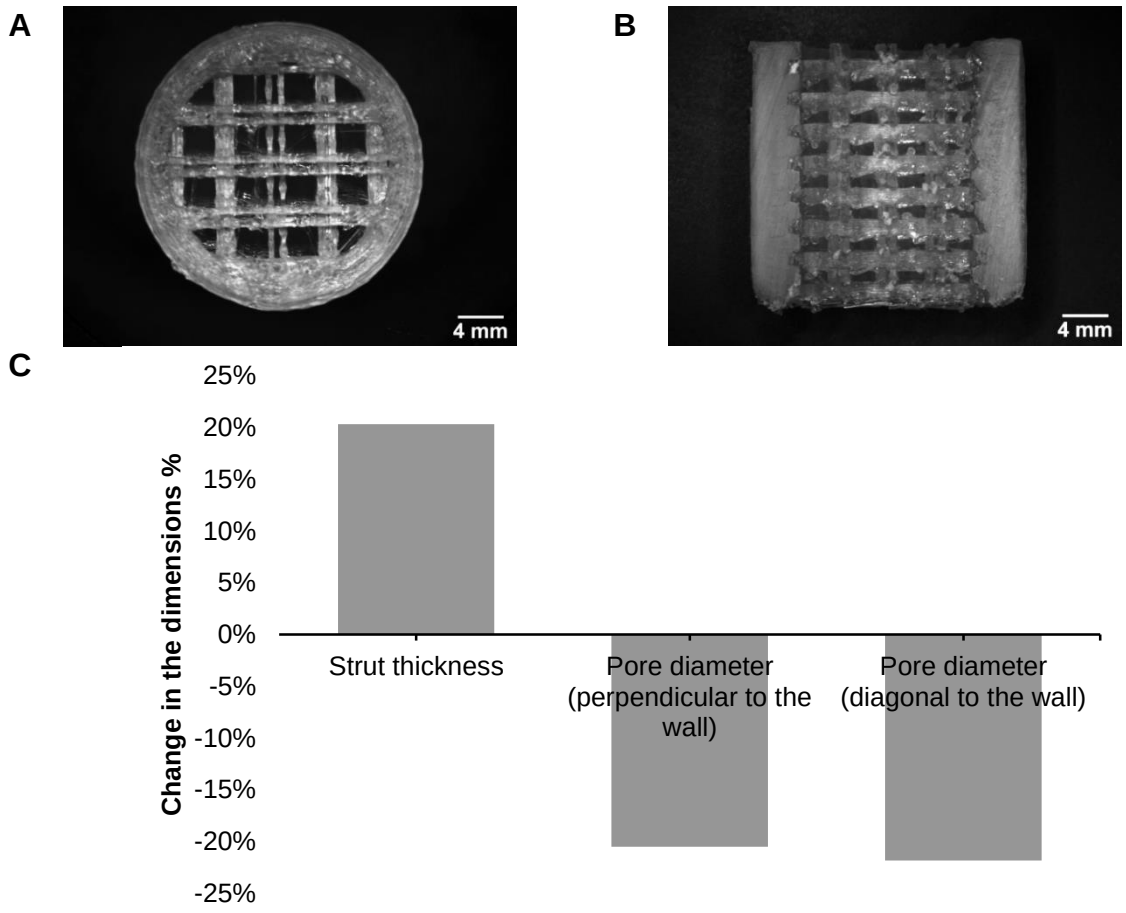

Figure 3-45: PLA negative mould fabricated on RapMan. Representative bright field images of the first two layers (A) and a cross section of the whole printed mould (B). Illustration of the deviation between the CAD designed mould and the FFF printed (C).

Figure 3-46 shows A-W scaffolds that were sintered in the FFF-PLA negative moulds at different heat treatments. Scaffolds that were sintered according to the heat treatment B (A) formed pores according to the negative mould. Scaffolds that were sintered according to the heat treatment E (B) were distorted with smaller pores. After either heat treatment, the majority of the scaffold collapsed.

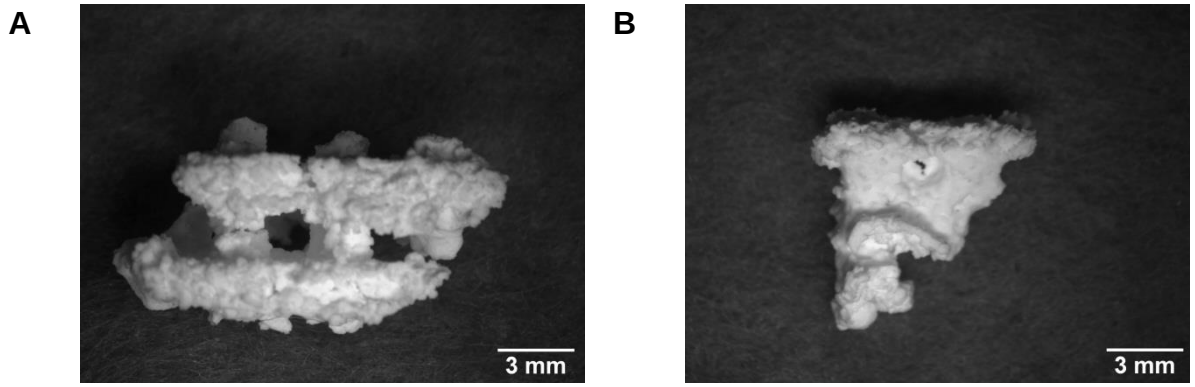

Heat treatment B **Heat treatment E (T_m=190ºC)**

Figure 3-46: Scaffolds fabricated by pouring A-W (54- 90 µm) into the negative moulds and heat treated according to the heat treatments B and E respectively.

In Figure 3-47 the FFF- PLA core is shown (A-B). In addition, different views of the sintered loose powder scaffold with the burnt off PLA FDM core are illustrated (C-M). The images clarified that after sintering the PLA FDM core was burnt off leaving the negative imprint as the loose sintered scaffold has large channels of approximately 1mm.

Images I-K revealed cracks vertical to the orientation that the scaffolds was standing whilst sintering. Also, in image I small pores appear towards the bottom of the scaffold. Images L and M demonstrated the degree of sintering on the outer surface of the scaffold (L) and inside (M). When the same scaffolds was replicated with smaller height, the structure collapsed or it broke during the procedure of de-moulding.

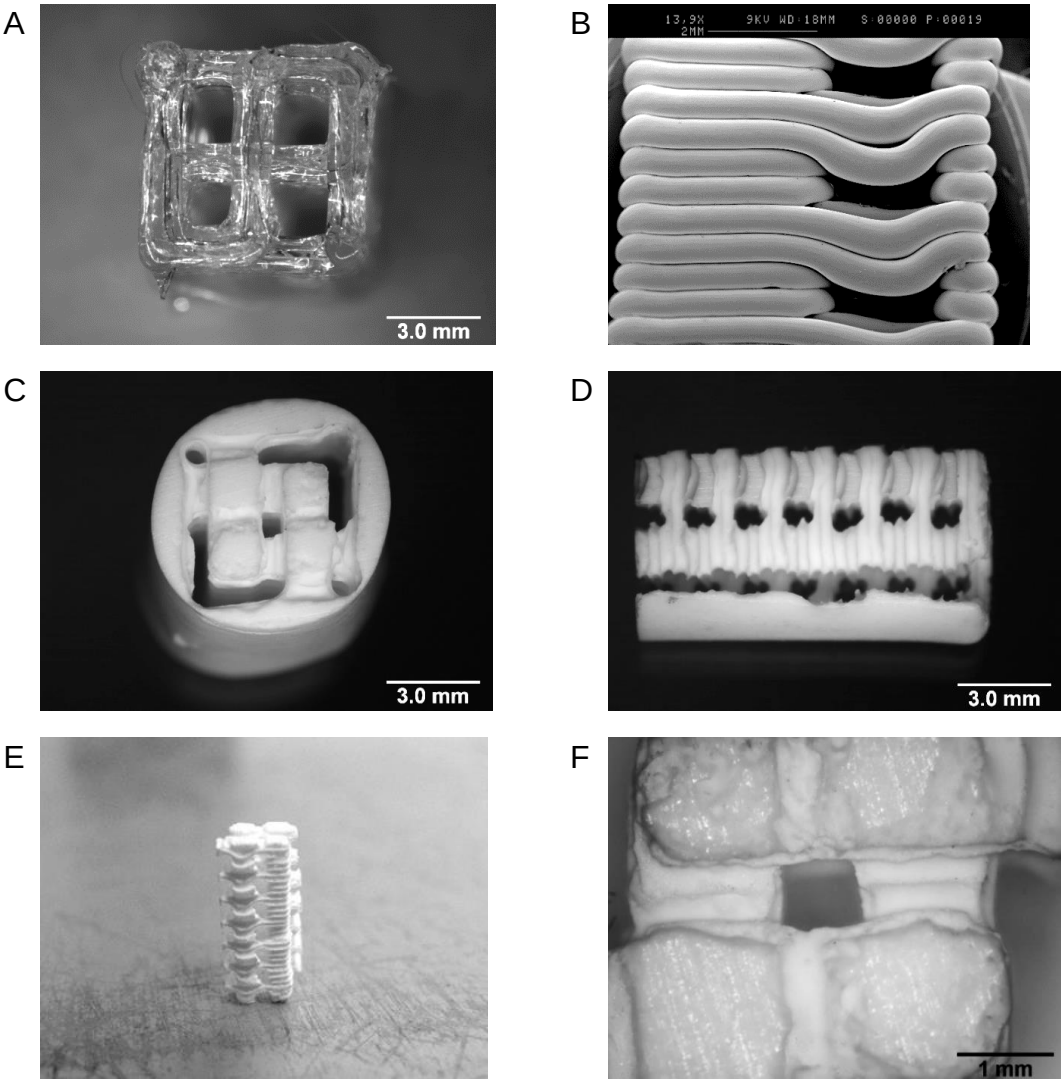

Figure 3-47: Loose powder scaffolds with PLA FDM core. Representative images of the PLA FFF core - bright field (A), SEM (B). Micrographs of the sintered scaffold- bright field (C-H), SEM (I-M). Samples were fabricated using A-W 20- 53 µm and sintered according to heat treatment B.

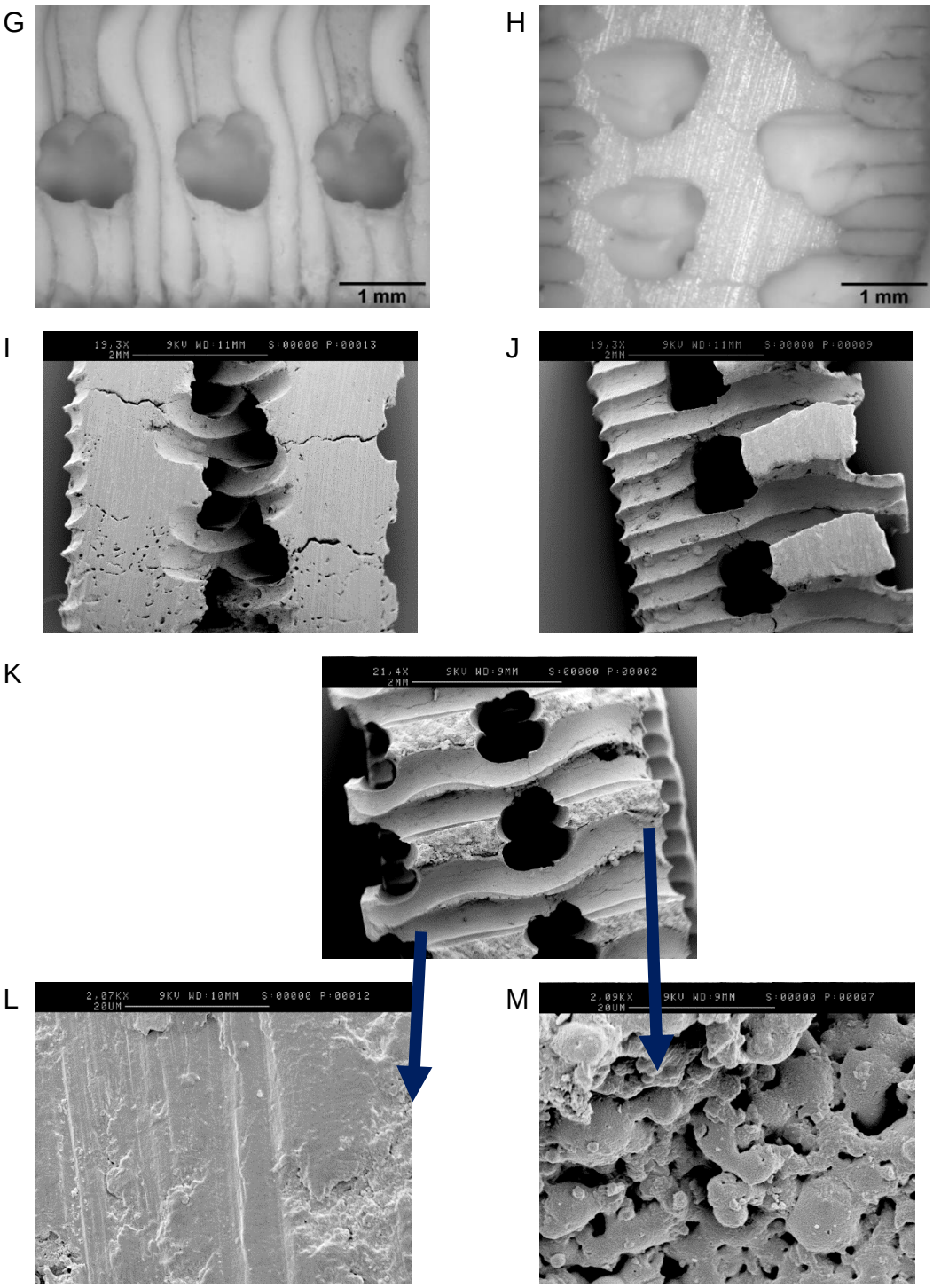

Figure 3-47: Loose powder scaffolds with PLA FDM core. Representative images of the PLA FFF core - bright field (A), SEM (B). Micrographs of the sintered scaffold- bright field (C-H), SEM (I-M). Samples were fabricated using A-W 20- 53 µm and sintered according to heat treatment B.

3.6 Sintering of Cast Slurries

In pursuit of scaffold for culturing cells on the surface in order to investigate how the topography produced by different particle ranges and the microporosity could affect hMSC processes *in vitro*, scaffolds were produced by sintering cast slurries.

A-W powder was mixed with deionised water to result in slurry before it was poured in platinum moulds. Water was used as a binder instead of isopropanol that was used in §3.4, because when isopropanol was trialled, it evaporated at a fast rate causing inconsistencies in the powder flow whilst it was poured in the moulds. This type of scaffold was developed to improve the powder distribution and result in a scaffold with smaller pore sizes in comparison to the loose powder scaffolds, with more homogenous morphology and with structural integrity.

This group of scaffolds had the same aims with the pellet and loose powder scaffolds.

3.6.1 *Methods and Materials*

A-W slurries of deionised water were poured in platinum tubes closed on the one end using Parafilm® M to improve the distribution of the ceramic powder. After samples were poured in the moulds were either manually agitated to distribute evenly in the mould or sonicated at 250 rpm for 1 min.

3.6.2 *Results*

Loose powder in combination with deionised water was trialled with two different particle ranges as described for the loose powder scaffolds (20- 53 μm and 54- 90 μm) and different heat treatments were investigated (Figure 3-48). The scaffolds that were fabricated using the larger particle range collapsed during sintering using heat treatments B, C and D (Figure 3-48). Only the scaffolds that were sintered according to heat treatment F remained intact and the outer surface of the particles had started sintering forming very small necks, but the scaffolds had poor structural integrity when they were removed from the mould. The samples using the smaller particle range (20- 53 μm) were successfully sintered and as the temperature and as the duration of the sintering increased, the particles seemed to melt more.

Scaffolds were prepared using A-W with particle range 20- 53 μm and with particle range mixtures of 54- 90 μm : <20 μm with ratios 90: 10 w/w, 80: 20 w/w and 70: 30 w/w. All the different slurries were sonicated to distribute the powder evenly and

sintered according to heat treatments B, C, D and F. The graph that is presented in Figure 3-49 portrays the porosities of these groups. After analysing data using two–way ANOVA, it was noted that only the heat treatment had no significant effect on the porosity of the scaffolds (p= 0.0659). The particle size and the interaction between the particle range and the heat treatment had extremely significant influence on the porosity (both p< 0.0001).

Scaffolds with particle range 20- 53 µm sintered with heat treatment D and F were difficult to de-mould and they were glassier than the scaffolds sintered according to heat treatment C. Scaffolds sintered according to heat treatment B were friable.

In heat treatment C, there was no significant difference in porosity between scaffolds prepared using 20- 53 µm, 54- 90 µm: <20 µm with ratios 80: 20 w/w and 70: 30 w/w. For the following experiments, scaffolds with particle ranges 20- 53 µm and 54- 90 µm: <20 µm with ratio 80: 20 w/w were selected.

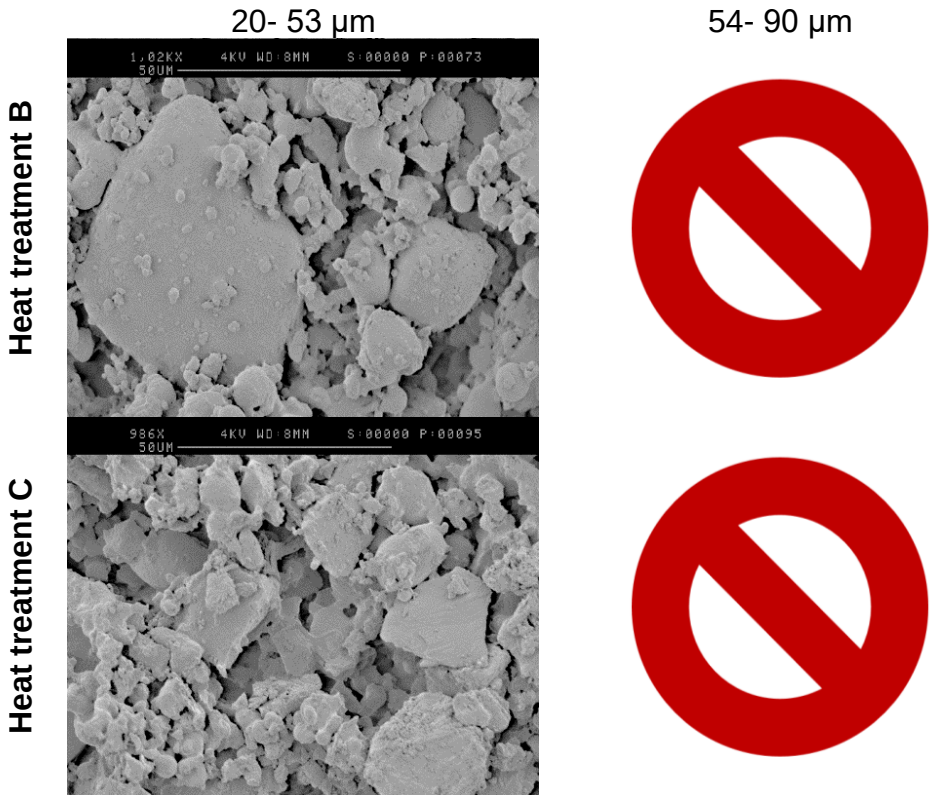

Figure 3-48: SEM micrographs of A-W loose powder with deionised water made using 20- 53 µm and 54- 90 µm sintered according heat treatments B, C, D and F.

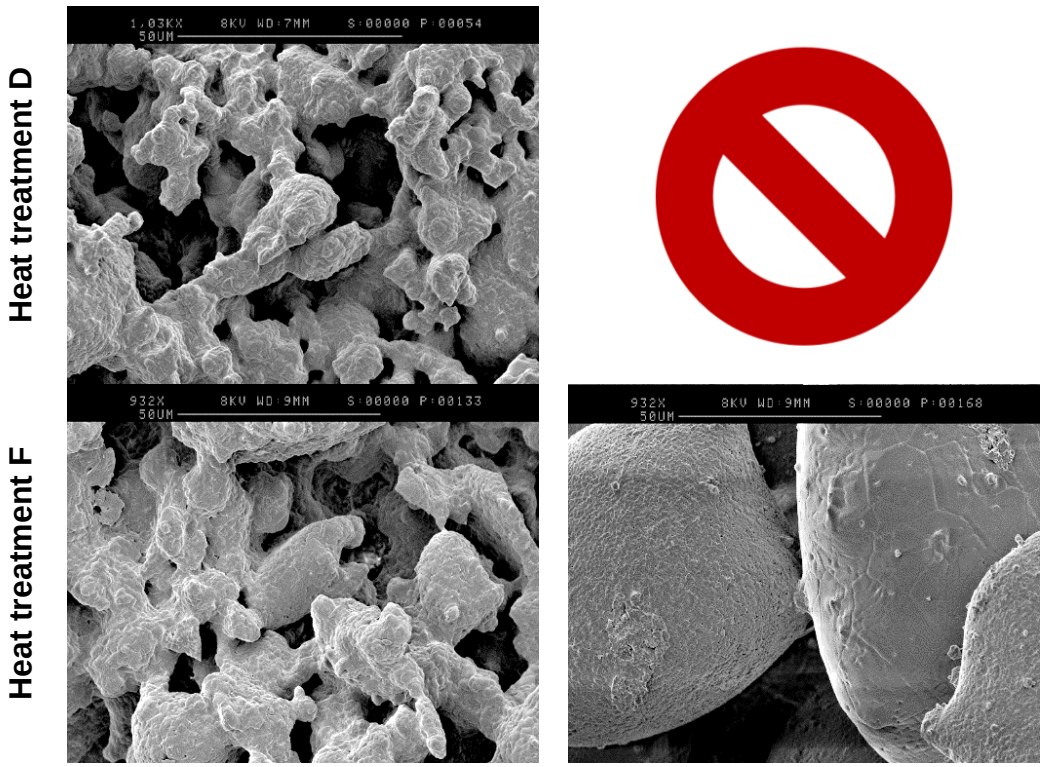

Figure 3-48: SEM micrographs of A-W loose powder with deionised water made using 20- 53 µm and 54- 90 µm sintered according heat treatments A, B, C and D.

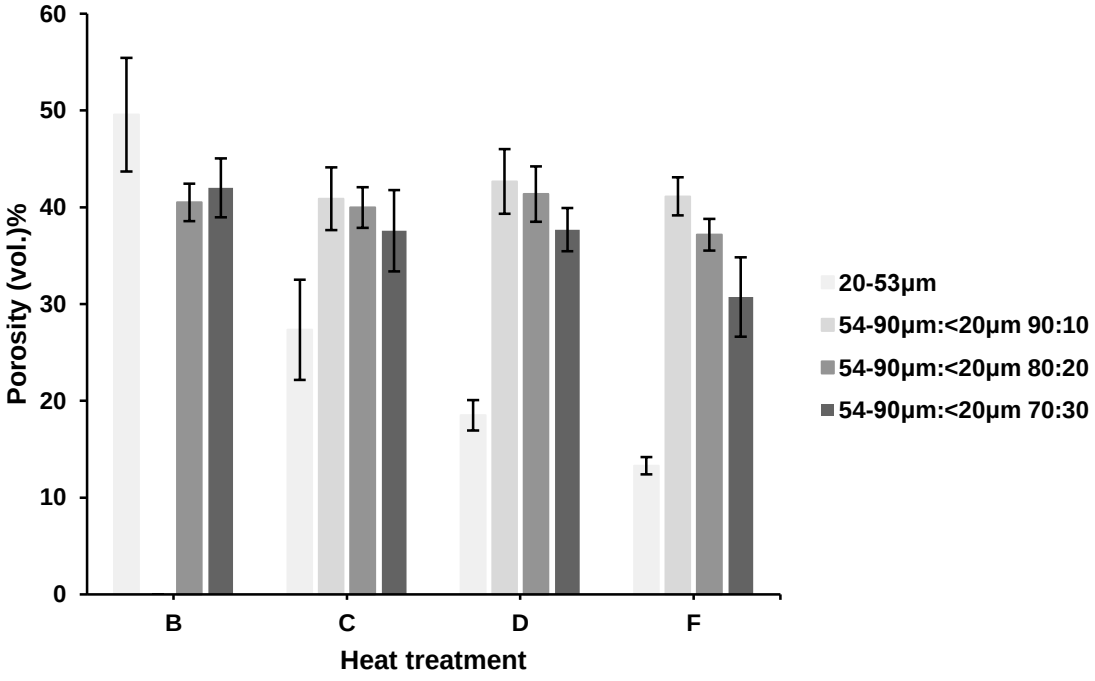

Figure 3-49: Porosity of pure A-W scaffolds from sintered cast slurries fabricated using particle range 20-53µm and different mixtures of 54-90 µm: <20 µm sintered according to the heat treatments B, C, D and F.

Either manual agitation or sonication produced evenly distributed slurries. In Figure 3-50, the subsequent scaffolds were illustrated with dry loose powder scaffolds using

the corresponding particle ranges as control. Scaffolds that were made using dry powder were not very flat. Scaffolds prepared using A-W slurry were flatter and the powder distributed more evenly. Sonicated scaffolds appeared to have bubbles on their surface especially on scaffolds with particle range 20- 53 µm. Scaffolds with mixed particle ranges 54- 90 µm: <20 µm (80: 20 w/w) that were sonicated had less small particles on the surface and they were not as well distributed as the non-sonicated ones.

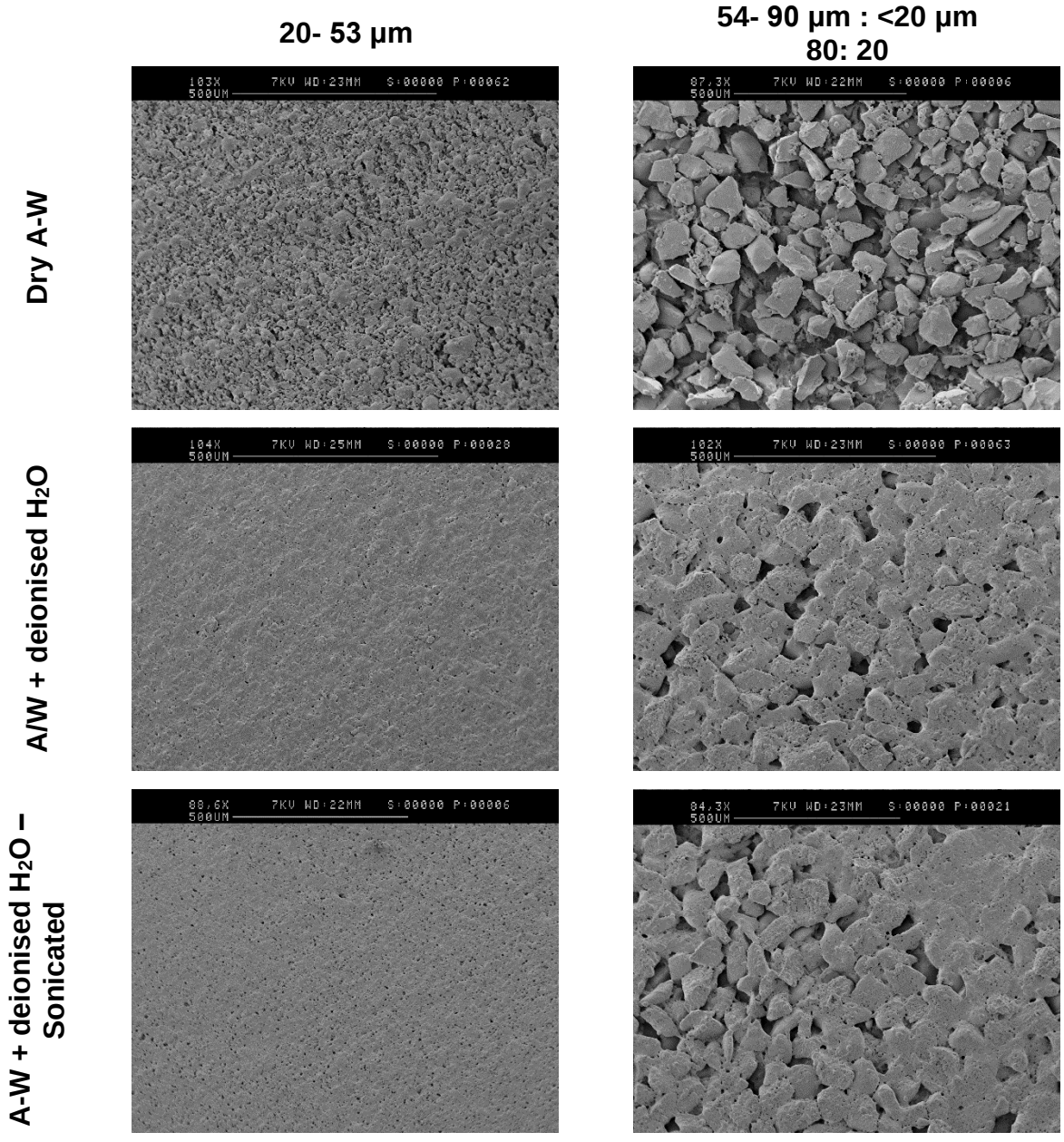

Figure 3-50: Demonstrative SEM images of different packing techniques for A-W powder as dry powder and slurry using deionised water with or without sonication.

The porosity of sintered cast slurries without sonication according to heat treatment C was assessed (Figure 3-51). There was no significant difference between the two particle groups (p= 0.1548) after data was analysed using student's t-test.

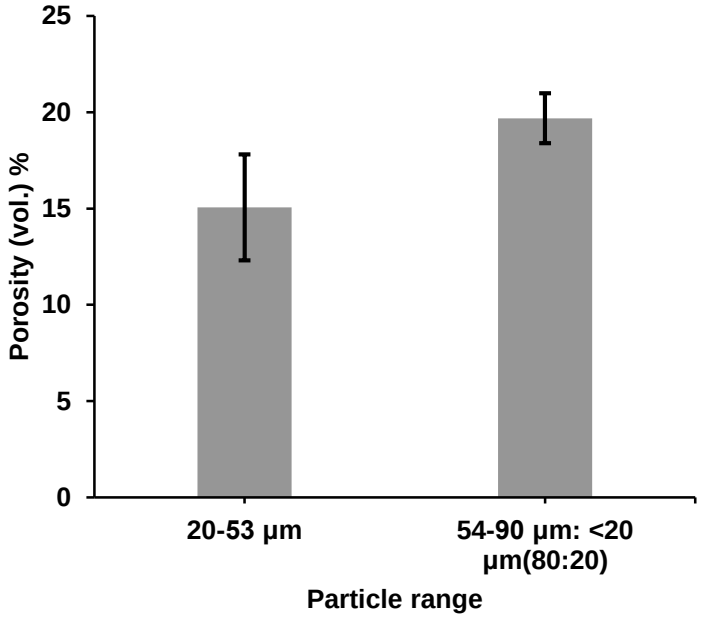

Figure 3-51: Porosity of sintered loose powder scaffolds fabricated using A-W with 20- 53 µm and 54- 90 µm: <20 µm (80: 20) particle ranges in combination with deionised water.

3.7 Sintering of Green Parts prepared Using TIPS

Scaffolds fabricated with thermally induced phase separation (TIPS) followed by freeze drying have been reported to be highly porous with channels that indicate interconnectivity (Yang et al., 2006).

To fabricate hard, mechanically robust scaffolds for bone tissue engineering applications, A-W was incorporated into PLA- TIPS process and then sintered to burn out the polymeric phase and leave behind a hard, rough ceramic scaffold.

The development and optimisation of this method aimed to produce highly porous and interconnected ceramic scaffolds with structural integrity. These scaffolds could be used as matrices for cultivating hMSCs in a 3D environment to examine cellular behaviour.

In an effort to produce highly porous and interconnected scaffolds that would replicate the lamellar bone architecturally, a variety of parameters were investigated.

3.7.1 *Methods and Materials*

To prepare the negative polymeric TIPS template PLA, dioxane and water were selected as materials. Dioxane was selected, because is a miscible solvent to water and also separates from PLA at low temperatures. The ternary system PLA: dioxane: water has been studied extensively in the past years (Ma & Zhang 2001; La Carrubba et al. 2008; Hua et al. 2002).

3.7.1.1 Determination of cloud point curve

PLA with concentration 5% w/v was added in 1, 4-dioxane: distilled water mixtures and sealed in glass bottles. Volume ratios of dioxane and water were set at 90: 10, 87: 13, and 85: 15 v: v. PLA was first dissolved at 85˚C for 1h by placing the sealed bottles in an oven and then, the dissolved polymer solutions were placed in an ultrasonic water bath to ensure sample homogeneity. The samples were then put in a water bath (Julabo ED) and heated to 20˚C above the expected cloud point until the solutions were completely transparent. The cloud-points of the ternary system were determined by visual turbidimetry and they were defined as the step at which the polymeric solution changes from clear to turbid. Each bottle contained a magnetic stirrer to guarantee the best estimation of the cloud point. The samples were first cooled in steps of 5 ˚C, equilibrating the system for 10 min at each new temperature.

For a more accurate cloud-point determination, the samples were re-heated and the solutions were cooled in steps of 1˚C every 10min (Schugens et al. 1996).

3.7.1.2 TIPS in combination with freeze drying scaffolds

The green body of the A-W – PLA scaffolds using TIPS in combination with freeze drying was prepared following the methodology described below (Figure 3-52). PLA (3, 5, 7 % w/v) was dissolved in a mixture of anhydrous dioxane-1, 4: distilled water (100: 0, 90: 10, 87: 13, 85: 15 % v/v) at 60˚C in an oven. When the PLA was completely dissolved, A-W powder (25 – 175 % w/v) with particle range 20- 53 µm or <20 µm was added in the ternary system. To obtain homogenous slurry, the slurry was stirred (for 1-4 h) in a water bath on a magnetic stirrer hot plate (C-MAG HS7, Ika: UK) to retain homogenous temperature through the solution. The slurry was poured into cylindrical glass moulds.

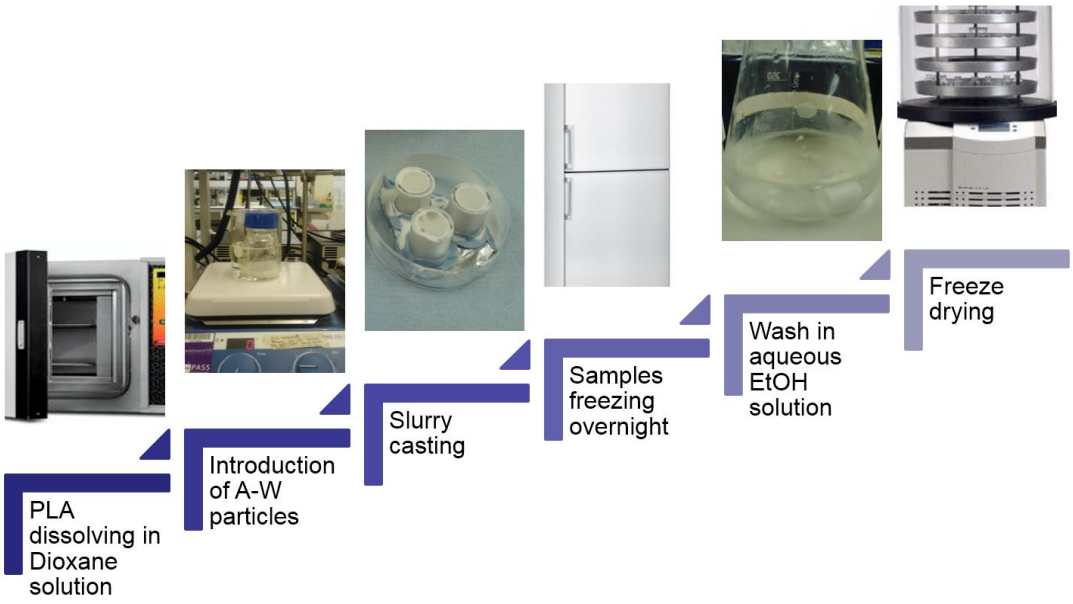

Figure 3-52: Green body fabrication method using TIPS method followed by freeze drying.

The glass moulds were previously stabilised on aluminium foil that was placed in a petri dish. Aluminium foil was also used to cover the lid of the petri dish. The moulds were tested at room temperature and pre-warmed in an oven (GenLab; UK) at 60˚C for 1 h. The petri dish with the aluminium foil was kept in a freezer (at -20, -80 ˚C) for the corresponding duration with the moulds in the oven.

When the slurry was poured in the glass moulds, the moulds in the petri dish were on ice. The moulded scaffolds were stored overnight at low temperature (-20, -80, or -

196°C). The frozen scaffolds were immersed in pre-cooled ethanol aqueous solution (80 % v/v) at -20 or -80°C depending on the temperature they were frozen. The aqueous ethanol was replaced every 2 h for a day. The dioxane was extracted out of the frozen scaffolds due to the miscibility between the dioxane (solvent for PLA) and the ethanol aqueous solution (non-solvent for PLA) (Ho et al. 2004).The scaffolds were removed from the moulds and stored at -80°C until they were transferred in dry ice to a freeze dryer (ALPHA 1-2 LD plus; Martin Christ Freeze Dryers GmbH, UK). Samples were lyophilised at -52°C and at 0.01 mbar for 24h to obtain the A-W – PLA green bodies.

The default parameters for the optimisation of the TIPS A-W scaffolds were described in Table 3-5.

Parameters	Default
Polymeric concentration (w/v)	5%
Solvent: non-solvent concentration (v/v)	100: 0
A-W concentration (w/v %)	25%
A-W particle range (µm)	20-53
Quenching temperature (°C)	25
Quenching duration (min)	0
Cooling (quenching 2) temperature (°C)	-20
Mixing slurry duration (h)	1
Mould temperature (°C)	25
Heat treatment	B

Table 3-5: Default parameters for TIPS A-W scaffolds

3.7.2 *Results*

A range of parameters were assessed for A-W TIPS scaffolds to identify which parameters affect the volume and quality of the porosity.

3.7.2.1 Cloud point curve

The dependence of the cloud points on the polymeric content of the solution and the concentration of solvent versus non-solvent was studied. As illustrated in Figure 3-53, cloud points in solutions with dioxane: water ratio 87: 13 (v/v) increased with the increase in polymer concentration. The cloud points in solutions with dioxane: water – 90: 10 and 85: 15 (v/v) increased when the polymer concentration was raised from 3% to 5% (w/v) and then decreased, as the polymer levels were further elevated

from 5 to 7% (w/v). The increase in dioxane in the system resulted in a decrease of cloud points for the solutions comprising of 3 and 5 (w/v) % PLA. The cloud points of the solutions using 7 (w/v) % PLA differed from the other two groups. Specifically, the cloud point augmented when the dioxane was modified from 85% to 87% by 20°C.

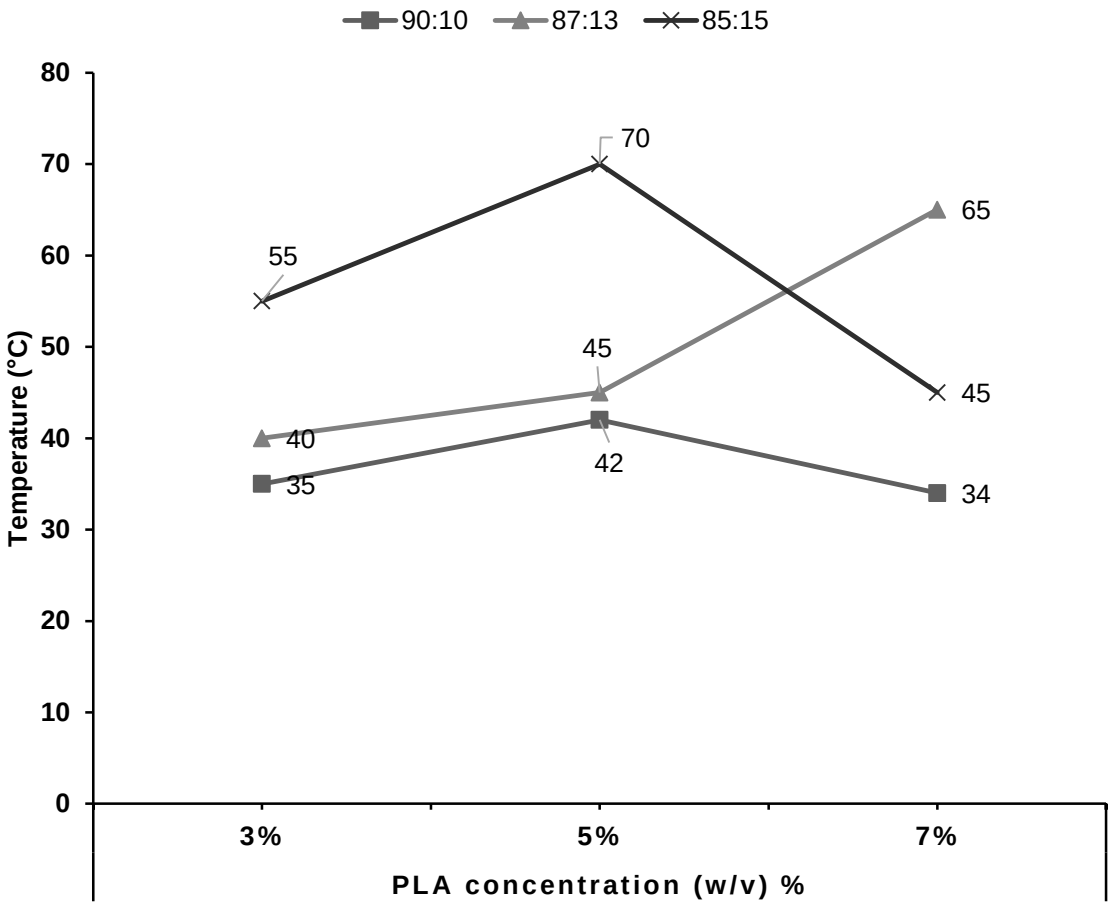

Figure 3-53: Cloud points determined for varied PLA concentrations (3, 5, 7 w/v %) in dioxane: water solutions with concentrations 85: 15, 87: 13, 90: 10 (n= 5)

3.7.2.2 Influence of different ratios of solvent: non-solvent on A-W TIPS scaffolds

The effect of solvent: non-solvent concentration in the ternary system was tested on scaffolds prepared using 5% w/v PLA, 25% A-W with particle range (20- 53 μm) varying the dioxane: water (v/v) ratios. After the introduction of the ceramic these samples were stirred for 1h, poured in moulds stored at -20°C. Then, freeze-dried for 1 day and sintered according to heat treatment B.

Green bodies of TIPS A-W scaffolds are portrayed in Figure 3-54. The A-W particles seem to be mainly embedded in a thin coating of the polymer. The scaffold that was prepared with more water (dioxane: water - 85: 15 (v/v)) had smaller pores, but the polymer seemed more fibrous with more nanopores.

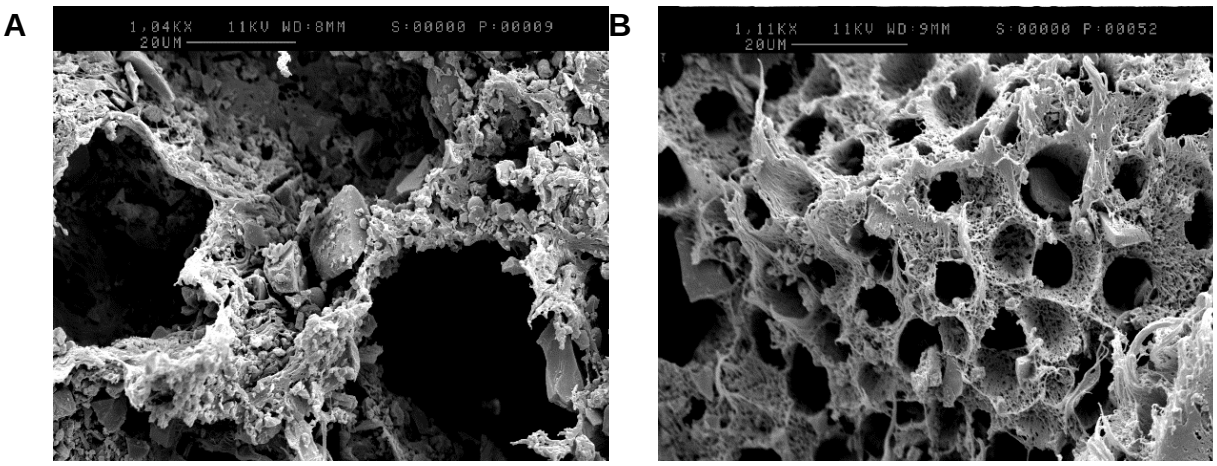

Figure 3-54: Representative SEM micrographs of green bodies of TIPS A-W scaffolds. Sample in image A was prepared with dioxane: water ratio 85: 15 and B; with 87: 13.

In the Figure 3-55, the graph demonstrates that the effect of the solvent: non-solvent ratio of the slurry was highly significant for the porosity of the TIPS A-W scaffolds. After analysing the results using Bonferroni's multiple comparison test, it was identified that the difference in porosity between scaffolds prepared using dioxane: water solution with concentration 85: 15 v/v and 87: 13 v/v was very significant ($p = 0.007$). All other scaffolds showed significant differences in porosity ($p<0.0001$). The higher the concentration of water in the system, the lower the porosity. Scaffolds that were prepared with no water and purely only dioxane had the highest porosity (82.65 ± 0.4857 vol. %).

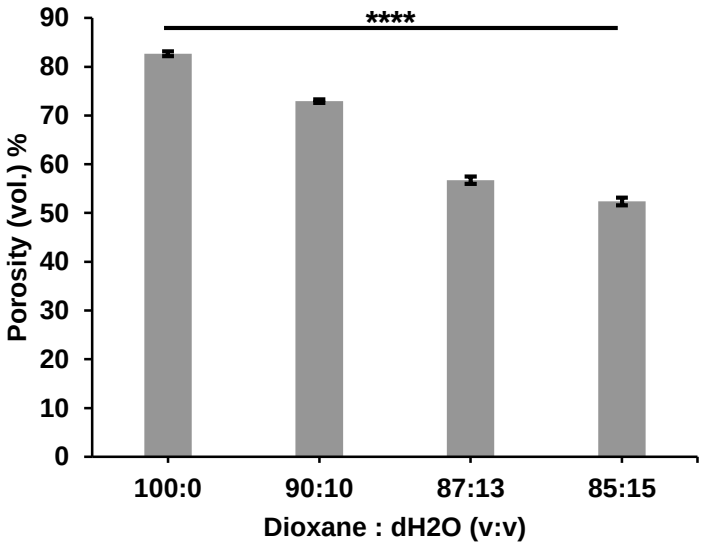

Figure 3-55: Porosity measurements of TIPS A-W scaffolds using a variety of solvent: non-solvent solutions. Bars demonstrated dioxane: water solutions with concentrations 100: 0, 90: 10, 87: 13 and 85: 15 (v/v) %. (n=3)

The scaffolds prepared using slurry that contained only dioxane (Figure 3-56; A) had the largest and the most opened pores in comparison to all the other scaffolds. Figure 3-56; B-D, shows that the more water was introduced in the solvent: non-solvent system, the smaller the pores were and they were less open.

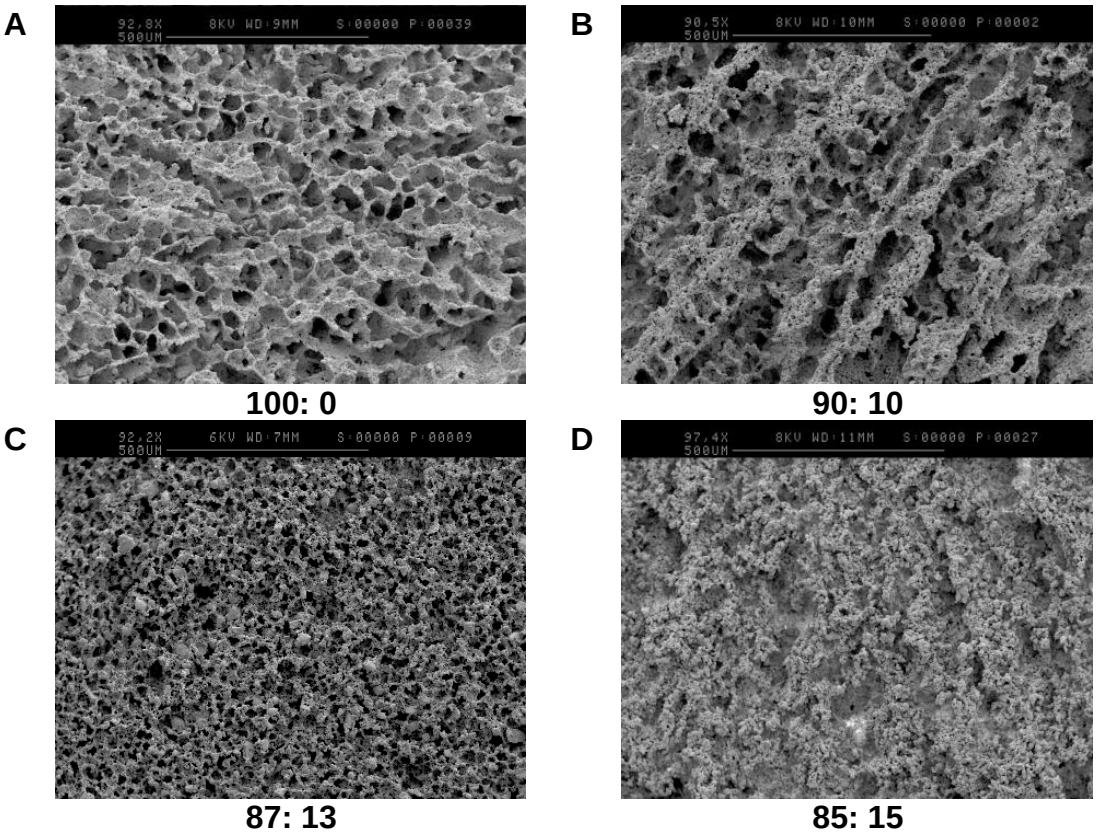

Figure 3-56: SEM micrographs of TIPS A-W scaffolds using: B; 100: 0 (v/v), C; 90: 10 (v/v), D; 87: 13 (v/v) and E; 85: 15 (v/v) dioxane: water solutions.

3.7.2.3 Influence of different polymeric concentrations on A-W TIPS scaffolds

Scaffolds to investigate the influence of the polymeric concentration on TIPS A-W porosity and morphology were prepared using 100 vol. % and 25 (w/v) % A-W (20-53 μm). The slurries were stirred for 1h, then were frozen down at -20°C. Sintering according to heat treatment B was followed after lyophilisation.

In Figure 3-56 and Figure 3-57, the porosity and the morphology of TIPS A-W scaffolds fabricated using 3 (w/v) %, 5 (w/v) % and 7 (w/v) % PLA are compared. One way ANOVA and Bonferrroni post-test were used to assess the influence of the PLA content on the porosity of the TIPS A-W scaffolds (Figure 3-56). The modifications of PLA w/v % had extremely significant effects on the porosity of the scaffolds ($p= 0.0001$). Scaffolds prepared with 7 (w/v) % PLA were less porous in comparison to scaffolds with 3 and 5(w/v) % PLA. The p value of samples with 7 w/v % PLA versus samples with 3w/v % PLA was 0.0003 and versus 5 w/v % PLA

was 0.0002. There was no significant difference in porosity between scaffolds prepared with the lowest polymer concentrations.

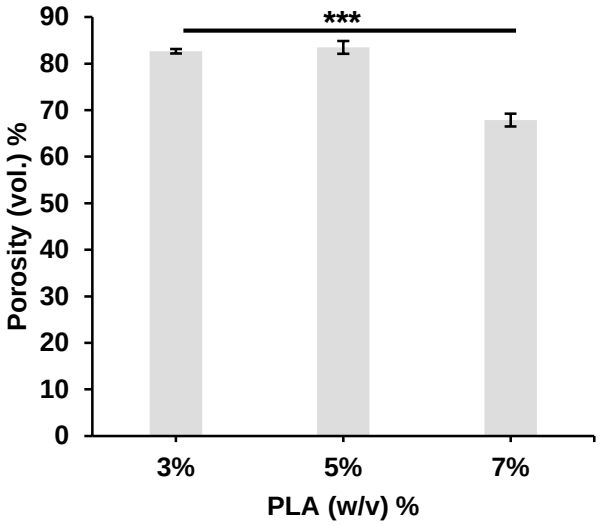

Figure 3-56: Porosity measurements of TIPS A-W scaffolds prepared using: 3 (w/v) %, 5 (w/v) %, 7(w/v) % PLA, 25 (w/v) % A-W (20- 53 µm).

Figure 3-57; A, shows that for the system with 3w/v% polymer, the morphology of the pores was heterogeneous with many irregular and closed pores. For the systems with 5w/v% and 7w/v% polymer in Figure 3-57; B-C, the structure of the scaffold appeared homogenous with ladder-like channels. The scaffolds with the higher polymeric concentration appeared to have smaller pores than the other. Both scaffolds appeared to contain channels.

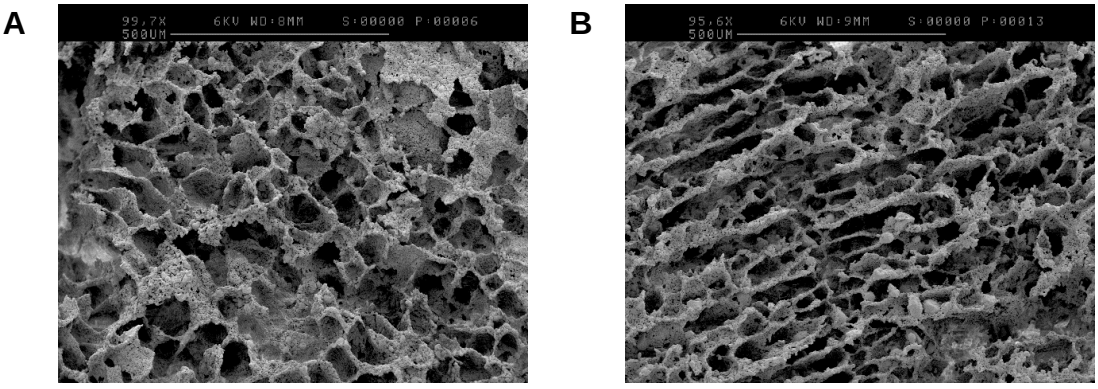

Figure 3-57: Representative SEM images of TIPS A-W scaffolds prepared using: A; 3 (w/v) %, B; 5 (w/v) %, C; 7(w/v) % PLA.

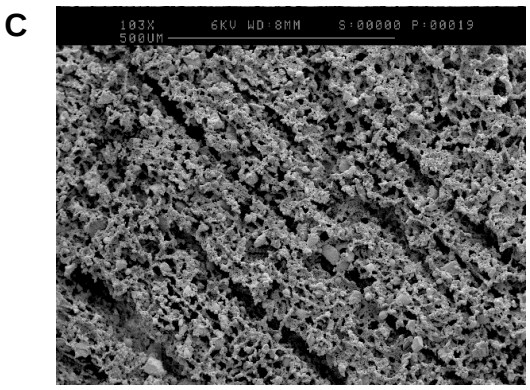

Figure 3-57: Representative SEM images of TIPS A-W scaffolds prepared using: A; 3 (w/v) %, B; 5 (w/v) %, C; 7(w/v) % PLA.

3.7.2.4 Effect of freezing on A-W TIPS scaffolds

To evaluate the impact of the cooling rate and final freezing temperature on TIPS A-W scaffolds, 5 (w/v) % PLA was dissolved in 100 (vol.) % dioxane and 25 (w/v) % A-W (20- 53 µm. The slurry was mixed for one hour and was frozen at -20°C, -80°C and in liquid nitrogen (-196°C). The different freezers and liquid nitrogen have different cooling rates and end temperatures. The porosity and morphology of the various groups were assessed after they were freeze-dried and sintered according to heat treatment B.

One way ANOVA statistical analysis and Bonferroni's multiple comparisons test of the data shown in Figure 3-58, indicated that the freezing temperature of the scaffolds had a significant impact on the porosity of the scaffolds (p= 0.0003). Samples frozen at -196°C had a significant decline in porosity in comparison to samples frozen -20°C (p= 0.0003) and a significant difference in comparison to samples frozen at -80°C (p= 0.004). Samples that were stored at -20°C had significantly higher porosity (p= 0.0472) in comparison to samples frozen at -80°C.

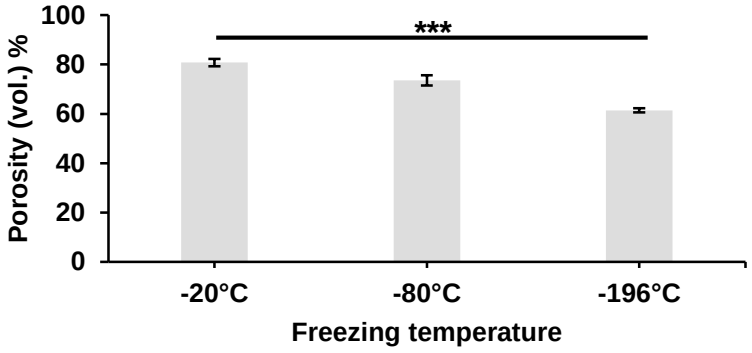

Figure 3-58: Porosity measurements of TIPS A-W scaffolds that were frozen at -20°C, -80°C and -196°C.

Figure 3-59 shows scaffolds that were frozen down at -196°C had very few opened pores in comparison to scaffolds frozen down at -20°C and -80°C respectively. Scaffolds that were stored at -20°C freezing temperature appeared to have more homogenous pore distribution and relatively bigger pores.

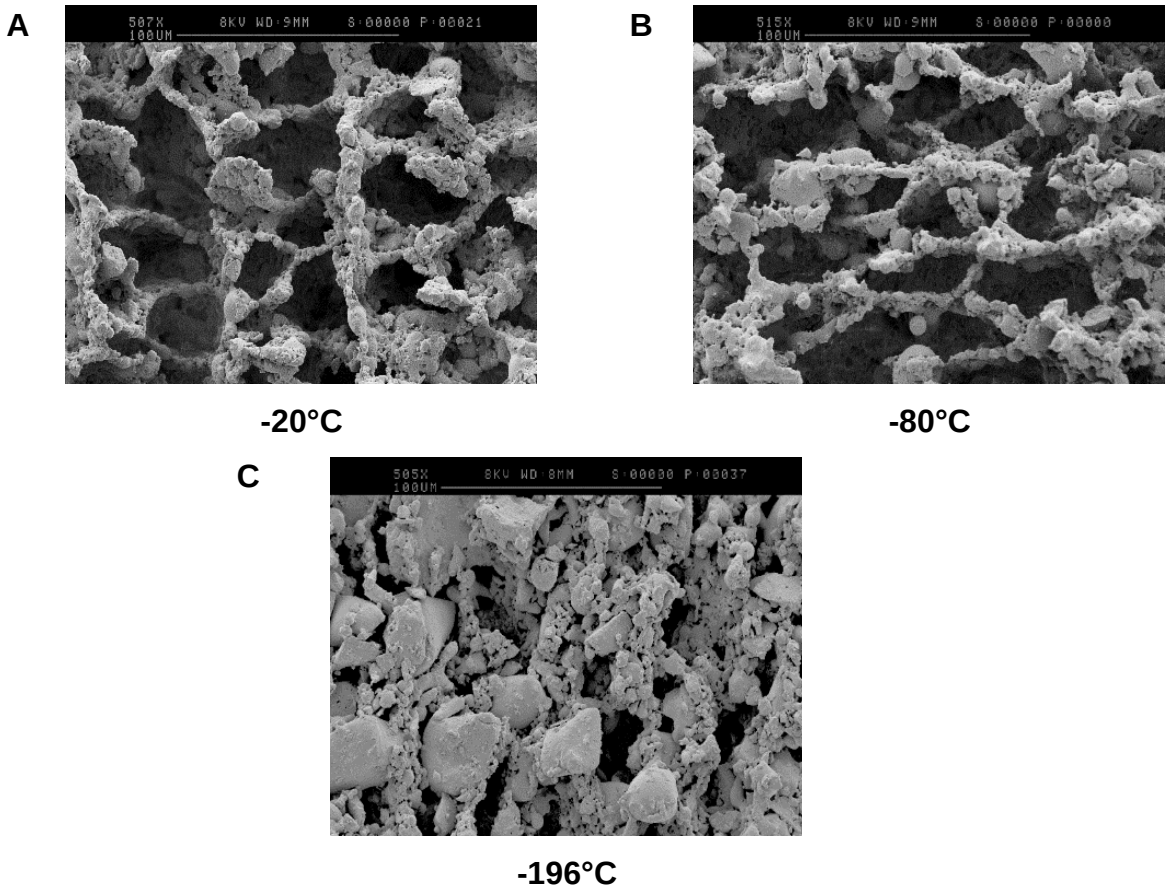

Figure 3-59: Representative SEM micrographs of TIPS A-W scaffolds frozen at: A; -20°C, B; -80°C, C; -196°C.

3.7.2.5 Effect of various stirring durations of A/W slurry on A-W TIPS scaffolds

Slurry containing 25 w/v% A-W in solution with 5 w/v% PLA and 100% dioxane was prepared for the evaluation of the slurry mixing duration before being poured in moulds and frozen down. Samples were mixed using a magnetic stirrer after different time points to assess their influence on the final scaffold. Samples were frozen at -20°C, lyophilised and sintered according to heat treatment B.

One way ANOVA and Bonferroni's multiple test analysis were performed to analyse the data from Figure 3-60. The duration of stirring the slurry after the introduction of A-W in the polymeric solution affects significantly the porosity ($p= 0.0114$). After 4h of stirring the porosity of the samples decreased significantly in comparison to the samples that were stirring for 2 and 3 h respectively.

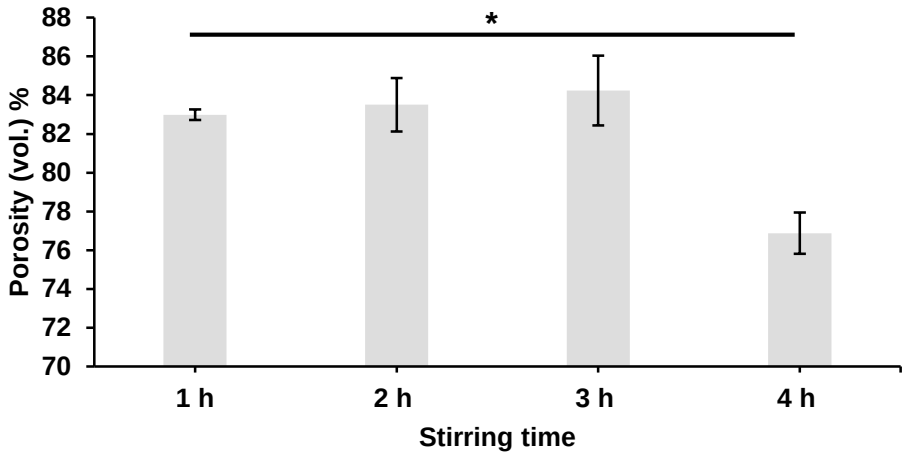

Figure 3-60: Porosity measurements of TIPS A-W scaffolds that their slurries were mixed for 1h, 2h, 3h and 4h.

As illustrated in the SEM images (Figure 3-61; A-D), the corresponding scaffold to the slurry that was stirred for 2 hours appeared to have more homogenous and larger pores and channels in comparison to the rest. Not very obvious differences could be identified morphologically between the scaffolds where the slurry mixing was stopped after 1h and 2h. The slurries that were frozen after they were mixed for 3 h resulted in scaffolds with smaller pores than the previous two and the sample mixed for 4h had the smallest pores and some closed pores in comparison to the other samples.

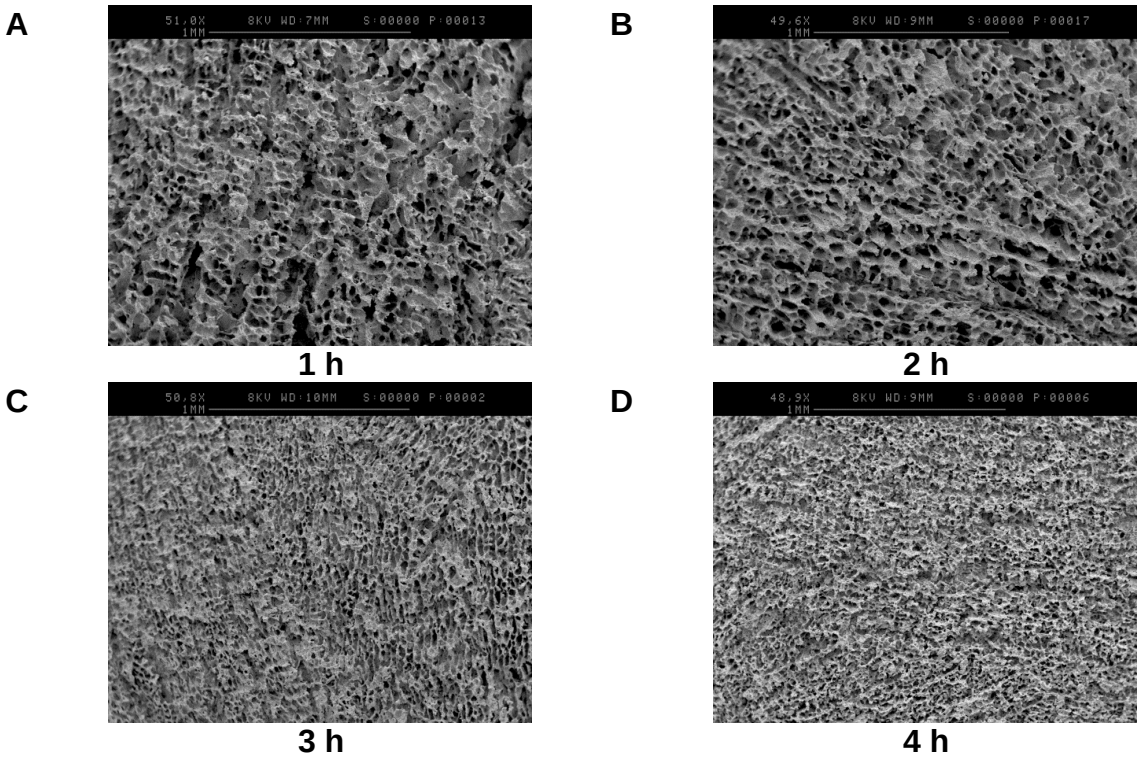

Figure 3-61: Representative SEM micrographs corresponding to TIPS A-W scaffolds that their slurries were frozen after various stirring durations: 1h, 2h, 3h and 4h.

3.7.2.6 Influence of mould temperatures on A-W TIPS scaffolds

To investigate whether the temperature of the mould affected the porosity by influencing the freezing rate of the slurry, a group of moulds was pre-warmed at the same temperature as the slurry and another group remained at room temperature.

A-W slurry was prepared using 25 w/v% A-W in 100% dioxane with 5 w/v% PLA. All samples were frozen at -20°C, lyophilised and sintered according heat treatment B.

Figure 3-62, with analysis using one-tailed student t-test, illustrates that the temperature of the mould did not affect the porosity significantly (p= 0.4105).

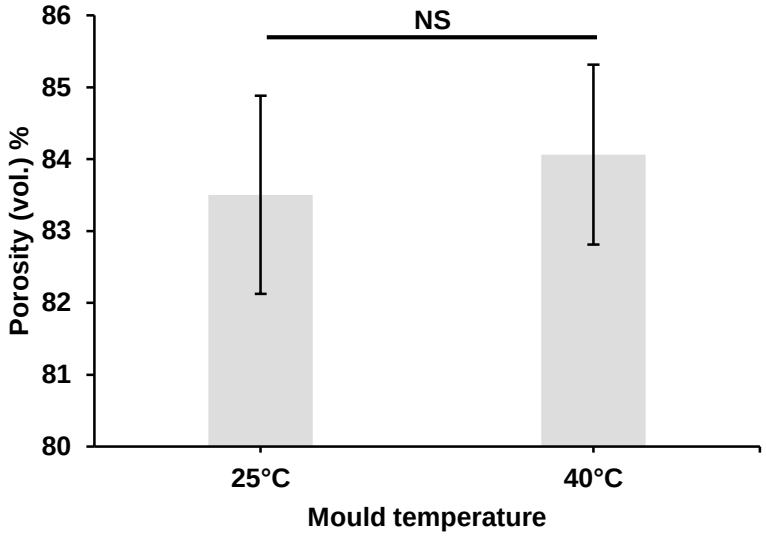

Figure 3-62: Porosity measurements of TIPS A-W scaffolds that their slurries were poured in pre-warmed glass moulds at 25°C and 40°C.

3.7.2.7 Influence of quenching temperature on the A-W TIPS scaffolds

In an effort to assess whether the quenching temperature or duration could affect the porosity of A-W TIPS scaffolds were prepared with 5% (w/v) PLA, dioxane 100%(v/v), 25% A-W (20- 53 μm). These samples were mixed for 2 h after the polymer was completely dissolved and the ceramic was poured in the polymeric solution. The samples were quenched at different temperatures (0°C, 4°C, 25°C) for various time points (0 min, 2 min, 5 min, 10 min, 20 min, 30 min, 60 min) before they were stored at -20°C overnight, lyophilised and sintered.

Two-way ANOVA analysis was used to analyse the data presented in Figure 3-63. The influence of quenching duration had a significant effect (p= 0.0008) on the porosity of the resulting scaffolds. The effect of the quenching temperature and the interaction between temperature and time were considered not significant (p>0.05).

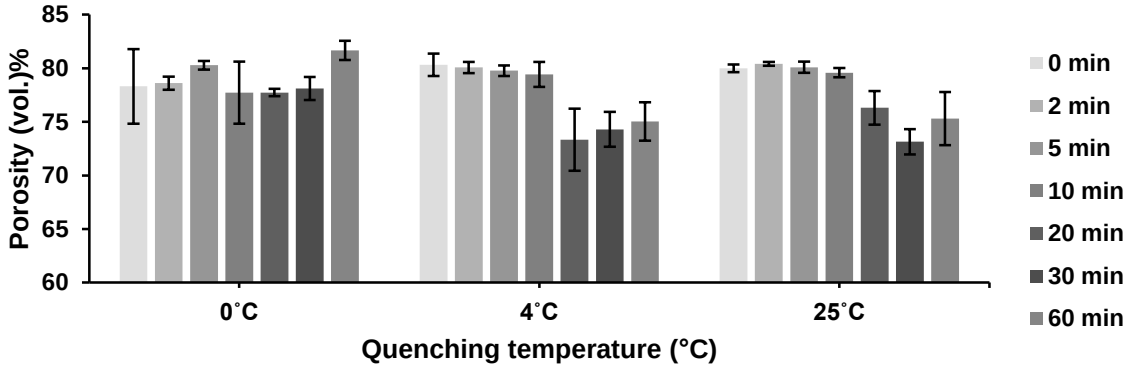

Figure 3-63: Porosity measurements of TIPS A-W scaffolds that were quenched before being frozen at 0°C, 4°C, 25°C for 0 min, 2 min, 5 min, 10 min, 20 min, 30 min, 60 min.

Figure 3-64 and Figure 3-65 demonstrate that there were channels in all the samples. In addition, it was observed from both figures that similar morphology of pores and channels was noticable for the first 10 minutes. After 2 minutes of quenching, the pores and channels looked more homogenous and larger for all the temperatures. Subtle changes in the morphology existed after 20 and 30 min with more heterogenous pores and channel ranges. After the samples were quenched for one hour, large pores appeared in samples quenched at all the quenching temperatures. However, the pores of the ones quenched at 4°C and 25°C seemed less deep and interconnected in comparison to samples that were quenched for the same duration, but at lower temperature.

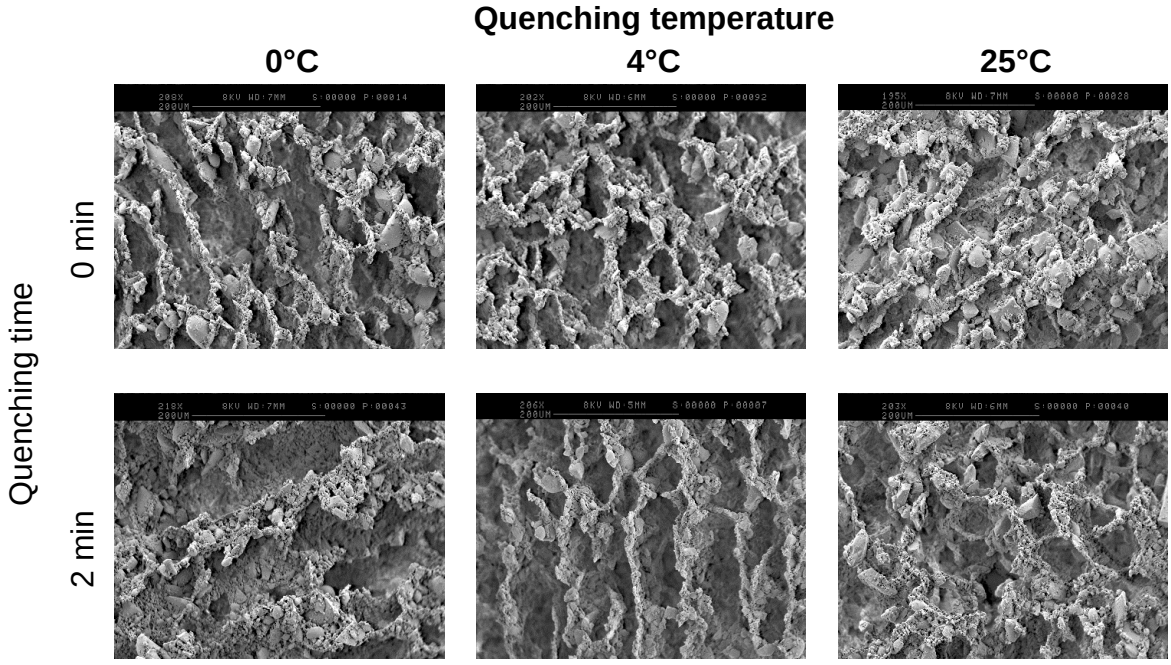

Figure 3-64: Representative SEM micrographs of TIPS A-W scaffolds that were quenched at 0°C, 4°C, 25°C for 0 and 2 min before they were stored at -20°C.

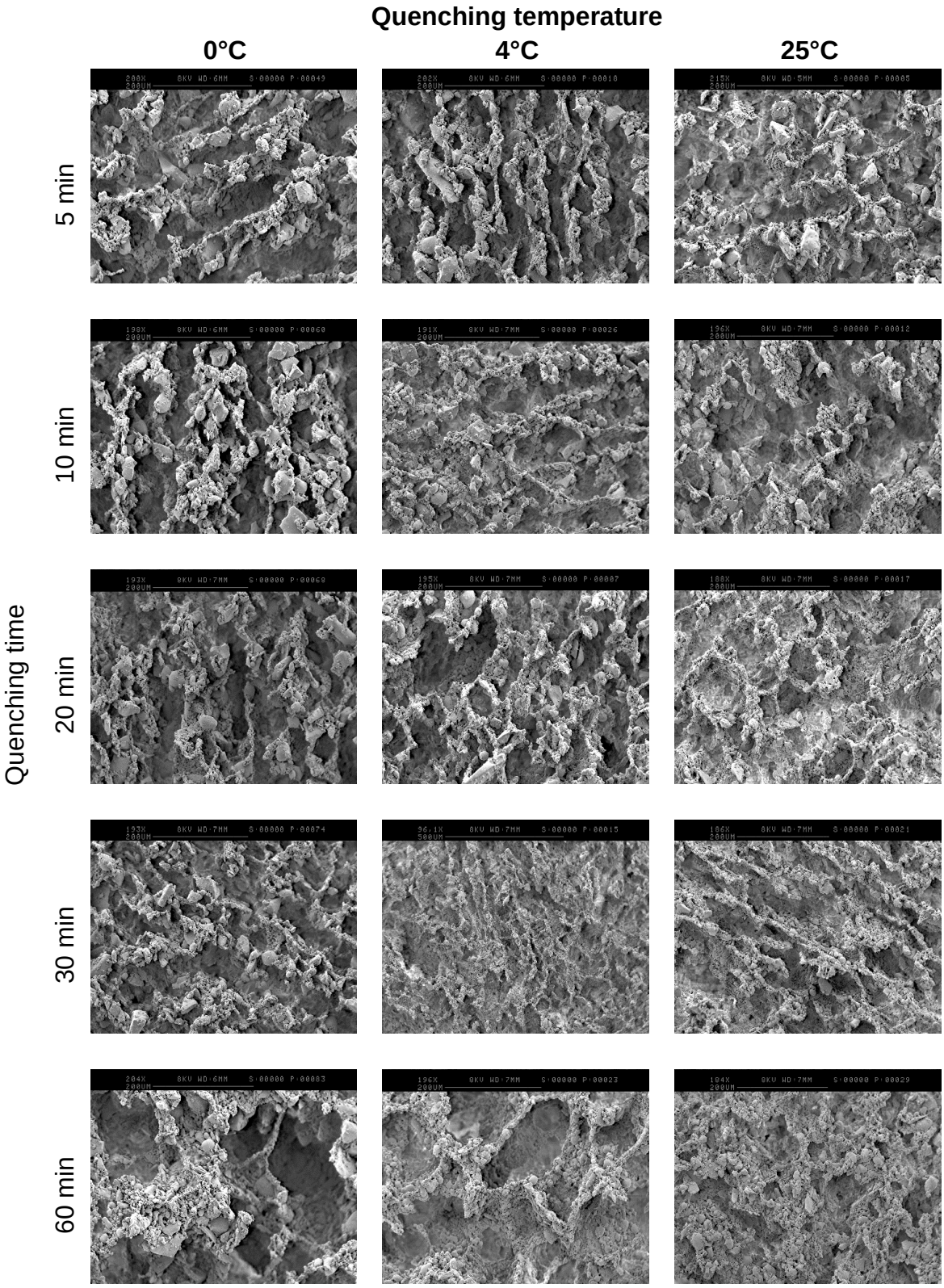

Figure 3-65: Representative SEM micrographs of TIPS A-W scaffolds that were quenched at 0°C, 4°C, 25°C for 5 min,10 min, 20 min, 30 min, 60 min before they were stored at -20°C.

3.7.2.8 Influence of different particle ranges and sintering temperature on A-W TIPS scaffolds

Scaffolds prepared using a slurry consisted of 5 (w/v) % A-W, 100 (vol.) % dioxane, were frozen at -20°C, freeze-dried and sintered. These scaffolds were fabricated using two different particle ranges; <20 μm and 20- 53 μm; and three different heat treatments; B, C and D.

The porosity of these specimens was assessed using two-way ANOVA and Bonferonni's post-tests. Figure 3-66 indicates that there was a significant effect on the porosity by the interaction of the heat treatment and the particle ranges (p= 0.0391). The heat treatment affects the porosity significantly (p= 0.0207). In general, as the maximum temperature increased, the porosity decreased for both ranges. The longer sintering step affected mainly the scaffolds with particle range <20 μm by diminishing their porosity. The particle range had a very significant influence (p= 0.0075) on the porosity of scaffolds. The smaller the particle, the less porous the scaffold was. The scaffolds with particle range <20 μm demonstrated a very significant (p<0.01) decline in porosity between heat treatments B and D and a significant decrease in porosity (p<0.05) between heat treatment C and D.

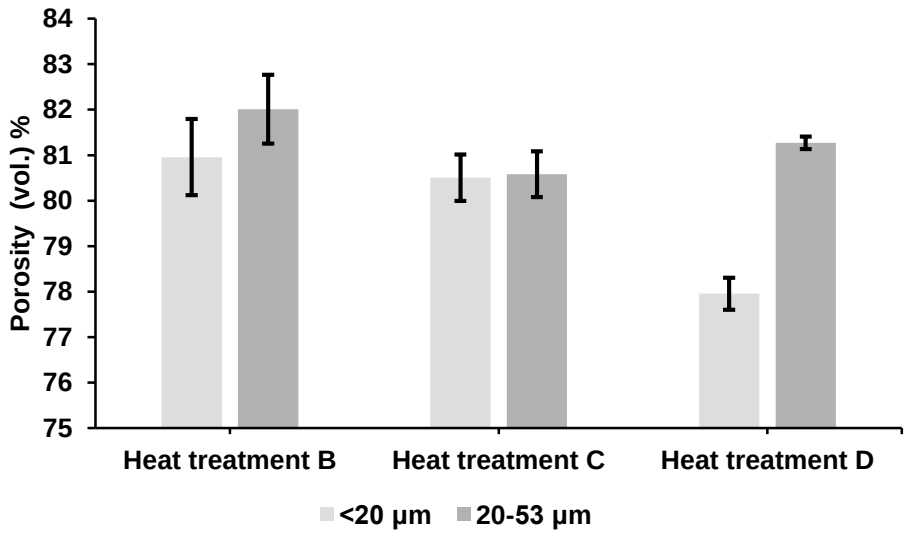

Figure 3-66: Porosity measurements of TIPS A-W scaffolds fabricated using two different particle ranges (<20 μm and 20- 53 μm) and sintered under various heat treatments (B, C and D).

The Young's modulus of the scaffolds prepared with A-W 20- 53 μm was analysed on the graph in Figure 3-67. One-way ANOVA was used to analyse the data and was followed by Tukey's post-test. The sintering program had a very significant effect (p=

0.0061) on the Young's modulus of the scaffolds. The difference in porosity between samples sintered according to heat treatment B and C was very significant (p<0.01).

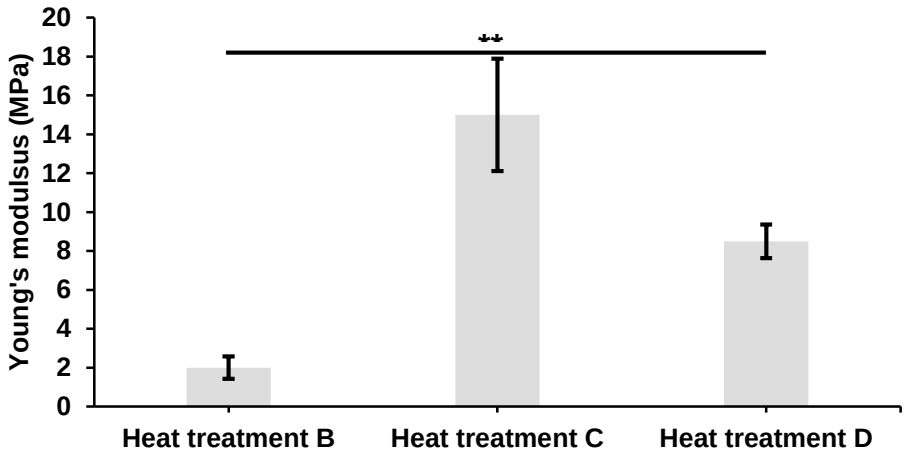

Figure 3-67: Young's modulus of TIPS A-W scaffolds using particle range 20-53 µm that sintered under various heat treatments (B, C and D).

3.7.2.9 Influence of different A-W concentration on A-W TIPS scaffolds

The effect of different percentages of A-W powder in the A-W TIPS scaffolds was investigated. Samples were prepared with A-W with particle range 20- 53 µm at concentrations 25, 50, 75, 100, 175 (w/v) %. They were all freeze-dried and sintered according to heat treatment C.

The difference in porosity throughout all the different groups illustrated in Figure 3-68 was tested using one-way ANOVA analysis and was significant (p<0.0001). All samples were compared with each other using Bonferroni's multiple comparisons test. Scaffolds prepared using 25 w/v% A-W had a significant rise in porosity in comparison to scaffolds prepared with 50 w/v% A/W (p= 0.0061) and a significant increase in porosity in comparison to all the other scaffolds (p<0.0001). Samples with 50 w/v% A-W demonstrated no significant difference in comparison to scaffolds with 75 w/v% A-W, but they had a significant difference in comparison to scaffolds made with 100 w/v% (p= 0.0007) and 175 w/v% (p=<0.00001). No significant difference appeared between scaffolds with 75 w/v% and 100 w/v% A-W. Scaffolds with 175 w/v% A-W had a significant decline in porosity in comparison to scaffolds with 75 w/v% A-W (p<0.0001) and 100 w/v% A-W (p<0.0001).

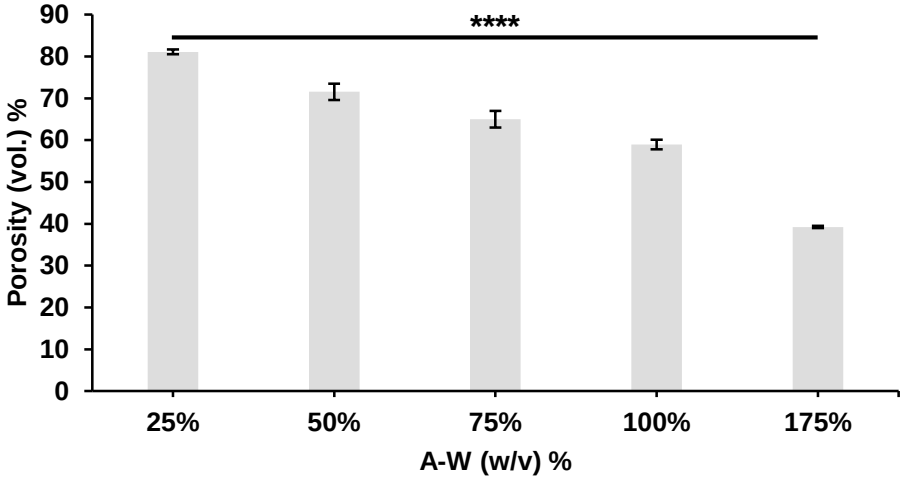

Figure 3-68: Porosity measurements of A-W TIPS scaffolds prepared using different percentages of A-W (w/v)% with particle range 20- 53 µm. Bars represented scaffolds with A-W content of 25%, 50%, 75%, 100% and 175% w/v.

In Figure 3-69, two different magnifications of SEM images taken from scaffolds with different particle ranges are shown. The pores became smaller and the channels thinner as the powder concentration increased.

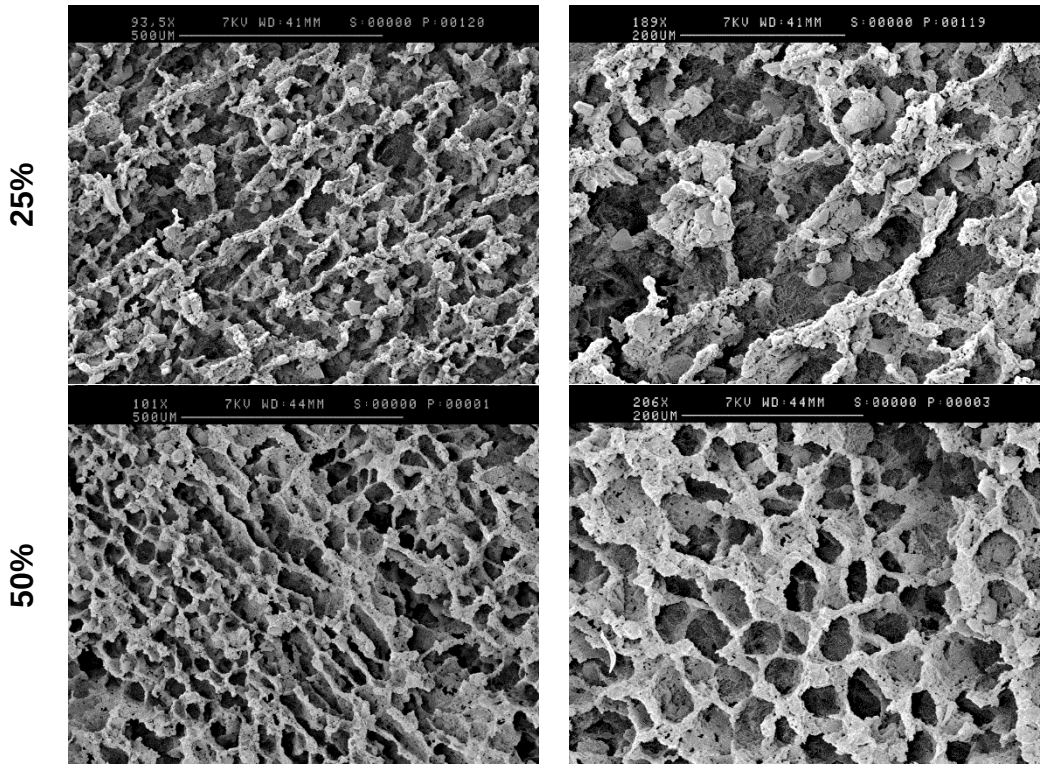

Figure 3-69: Illustrative SEM micrographs representing scaffolds prepared with 25, 50, 75, 100, 175 w/v% A-W with particle range 20- 53 µm.

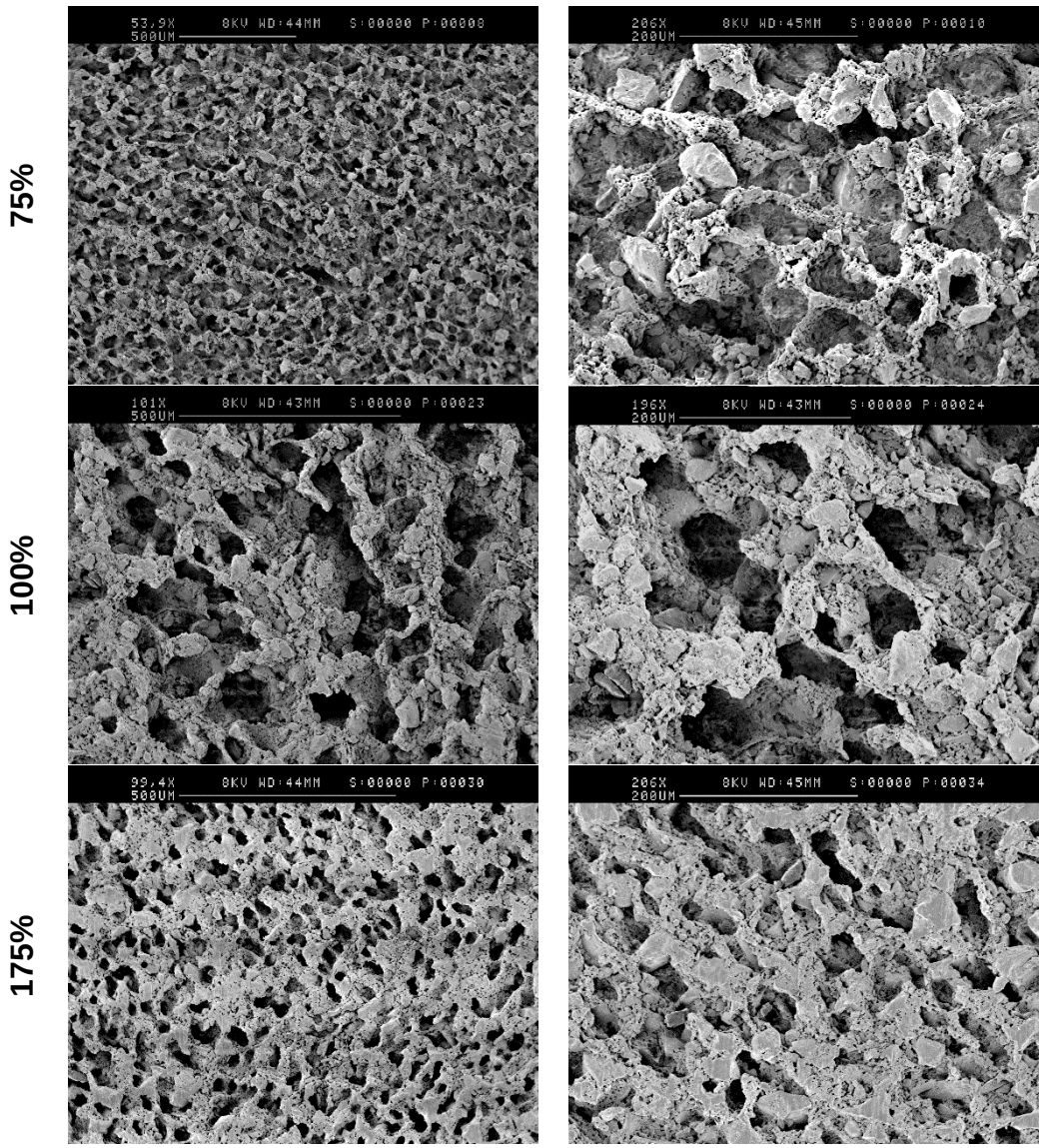

Figure 3-69: Illustrative SEM micrographs representing scaffolds prepared with 25, 50, 75, 100, 175 w/v% A-W with particle range 20- 53 µm.

Similar results were evident in Figure 3-70, where µCT slices are shown. These images better represent the thickening of the walls between channels as the ceramic content was higher; and the decline in pore size. Furthermore, the interconnectivity throughout the samples was highlighted in these micrographs.

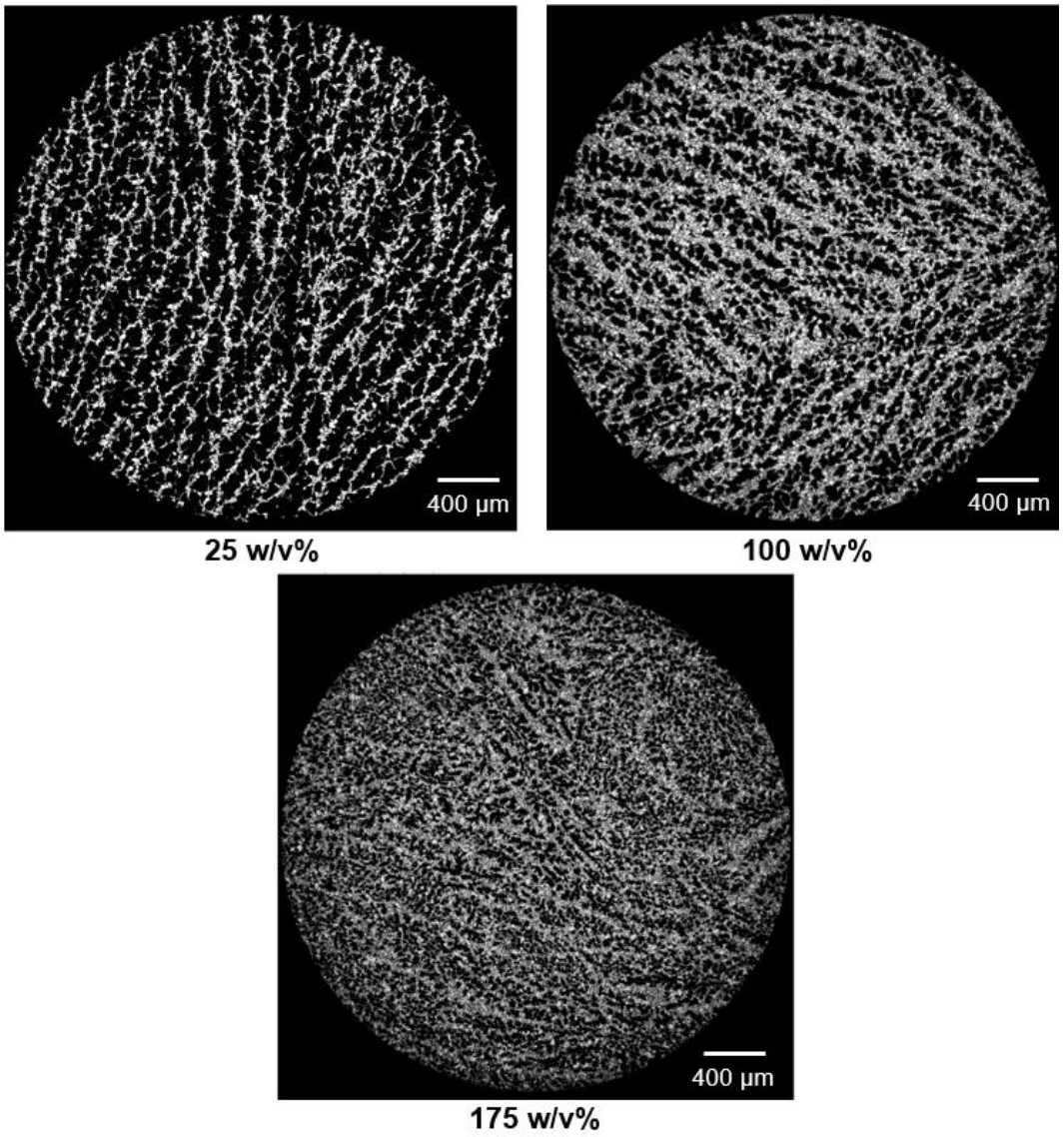

Figure 3-70: Representative µCT micrographs representing scaffolds prepared with 25, 100 and 175 w/v% A-W with particle range 20- 53 µm.

Figure 3-71 highlights that this type of scaffold had a gradient in porosity resembling the bone tissue (cortical to lamellar).

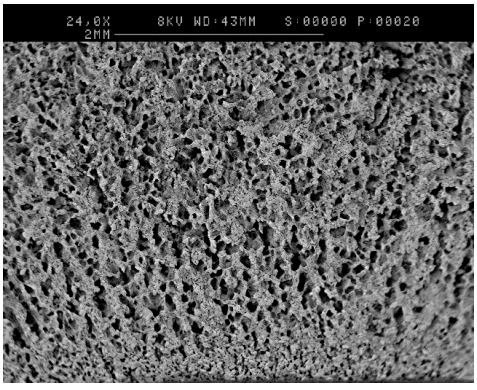

Figure 3-71: Illustrative SEM image of A-W TIPS scaffold prepared with 100 w/v % A-W (20- 53 µm).

3.8 Summary of Results

The major aim of this work was to identify the appropriate scaffold fabrication techniques that would result in two different types of scaffolds; primarily, relatively dense scaffolds to assess the particle range influence on hMSC behaviour *in vitro* and then, highly porous interconnected scaffolds for further *in vitro* investigation of hMSC fate with the ultimate goal of supporting osteogenesis *in vivo*.

3.8.1 *A-W*

The main material that was used for all scaffolds was A-W, because it has been demonstrated that it has bioactive and osteoinductive properties (Xiao et al. 2008b; Dyson et al. 2007; Sautier et al. 1994) with robust mechanically properties when sintered (Kobayashi et al., 1998, Kokubo et al., 1985).

A-W was characterised using XRD before and after sintering using heat treatment B (Figure 3-6). The XRD pattern revealed that both materials were composed of glass and crystal phases, but the heat treated powder had more crystalline phases. The crystals that were precipitated in the sintered glass were hydroxyapatite, wollastonite, diopside and calcium magnesium hydrogen phosphate. Diopside was the only crystal phase that appeared only after the heat treatment. Diopside has been reported to have good bioactivity *in vitro*, enhanced cell proliferation compared to other Mg-containing ceramics, good osseointegration, advanced mechanical properties and resistance to acidic conditions (Wu et al. 2010; Wu & Chang 2007; Roman et al. 2001).

3.8.2 *Identification of scaffolds for assessing the influence of particle range on hMSCs in vitro*

Dry loose powder (§ 3.5.1.1) and compacted powder scaffolds (§ 3.4.1.1) were the two first types of scaffolds that were fabricated. Loose powder scaffolds had more irregular shape (Figure 3-42; A) than the pellets (Figure 3-14). One factor that affected the shape of the loose powder scaffolds was the mould in which the ceramic was poured. Originally holes in a brick mould each with diameter 14-16 mm, height 36.7-37.1 mm; was used to sinter the ceramic. The brick mould (Figure 3-27; B) was a porous material, so the machined holes were irregular. For the remaining experiments platinum tubes (Figure 3-27; C) were used as moulds and the external definition was improved (Figure 3-42; B). In addition, the cast A-W ceramic particles were not homogenously distributed (Figure 3-37). It was likely that this was caused by the formation of particle aggregates that simultaneously caused gaps in the scaffolds, resulting in crack formation. Compacted powder scaffolds also presented cracks, but mainly a large crack in the middle horizontal plane of the scaffold (Figure 3-15).

Different strategies were employed to eliminate these cracks. One strategy was to dry the powder to remove any potential residue of humidity, which had no effect (§3.5.2.3). Another was the introduction of small polymeric particle (PA) to promote the powder distribution; however this resulted in extra micro cracks and loss of structural integrity in pellet scaffolds (Figure 3-19), and loose powder scaffolds (§3.5.2.4). Different heat treatments (pellets (§3.4.2.2); loose (Figure 3-39)), particle range blends (pellets (Figure 3-17); loose (Figure 3-37)) - in addition to different pressures (pellet (Figure 3-16)) - were investigated to promote the liquid phase during sintering, but no improvement was observed. Mixing the A-W powder with deionised water and preparing a slurry to be cast in moulds (Figure 3-50), aided the particle distribution and the packing of the powder without the appearance of formed cracks. The sintered cast slurries were more controllable and reproducible than the pressed or loose powder scaffolds.

3.8.3 *Identification of scaffolds for investigating 3D A-W environment on hMSC fate*

Polymeric templates were used to introduce macroporosity and interconnectivity in the dry mixed ceramic scaffolds. Polymeric (PE) particles with particle range 101-400 μm were introduced in loose (§3.5.2.5) and pellet scaffolds (§3.4.2.6) (Brovarone et al. 2006). The loose powder scaffolds collapsed after sintering (Figure 3-43), most likely because the polymer burnt off at very low temperature in comparison to the ceramic sintering temperature. The pellet remained intact (Figure 3-22), this is likely due to the increased surface area contact between A-W particles, resulting in increased liquid phase. Micro-cracks were found at the peripheries of the pores within the pellet scaffolds (Figure 3-23; A-B). A polymer melting step was added during the heat treatment, to encourage channel formation by the viscous polymer. This method resulted in a scaffold with graded porosity, however it still appeared to have micro-cracks (Figure 3-23; C-D).

The addition of polymeric fibres in the scaffolds was designed to ensure interconnectivity. This method had satisfactory results for the loose powder scaffolds (Figure 3-44), but large cracks occurred in the pellets (Figure 3-26), likely formed from the pressure. No further investigation for the pellet scaffolds took place after this stage.

Since the burning off of the polymeric filament had encouraging results in combination with the loose powder scaffolds, negative templates were FFF printed. As a first attempt a negative template that was combining a grid - to promote porosity and interconnectivity – and mould to enclose the powder was trialled (§3.5.1.6). The subsequent construct mainly collapsed (Figure 3-46) due to the high content of polymer that burnt off before the construct could stay intact alone. The next step was to use the same grid without the surrounding wall that was acting as mould. Instead this grid was used as a core inside a platinum tube (§3.5.1.7). The sintered scaffold remained intact, but it had some micro-cracks around the pores (Figure 3-47).

All the different strategies using polymeric burning off led to crack formation in the scaffolds. This could be caused by gas release leading to particle rearrangement as a result of the polymer: ceramic ratio.

TIPS combined with sintering was then evaluated (§3.7). Ceramic particles were incorporated in a polymeric slurry at elevated temperature. The slurry was frozen and as the temperature decreases, two different phases were created; polymer lean and

polymer rich. A-W particles were blended in the polymer rich phase. After freeze drying the green part was already porous by the sublimation of the polymer lean phase (Figure 3-54). After sintering, the polymer was burned off leaving a highly porous interconnected ceramic scaffold with gradient porosity (Figure 3-71).

This technique was very sensitive and a variety of parameters were optimised to obtain a reproducible scaffold to be used to study the influence of A-W in a 3D highly porous and interconnected scaffold *in vitro* (§3.7).

3.9 Selection of Scaffolds for *In Vitro* Testing

Scaffolds selected for further *in vitro* investigation were the sintered cast slurries (§3.6) and the scaffolds prepared using TIPS and sintering (§3.7).

The sintered cast slurries were homogenous microporous scaffolds with a relatively flat surface and structural integrity (Figure 3-50). The pellets and loose powder scaffolds appeared to have cracks and poor powder distribution that would compromise the mechanical properties of the scaffold. For the sintered cast slurries the particle range and heat treatment (Figure 3-49) were optimised to obtain slurry loose powder scaffolds with different particle range that would have similar porosity. Two groups of slurry scaffolds with particle range 20- 53 μm and 54- 90 μm :< 20 μm (80: 20) sintered according to heat treatment C (Figure 3-51) were selected to be used for further *in vitro* analysis (Chapter 4). This category was used to investigate cell interaction with different surface topographies, produced by varying the A-W particle ranges. In addition these scaffolds were tested in SBF in Chapter 4; §4.3.2.

Of the techniques evaluated, TIPS with sintering was the only approach that successfully produced highly porous and interconnected scaffolds with no crack formation. The advantages of this method were the manipulation of pore size, whilst maintaining interconnectivity of the construct and the pore size gradient as a consequence of sedimentation (Figure 3-71).

This group of scaffolds were assessed *in vitro* as materials and as matrices for promoting early osteogenic differentiation on hMSCs in Chapter 5.

Chapter 4 IN VITRO ASSESSMENT OF CAST SLURRY SCAFFOLDS

4.1 Introduction

In this chapter the sintered casted slurry samples that were selected and optimised in Chapter 3; §3.6 were used for further *in vitro* assessment. These scaffolds were manufactured by making a slurry using deionised water and A-W powder (§3.6). This slurry was cast in moulds and sintered. Two different particle ranges 20- 53 μm and 54- 90 μm: <20 μm were selected that gave similar porosity with different surface topography, micropore size and surface area.

The main goal of this chapter was to identify whether changing structural parameters would have an effect on biodegradation and bioactivity of these A-W scaffolds. A secondary aim was to characterise how these scaffold characteristics could influence human mesenchymal stem cell fate and in particular osteogenesis.

4.2 Materials- Methods

4.2.1 *Image analysis*

ImageJ was first calibrated by measuring the scale bar using the line tool, then "Analyze" →set scale bar (A). The upper insert of the SEM image was selected using the rectangular tool and removed (ctrl+x) (B). A threshold was used to distinguish individual pores in monochrome image. The analysis tool was used to select object > 0.05µm in size ("Analyze" → "Analyze Particles…"). Area was used to calculate average pore diameter (Figure 4-1).

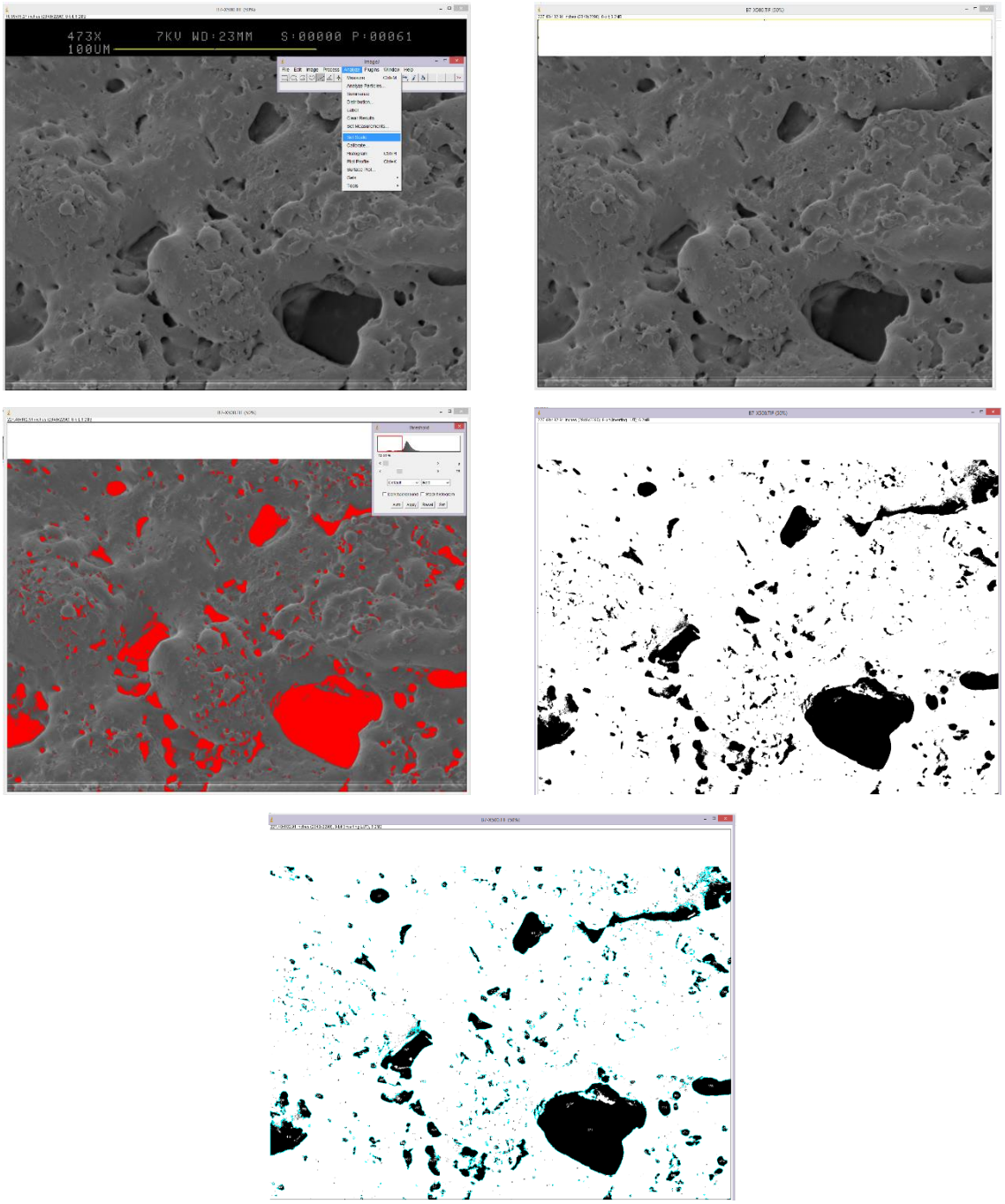

Figure 4-1: Example images of ImageJ processing

4.2.2 *Profilometry*

The surface topography of the sintered cast slurry scaffolds was imaged and characterised using an optical profilometer (Alicona).

4.2.3 *Cell seeding*

The cell population that was seeded on the sintered cast slurry A-W scaffolds was decided when cells reach ~80% confluency. The follow equation was used to calculate how many flasks were needed was (Equation 5-1).

$$\textbf{Number of flasks needed} = \frac{\textbf{Total surface area of wells need seeding}}{\textbf{Surface area of flask}}$$

Equation 4-1: Calculation of flasks needed for seeding a number of scaffolds in well plates.

Following the medium introduced for the cell pellet resuspension was:

$$Medium = Well\ number\ x\ 500\ \mu l$$

Where 500µl was the medium used per scaffold.

4.2.4 *Histological staining*

Samples were fixed for 1 hour in neutral buffered 10% formalin. Following fixation were dehydrated by immersing them in a series of ethanol: water solutions: 25%, 50%, 75%, 90% and 100%. The last step was repeated three times and samples were left to air dry before further use.

A combination of Von Kossa and Toluidine Blue staining were used to identify calcium deposits in the mineralised tissue and the acidic sulphated mucosubstances on the same sample.

Minerals should be stained black or black-brown with Von Kossa. Toluidine blue should stain the strongly acidic sulphated mucosubstances blue. Different shades of blue are related to the calcification of the tissue.

Solutions and Reagents:

Solution	Reagents	Quantity	Preparation
1% Aqueous Silver Nitrate Solution	Silver nitrate	1 g	
	Distilled water	100 ml	

Table 4-1: Solutions and reagents to prepare solution for Von Kossa and Toluidine blue staining.

Solution	Reagents	Quantity	Preparation
5% Sodium Thiosulfate	Sodium thiosulfate	5 g	
	Distilled water	100 ml	
Toluidine blue stock solution	Toluidine blue O	1 g	Mix to dissolve. Adjust pH to 2.0-2.5 using glacial acetic acid or HCl. Make fresh every time.
	70% ethanol	100 ml	
Sodium chloride (1%)	Sodium chloride	0.5 g	Mix to dissolve (make this solution fresh each time). Adjust pH to 2.0~2.5 using glacial acetic acid or HCl.
	Distilled water	50 ml	
Toluidine Blue Working Solution (pH 2.0~2.5)	Toluidine blue stock solution	5 ml	Mix well. The pH should be around 2.3 and more than 2. Make this solution fresh and discard after use. pH higher than 2.5 will make staining less contrast.
	1 % sodium chloride pH 2.3	45 ml	

Table 4-1: Solutions and reagents to prepare solution for Von Kossa and Toluidine blue staining.

- Procedure:

Samples were hydrated in different concentrations of ethanol: 100%, 75%, 50%, 25%, 10% and rinsed in three changes of distilled water. Samples were incubated in 1%(w/v) silver nitrate solution in a clear glass petri dish that was placed under ultraviolet light for about 10-15 min. Samples were checked upon frequently to avoid overstaining. Then they were washed using distilled water and the unreacted silver was removed by soaking the samples in 5 % (w/v) sodium thiosulfate for 5 minutes. Samples were rinsed again with distilled water and stained using toluidine blue solution for 2-3 minutes. Finally they were washed again and imaged when they were still immersed in water.

4.2.5 *SBF assay*

Sintered cast A-W slurry scaffolds were immersed in SBF using a ratio of 2.25 g scaffold in 50 ml SBF solution based on Maçon et al. 2015.

4.3 Results

4.3.1 *Surface morphology characterisation of A-W sintered cast slurries*

The surface topography of the scaffolds was primarily characterised using SEM imaging and optical profilometry. Figure 4-2 demonstrates that the scaffold prepared with smaller particles had a relatively smoother surface with an average peak to valley height (Rz) 1.49 µm; whereas the scaffold prepared with larger particle range had a rougher topography with Rz= 9.43 µm.

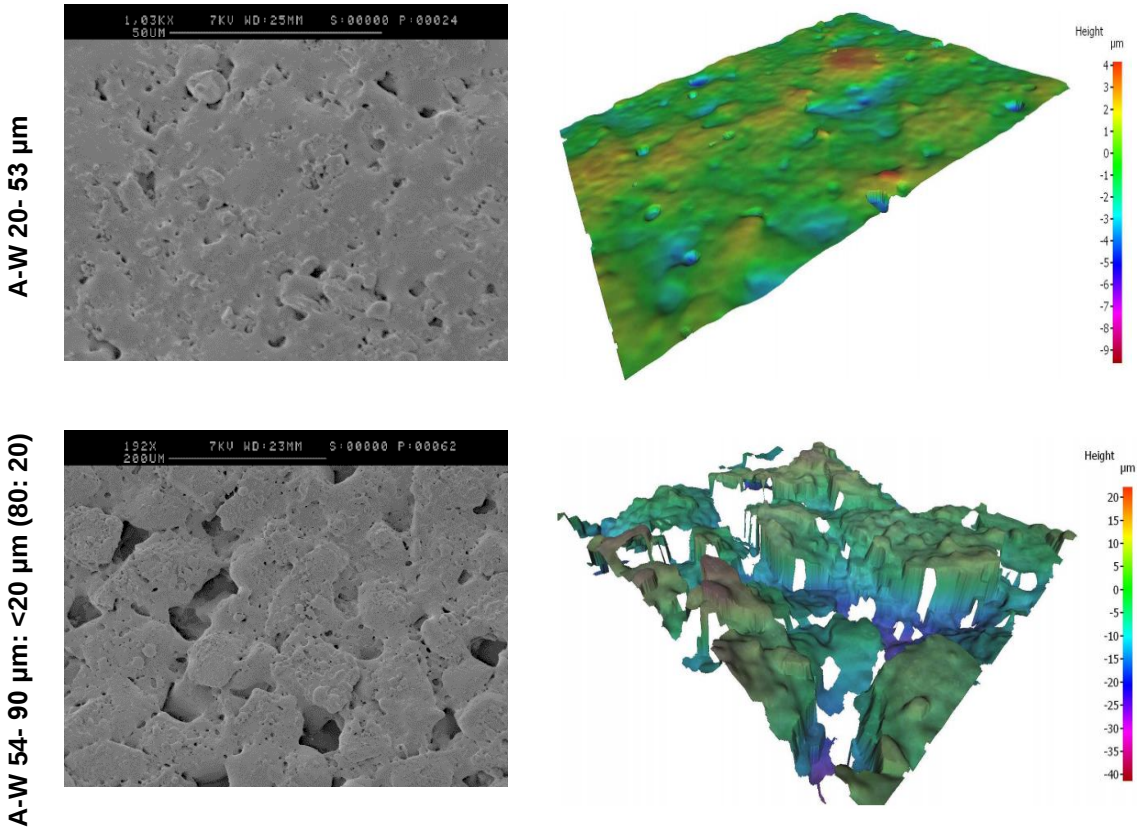

Figure 4-2: Indicative SEM and 3D micrographs of the top of sintered cast slurries using two different particle ranges; 20- 53 µm and 54- 90 µm: <20 µm (80: 20) respectively. The 3D images were captured using an optical profilometer.

4.3.2 *In vitro biodegradation study of A-W sintered cast slurries*

SBF was prepared as previously described in Chapter 2: §2.3.1. Sintered cast slurries were immersed in SBF for different soaking durations: 4h, 8h, 1 day (Figure 4-3), 3 days, 7 days and 21 days (Figure 4-3). On day 3 granular crystals started to appear precipitated on the scaffolds (Figure 4-3), especially on those prepared with A-W particle range 20- 53 µm. After 7 days of immersion in SBF, cauliflower – like precipitated calcium phosphate crystals were prominent in both scaffolds. The main highlighted differences between the two A-W scaffolds on day 7 were the size and

surface coverage of the precipitated crystals. Micro-cracks appeared in the newly formed layer of apatite only on the scaffold with the smaller particle range.

The precipitated crystal and the micro-cracks were exaggerated by the 21st day that the scaffolds were soaked in SBF. In particular, the precipitated crystals formed an almost homogenous surface on scaffolds with particle range 20- 53 μm and the cracks were deepened revealing the degree of the thickening of the newly formed surface. At the same time-point, more large cauliflower-like crystals were protruding on the scaffold prepared with A-W particle range 54- 90 μm: <20 μm and no surface cracks were evident.

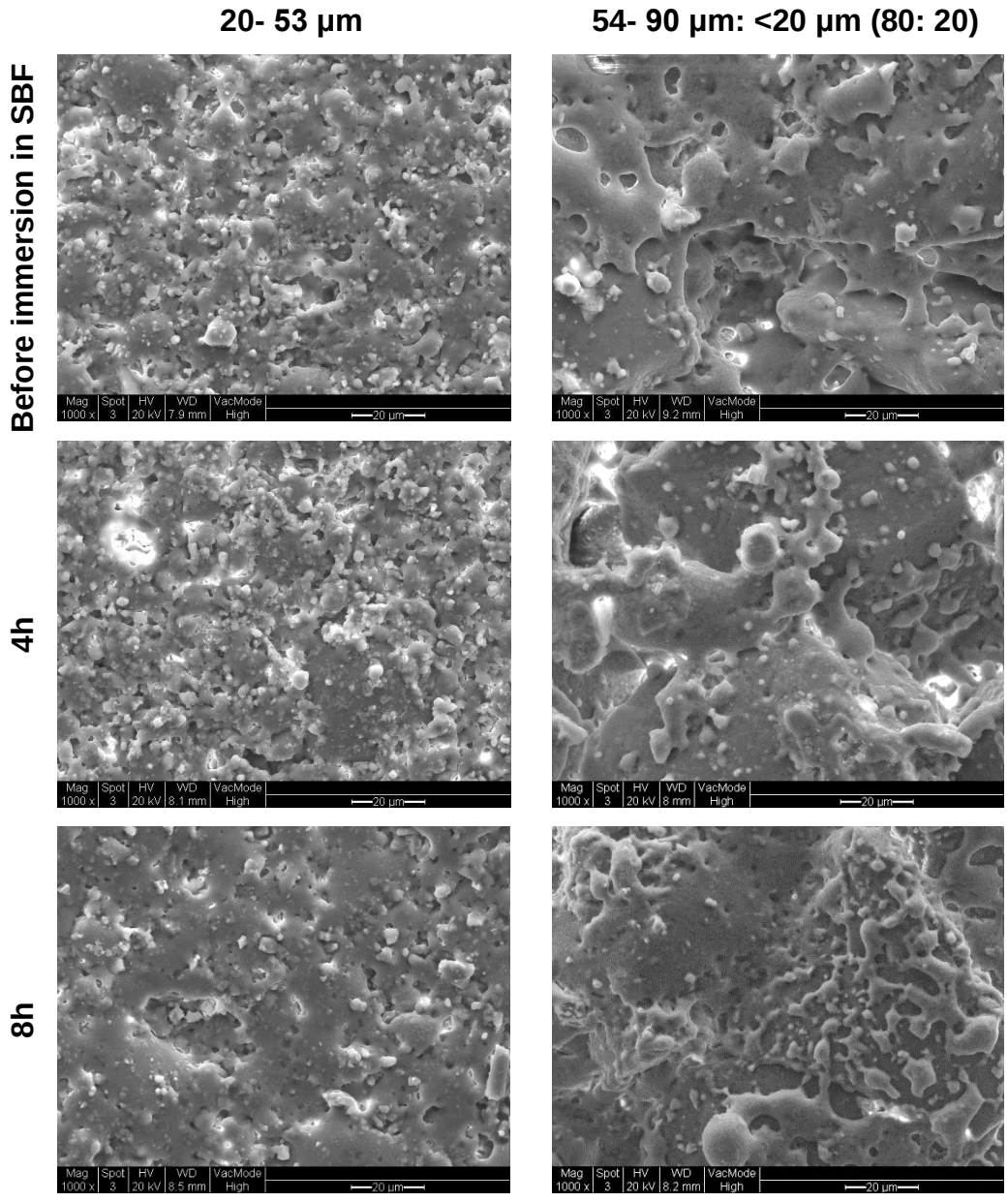

Figure 4-3: Indicative SEM micrographs of the top of sintered cast slurry scaffolds before and after they were immersed in SBF solution for different time-points (0h, 4h, 8h, 1 day, 3 days, 7 days and 21 days). These scaffolds

were prepared using A-W with particle ranges 20- 53 µm and 54- 90 µm: <20 µm (80: 20) respectively. The red arrows indicated precipitated crystals and the orange micro-cracks on the surface of the newly precipitated crystal surface.

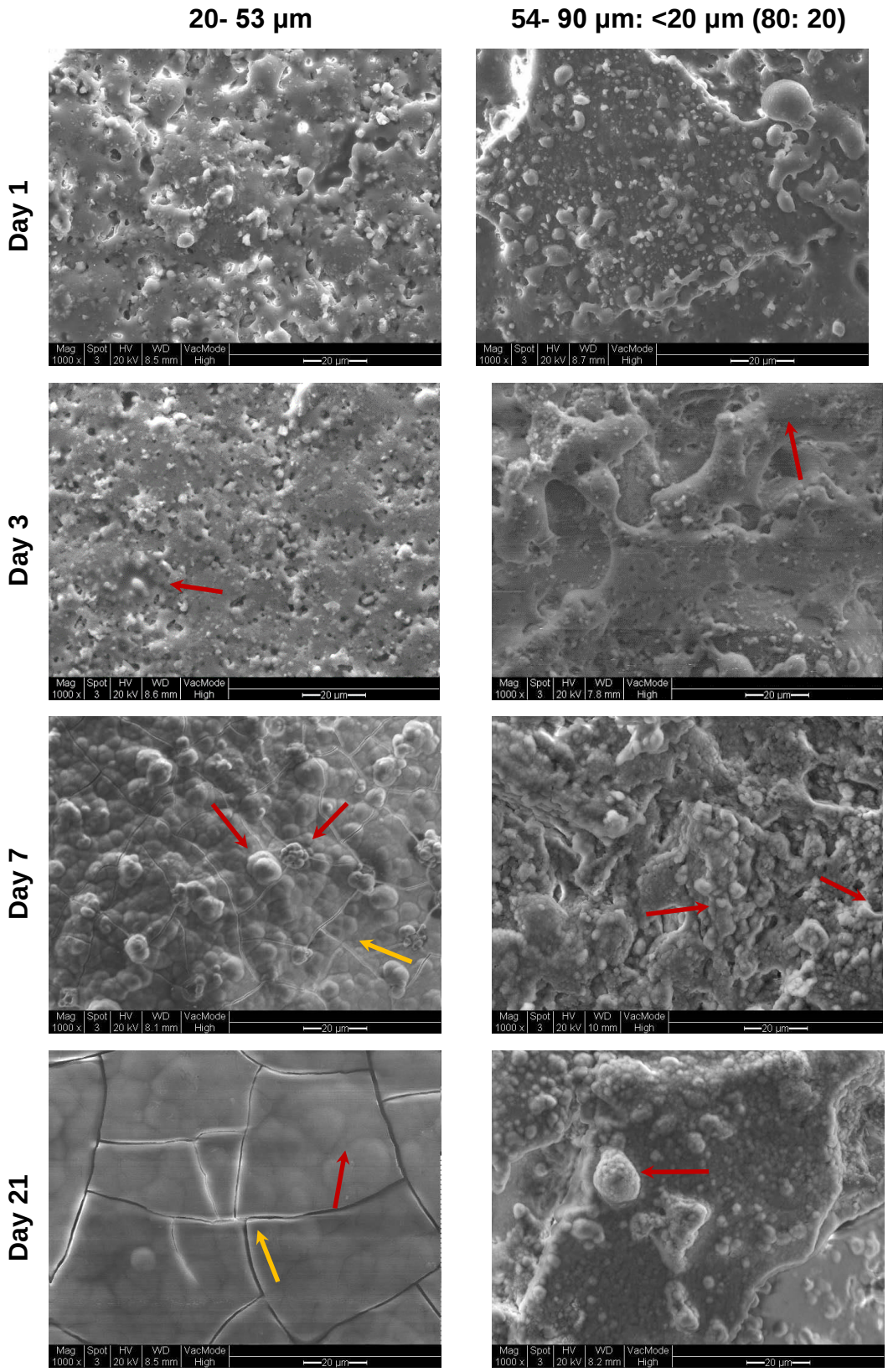

Figure 4-3: Indicative SEM micrographs of the top of sintered cast slurry scaffolds before and after they were immersed in SBF solution for different time-points (0h, 4h, 8h, 1 day, 3 days, 7 days and 21 days). These scaffolds

were prepared using A-W with particle ranges 20- 53 μm and 54- 90 μm: <20 μm (80: 20) respectively. The red arrows indicated precipitated crystals and the orange micro-cracks on the surface of the newly precipitated crystal surface.

The main elements that were observed at the EDS spectra were calcium, phosphate, magnesium, silicon and oxygen. In both scaffolds, the silicon concentration dropped and the phosphorus concentration increased after they were incubated in SBF solution. In addition, the concentrations of calcium and magnesium had different end-points for the two scaffolds. Calcium concentration increased and magnesium concentration decreased in scaffolds with particle range 20- 53 μm. The inverse trend for changes in calcium and magnesium concentrations was observed in scaffolds with particle range 54- 90 μm before and after SBF immersion.The elements that were present on the surface of the scaffolds before and after their immersion in SBF analysed using EDS during SEM imaging (Figure 4-4). The calcium concentration was higher for the scaffolds with the larger particle range before the samples were immersed in SBF. The calcium concentration fluctuated for both samples between 30 and 40 wt% from 8 hours to 21 days. The calcium concentrations on the two scaffolds (approximately 35 wt%) were similar at 4h, 3 days and 7 days after immersion in SBF.

The phosphorus concentrations on the two scaffolds were very similar until day 3 (Figure 4-4; B). There was rapid phosphorus precipitation on the scaffolds with the smaller particle range between days 3 and 7which then stabilised which then stabilised during the next 14 days of the experiment. The phosphorus concentration on the scaffolds with the larger particle range also increased over the same time frame, but in a more gradual manner.

In Figure 4-4; C the silicon concentrations on both scaffolds had similar abundance until day 3. After day 3, they both follow a similar trend, but the silicon concentration on scaffolds with smaller particle range reduced to a higher degree than the silicon concentration on the scaffold with larger particle range between days 3 and 7.

The magnesium concentrations varied for both scaffolds during the experiment are shown in Figure 4-4; D. On both scaffolds the magnesium varied between 3 and 4.5% over the time period, with no clear trends.

The precipitated Ca/P ratio on the two surfaces was calculated and illustrated in Figure 4-4; E- F. On both surfaces, the Ca/P ratio decreased gradually and after day 7, the ratio was close to 1.96 for both scaffolds.

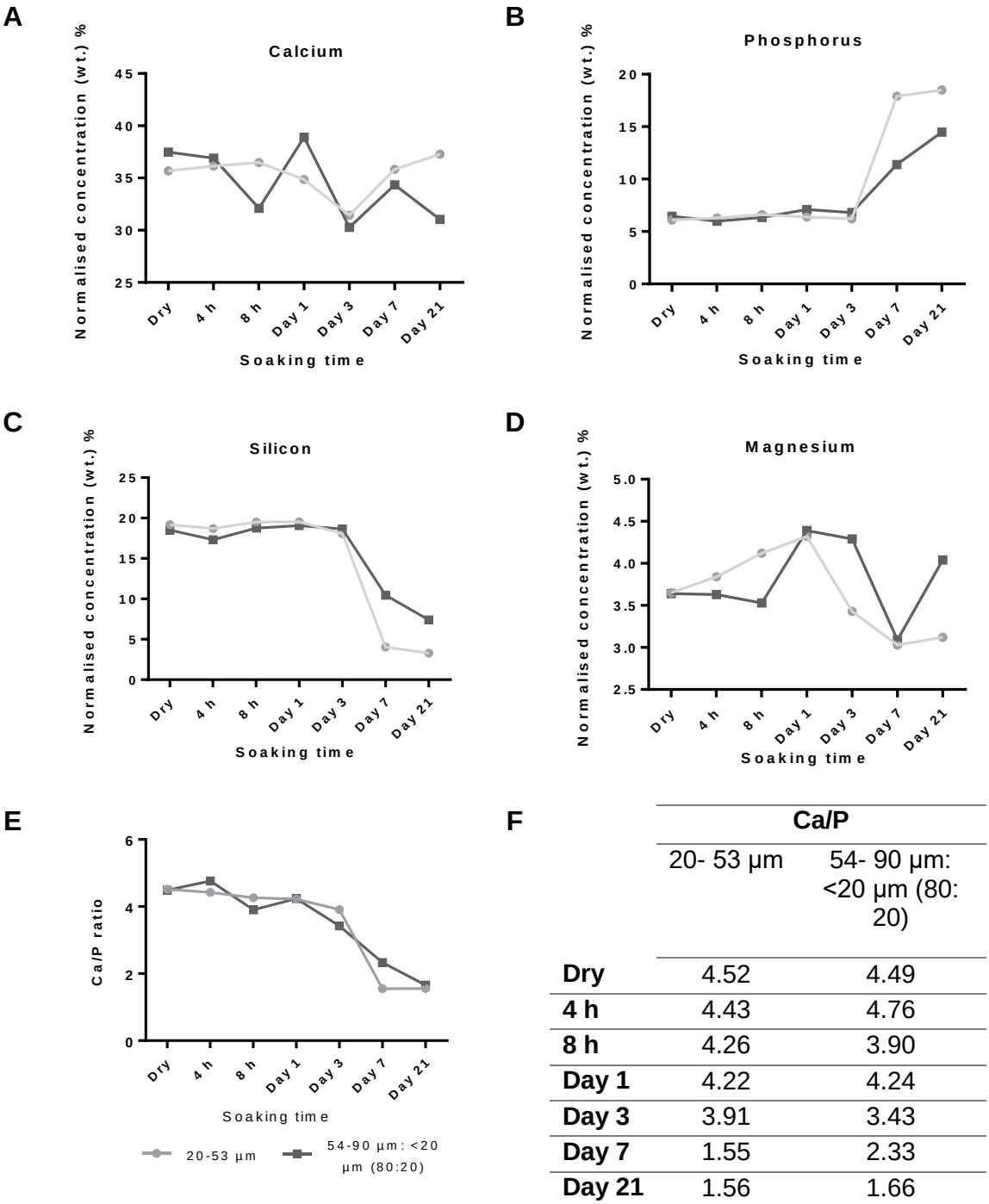

F

	Ca/P	
	20- 53 µm	54- 90 µm: <20 µm (80: 20)
Dry	4.52	4.49
4 h	4.43	4.76
8 h	4.26	3.90
Day 1	4.22	4.24
Day 3	3.91	3.43
Day 7	1.55	2.33
Day 21	1.56	1.66

Figure 4-4: The concentration of elements (A-D) and Ca/P ratio (E-F) precipitated on the surface of scaffolds fabricated using 20- 53 µm and 54- 90 µm before their immersion in SBF and at the various time-points during their soaking in SBF.

Figure 4-5 portrays the ionic profile (§2.5.2) in SBF solution after A-W scaffolds immersion for 21 days. There was slow ionic release of calcium, phosphorus and

silicon for the first 8 hours illustrated as plateaus in the corresponding graphs for both groups of scaffolds (Figure 4-5).

Figure 4-5; A illustrates that there was higher release of calcium from the scaffolds with the larger particle range. Scaffolds with particle range 20- 53 µm absorbed the calcium in the SBF after day 3.Phosphorus concentration in the SBF is demonstrated in Figure 4-5; B. Both samples were absorbing phosphorus slowly up to 8 h and more rapidly after day 1. Scaffolds with the large particle range favoured increased precipitation of phosphorus containing crystallites. Silicon and magnesium ions were released from both scaffolds, but scaffolds with particle range 54-20 µm: <20 µm released higher concentration of both ions more rapidly (Figure 4-5; C-D).

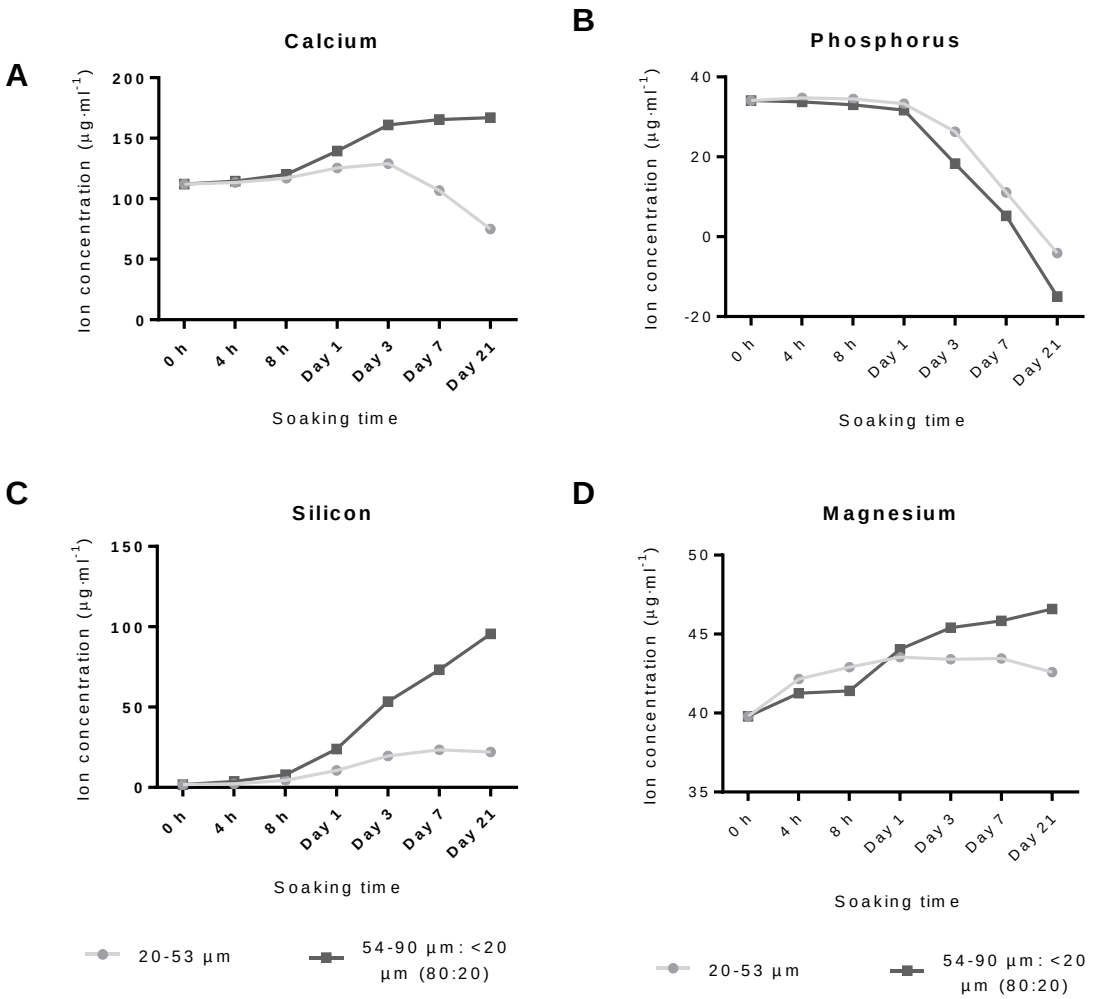

Figure 4-5: Ionic concentration of calcium (A), phosphorus (B), silicon (C), and magnesium (D) released in SBF after immersion of two different groups of A-W sintered cast slurryscaffolds with particle ranges 20- 53 µm and 54- 90 µm: <20 µm (80: 20) in SBF solution during 21 days.

In Figure 4-6 the mass alterations in the scaffolds during immersion in SBF is illustrated. Scaffolds with small particle range increased their mass by approximately 1% and the scaffolds with large particle range lost mass by approximately 1% of their mass. The mass change was significantly affected by the duration of the immersion ($p<0.0001$) and the interaction between duration and particle range ($p<0.00001$). After Bonferroni's multiple comparison test, it was highlighted that for both scaffolds there was a significant change in mass on Day 21 ($p<0.0001$) in comparison to the previous days. The mass difference between the two groups were significant on day 7 ($p= 0.0005$) and day 21 ($p<0.0001$).

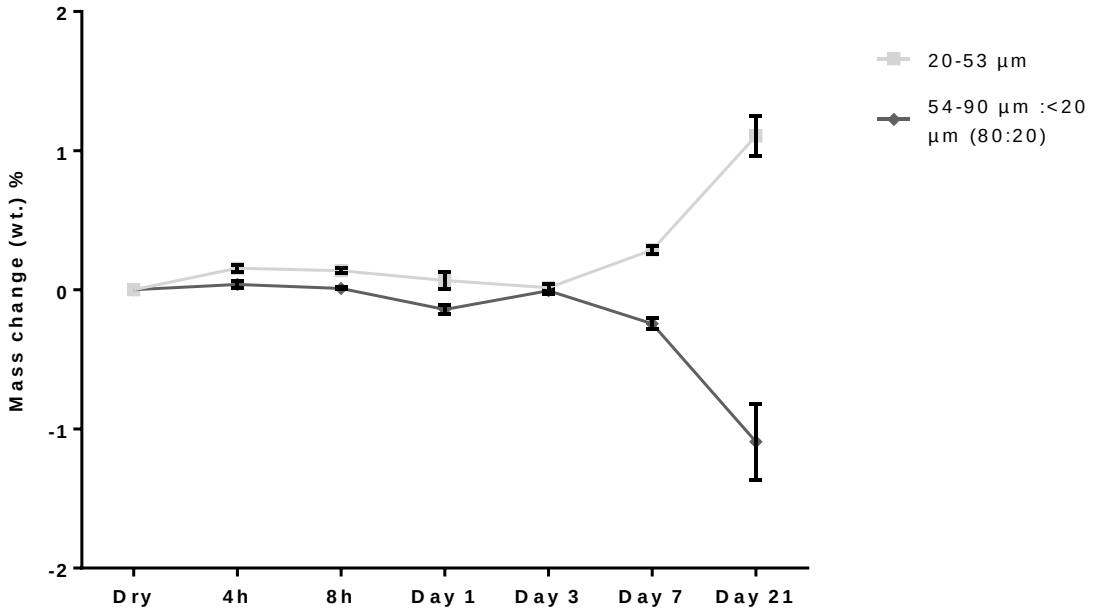

Figure 4-6: Mass change of scaffolds in SBF solution during 21-day period.

In Figure 4-7 the Young's modulus (§2.5.4) of scaffolds before and after the end of the biodegradation assay is illustrated. After analysing the data using two-way ANOVA, there was a significant effect on the Young's modulus from the immersion in SBF ($p= 0.0246$). According to Bonferroni's multiple comparison test, there is significant decrease in Young's modulus in the scaffolds with the large particle range after it was removed from the SBF ($p= 0.0385$). No significant effect was observed for the scaffold with the smaller particle range.

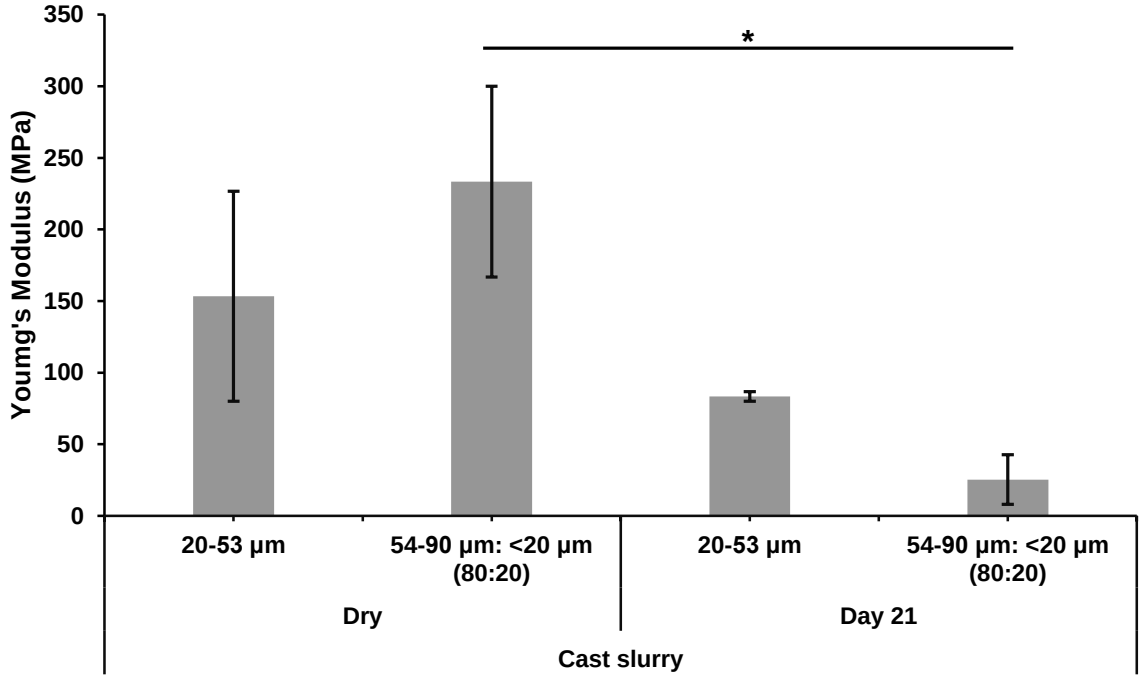

Figure 4-7: Young's modulus of scaffolds before and after the incubation in SBF for 21 days.

4.3.3 *Effect of scaffold topography on hMSC fate*

The influence of substrate topography and chemistry on cell adhesion was investigated by seeding Y201 cells (§4.2.3) on the top surface of the two groups of sintered cast slurry scaffolds and on coverslips as control. This was performed under routine culture conditions or in media supplemented with factors that favoured osteogenesis. Figure 4-8 demonstrates that the type of substrate significantly influenced the cell attachment ($p<0.0001$). There was a significantly higher cell population adhered on the scaffolds prepared with particle range 20- 53 µm in both media in comparison to the other two substrates. Also the scaffolds prepared using A-W with particle range 54- 90 µm: <20 µm (80: 20) facilitated enhanced cell adhesion in comparison to the coverslips in both media ($p<0.0001$). The different media had no effect on the cell adhesion ($p= 0.56936$).

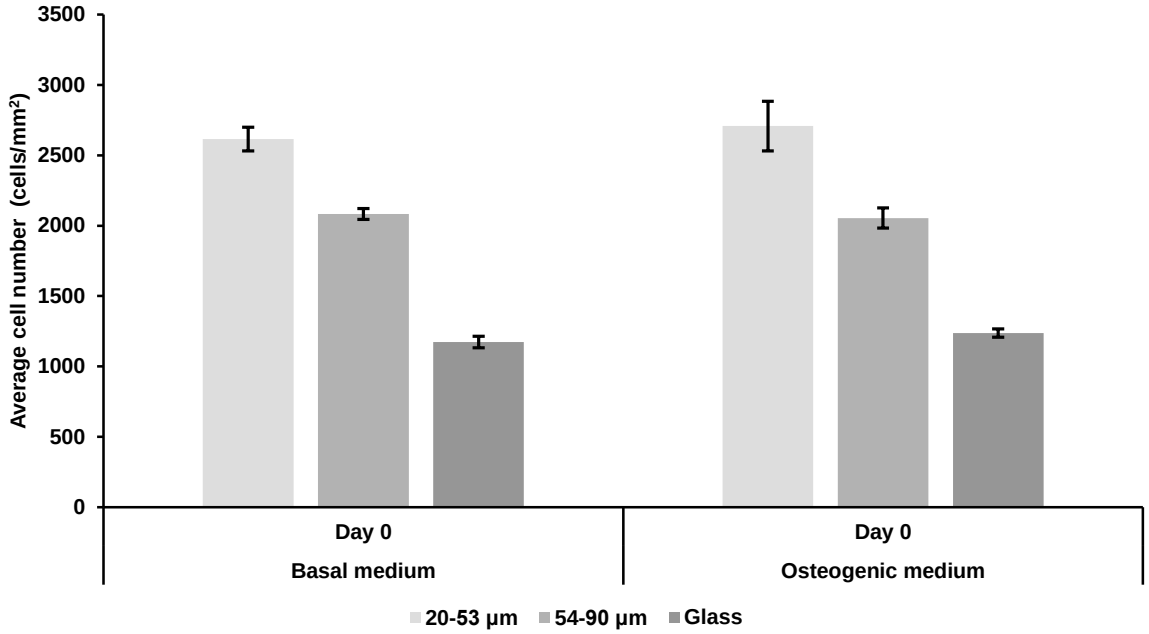

Figure 4-8: Average cell number per mm^2 adhered on the different substrates following 4 hours incubation after seeding.

Figure 4-9 illustrates Y201 cells adhered on the different substrates 1 day post-seeding. Cells adhered on the scaffolds prepared using 20- 53 µm particle size range (Figure 4-9;A) and coverslips (Figure 4-9; C) have similar morphology. In both photos cells seem to have spread out. The main difference between the cells on these two surfaces was that the cytoskeleton of the cells on the coverslips was more prominent. Cells seeded on scaffolds with large particle range (Figure 4-9;B) tended to prefer homing between adjacent particles and were more enlogated and stretched. In addition, cells on the 54- 90 µm: <20 µm (80: 20) had extended filopodia linked to neighbouring particles and migrated in the opened pores.

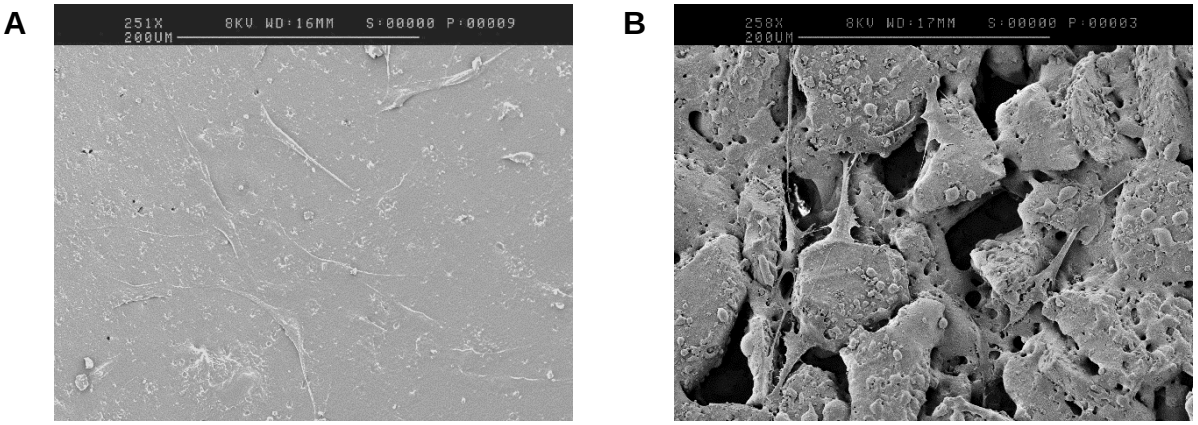

20- 53 µm **54- 90 µm: <20 µm (80: 20)**

Figure 4-9: SEM micrographs of Y201 cells cultured on the top of different surfaces for 24 h.

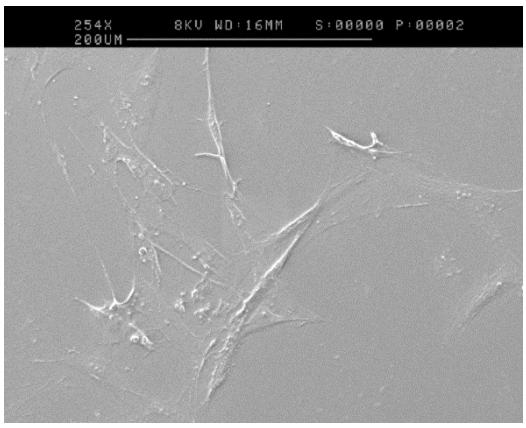

Figure 4-9: SEM micrographs of Y201 cells cultured on the top of different surfaces for 24 h.

Figure 4-9 highlights the differences in proliferation of the Y201 cells on the different surfaces over 28 days in both basal and osteogenic medium. The two different media had no effect on the cell proliferation. The number of the cells seeded on the ceramic scaffolds reduced significantly from day 0 to day 1 ($p<0.0001$ for both scaffolds) and they only fully recovered on day 14. In contrast cells on the coverslips appeared to have no significant difference in viability and proliferation throughout the duration of their cultivation ($p= 0.0568$). On day 14, cells on scaffolds with the smallest particle range had the highest viability and the lowest on glass. Cells on the two ceramic scaffolds had no significant differences in viability during days 21 and 28; however in comparison to the coverslips their viability was significantly enhanced ($p\leq0.0001$ on Day 21 and $p<0.0001$ on Day 28).

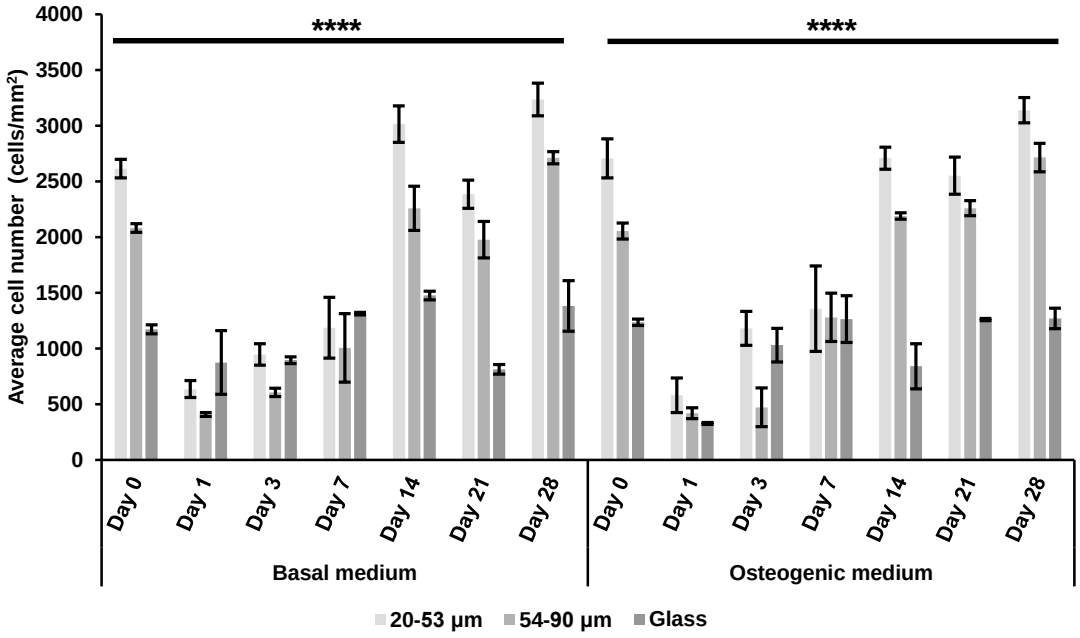

Figure 4-10: Viability of Y201 cells seeded on different substrates.

Alkaline phosphatase enzymatic (Chapter 2, §2.7.2) was assessed after 28 days to examine the influence of the substrates on Y201 cells differentiation to the osteogenic lineage. Cells were cultivated in basal and osteogenic medium to examine whether the surfaces solely had the potential to induce osteogenesis or they needed the participation of other supplements. Figure 4-11 shows illustrated that the substrate, the culture medium and duration of cultivation have significantly influence on the ALP activity. The cells on the scaffolds with the large particle range had significant increased ALP enzymatic activity on day 14 ($p= 0.0266$) similarly to the coverslips ($p= 0.002$). No significant increase in ALP was observed at cells cultured on the scaffolds with the small particle range in basal medium.

In the osteogenic medium all the surfaces had significant rise in ALP activity. Cells on the scaffolds with the small particle range had significantly increase ALP activity on day 14 and peaked on day 21, remaining elevated through day 28. The cells on the coverslips and the scaffolds with particle range 54- 90 μm: <20 μm had significant elevated ALP activity on day 7and for both peaked on day 21 followed by a drop on day 28.

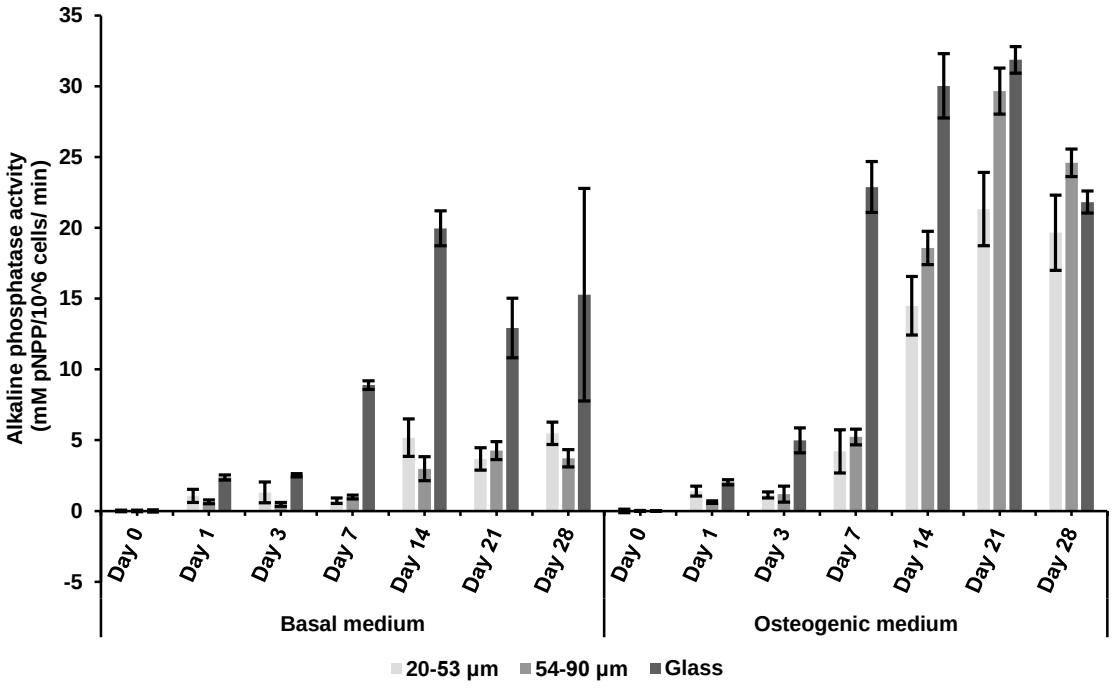

Figure 4-11: Alkaline phosphatase activity of cells cultured on different surfaces.

RT-PCR was used to quantify the gene expression from cells cultivated on the sintered cast slurry and the coverslips to assess whether there substrates promoted the osteogenic gene cascade in the Y201.

Figure 4-12 demonstrates the relative gene expression of specific osteogenic genes of interest after values were normalised to GADPH used as a ubiquitously expressed "housekeeping gene".

T2Runx2 (Figure 4-12; A-B) was not influenced by the substrate in either of the two media used; however, its expression was affected significantly by the duration the cells were cultivated on the substrates in the osteogenic medium ($p= 0.0324$). After analysing the data using Bonferroni's multiple comparison tests on day 7, T2Runx 2 was significantly ($p= 0.0101$) higher in cells cultured on scaffolds with smaller particle range than the bigger particles in basal medium. On day 21, the expression of T2Runx2 from the cells growing on the coverslip was significantly increased in comparison to the cells on the other two substrates. A drop in the expression of T2RUNX2 was evident on days 7 and 21 in comparison to day 1. The expression of T2Runx2 was significantly increased on day 1 in osteogenic medium in comparison to the other two time-points ($p<0.0001$) and to day 1 in basal medium ($p<0.0001$). In basal medium on day 21, the cells on coverslips expressed significantly more T2Runx2 in comparison to the cells on the ceramic scaffolds.

In Figure 4-12; B-C Cells cultured on the ceramics with the larger particle ranges in osteogenic medium had significantly increased osteopontin at day 1 ($p= 0.0331$ in comparison to glass and $p= 0.0320$ in comparison to ceramics with particle range 20-53 μm). On day 7 the osteopontin expression from cells on scaffolds with 20- 53 μm particle range in osteogenic medium was significantly increased in comparison to cells on the other two substrates and in basal medium. On day 21, cells on glass in osteogenic medium had higher expression of osteopontin from the cells on A-W scaffolds ($p= 0.0008$). No significant differences were observed in osteopontin expression on cells cultured in basal medium.

The expression of osteocalcin was not significantly affected by the substrate, the culture duration or the medium (Figure 4-12; E-F).

Collagen type I expression (Figure 4-12; G-H) by cells seeded on coverslips cultured in basal medium reached its peak on day 7. Collagen type I was expressed

significantly in cells on glass when cultured in osteogenic medium on day 1 in comparison to cells growing on scaffolds with particle range 54- 90 µm: <20 µm and in comparison to cells on coverslips in basal medium (p= 0.0312). Similar difference in collagen type I expression on cells growing on coverslips was observed on day 7 between osteogenic and basal medium (p= 0.0368).

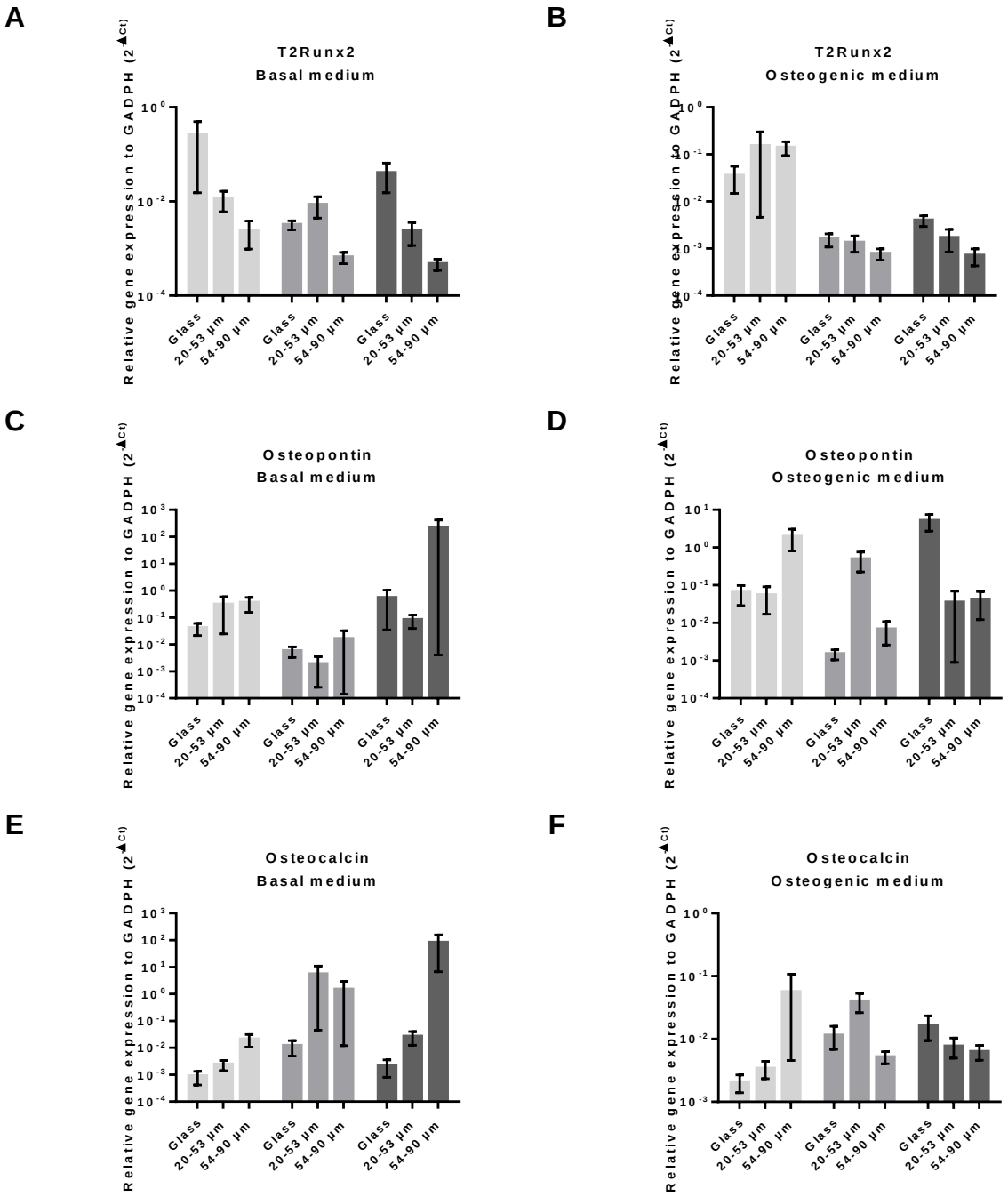

Figure 4-12: mRNA expression of T2Runx2, osteopontin, collagen type I and osteocalcin relative to GADPH of cells cultured on different substrates.

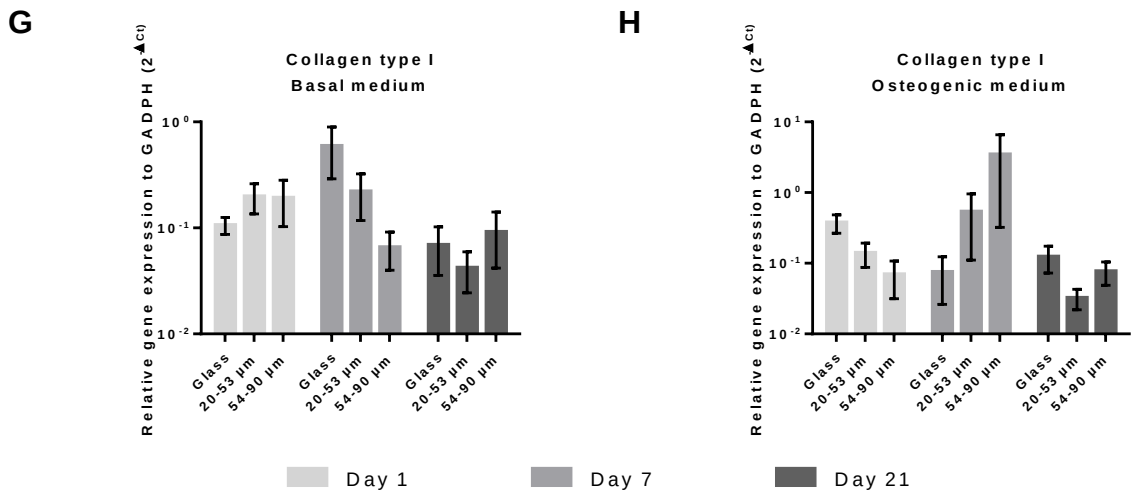

Figure 4-12: mRNA expression of T2Runx2, osteopontin, collagen type I and osteocalcin relative to GADPH of cells cultured on different substrates.

Figure 4-13 illustrates the expression of the transcription factors SOX9 and the proteoglycan, aggrecan (both reflecting the chondrogenic pathway) in cells seeded on the different substrates over the course of 21 days.

SOX9 (Figure 4-13; A-B) decreased significantly on cells cultured on glass and scaffolds with small particle range in comparison to cells on the A-W scaffolds with the larger particle range at day 21 in basal medium (p= 0.0019 and p= 0.0034 respectively).In addition, cells seeded on scaffolds with larger particle range lost the expression of SOX9 in basal medium over the duration of the experiment (p= 0.0004 for day 7 and p= 0.0002 for day 21). The medium affected the SOX9 expression from the cells seeded on the scaffolds with the larger particle range with the gene expression dropping significantly on day 21 when cells where cultured in osteogenic medium (p= 0.0123).

Aggrecan expression (Figure 4-13; C-D) decreased significantly on coverslips after day 1 in both basal and osteogenic medium. Cells that were seeded on scaffolds with larger particle range in basal medium had significantly increased aggrecan expression in comparison to the other two groups (p= 0.0242 in comparison to glass and p= 0.0278 in comparison to scaffold with particle range 20- 53 µm).

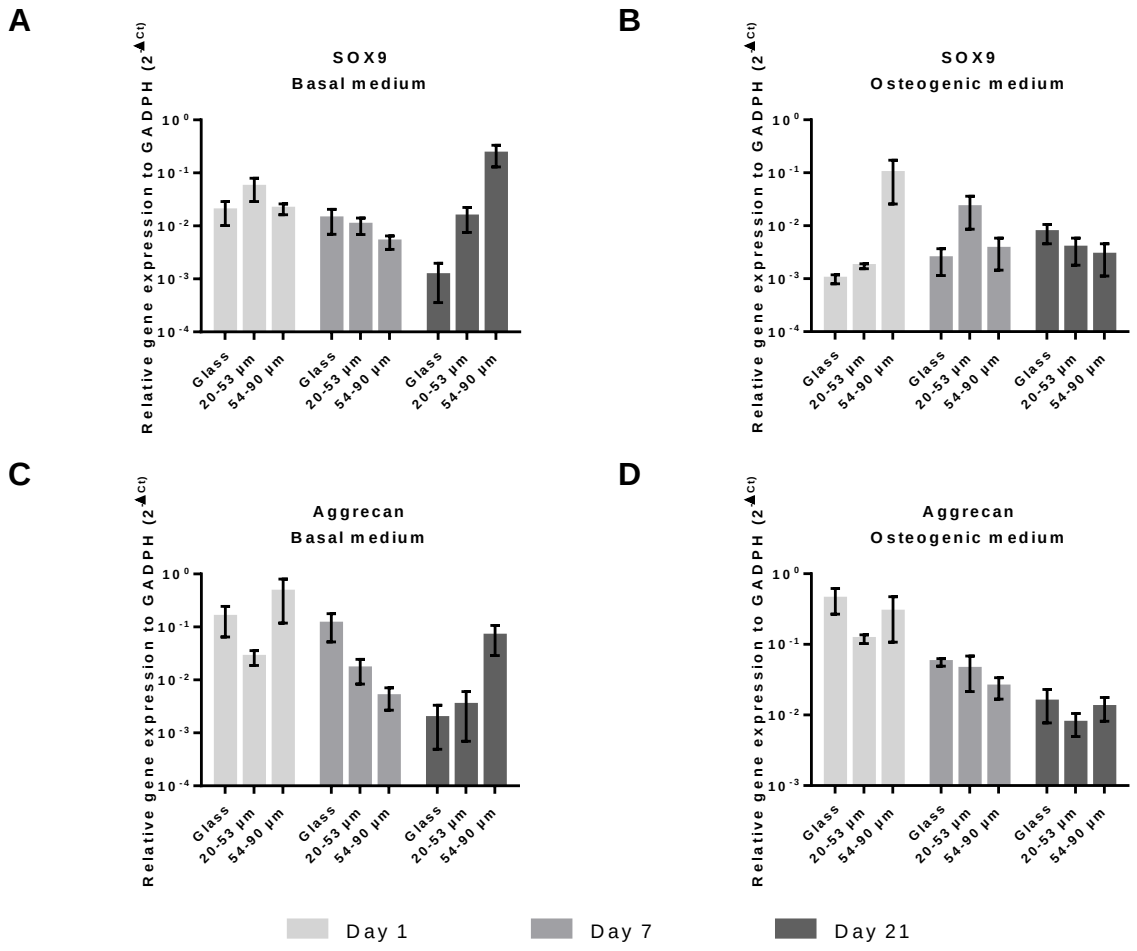

Figure 4-13: mRNA expression of SOX9 and aggrecan relative to GADPH of cells cultured on different substrates.

Toluidine blue in combination with Von Kossa staining were used to identify sulphated mucosubstances and mineral deposition on the scaffolds on days 7, 14 and 21 in both basal and osteogenic medium.

Figure 4-14 illustrates samples that were incubated in basal medium. On day 7, the matrix formed on the scaffold with the larger particle range is more intense purple and more densely populated in comparison to the matrix on the smaller particle range. On day 14, increase in the sulphated mucosubstances were observed in combination with some mineral deposition; whereas the matrix on the scaffold with the larger particle range seemed to have become sparser than that observed at the previous time-point, however there was still an area that had some mineral depositions. On day 21, the scaffold with smaller particle range was covered with mineralised matrix. At the same time-point, there were strongly purple stained mucosbstances and pockets with mineral deposition.

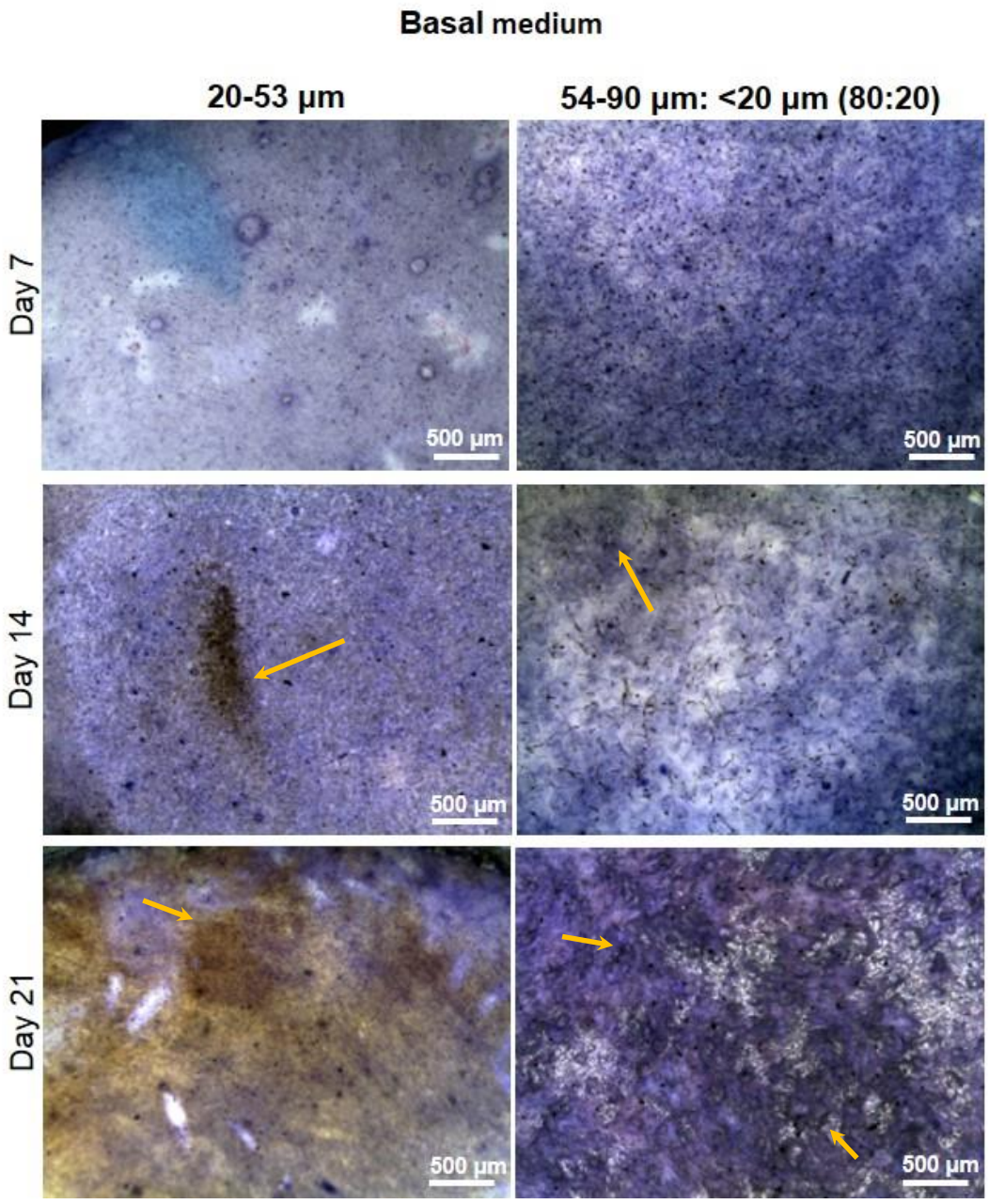

Figure 4-14: Toluidine blue and Von Kossa histological staining of Y201 cultured on sintered casted slurries with particle ranges 20- 53 µm and 54- 90 µm: <20 µm in basal medium for 7, 14 and 21 days. Blue is toluidine blue staining and brown-black is Von Kossa staining. Orange arrows point indicative mineralised points. Top view of the cell seeded scaffolds.

Figure 4-15 demonstrates samples cultured in osteogenic medium. All samples were stained strongly blue at all the time-points. Mineral deposition appeared to gradually increase during the experiment, forming a mineral nodule on day 14 and covering all the scaffold by day 21. Mineral deposition was also observed at some areas during

all the time-points on the scaffolds with particle range 54- 90 µm: <20 µm.

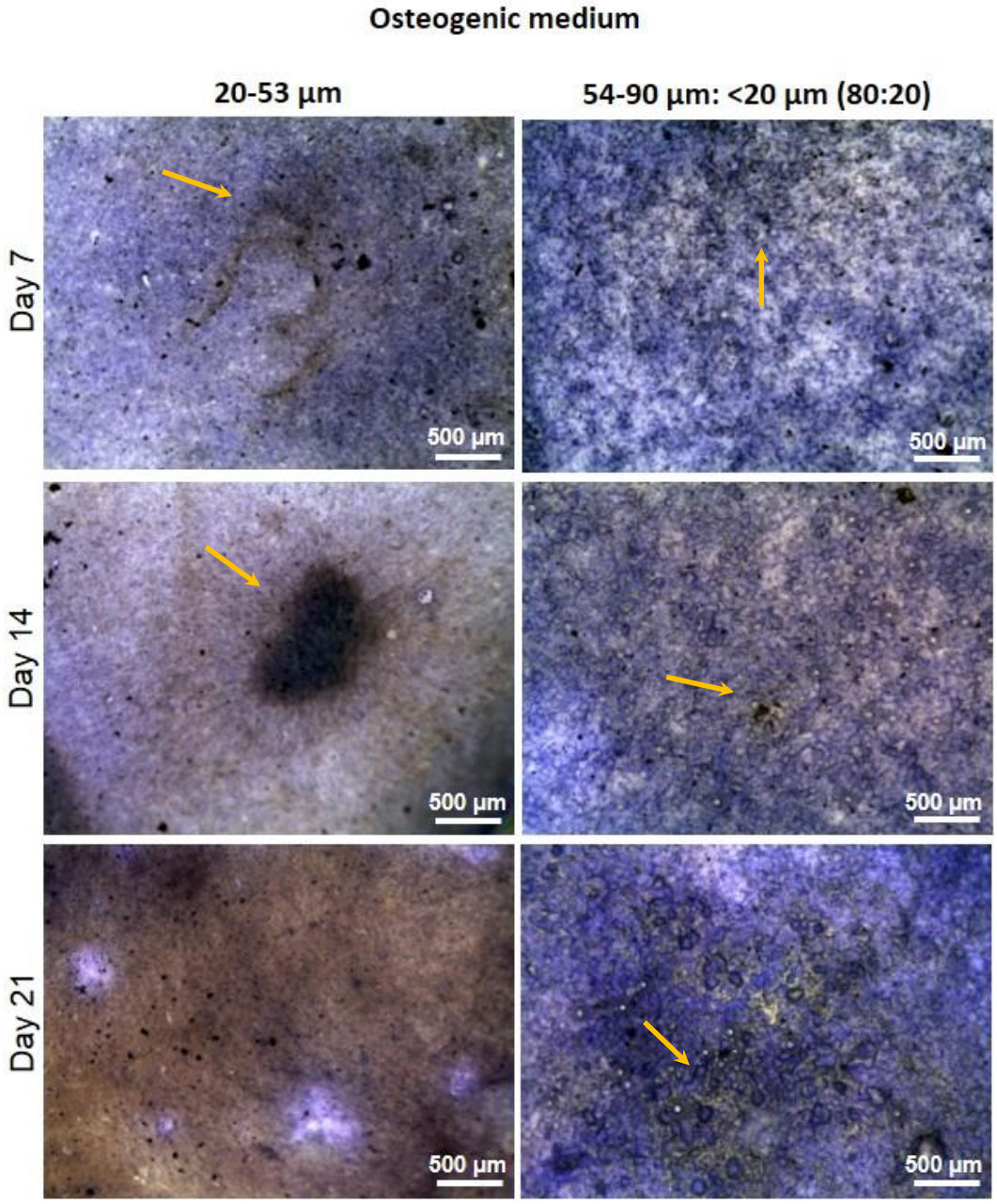

Figure 4-15: Toluidine blue and Von Kossa histological staining of Y201 cultured on sintered casted slurries with particle ranges 20- 53 µm and 54- 90 µm: <20 µm in osteogenic medium for 7, 14 and 21 days. Blue is toluidine blue staining and brown-black is Von Kossa staining. Orange arrows point indicative mineralised points. Top view of the cell seeded scaffolds.

In Figure 4-16 cells were cultivated in osteogenic medium for 21 days and had evidence of a bone nodule that had de-adhered from the substrate and anchored at the periphery of the scaffold.

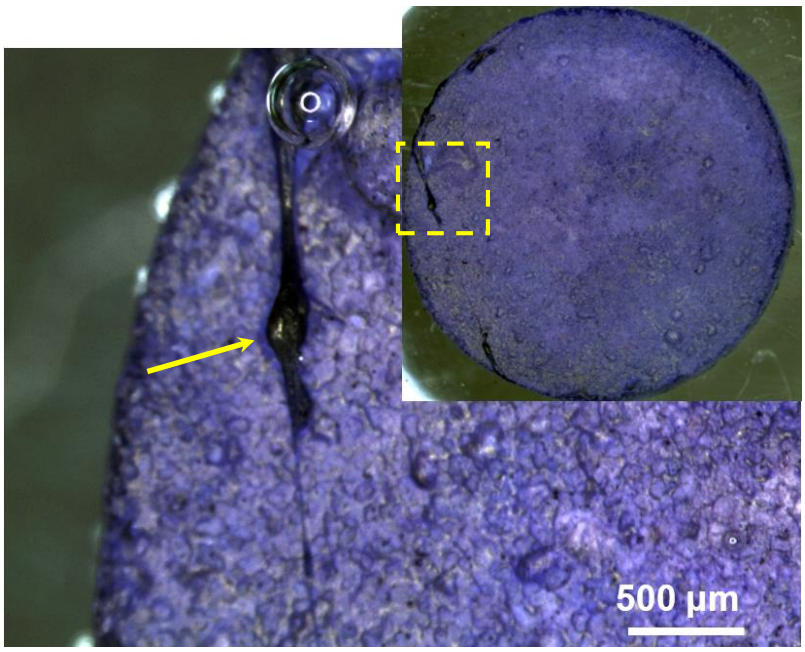

Figure 4-16: Toluidine blue and Von Kossa stained Y201 cells on sintered casted slurries with particle ranges 54- 90 µm: <20 µm in osteogenic medium 21 days after seeding. Yellow arrows point indicative mineralised mass. Top view of the cell seeded scaffolds.

4.4 Summary

This chapter demonstrates that scaffolds prepared using the slurry casting and sintering method with two differently sized A-W particle ranges resulted in the fabrication of scaffolds with different surface topography and micropore sizes (Figure 4-2). In addition, it was revealed that the bioactivity in terms of calcium phosphate deposition was faster on scaffolds fabricated from smaller sized particles. In a time-period of 21 days both samples formed a calcium phosphate deposit that had covered much of the surface of the samples (Figure 4-3). The samples with smaller particle ranges exhibited more rapid element deposition and the samples with the larger particle range had higher ion release in the SBF solution (Figure 4-4; Figure 4-5). Interestingly, scaffolds with the smaller particle range increased their mass during the biodegradation-bioactivity test (Figure 4-6), whereas the samples with the larger particle range decreased in mass concluding that surface area can influence the bioactivity and biodegradation of A-W. This coincided with no change in mechanical properties of the former and decrease in Young's modulus of the latter (Figure 4-7).

Both scaffolds promoted cell adhesion and proliferation in comparison to glass (Figure 4-8; Figure 4-10). The scaffold formed from the smaller particle range had a more significant influence on the cells in comparison to the other A-W scaffold. Cell morphology varied depending upon the topography of the individual substrate. Cells on the small particle range scaffolds and glass slides had similar flattened and spread morphology, whereas cells on the rougher and microporous scaffold were more elongated (Figure 4-9).

The A-W scaffolds, which were used, had lower ALP activity in comparison to the control glass in both media (Figure 4-11). However, at later time-points in the osteogenic medium the differences in ALP activity shrank. RT-PCR results (Figure 4-12) verified that glass promoted more osteogenesis in osteogenic medium relative to basal medium. In basal medium, the cells on the scaffold with the smaller particle range had increased osteogenic properties over the larger particle range, comparable to the glass control. Scaffolds with larger particle range demonstrated higher expression of genes related to chondrogenesis (Figure 4-13).

Chapter 5 *IN VITRO* ASSESSMENT OF SINTERED A-W TIPS SCAFFOLDS

5.1 Introduction

Sintered A-W TIPS scaffolds were described and optimised in Chapter 3 §3.7. This group of scaffolds was selected for further *in vitro* investigation due to exhibited high interconnectivity and porosity.

These scaffolds were fabricated by adding A-W powder with particle range 20- 53 μm in a dioxane- PLA solution. The solution was mixed and poured in moulds to be frozen at -20^{o}C. Samples were the freeze-dried and sintered.

The main goal of this chapter is to evaluate how the high porosity in combination with interconnectivity influence A-W bioactivity and biodegradability. An additional aim was to study whether this group could promote *in vitro* osteogenesis to the hTERT cell line.

5.2 Materials- Methods

5.2.1 *SBF assay*

Sintered A-W TIPS scaffolds were immersed in SBF using a ratio of 0.375 g scaffold in 50 ml SBF solution based on Maçon et al. 2015.

5.2.2 *Seeding scaffolds*

Scaffolds were seeded using three different techniques: droplet , filter paper (Yamanaka et al. 2015) and capillary seeding (Bai et al. 2015). For assessing seeding techniques 200,000 cells were used per sample, but for the main experiment 500,000 cells per scaffold were used.

Figure 5-1 demonstrates droplet seeding. Scaffolds were organised in 24 well plates. The prepared cell suspension was added on the top of each scaffold using a pipette.

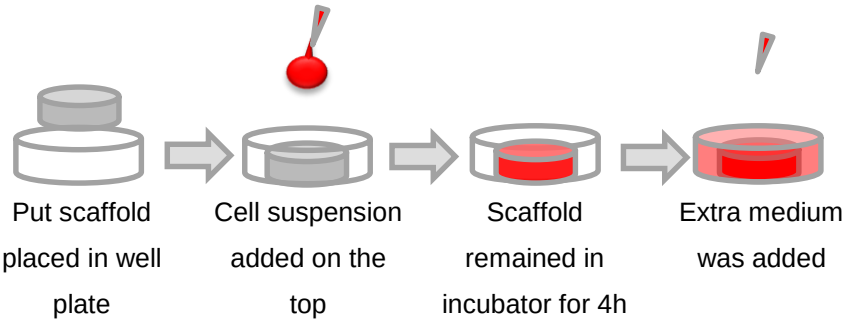

Figure 5-1: Illustration of droplet seeding

In Figure 5-2 seeding using filter paper is described. Filter paper was cut using a pair of scissors into pieces to fit the wells. After it was placed on the bottom of the well plate and the scaffold was placed on top. The cell suspension was applied on the top of the scaffold to be absorbed by the filter paper and pass rapidly through the scaffold.

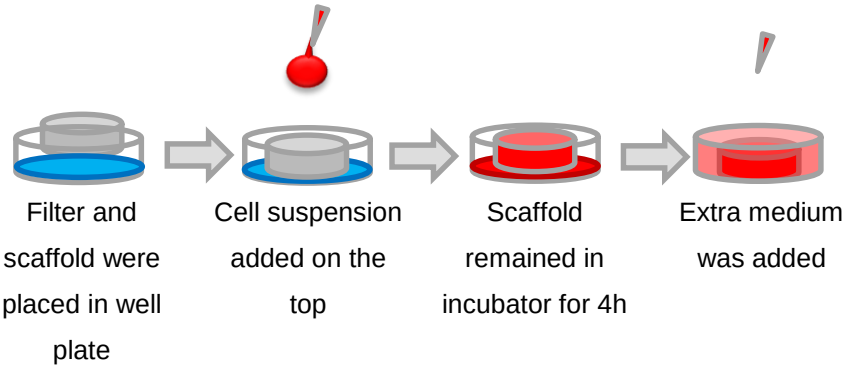

Figure 5-2: Illustration of seeding technique using filter paper.

Figure 5-3 demonstrates scaffold self-seeding using capillary forces. Cell suspension was added as a drop on the bottom of the well plate. The scaffold was placed on the top of the cell suspension.

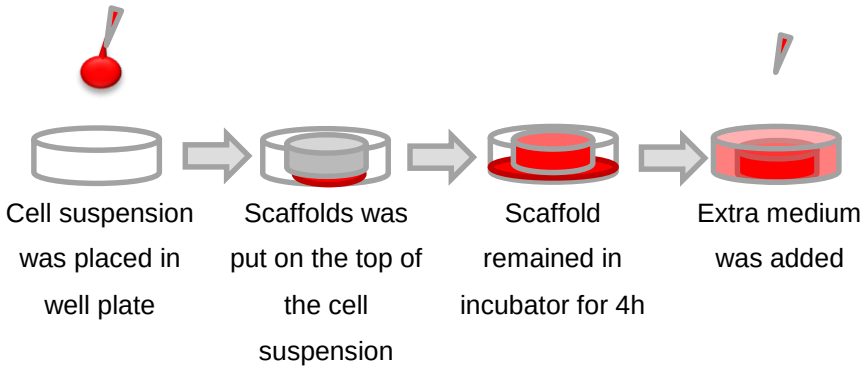

Figure 5-3: Illustration of self- seeding technique using capillary forces.

For all the methods, scaffolds were left in the incubator for 4 hours to allow cell adhesion. Then, they were washed with PBS to remove non-adherent cell and transferred in new well plates containing 500 µL fresh medium per well.

5.2.3 *Immunofluorescent staining and confocal microscopy*

Samples were fixed using pre-warmed 4 w/v % paraformaldehyde for 20 minutes. They were washed three times using PBS and then, they were washed in 0.1% v/v Tween20® (P2287) PBS for 5 minutes. Rhodamine phalloidin was prepared using 1:1000 dilution of phalloidin–tetramethylrhodamine B isothiocyanate (P1951) in 0.1% Tween20® PBS. Samples were immersed in rhodamine phalloidin for 5 minutes. Scaffolds with cells were washed three times with PBS and were immersed in DAPI: PBS solution for the confocal microscopy. Rhodamine phalloidin stains the cytoskeleton red and DAP the nuclei red (Figure 5-4). Leica TCS SP2 UV AOBS MP confocal microscope was used for the imaging.

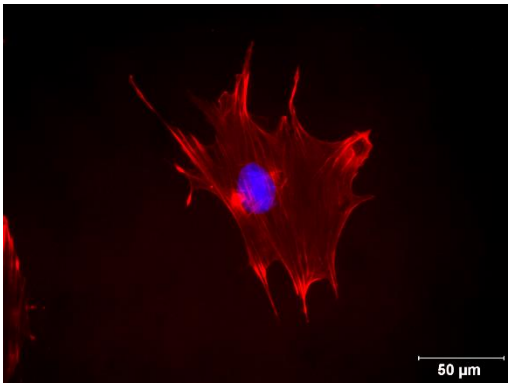

Figure 5-4: Representative immunofluorescent image of a cell that stained with rhodamine- phalloidin and DAPI.

5.3 Results

5.3.1 *In vitro biodegradation study of A-W sintered A-W TIPS scaffolds*

Samples were immersed in SBF solution according to the protocol described in Chapter 2: §2.5.10 for 4h, 8, 1 day, 3 days, 7 days, 14 days and 21 days. Figure 5-5 demonstrates SEM images of the samples. It was observed that on day 7, some spherulite-structure crystals appeared on the A-W sintered particles. The precipitated crystals appeared to become larger in size and spread more on the surface of the ceramic over the time-course of the experiment.

The main elements that appeared on the surfaces of these scaffolds were calcium, phosphorus, magnesium and silicon (Figure 5-6).

Calcium concentration (Figure 5-6; A) decreased rapidly during the first 8 hours and continued decreasing for the next 16 hours. Between day 1 and day 14 there fluctuations in its concentration on the scaffold with the highest reduction observed on day 7. During the last week calcium remained relatively stable. On day 21 the concentration of calcium had lower concentration in comparison to the beginning.

Phosphorus concentration (Figure 5-6; B) increased over the duration of this experiment. Only from day 1-3, a small decrease in concentration was observed, however its increase recovered over the next days.

The concentration of silicon (Figure 5-6; C) increased during the first 8 hours and then decreased by the end of the experiment. The only exception in this trend was noticed between day 3 and day 7, where silicon concentration increased.

In Figure 5-6; D, magnesium concentration fluctuated with its end-point to coincide with the magnesium concentration existing on the scaffold before immersing in SBF.

In Figure 5-6; E-F, the CA/P ratio is demonstrated. It was observed that the ratio decreased gradually and after day 7 remained at similar levels with final value 3.033.

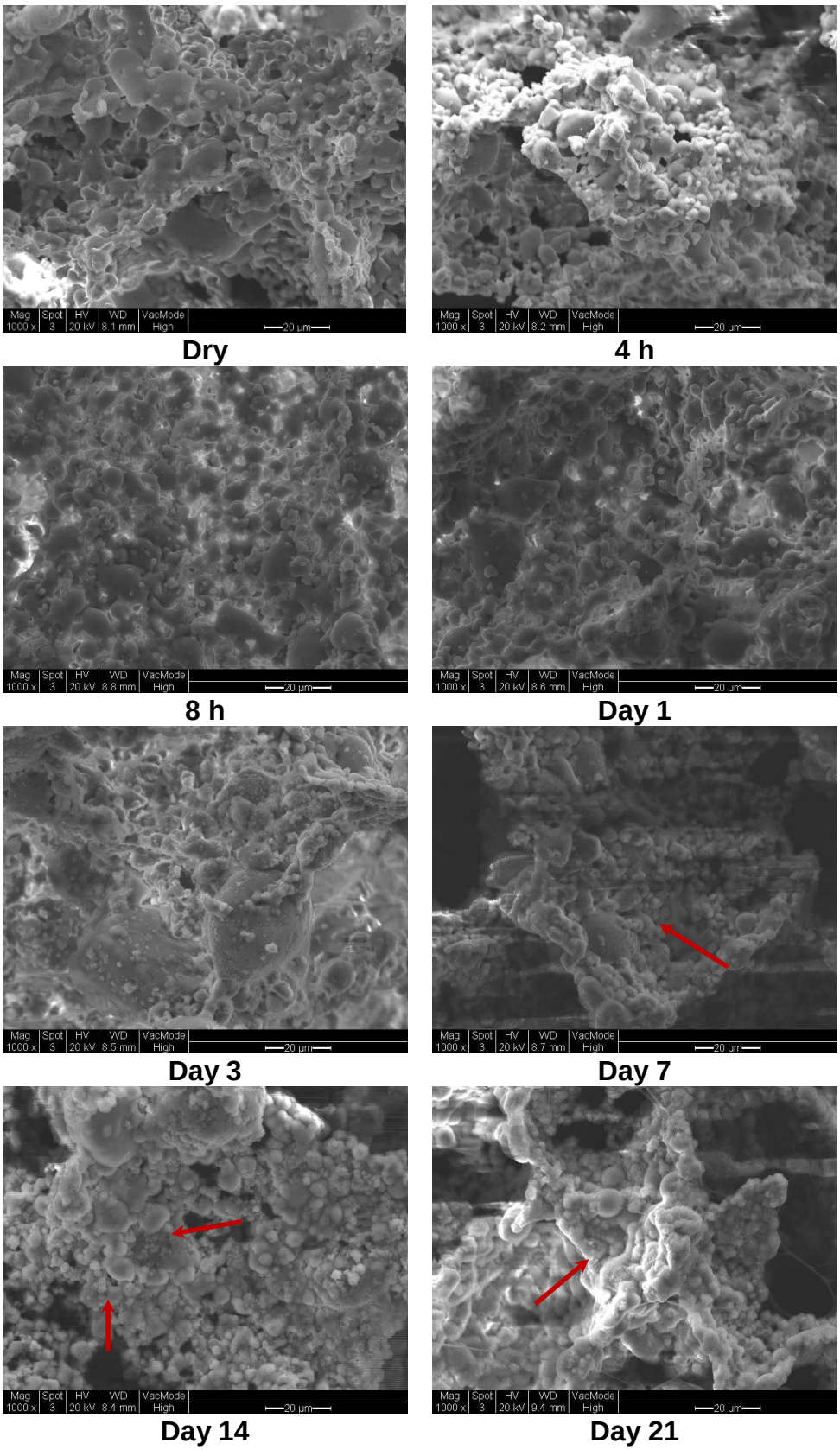

Figure 5-5: Indicative SEM micrographs of sintered A-W TIPS scaffolds with particle range 20- 53 µm before and after they were immersed in SBF solution for different time-points (0h, 4h, 8h, 1 day, 3 days, 7 days, 14 days and 21 days). Longitudinal cut of the scaffolds. The red arrows indicated precipitated crystals.

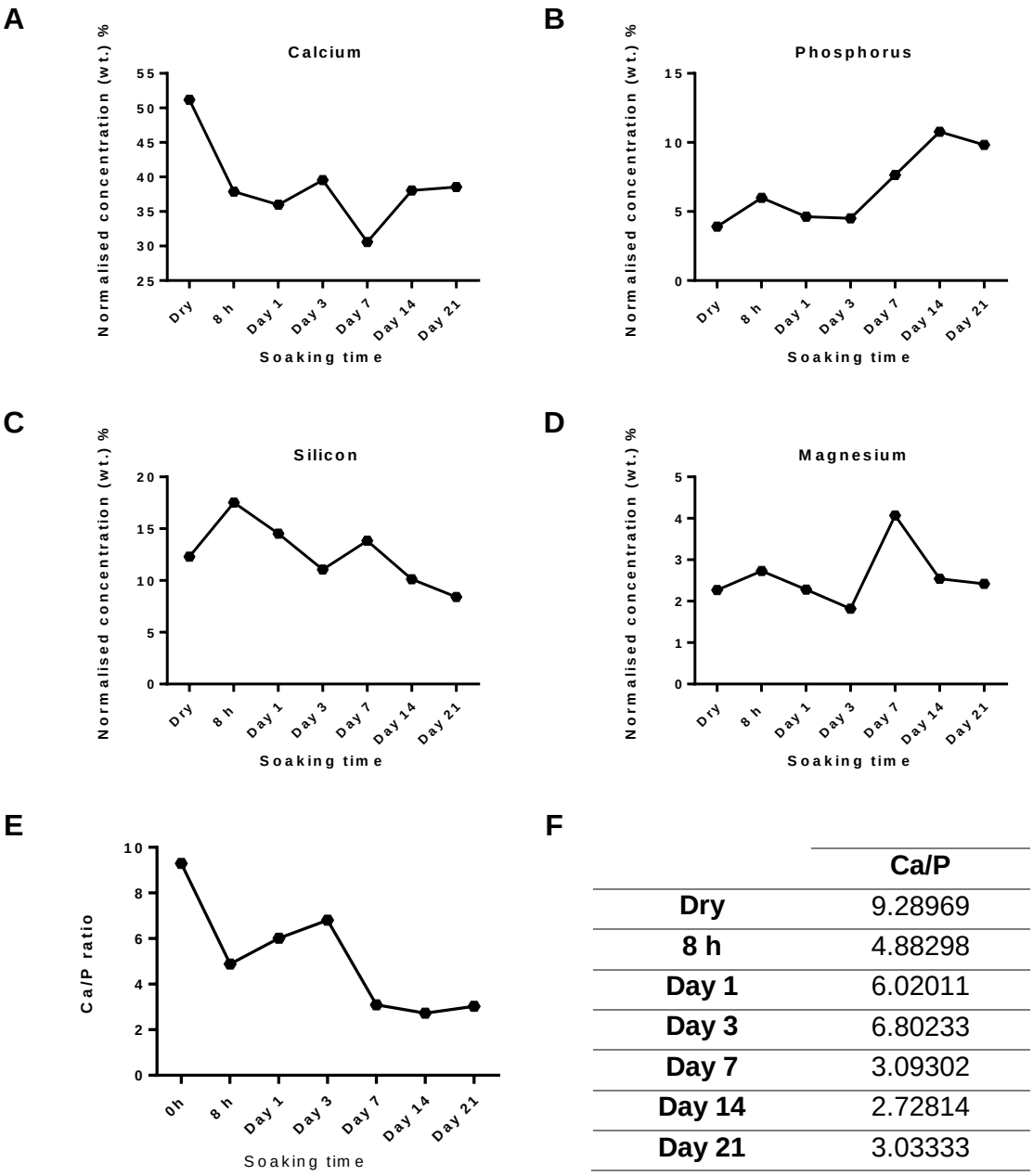

F

	Ca/P
Dry	9.28969
8 h	4.88298
Day 1	6.02011
Day 3	6.80233
Day 7	3.09302
Day 14	2.72814
Day 21	3.03333

Figure 5-6: The concentration of elements (A-D) and Ca/P ratio (E-F) precipitated on the surface of sintered A-W TIPS scaffolds with particle range 20- 53 µm before their immersion in SBF and at the various time-points during their soaking in SBF.

Figure 5-7 illustrates the ionic profile of the same elements that the EDS identified. These ions were released of absorbed during the sintered A-W TIPS scaffolds immersion in the SBF solution.

Calcium ions (Figure 5-7; A) were released from the scaffolds following SBF solution immersion until the first 24 hours. Then, they were depleted form the SBF over the next 6 days and finally calcium ions increased until day 21.

Figure 5-7; B demonstrates phosphorus ion absorption from the sintered A-W TIPS scaffolds throughout the duration of the experiment apart from day 7, where phosphorus ion concentration increased in the SBF solution.

Silicon ionic concentration (Figure 5-7; C) rapidly increased during the first 8 h and continued increasing with a gradual manner for the rest of the time-course. On day 7, the silicon ion concentration decreased in the SBF. For the following 7 days, silicon ions released promptly.

Figure 5-7; D magnesium ions were slowly depleted from the SBF solution over the time-course of the experiment.

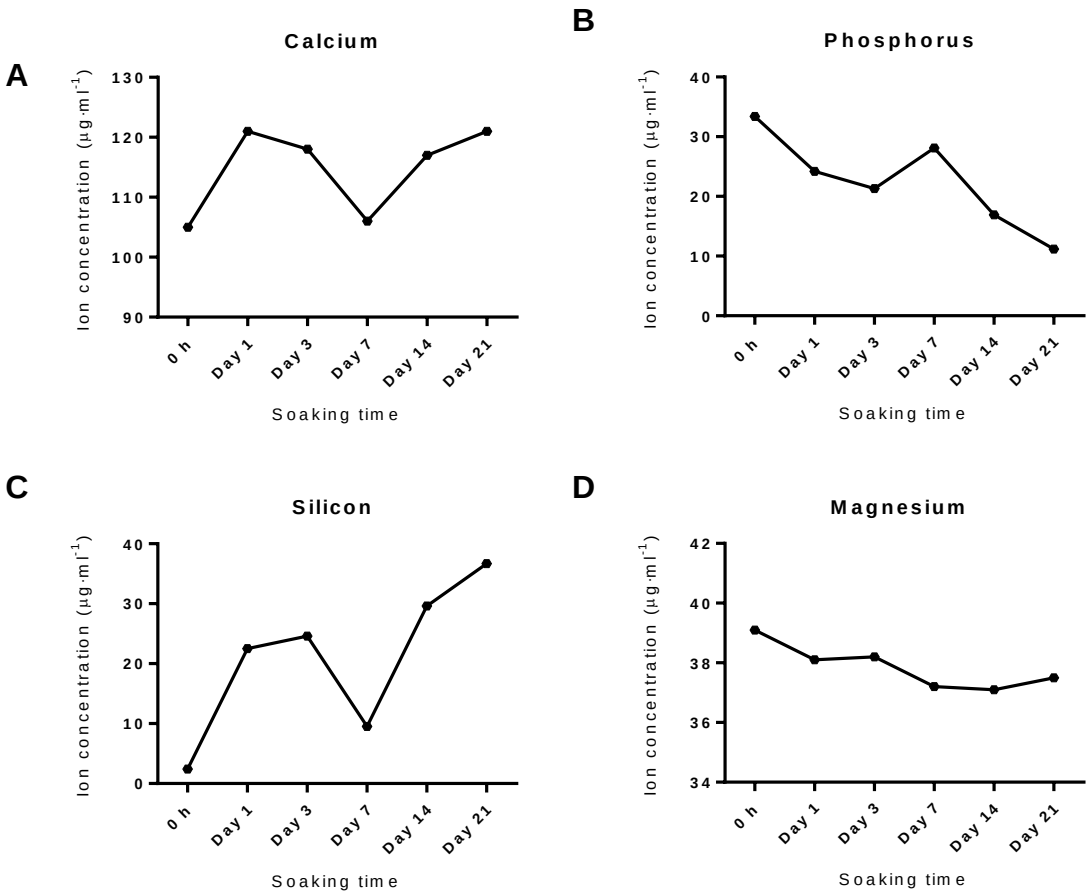

Figure 5-7: Ionic concentration of calcium (A), phosphorus (B), silicon (C), and magnesium (D) released in SBF after immersion of sintered A-W TIPS scaffolds with particle range 20- 53 µm in SBF solution during 21 days.

In Figure 5-8 presents the degradation of sintered A-W TIPS scaffolds during SBF immersion. There was a significant difference in mass throughout the experiment ($p<0.0001$).

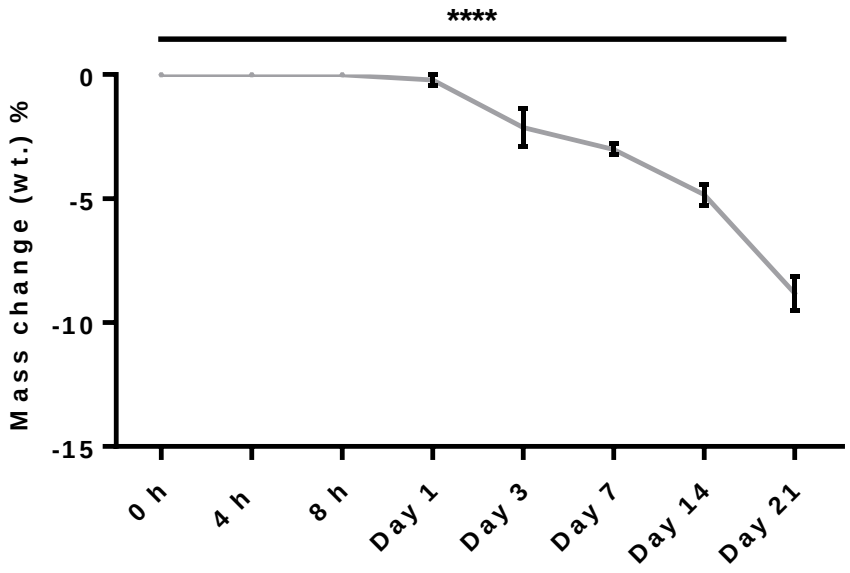

Figure 5-8: Mass change of sintered A-W TIPS scaffolds in SBF solution during 21-day period. (n=6)

In Figure 5-9 illustrates the Young's modulus (§2.5.4) of sintered A-W TIPS scaffolds before the biodegradation assay and after the immersion of the scaffolds in SBF at 4h and 21 days. After analysing the data using one-way ANOVA, there was a significant effect on the Young's modulus from the immersion in SBF (p= 0.0256). No significant difference was observed in the mechanical properties of the scaffold during the first 4 hours of the biodegradation assay, however the Young's modulus of the scaffold on day 21 was decreased significantly in comparison to the corresponding at 4h (p= 0.0278).

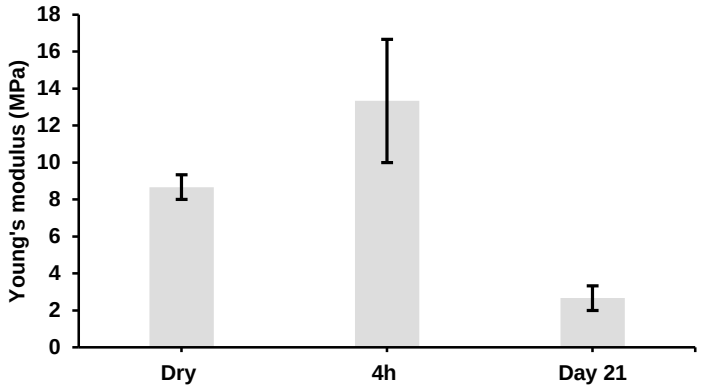

Figure 5-9: Young's modulus of scaffolds before and after the incubation in SBF for 21 days. (n=3)

5.3.2 *hTERT Y201 cells on sintered TIPS- A/W scaffolds*

Different seeding techniques (§5.2.1) were investigated to identify which technique would enhance cell infiltration. This was measured by assessing the total number of adherent cells 4 hours post-seeding.

Figure 5-10 demonstrates the cell number that attached on the scaffold after each seeding procedure. There was no significant difference between the three methods. The faster and more reliable method was the droplet seeding, this was therefore selected as the seeding methodology for the rest of this chapter.

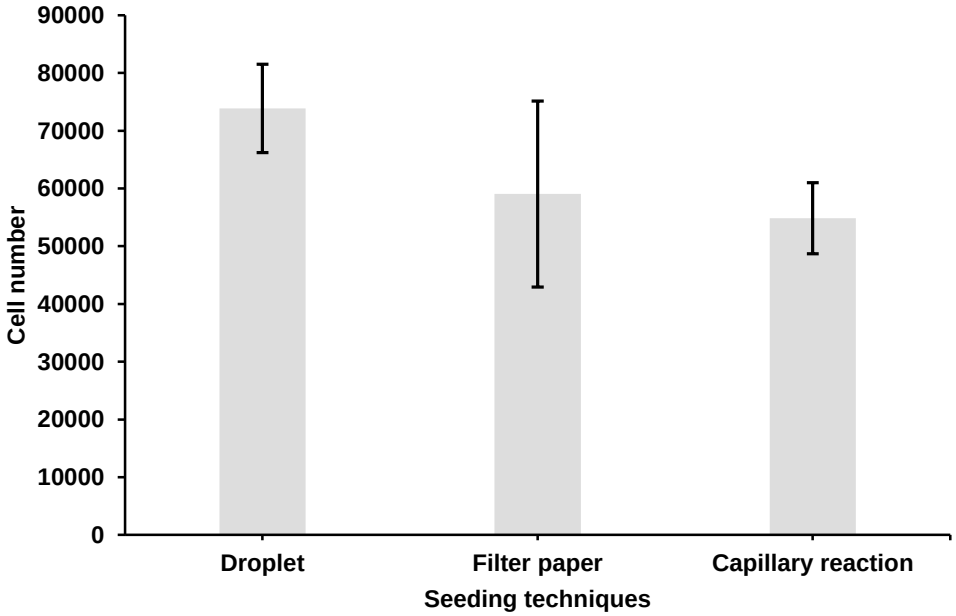

Figure 5-10: Cell seeding techniques for the sintered A-W TIPS scaffolds.

The sintered A-W TIPS scaffolds that were used for this chapter had a range of porosities (82%-89%) (Appendix- Table 1). For the scaffolds that were assessed using Alamar blue (§2.7.1) and alkaline phosphatase enzyme (§2.7.2) the porosities that were used were: 83, 85 and 86 (vol) % (Appendix- Table 1). The influence of different porosities on cell attachment after seeding was assessed using Alamar blue. Figure 5-11 demonstrates that there was no significant difference in cell number that adhered on the scaffolds with different porosities 4 hours after droplet seeding.

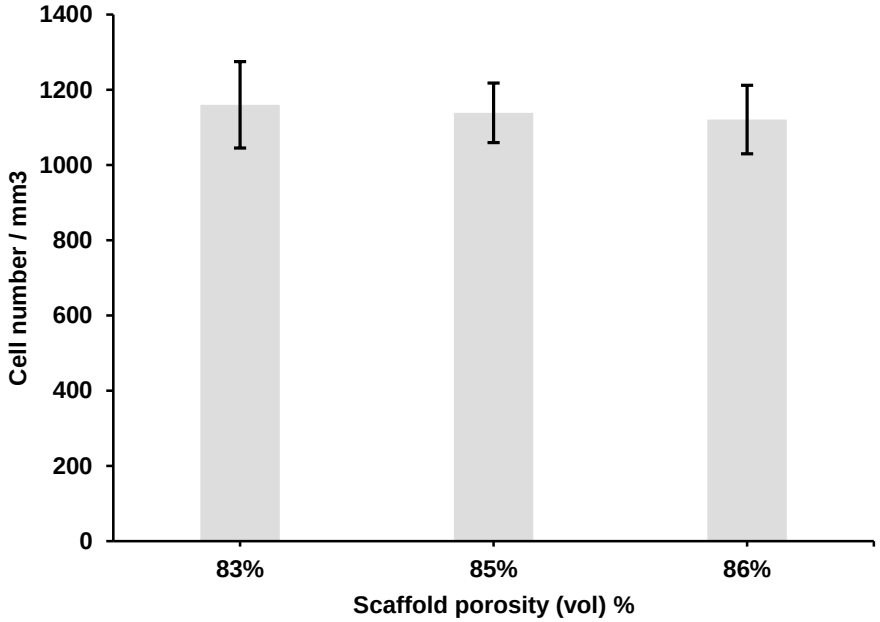

Figure 5-11: Average cell number per mm^3 adhered on sintered A-W TIPS scaffolds with porosities 83, 85 and 86 vol.% 4 hours after seeding. (n=6)

The cytoskeleton and nuclei of the cells were stained using phalloidin and DAPI (§5.2.3) correspondingly. The seeded Y201 cells were observed on sintered A-W TIPS scaffolds using confocal microscopy. The scaffold appears as grey on the images. Cells were imaged after one and three days of culturing in both basal and osteogenic media (Figure 5-12). In Appendix- Figure 4, the different channels of the confocal imaging were separated to study each the scaffold, cytoskeletons and the nuclei of the cells individually. On both groups, cells were enlogated with no noticeable differrences between the media they were cultivated. In Figure 5-12 it is demonstrated that cells adhered on the surface of A-W struts of the scaffold.

On day 3 (Figure 5-12), more cells appeared on the photos. Some of the cells traversed the pores (orange arrows) and some others appear to have started covering the pores.

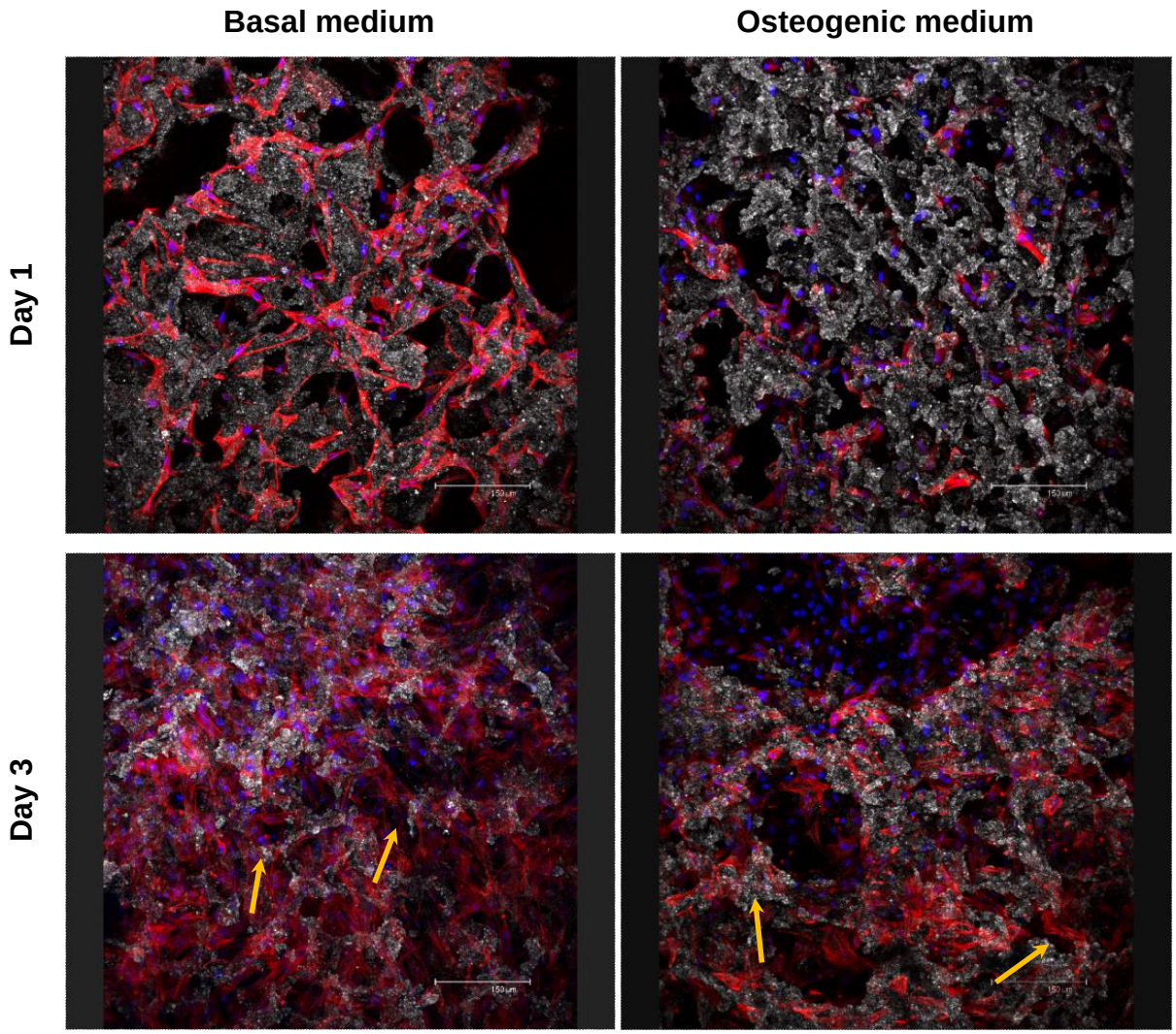

Figure 5-12: Confocal microscopy images of the top of seeded sintered A-W TIPS scaffolds with Y201 after three days of culting in basal and osteogenic media respectively. Red was rhodamine-phalloidin staining for the cytoskeleton and blue was DAPI stained the nuclei of the cells. Orange arrows indicate cells transversing the pores.

The viability of cells in the two different media was monitored using the Alamar blue metabolic assay (Figure 5-13). The assay was performed on the same three scaffolds for each medium demonstrated in Figure 5-13. Analysing the data using two-way ANOVA there was significant difference between the days ($p<0.0001$), but no significant difference between the two media. Using Bonferroni's multiple test, it was indicated that in the osteogenic medium there were significantly more cells on days 14 ($p= 0.0075$) in comparison to day 0. On day 21 there was a significant increase population in comparison to day 0 ($p<0.0001$), day 1 ($p= 0.0046$), day 3 ($p<0.0001$) and day 7 ($p= 0.0001$). Additionally, on day 21 there were significantly more viable cells in the osteogenic medium in comparison to the basal medium ($p= 0.0152$).

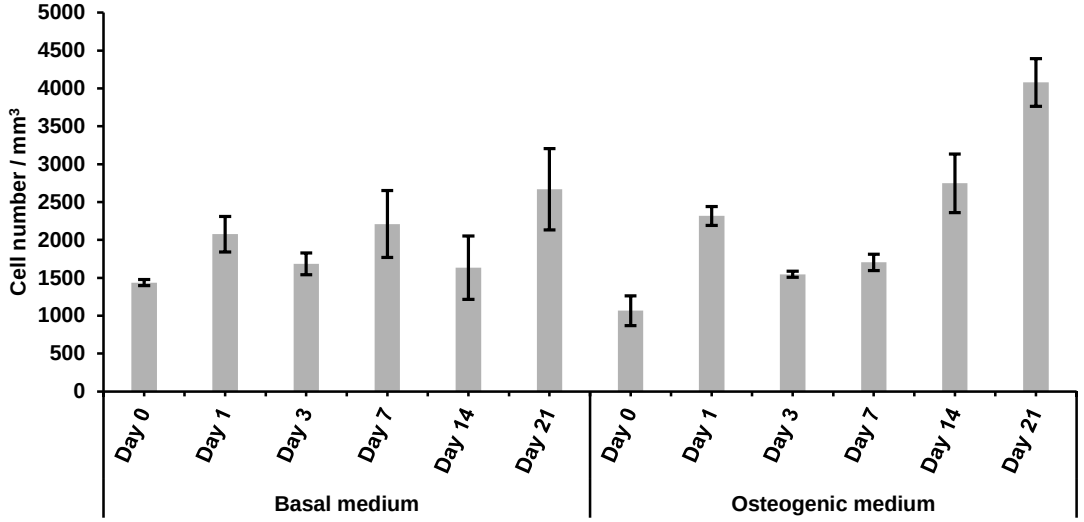

Figure 5-13: Viability of Y201 cells seeded on sintered A-W TIPS scaffolds. (n=3)

Figure 5-14 illustrates Y201 cells adhered on sintered A-W TIPS scaffolds with different porosites over the course of 7 days. In both basal and osteogenic medium, there were significant differences in viability depending the day (<0.0001) and the porosity (p= 0.0054 for basal medium and p= 0.014 for osteogenic medium). After using Bonferroni's multiple tests, it was highlighted that scaffolds with porosities 86 vol. % have better viability that the cells seeded in scaffolds with porosity 85 vol. % (p= 0.0070) in basal medium. In osteogenic medium, there was no difference in viability between the cells seeded in scaffolds with 85 and 86 vol. % (p= 0.7406). However, there were more cells in the scaffolds with porosity 85 vol. % than in the scaffolds with porosity 83 vol. % (p= 0.0157).

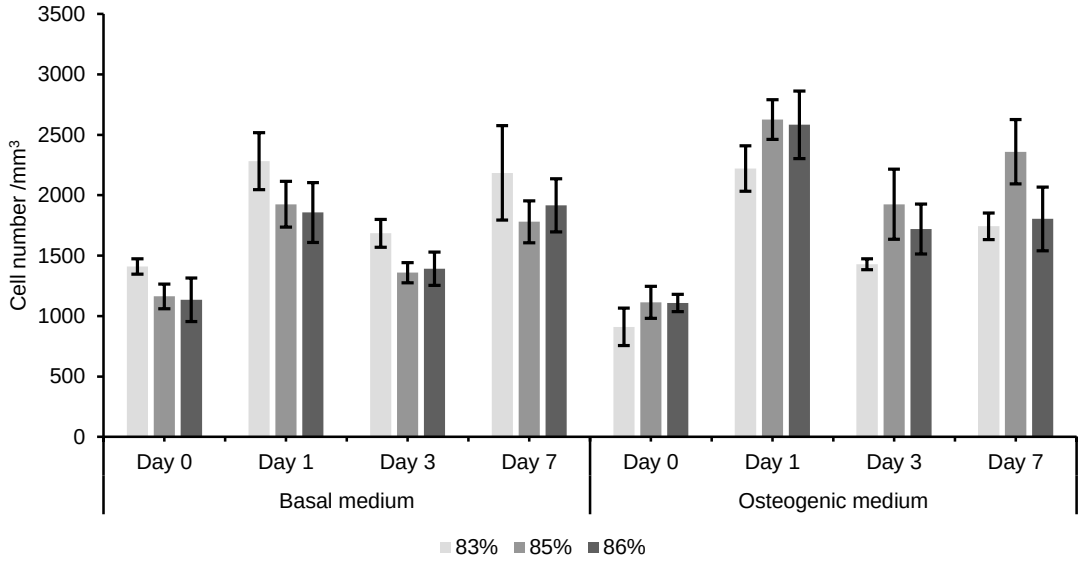

Figure 5-14: Viability of Y201 cells seeded on sintered A-W TIPS scaffolds with porosities 83, 85 and 86 vol. %. (n=3)

Cells cultured for 28 days in both basal and osteogenic medium were tested for alkaline phosphatase enzymatic activity (Chapter 2, §2.7.2) to assess whether the scaffold promote osteogenesis. Figure 5-15 demonstrates that the duration of cell culture ($p<0.0001$) and the different media ($p<0.0001$) had a significant influence on the cells. No significant differences were observed between the different time-points in the basal medium. The ALP activity increased significantly on day 14 and doubled from day 14 to day 21 ($p= 0.0028$). Between the two different media that were used for this experiment, the ALP activity was significantly increased in the osteogenic medium on Day 14 ($p= 0.0018$) and Day 21 ($p<0.0001$) in comparison to the corresponding time-points in the basal medium.

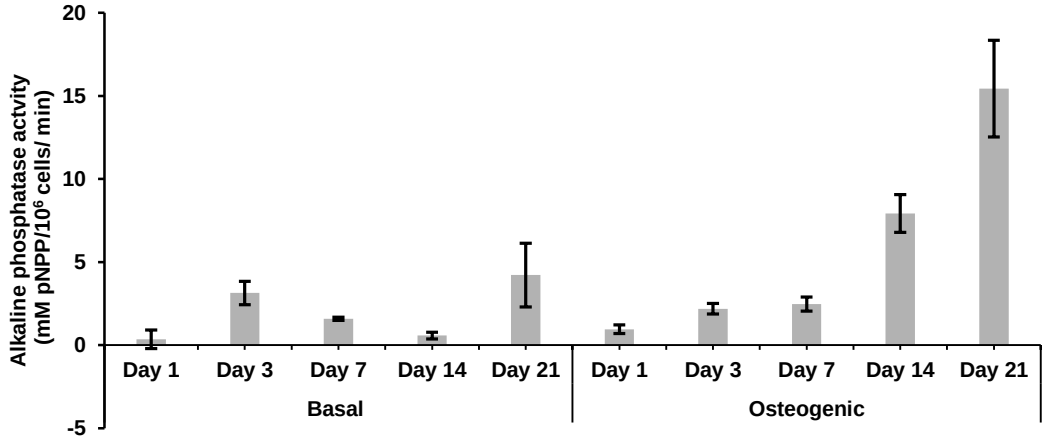

Figure 5-15: Alkaline phosphatase activity of cells cultured on sintered A-W TIPS scaffolds. (n=3)

To assess how the sintered A-W TIPS scaffolds affect the cell behaviour, RT-PCR (§2.8.3) was used to quantify the gene expression of the Y201 cells seeded on the scaffolds. Figure 5-16 illustrates the relative gene expression of specific osteogenic (T2Runx2, alkaline phosphatase, osteopontin, osteocalcin, collagen type I) and chondrogenic genes (aggrecan, SOX9, collagen type I) of interest after values were normalised to GADPH used as a ubiquitously expressed “housekeeping gene”.

There was no significant difference between the different media and the different time-points at T2Runx2, osteopontin, osteocalcin and collagen type I expressions (Figure 5-16; A, C, D and G correspondingly).No significant difference was observed in alkaline phosphatase expression (Figure 5-16; B) between the different time-points in the osteogenic medium. However, the alkaline phosphatase expression was significantly increased on day 7 in comparison to day 1 ($p= 0.0210$) and day 21 ($p= 0.0363$) in basal medium.

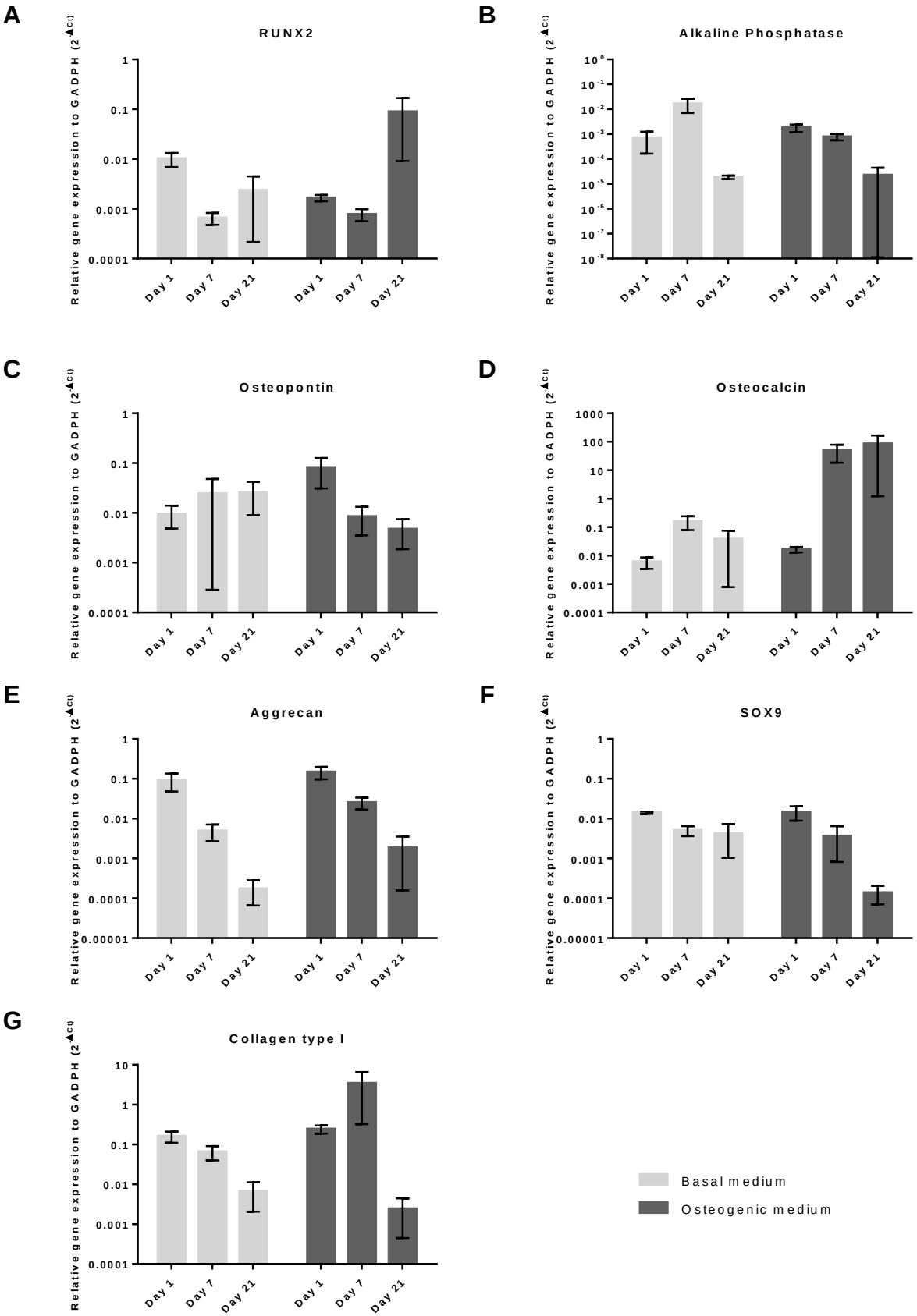

Figure 5-16: mRNA expression of T2Runx2, alkaline phosphatase, osteopontin, osteocalcin, aggrecan, SOX9 and collagen type I relative to GADPH of cells cultured on sintered A-W TIPS scaffolds. (n=5).

SEM imaging was used to study the behaviour of Y201 cells on the scaffolds whilst they were cultured in basal and osteogenic medium.

In Figure 5-17 the two scaffolds with cells culture in the two media respectively were imaged. Cells were observed on the top of the scaffold and in the cross-section. Many of the pores on the top of the scaffold and in the cross-section looked blocked from the cells. In addition, it is demonstrated that cells were attached on the walls of the scaffold traversing the pores. No cells were observed at the bottom side of the scaffold.

On day 3, in Figure 5-18 cells were densely populating the top of the scaffold. Some cells appeared at the bottom of the scaffold in the basal medium, but there was no image was available for the bottom side of the scaffold. The centre of the scaffold became more populated than day 1 for both media. In the cross-section of the basal medium is not clear how many cells there were, but they were tangled together; whilst they were anchored, straddling the inside of a large pore. In the cross-section of the scaffold in the osteogenic medium, cells seemed to surround the peripheries of pores.

On day 7 (Figure 5-19), the top and the cross-section of the scaffold had made a layer of cells on the top and in the centre of the scaffold especially in the basal medium. The cells on the top of the scaffold with basal medium have some ectopic surface features (red arrow) on top of the cells. It is not clear if something similar was occurring on the top of the scaffold in the osteogenic medium, because the sample was charging. Cells were observed at the bottom of the scaffold in the basal medium. There was no available photo for the bottom side of the scaffold in the osteogenic medium. In the cross-section from the scaffold in the basal medium, a red square indicated an area where a number of cells have joined together and they have extended to connect the two sides of the diameter of a large pore. The cells in the scaffold in the osteogenic medium that were imaged at higher magnification presented a precipitate on their membrane.

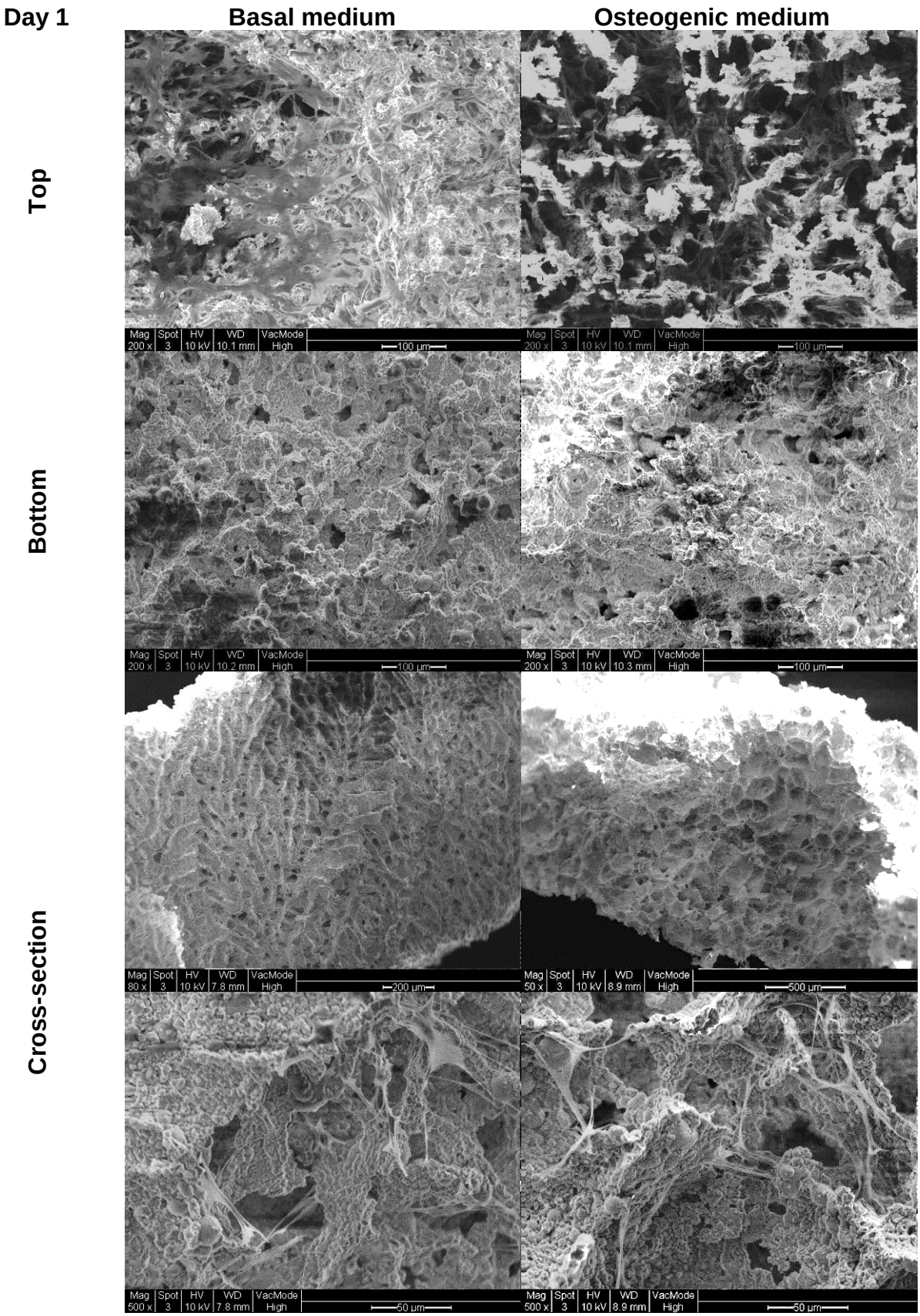

Figure 5-17: SEM micrographs from different sites of the sintered A-W TIPS scaffolds seeded with Y201 cells in basal and osteogenic medium correspondingly on day 1.

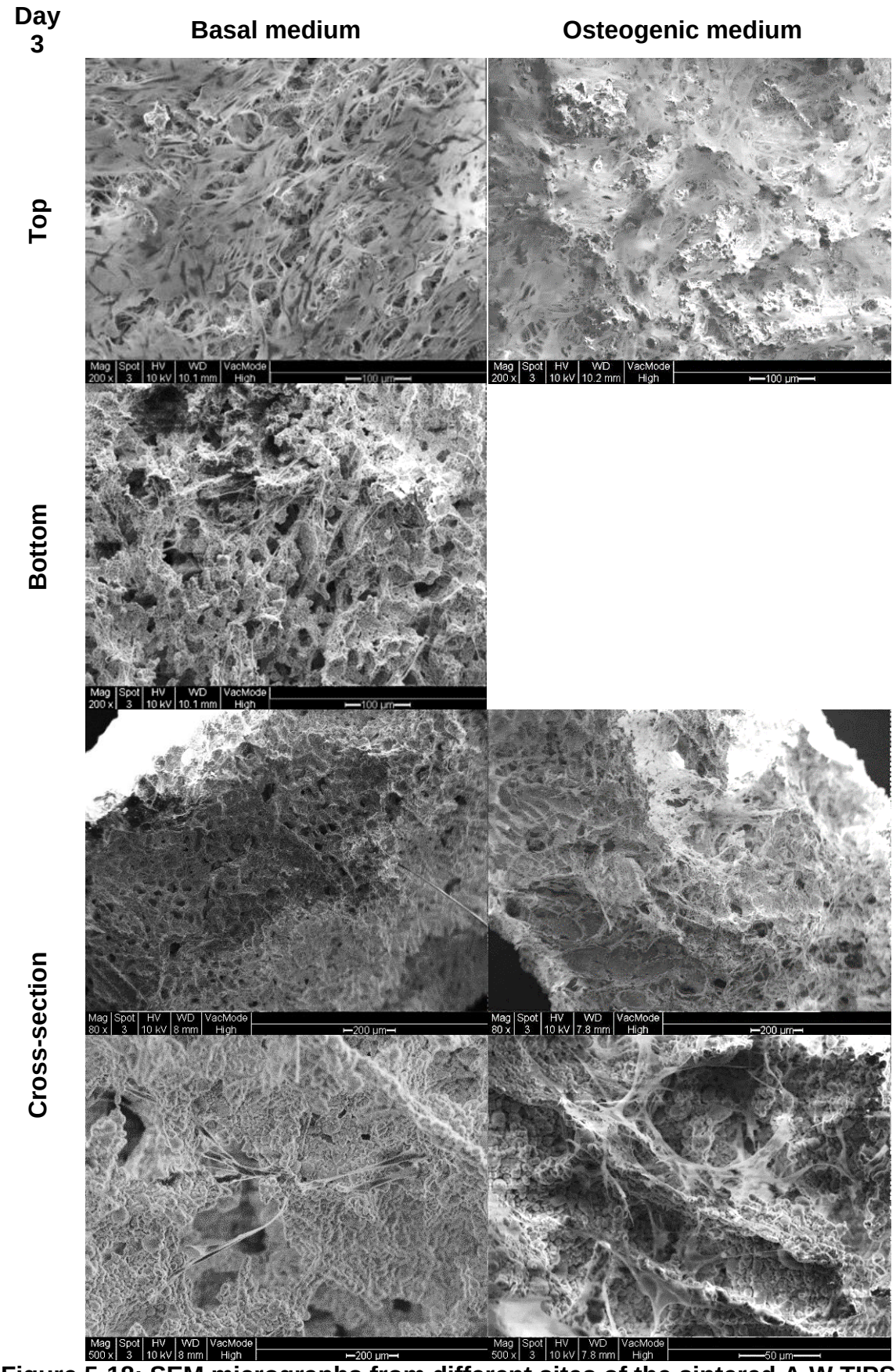

Figure 5-18: SEM micrographs from different sites of the sintered A-W TIPS scaffolds seeded with Y201 cells in basal and osteogenic medium correspondingly on day 3.

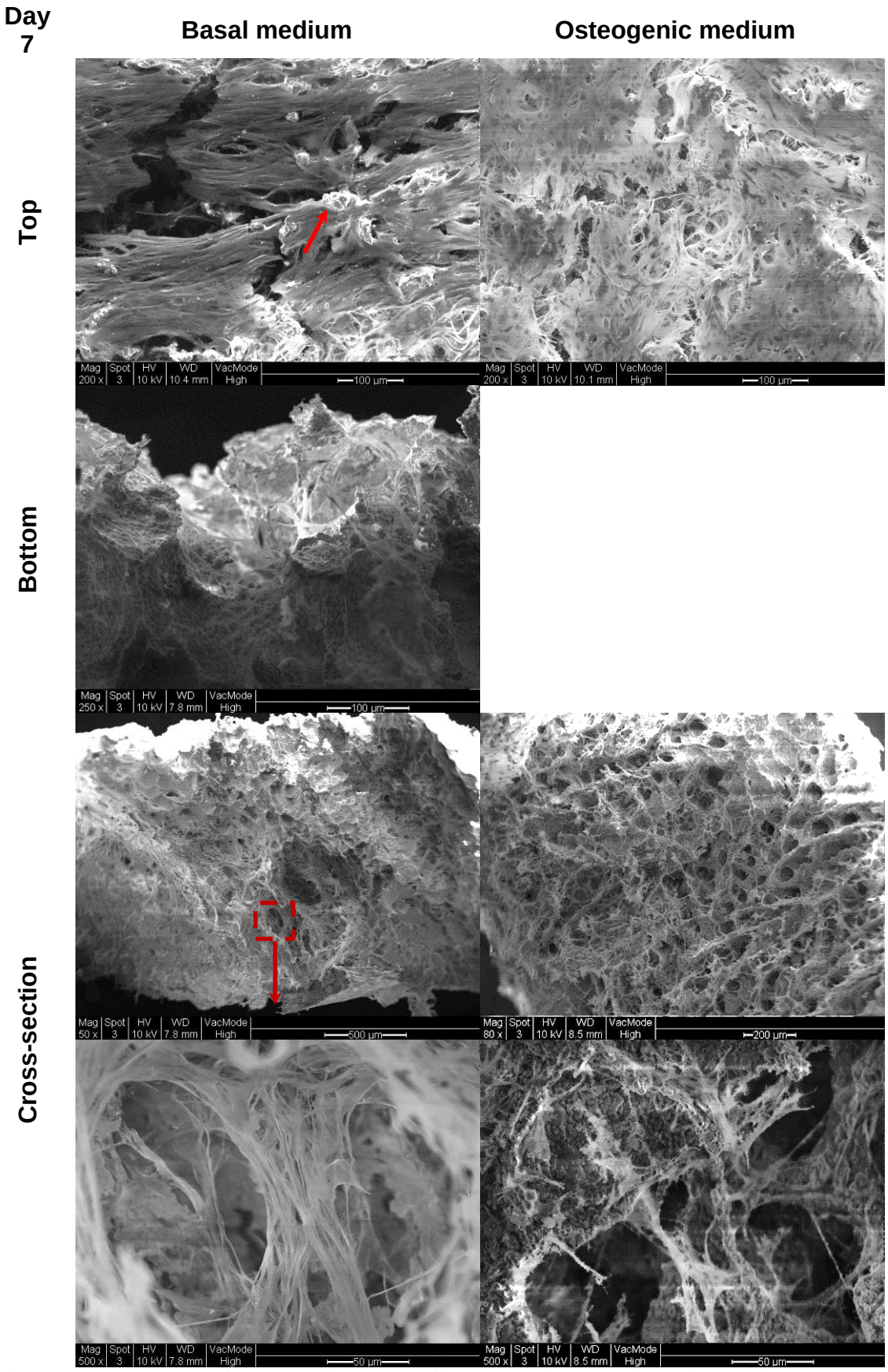

Figure 5-19: SEM micrographs from different sites of the sintered A-W TIPS scaffolds seeded with Y201 cells in basal and osteogenic medium correspondingly on day 7. Red square indicates the area imaged below. Red arrow indicates ectopic feature.

Figure 5-20 illustrates the cells in the scaffold after 14 days culture. In both scaffolds there was mineralisation. In the basal medium, a bone nodule was identified and in the osteogenic medium, amorphous apatite formation was observed deposited on the cells.

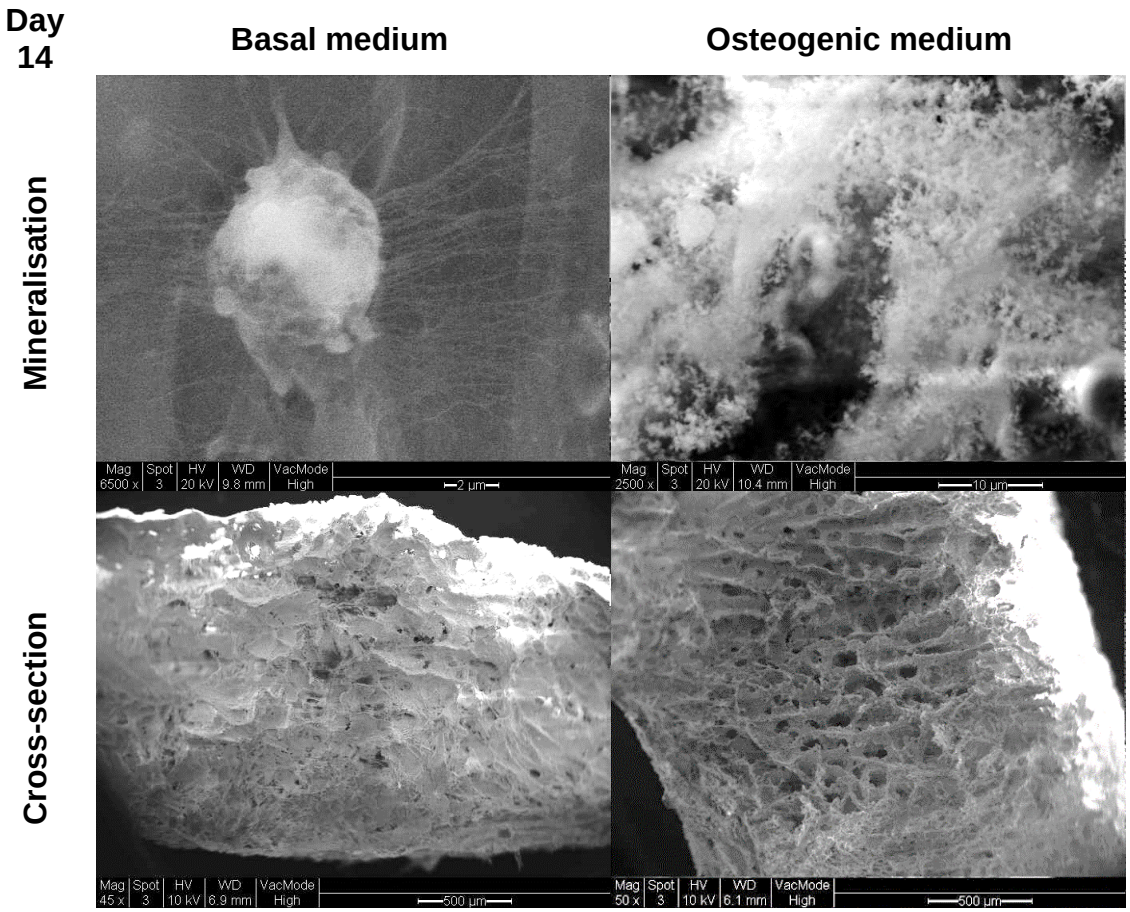

Figure 5-20: SEM micrographs from different sites of the sintered A-W TIPS scaffolds seeded with Y201 cells in basal and osteogenic medium correspondingly on day 14.

Figure 5-21 demonstrates scaffolds that were left in basal and osteogenic medium for 40 days. The sintered A-W TIPS scaffold in the osteogenic medium (Figure 5-21; B) seemed to have similar morphology with the scaffolds that were in SBF (Figure 5-5), but with higher calcium/phosphate precipitation. Also, the cells in the osteogenic medium (Figure 5-21; D) appeared to have mineral covering their membrane.

Scaffolds that were incubated in the basal medium had precipitated a different form of crystal with a more crystalline star-like morphology (Figure 5-21; A). Additionally, cells that were growing in basal medium (Figure 5-21; C) had precipitated not only the precipitate that were similar to the osteogenic medium; but also, a different type of crystal that was not identified (orange arrows). The scaffold in photo E had two

different types of crystals appearing; the precipitate, the crystal type that was observed on the scaffolds in osteogenic medium and the unknown crystal that was imaged in Figure 5-21; A.

During the 21 days of the experiment, on day 7 it was observed that the cells in the basal medium had developed a viscous transparent matrix and when the wells were checked under the microcroscope this matrix contained a large number of the unknown crystals that co-existed with the cells and had a similar morphology to the crystal in Figure 5-21 ; C.

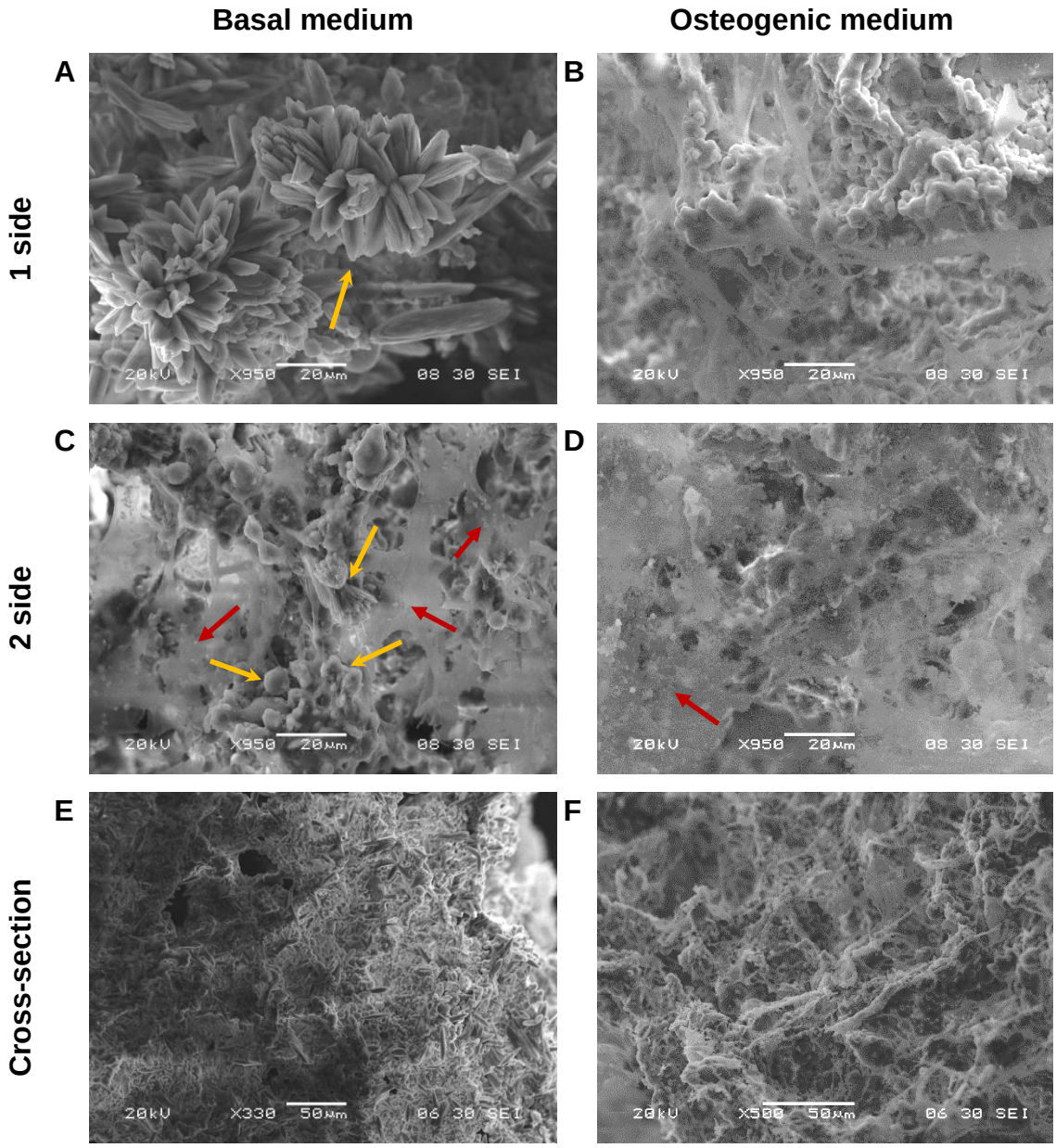

Figure 5-21: SEM micrographs from different sites of the sintered A-W TIPS scaffolds seeded with Y201 cells in basal and osteogenic medium correspondingly on day 40. Red arrows indicate precipitate produced by the cells and orange arrows show unknown mineral precipitated by the cells.

5.4 Summary

This chapter demonstrates that scaffolds prepared using combination of TIPS and sintering started to precipitate calcium phosphate crystals on day 7 that by day 21 had not covered the whole scaffold (Figure 5-6). In the collected SBF solution, magnesium remained relatively stable, calcium and silicon increased and phosphorus decreased (Figure 5-7). The scaffold lost 8.84±0.7 % of its mass during the biodegradation assessment (Figure 5-8). The Young's modulus decreased by day 21. It was significantly low with the Young's modulus after the scaffold was immersed in SBF for 4 hours; however, there was no significant difference in comparison to the mechanical properties that it had before it was soaked in SBF (Figure 5-9).

Different seeding techniques were been reported to have improved efficiency in highly porous interconnected scaffolds were investigated (Bai et al. 2015; Yamanaka et al. 2015). No significant difference observed in comparison to the widely used droplet seeding and consequently the droplet seeding was for the seeding method (Figure 5-10). Seeded cells infiltrated the scaffold and migrated in the construct (Figure 5-12;Figure 5-17- Figure 5-21). Cells were covering all the surface of the scaffold. There were significant changes in cell number and ALP activity in the osteogenic medium since day 14, but not in the basal medium (Figure 5-15).

Sintered TIPS A-W scaffolds have a gradient of porosities in their construct and when they were ground, there was a range of porosities. The cell number seemed to be influenced by the porosity of the scaffold Scaffolds with 86 vol. % porosity had higher cell numbers than scaffolds with 85 vol. % and in osteogenic medium, 83 vol. % had the lowest cell number in comparison to the other two porosities (Figure 5-14).

Gene expression data demonstrated that there was a degree of differentiation towards the chondrogenic lineage (Figure 5-16).

SEM imaging revealed that there was a degree of mineralisation on the cells in both groups with more frequent precipitation on the cells in the osteogenic medium (Figure 5-19, Figure 5-20, Figure 5-21).

Cells cultured on the sintered TIPS A-W scaffolds in the basal medium were observed on day 7 forming a viscous matrix that contained some unidentified

crystals. These characteristics was not observed in the scaffolds with osteogenic medium and requires further investigation (Figure 3-16).

Chapter 6 DISCUSSION

6.1 Summary of Results

Chapter 3 describes the development of fabrication techniques to manufacture two different groups of A-W scaffolds; microporous and interconnected macroporous. Sintering compacted powder, cast loose powder and cast slurries were investigated to fabricate microporous scaffolds. Crack formation excluded the pelleted powder technique, cast loose powder scaffolds exhibited lack of uniformity; whereas sintered cast slurry scaffolds had structural integrity and homogenous flat surfaces. Two different particle ranges; 20- 53 μm and 54-90: <20 μm (80: 20) were selected for further investigation. These two scaffolds had no significant difference in porosity, but the different particle ranges resulted in different surface topographies. Burning off polymeric templates during sintering resulted in interconnected highly porous A-W constructs, this technique was applied as the main principle behind the different techniques that were developed further. Compacted powder and loose powder were mixed with polymeric particles and fibres, loose powder was combined with FFF negative and FFF core moulds. TIPS was used to prepare ceramic-polymeric foams. Sintered compacted A-W powder with polymeric particles resulted in fractures. Sintered loose A-W powder with polymeric particles collapsed; whereas with fibres they had opened channels, this was used as predecessor for the scaffolds combined using the FFF negative templates. Sintered compacted powder with FFF negative mould alone collapsed and the FFF negative core method had fractures. Sintered TIPS A-W scaffolds displayed high porosity and interconnectivity. Results from Chapter 4 and Chapter 5 revealed that surface area affects the bioactivity and biodegradation of A-W scaffolds. Results showed, the higher the surface area, the lower the bioactivity and the higher the mass loss. Cells on the scaffolds with smaller surface area had more cell-cell interaction and demonstrated more osteogenic characteristics; whereas cells on scaffolds with larger surface area have more chondrogenic gene expression.

6.2 Novelty

This thesis presents two novel methods to fabricate ceramic structures with combined macro and microporosity: casting dry ceramic powders with a FFF core (§3.5.2.7), and sintering of green parts produced by TIPS (§3.7).

Whilst it has previously been reported that A-W resorbs *in vivo* and *in vitro* by osteoclasts (Teramoto et al. 2005; Yamada et al. 1994), the results in Chapter 4 and Chapter 5 demonstrate that increased surface area of A-W increases the physiochemical dissolution rate.

A-W scaffolds have been reported to promote osteogenesis *in vitro* and *in vivo* (Dyson et al. 2007; Lee et al. 2015; Zhang et al. 2009). This study has confirmed this and also shown that cells seeded on A-W ceramic with larger surface areas demonstrate higher expression of genes related to chondrogenesis (Figure 4-13).

6.3 Use of A-W powder as material for bone scaffold

A-W was characterised using XRD before sintering and after sintering according to heat treatment B (Figure 3-6). The XRD pattern revealed that both materials are composed of glass and crystal phases with the heat treated powder having more crystalline phases. The crystals that were precipitated in the sintered glass were hydroxyapatite (calcium phosphate hydroxide), wollastonite (calcium silicate), diopside (calcium magnesium silicate) and calcium magnesium hydrogen phosphate. These results have been replicated in the past from other groups (Cannillo et al., 2009, Kokubo et al., 1982b, Kokubo et al., 1985), but contradict the results that Chang et al. demonstrated (Chang et al., 2000). According to Chang et al., (2000), sintering the glass with at 5°C/min inhibits the precipitation of apatite and promotes the precipitation of whitlockite, which is also composed of calcium phosphate, due to the fast sintering rate.

The properties of the various crystalline phases that were formed from sintering were diopside, wollastonite, hydroxyapatite, calcium phosphate hydroxide and calcium magnesium hydrogen phosphate are described in the literature survey.

Diopside and wollastonite are silicate biomaterials that stimulate osteoblastic growth and differentiation due to Si ion release. In addition, they have exhibit good bioactivity by promoting *in vitro* osteogenesis and *in vivo* bone formation. Diopside has a slower degradation rate rather than wollastonite (Wu et al. 2010; Wu & Chang 2007).

Hydroxyapatite and calcium magnesium hydrogen phosphate are calcium phosphates. Calcium phosphates slowly degradable/ non-degradable- depending the crystallinity. Their main characteristic is their osteoinductivity (S. V Dorozhkin 2010). They also promote cell adhesion and osteogenesis (Samavedi et al. 2013).

Taken together the results presented in this thesis suggest that A-W is a very good bone scaffold material, with loading carrying capacity and a slow resorption rate.

6.4 Fabrication techniques for microporous scaffolds

Scaffolds prepared by compacting powder had homogenous and microporous structure (Figure 3-10; Figure 3-14). Also, the two different particle ranges, which were used for their fabrication, significantly influenced scaffold porosity and shrinkage (Figure 3-11). The pellets exhibited fractures parallel to the direction to the press. A-W has high fracture toughness (Kokubo et al. 1987) and it has been reported that ceramics with high fracture toughness are not affected by thermal shock (You et al. 2005) ; however, different heat treatments were investigated to increase the liquid phase of the ceramic with slower sintering rate to avoid thermal shock during sintering. No improvement was observed. Due to the orientation of the fracture, it was hypothesised that the high pressure could have caused the internal crack and different pressure were assessed with no change in the final result (Figure 3-16). The effect of non-homogenous powder distribution that would result in density variation in the pellet was hypothesised (Egeland et al. 2010). The theory that the crack was an effect of “end capping” (Egeland et al. 2010; Johnson & German 1996; Balakrishna et al. 1996) is supported by the similarities in the morphology of the identified cracks.

Polymeric particles (PA) as a more ductile material were mixed with the A-W powder in an effort to increase the uniformity of the powder. The large crack in the middle was eliminated; however, there was formation of new microcracks on the whole surface of the pellet and loss of structure integrity (Figure 3-19- Figure 3-20).

Microcracks also appeared in the cast loose powder scaffolds and new hypotheses were raised. One suggestion was that the powder could be affected by humidity that can reinforce capillary forces, which depend on the diameter of the pores between the particles and the tension from the hydrogen bonding of water. After heating the A-W powder in the oven, the problem was not solved. Similarly to the pellets different heat treatment were used, which influenced the porosity (Figure 3-41) and the

shrinkage of the scaffold (Figure 3-40), but the microstructure did not improve (Figure 3-39). Particle aggregates could be caused by mechanical interlocking due to particle surface roughness or irregular shape because of the irregular particle shape of A-W. PA polymeric particles were introduced in the powder to improve the homogeneity of the mix. These samples lost their mechanical properties similarly to the compacted powder scaffolds (§3.5.2.4).

Ceramic powders tend to agglomerate due to particle roughness or Van der Walls forces when particle size is <10 μm. Deionised water was used as a binder to overcome this problems and scaffolds were formed using the cast slurries (§3.6) (Tsetsekou et al. 2001). No crack formation after sintering was observed using this method, but the particle 54- 90 μm had different particle average size in comparison to the previous batch and different heat treatments, particle ranges mixtures and packing techniques were assessed to optimise the scaffold (Figure 3-48). A-W slurries were packed using sonication to improve the particle distribution, but bubbles were formed on the top of the scaffold that were undesirable (Figure 3-50). Scaffolds prepared using heat treatment B with ranges 20- 53 μm and 54- 90 μm : <20 μm (80: 20) had no significant difference in porosity (Figure 3-51), but different surface topography (Figure 4-2) that fulfilled the aim that was set for the fabrication of microporous scaffolds.

6.5 Fabrication techniques for interconnected macroporous scaffolds

The fabrication of porous interconnected scaffolds with good mechanical properties was the next aim of this study.

Compacted powders were mixed with polymeric particles (PE) and sintered to produce macroporous scaffolds (§3.4.1.3). The porosity was enhanced (Figure 3-25), but the interconnectivity was very poor (Figure 3-23). Additionally, many microcracks appeared at the peripheries if the pores. In theory, as the polymeric material burns out, gases are produced that open pores and promote interconnection between the pores (Chevalier et al., 2008). Vitale-Brovarone et al., (2008) followed the same methodology using the same polymer previously with success. It was reported that their scaffold was crack-free, highly porous and interconnected. The main difference in the protocols that were used a glass belonging to the SiO_2-$CaOK_2O$ (SCK) system. This glass had lower sintering temperature than A-W. PE was burnt at very low temperature and it was hypothesised that the A-W particles could rearrange, closing

the existed pores and cause microcracks. Therefore, an extra step was added before the usual heat treatment, in order for the polymer to melt, become viscous and form channels (Collin et al., 2005). This method had as a result the formation of scaffolds microfractures and heterogeneity in the pore distribution/size.

The elimination of fracture formation on the compacted powder was unsuccessful and the same strategies were employed to the cast loose powder scaffolds. Mixing the A/W with PE particle caused the loss of structural integrity of the scaffold after sintering.

Additionally, loose powder scaffold with PE particles collapsed (Figure 3-43), possibly, because the A-W did not have enough common surface area in order to sinter, so during their rearrangement, the structure could not be supported. The pellets with PE have many microfractures (Figure 3-23), which are also caused due to the particle rearrangement after the burning out of the polymer. PE particles were excluded for the options to assess whether their low melting temperature had influenced the microcracks in the compacted and the collapse of the cast loose scaffold. The end product of this procedure was a crack free scaffold with a large pore in the middle (Figure 3-44). This polymeric filament was used as predecessor for the next strategy. FFF moulds with internal grid were used to provide interconnected channels to the loose powder that was cast in. The scaffolds that were prepared using this technique collapsed (Figure 3-46), because the PLA burnt off at very low temperature in comparison to the sintering temperature of A-W. Consequently, the FFF mould was replaced with the previously used platinum tube, and the grid was used as core in the centre of the tube. These scaffolds maintained their structural integrity because the platinum tube kept the powder in place, but microcracks appeared horizontally along the FFF axis pores. Interestingly, these microcracks did not appear when there was one or two filaments vertical to the axis of the scaffold (Figure 3-44).

Two hypothesis arose from the formation of these microcracks through the burning off the particle and FFF polymer. The one is that possibly as the polymer burnt off, there was gas release that moved some particles creating gaps. Another hypothesis is that the particles and filaments support the ceramic particles, so as the polymer melts, the particles move as they have not started sintering at that temperature. In both cases, the small gaps between the A-W did not allow the ‘rearranged’ particles

to form necks with their adjacent particles. During the shrinkage phase these gaps were exacerbated into cracks as the A-W contracted. A similar hypothesis was suggested when microcracks where formed during sintering impregnated foams in hydroxyapatite without explaining though how the particles moved (Zhao et al. 2006). This group eliminated the microcracks using hot isostatic pressure.

As mentioned earlier other groups had fabricated scaffolds by sintering ceramic powders mixed with polymeric particles. This implements that maybe by using different ceramics with lower sintering temperatures or polymers with higher burning off temperature the methods described above could provide highly porous interconnected scaffolds.

Since it was established that the methods above were not suitable for the fabrication of macroporous interconnected scaffolds using A-W ceramics, a new method was developed. A highly porous interconnected polymer-ceramic composite was fabricated using TIPS and then sintered to remove the polymer and strengthen the ceramic (§3.7). Scaffolds prepared using this technique exhibit no cracks, gradient porosity that was controllable by modifying the A-W content in the system. This technique has not been recorded before, but techniques that included freeze drying, such as freeze casting (Li et al. 2012; Mallick et al. 2012; Huang et al. 2011; Deville 2010) and reverse freeze casting (Yook et al. 2012) have been flourishing the last years, because they provide high interconnectivity.

6.6 Surface topography of A-W sintered cast slurries

Optical profilometry was used to obtain additional information about the sample topography and those samples with the larger particle range had higher average peak to valley height. Profilometry was used only as an extra tool to acquire additional information for the topography and not as a roughness measurement tool. These samples were porous and from Figure 4-2, it can be concluded that roughness measurements would not be valid since the pores resulted in gaps in the measurement.

Consequently, scaffolds with a larger particle range had larger surface area, since they had larger pores and they were deeper than the pores on the scaffold with formed with 20- 53 μm particles.

Thus, these scaffolds differed in topography, pore size and surface area, but they had the same chemical profile since they were fabricated from the same material.

6.7 Influence of topography on the biodegradation and bioactivity of A-W scaffolds

Considering the information all together from Chapter 5 and 6; it can be concluded that the higher ion release from the scaffolds with the larger surface area in comparison to the other scaffold (Figure 4-5; Figure 5-7). This possibly caused higher release of magnesium that led to higher release of silicon. Magnesium has been demonstrated to promote silicon release since it disrupts the silica network (Dietrich et al. 2009; Hoppe et al. 2011). Silicon is significant for calcium and phosphate precipitation (Kokubo et al. 1993). Consequently the apatite formation on this group of scaffolds was delayed and therefore there was more calcium release rather than precipitation.

In addition, during the bioactivity and dissolution assay, there were contradictory results in respect of the mass change of A-W when is immersed in SBF. It was observed that scaffolds with the smallest surface area gained weight and scaffolds with larger surface area lost weight during the experiment. In fact, between the microporous sintered cast slurry with particle range 54- 90 μm: <20 μm (80: 20) and the A-W TIPS scaffolds with particle range 20- 53 μmm (Figure 4-6), the TIPS scaffold had higher degradation rate (Figure 5-8). This phenomenon is linked to the lower precipitation of Ca/P on the matrix (Figure 5-7).

The resorption of the scaffold with the larger particle range influenced its mechanical properties. The Young's modulus was measured 21 days after its immersion in SBF and its mechanical properties decreased significantly. However, it was still comparable to the mechanical properties of the cancellous bone (Figure 4-7)

It has been reported that dense A-W scaffolds presented Ca/P crystals on their surface by day 3 and had improved mechanical properties after being soaked for a month in SBF (Kokubo 1990; Kokubo et al. 1987). This result supports the theory that the surface area can affect the modification and dissolution of A-W glass ceramic. The increase in nucleation sites results in less evident deposition of Ca/P that leads to a more rapid dissolution. The lower the surface area, the higher the Ca/P precipitation and the better the mechanical properties.

It was observed that on day 7, some spherulite-structure crystals appeared on the A-W sintered particles (Figure 5-5).

The sintered A-W TIPS scaffolds had a fast rate of resorption (Figure 5-8) and the mass decreased ten times faster in comparison to the loose powder scaffolds with the larger particle range (Figure 5-5). This could be explained due to the increased surface area and interconnectivity. The high resorption rate decreased significantly the mechanical properties of the scaffold (Figure 5-9).

The resorption rate of a bone scaffold need to be similar to the *de novo* bone formation that depending the defect, it can last from 9 months to 2 years. Longer dissolution study needs to be done for the sintered A-W TIPS with A-W content 25%, 100% and 175% w/v.

6.8 hMSC behaviour on sintered cast slurry scaffolds

After seeding Y201 h –TERT cells on the different substrates it was observed that A-W promoted cell attachment and cells had lower affinity for glass slides (Figure 4-8). Between the two A-W scaffolds, the scaffold with the smaller particle range had enhanced cell adherence because there was smaller surface area exposed and in this study the exhibit flatter topography. Similar results have been reported by Rea, Best, & Bonfield, 2004, where it was observed that there was increased cell response from surface finish and glass-ceramic content linked to increased glass-ceramic A-W surface area exposure. In their study, the flatter samples have larger surface area because they are polished and unpolished samples. Combining the results from both studies, it is demonstrated that A-W promotes cells attachment and cells prefer to adhere on surfaces that are flatter.

During the viability assay it was observed that after the seeding day, the cell number on the A-W scaffolds reduced significantly (Figure 4-10). A-W has been shown to promote cell proliferation (Zhang et al. 2009), but significant magnesium ion release in the cellular environment can cause cell death (Niederlaender et al. 2014). The magnesium release after the first 24 hours became stable on the scaffolds with smaller particle range and almost halved on the scaffolds with the larger particle range and thereafter cells increased in cell number by 55± 21% and 50±16% on each group of scaffolds respectively. It is noteworthy to mention that the prolife ration of cells seeded on the scaffold with the larger particle range was doubled in comparison

to the cell seeded on the scaffold with the smaller particle range during days 3 and 7, where the Si release was decreased by two thirds.

An additional factor that could have affected the cell adhesion on the scaffolds with the larger particle range is the concave structure of most of the particles. On SEM images it was observed that cells seeded on the larger particle range scaffolds had extended filopodia to neighbouring particles (Figure 4-9). It has been proposed that the concave structure causes weaker cell adhesion and the cell formed filopodia as a traction mechanism (Vogel & Sheetz 2006). Possibly this is the reason that most cells on these scaffolds home in the pores; adhering on the inside of pore where the curvature is more convex and during the seeding they favoured the scaffolds prepared using 20- 53 μm.

Cells seeded on glass slides and small particle scaffolds were more spread and flattened. The cytoskeleton was protruding on the cells that were seeded on the glass. Other studies have demonstrated that spread cells that had cytoskeletal tension, also had increased commitment to the osteogenic lineage (McBeath et al. 2004). In accordance to this statement the cells on the glass slides had higher ALP activity in the basal and osteogenic medium; whereas the cells on the scaffolds with small particle range had increased ALP activity mainly in the osteogenic medium (Figure 4-11).

The early osteogenesis on the glass slides and the scaffolds with small particle range was supported by the changes in osteogenic gene expression observed by RT-PCR analysis (Figure 4-12).

In this study the cells on the A-W scaffolds with small particle range increased ALP and OCN expression and higher mineral deposition in comparison to the other group of scaffolds. This could have been caused by the calcium and silicon releases which has been demonstrated to promote osteogenesis by increasing ALP and OCN gene expression in previous study (Matsuoka et al. 1999).

Cells on scaffolds with larger particle range did not have upregulated ALP and OCN regardless of the calcium and silicon release from their substrate. On the contrary, they expressed high osteopontin on day 1, and showed enhanced proliferation that was also indicated in the Alamar blue assay. In addition, these cells had increased SOX9 in relation to the other two groups and increased aggrecan expression on day

21 in the basal medium. This could suggest that possibly the cells on the large particle scaffold confine themselves in the pores maintaining cell-cell interactions that allow them to keep their multipotency during the first days (Zhang & Kilian 2013) and then express some cartilage related genes that are co-expressed in endochondral ossification. This hypothesis is supported by the histological images (Figure 4-14) where there was observed higher mucosbstances concentration on the scaffolds with larger surface area and more mineralisation on the scaffolds with smaller surface area (Figure 4-14 and Figure 4-15). Only when the cells seeded on the large particle range were cultivated in osteogenic medium was there upregulation of osteogenic genes and higher mineral formation during the histological staining.

6.9 Seeding techniques on 3D highly porous scaffolds

Assessing between the droplet seeding, seeding using filter paper under the scaffold and self-seeding using capillary forces different seeding techniques, no differences in adhered cell population was observed (Figure 5-10). The authors of the article in which the seeding technique using the filter paper has suggested, compared different seeding techniques including the droplet seeding that was assessed in this study (Bai et al. 2015). The main reason that in their study the filter paper promoted better cell seeding was due to the hydrophobic nature of the PLGA scaffolds that were used, where A-W scaffolds are hydrophilic. The authors suggesting the self-seeding did not compare other seeding methods, but they compared wet versus dry scaffold and different density on the surface that cells were seeded, because their scaffolds also had gradient porosity as they were fabricated using freeze-casting (Yamanaka et al. 2015). In this study, these two parameters were not investigated , but the scaffolds used were dry.

6.10 hMSC behaviour on sintered A-W TIPS scaffolds

Cell infiltration was observed throughout the experiment and cells were preferably adhering in the peripheries of the pores of scaffold (Figure 5-12), which coincides with the observations made at the sintered cast slurries with larger surface area. Cell number in the sintered A-W TIPS scaffold remained stable with no significant differences in basal medium (Figure 5-13), which is comparable to the results presented by (Zhang et al. 2009). The only differences in cells viability were observed on days 14 and 21 in osteogenic medium that resulted in increased results on the same days on ALP activity (Figure 5-15). Cell death was not observed and possibly it is related to the slow ion release. Interesting results appeared at the gene

expression data. The ALP expression was increased only in the basal medium on day 7, similarly to the sintered cast slurries with larger surface area and the SOX9 was decreased on day 21 in the osteogenic medium (Figure 5-16), which coincided with the data from sintered cast slurries with smaller surface area (Figure 4-13). In §6.8, it was mentioned that the larger surface area promotes a degree of differentiation towards the chondrogenic lineage that agrees with the finding from the highly porous scaffold in basal medium; whereas the smaller surface area has similar characteristics with the sintered A-W TIPS scaffold in osteogenic medium that could be due to the high number of cells and the increased cell-cell interaction

Cell mineralisation was observed at the SEM photos in both media (Figure 5-17), which means that more time-points need to be investigated and histological staining needs to be done to link all the data together.

The presence of unknown crystals precipitated from the cells (Figure 5-21) and on the scaffolds in the basal have raised more questions and they need further analysis.

A similar crystal to the one that was found precipitated on the cells and on the well plates was identified in the literature and is portrayed in Figure 6-1.

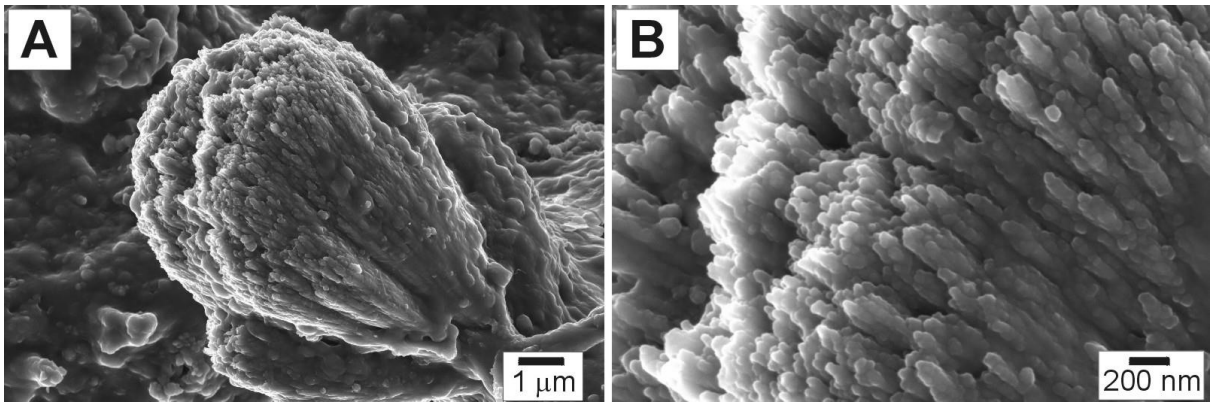

Figure 6-1: Calcium carbonate crystal adapted from Sánchez-navas et al. 2013**.**

6.11 Conclusions

6.11.1 *Scaffold fabrication techniques*

- New fabrication techniques were developed for the fabrication of high interconnected macroporous scaffolds that could be used with other ceramic materials for better results.

- Novel controllable fabrication technique for interconnected scaffolds with gradient porosity using TIPS and sintering. Porosity can be modified depending on the needs of the tissue

6.11.2 *A-W bioactivity and degradation*

- Increased surface area of A-W results in higher Ca/P faster and increase in scaffold mass
- Decreased surface area of A-W results in slower Ca/P due to the more nucleation points that allows scaffold degradation

6.11.3 *Surface area effect on hMSC osteochondral differentiation*

- Increased scaffold surface area limits cell –cell interaction, promotes migration and a degree of chondrogenic differentiation.
- Decreased surface area allow cell-cell interaction that enhanced proliferation and osteogenic differentiation.

REFERENCES

Albrektsson, T. & Johansson, C., 2001. Osteoinduction, osteoconduction and osseointegration. *European spine journal*, 10(Suppl 2), pp.S96–101.

Alves, N.M. et al., 2010. Designing biomaterials based on biomineralization of bone. *Journal of Materials Chemistry*, 20(15), p.2911.

Anderson, H.C., 2003. Matrix vesicles and calcification. *Current rheumatology reports*, 5(3), pp.222–226.

Anon, 1991. Controlling microporosity in bioceramic scaffolds for tissue engineering approaches in bone. , (Kokubo), p.280575.

Bai, H. et al., 2015. Biomimetic gradient scaffold from ice-templating for self-seeding of cells with capillary effect. *Acta Biomaterialia*, 20, pp.113–119.

Baino, F., Verné, E. & Vitale-Brovarone, C., 2009. Three-dimensional high-strength glass-ceramic scaffolds containing fluoroapatite for load-bearing bone portions replacement. *Materials Science and Engineering C*, 29(6), pp.2055–2062.

Balakrishna, P., Chakraborthy, K.P. & Singh, A., 1996. End-capping and other defects in pressed ceramic compacts. *Indian Journal of Engineering and Materials Sciences*, 3(5), pp.196–200.

Barry, F.P. & Murphy, J.M., 2004. Mesenchymal stem cells: clinical applications and biological characterization. *The international journal of biochemistry & cell biology*, 36(4), pp.568–584.

Bayliss, L., Mahoney, D.J. & Monk, P., 2012. Normal bone physiology, remodelling and its hormonal regulation. *Surgery*, 30(2), pp.47–53.

Benito, M.J. et al., 2005. Synovial tissue inflammation in early and late osteoarthritis. *Annals of the rheumatic diseases*, 64(9), pp.1263–7.

Billiet, T. et al., 2012. A review of trends and limitations in hydrogel-rapid prototyping for tissue engineering. *Biomaterials*, 33(26), pp.6020–6041.

Bonnet, C.S. & Walsh, D. a, 2005. Osteoarthritis, angiogenesis and inflammation. *Rheumatology (Oxford, England)*, 44(1), pp.7–16.

Brovarone, C.V., Verné, E. & Appendino, P., 2006. Macroporous bioactive glass-ceramic scaffolds for tissue engineering. *Journal of Materials Science: Materials in Medicine*, 17(11), pp.1069–1078.

Carrodeguas, R.G. & De Aza, S., 2011. α-Tricalcium phosphate: Synthesis, properties and biomedical applications. *Acta Biomaterialia*, 7(10), pp.3536–3546.

La Carrubba, V. et al., 2008. PLLA/PLA scaffolds prepared via Thermally Induced Phase Separation (TIPS): tuning of properties and biodegradability. *International Journal of Material Forming*, 1(S1), pp.619–622.

Castellani, C. et al., 2011. Bone-implant interface strength and osseointegration: Biodegradable magnesium alloy versus standard titanium control. *Acta biomaterialia*, 7(1), pp.432–40.

Chevalier, J. & Gremillard, L., 2009. Ceramics for medical applications: A picture for the next 20 years. *Journal of the European Ceramic Society*, 29(7), pp.1245–1255.

Clarke, B., 2008. Normal bone anatomy and physiology. *Clinical journal of the American Society of Nephrology : CJASN*, 3 Suppl 3, pp.131–139.

Collin, I. et al., 2005. Improvement of macroporous biphasic phosphocalcic ceramics for the filling of bone defects. *Itbm-Rbm*, 26(4), pp.247–248.

Deville, S., 2010. Freeze-casting of porous biomaterials: Structure, properties and opportunities. *Materials*, 3(3), pp.1913–1927.

Deville, S., 2008. Freeze-casting of porous ceramics: A review of current achievements and issues. *Advanced Engineering Materials*, 10(3), pp.155–169.

Dietrich, E. et al., 2009. In vitro bioactivity of melt-derived glass 46S6 doped with magnesium. *Journal of Biomedical Materials Research - Part A*, 88(4), pp.1087–1096.

Dimitriou, R. et al., 2011. Bone regeneration: current concepts and future directions. *BMC medicine*, 9, p.66.

Dinopoulos, H., Dimitriou, R. & Giannoudis, P. V, 2012. Bone graft substitutes: What are the options? *The surgeon : journal of the Royal Colleges of Surgeons of Edinburgh and Ireland*, 10(4), pp.230–9.

Dorozhkin, S. V, 2010. Bioceramics of calcium orthophosphates. *Biomaterials*, 31(7), pp.1465–85.

Dorozhkin, S. V., 2010. Calcium Orthophosphates as Bioceramics: State of the Art. *Journal of Functional Biomaterials*, 1(1), pp.22–107.

Dyson, J. a et al., 2007. Development of custom-built bone scaffolds using mesenchymal stem cells and apatite-wollastonite glass-ceramics. *Tissue engineering*, 13(12), pp.2891–2901.

Egeland, G.W. et al., 2010. Dry bag isostatic pressing for improved green strength of surrogate nuclear fuel pellets. *Journal of Nuclear Materials*, 406(2), pp.205–211.

Ferreira, A.M. et al., 2012. Collagen for bone tissue regeneration. *Acta biomaterialia*, 8(9), pp.3191–200.

Finkemeier, C.G., 2002. Bone-grafting and bone-graft substitutes. *The Journal of bone and joint surgery. American volume*, 84-A(3), pp.454–64.

Geiger, F. et al., 2005. Vascular endothelial growth factor gene-activated matrix (VEGF165-GAM) enhances osteogenesis and angiogenesis in large segmental bone defects. *Journal of bone and mineral research : the official journal of the American Society for Bone and Mineral Research*, 20(11), pp.2028–35.

Gerhardt, L.-C. & Boccaccini, A.R., 2010. Bioactive Glass and Glass-Ceramic Scaffolds for Bone Tissue Engineering. *Materials*, 3(7), pp.3867–3910.

Guarino, V. & Ambrosio, L., 2010. Temperature-driven processing techniques for manufacturing fully interconnected porous scaffolds in bone tissue engineering. *Proceedings of the Institution of Mechanical Engineers, Part H: Journal of Engineering in Medicine*, 224(12), pp.1389–1400.

Guilak, F., 2011. Biomechanical factors in osteoarthritis. *Best practice & research. Clinical rheumatology*, 25(6), pp.815–23.

Guilak, F. et al., 2009. Control of Stem Cell Fate by Physical Interactions with the Extracellular Matrix. *Cell Stem Cell*, 5(1), pp.17–26.

Hamid, R. et al., 2004. Comparison of alamar blue and MTT assays for high through-put screening. *Toxicology in Vitro*, 18(5), pp.703–710.

Hannink, G. & Arts, J.J.C., 2011. Bioresorbability, porosity and mechanical strength of bone substitutes: What is optimal for bone regeneration? *Injury*, 42(SUPPL.

2), pp.S22–S25.

Hench, L.L., 2009. Genetic design of bioactive glass. *Journal of the European Ceramic Society*, 29(7), pp.1257–1265.

Ho, M.H. et al., 2004. Preparation of porous scaffolds by using freeze-extraction and freeze-gelation methods. *Biomaterials*, 25(1), pp.129–138.

Hoppe, A., Güldal, N.S. & Boccaccini, A.R., 2011. A review of the biological response to ionic dissolution products from bioactive glasses and glass-ceramics. *Biomaterials*, 32(11), pp.2757–74.

Hua, F.J. et al., 2002. Macroporous poly(L-lactide) scaffold 1. Preparation of a macroporous scaffold by liquid-liquid phase separation of a PLLA-dioxane-water system. *Journal of Biomedical Materials Research*, 63(2), pp.161–167.

Huang, T.S. et al., 2011. Freeze extrusion fabrication of 13-93 bioactive glass scaffolds for repair and regeneration of load-bearing bones. *Ceramic Transactions*, 228, pp.45–55.

Hunter, D.J., 2011. Osteoarthritis. *Best practice & research. Clinical rheumatology*, 25(6), pp.801–14.

Hutmacher, D.W., 2000. Scaffolds in tissue engineering bone and cartilage. *Biomaterials*, 21(24), pp.2529–2543.

James, S. et al., 2015. Multiparameter Analysis of Human Bone Marrow Stromal Cells Identifies Distinct Immunomodulatory and Differentiation-Competent Subtypes. *Stem Cell Reports*, 4(6), pp.1004–1015.

Jang, J.-H., Castano, O. & Kim, H.-W., 2009. Electrospun materials as potential platforms for bone tissue engineering. *Advanced drug delivery reviews*, 61(12), pp.1065–83.

Janning, C. et al., 2010. Magnesium hydroxide temporarily enhancing osteoblast activity and decreasing the osteoclast number in peri-implant bone remodelling. *Acta biomaterialia*, 6(5), pp.1861–8.

Johnson, J.L. & German, R.M., 1996. Solid-state contributions to densification during liquid-phase sintering. *Metallurgical and Materials Transactions B*, 27(6), pp.901–909.

Kang, S.-J.L., 2005. Sintering Processes. In *Sintering- Densification, Grain Growth, and Microstructure*. Elsevier B.V., pp. 3–8.

Kim, K.-I., Park, S. & Im, G.-I., 2014. Osteogenic differentiation and angiogenesis with cocultured adipose-derived stromal cells and bone marrow stromal cells. *Biomaterials*, 35(17), pp.4792–804.

Kokubo, T. et al., 1982. Apatite and Wollastonite Containg Glass-Ceramics for Prosthetic Application. *Bulletin of the Institute for Chemical Research, Kyoto University*, 60(3-4), pp.260–268.

Kokubo, T., 1991. Bioactive glass ceramics: properties and applications. *Biomaterials*, 12(2), pp.155–163.

Kokubo, T. et al., 1993. Effects of ions dissolved from bioactive glass-ceramic on surface apatite formation. *Journal of Materials Science: Materials in Medicine*, 4(1), pp.1–4.

Kokubo, T. et al., 1987. Fatigue and life-time of bioactive glass-ceramic A-W containing apatite and wollastonite. *Journal of Materials Science*, 22(11), pp.4067–4070.

Kokubo, T. et al., 1985. Mechanical properties of a new type of apatite-containing glass-ceramic for prosthetic application. *Journal of Materials Science*, 20(6), pp.2001–2004.

Kokubo, T., 1990. Surface chemistry of bioactive glass-ceramics. *Journal of Non-Crystalline Solids*, 120(1-3), pp.138–151.

Kokubo, T. & Takadama, H., 2006. How useful is SBF in predicting in vivo bone bioactivity? *Biomaterials*, 27(15), pp.2907–15.

Kolk, A. et al., 2012. Current trends and future perspectives of bone substitute materials - from space holders to innovative biomaterials. *Journal of cranio-maxillo-facial surgery : official publication of the European Association for Cranio-Maxillo-Facial Surgery*, 40(8), pp.706–18.

Langenbach, F. & Handschel, J., 2013. Effects of dexamethasone, ascorbic acid and β-glycerophosphate on the osteogenic differentiation of stem cells in vitro. *Stem cell research & therapy*, 4(5), p.117.

Langer, R. & Vacanti, J.P., 1993. Tissue Engineering. *Science*, 260, pp.920–926.

Lee, J. a et al., 2015. In vivo biocompatibility of custom-fabricated apatite-wollastonite-mesenchymal stromal cell constructs. *Journal of Biomedical Materials Research Part A*.

Lee, J.T.Y. & Chow, K.L., 2012. SEM sample preparation for cells on 3D scaffolds by freeze-drying and HMDS. *Scanning*, 34(1), pp.12–25.

LeGeros, R., Daculsi, G. & LeGeros, J., 2008. Bioactive bioceramics. *Orthopedic Biology and Medicine: Musculoskeletal Tissue Regeneration*, pp.153–181.

Li, W.L., Lu, K. & Walz, J.Y., 2012. Freeze casting of porous materials: review of critical factors in microstructure evolution. *International Materials Reviews*, 57(1), pp.37–60.

Liao, X. et al., 2011. Bone physiology, biomaterial and the effect of mechanical/physical microenvironment on mesenchymal stem cell osteogenesis. *Cellular and Molecular Bioengineering*, 4(4), pp.579–590.

Lichte, P. et al., 2011. Scaffolds for bone healing: Concepts, materials and evidence. *Injury*, 42(6), pp.569–573.

Logeart-Avramoglou, D. et al., 2005. Engineering bone: challenges and obstacles. *Journal of Cellular and Molecular Medicine*, 9(1), pp.72–84.

Lu, H.H. et al., 2003. Three-dimensional, bioactive, biodegradable, polymer-bioactive glass composite scaffolds with improved mechanical properties support collagen synthesis and mineralization of human osteoblast-like cells in vitro. *Journal of biomedical materials research. Part A*, 64(3), pp.465–474.

Luyten, F.P. & Vanlauwe, J., 2012. Tissue engineering approaches for osteoarthritis. *Bone*, 51(2), pp.289–96.

Ma, P.X. & Zhang, R., 2001. Microtubular architecture of biodegradable polymer scaffolds. *Journal of biomedical materials research*, 56(4), pp.469–77.

Maçon, A.L.B. et al., 2015. A unified in vitro evaluation for apatite-forming ability of bioactive glasses and their variants. *Journal of Materials Science: Materials in Medicine*, 26(2).

Madeddu, P., 2005. Therapeutic angiogenesis and vasculogenesis for tissue regeneration. *Experimental physiology*, 90(3), pp.315–26.

Mallick, K.K. et al., 2012. Three-dimensional porous bioscaffolds for bone tissue regeneration: Fabrication via adaptive foam reticulation and freeze casting techniques, characterization, and cell study. *Journal of Biomedical Materials Research - Part A*, 100 A(11), pp.2948–2959.

Marklein, R. a. & Burdick, J. a., 2010. Controlling stem cell fate with material design. *Advanced Materials*, 22(2), pp.175–189.

Matsuoka, H. et al., 1999. In vitro analysis of the stimulation of bone formation by highly bioactive apatite- and wollastonite-containing glass-ceramic : Released calcium ions promote osteogenic differentiation in osteoblastic ROS17 / 2 . 8 cells. *Journal of Biomedical Materials Research Part A*, 47(2), pp.176–188.

Mauney, J.R. et al., 2004. Mechanical stimulation promotes osteogenic differentiation of human bone marrow stromal cells on 3-D partially demineralized bone scaffolds in vitro. *Calcified tissue international*, 74(5), pp.458–68.

McBeath, R. et al., 2004. Cell shape, cytoskeletal tension, and RhoA regulate stem cell lineage commitment. *Developmental Cell*, 6(4), pp.483–495.

Mirzaali, M.J. et al., 2015. Mechanical properties of cortical bone and their relationships with age, gender, composition and microindentation properties in the elderly. *Bone*, (In press).

Navarro, M. et al., 2004. New macroporous calcium phosphate glass ceramic for guided bone regeneration. *Biomaterials*, 25(18), pp.4233–4241.

Nejadnik, H. et al., 2010. Autologous bone marrow-derived mesenchymal stem cells versus autologous chondrocyte implantation: an observational cohort study. *The American journal of sports medicine*, 38(6), pp.1110–1116.

Niederlaender, J. et al., 2014. Cytocompatibility evaluation of different biodegradable magnesium alloys with human mesenchymal stem cells. *Journal of Materials Science: Materials in Medicine*, 25(3), pp.835–843.

O'Brian,J.,Wilson,I.,Orton,T.,Pognan, F., 2000. Investigation of the Alamar Blue(resazurin) fluorescent dye for the assessment of mammalian cell cytotoxicity. *Europan Journal of Biochemistry*, 267, pp.5421–5426.

Pampaloni, F., Reynaud, E.G. & Stelzer, E.H.K., 2007. The third dimension bridges the gap between cell culture and live tissue. *Nature reviews. Molecular cell biology*, 8(10), pp.839–845.

Patel, A. a. et al., 2010. Biophysical mechanisms of single-cell interactions with microtopographical cues. *Biomedical Microdevices*, 12(2), pp.287–296.

Pattanayak, D.K., 2009. Apatite wollastonite-poly methyl methacrylate bio-composites. *Materials Science and Engineering C*, 29(5), pp.1709–1714.

Perez, R.A. & Mestres, G., 2015. Role of pore size and morphology in musculo-skeletal tissue regeneration. *Materials Science and Engineering: C*.

Pramanik, S. et al., 2015. In Vitro Study of Surface Modified Poly(ethylene glycol)-Impregnated Sintered Bovine Bone Scaffolds on Human Fibroblast Cells. *Scientific Reports*, 5, p.9806.

Rambo, C.R. et al., 2006. Processing of cellular glass ceramics. *Journal of the American Ceramic Society*, 89(11), pp.3373–3378.

Rea, S.M., Best, S.M. & Bonfield, W., 2004. Bioactivity of ceramic-polymer composites with varied composition and surface topography. *Journal of Materials Science: Materials in Medicine*, 15(9), pp.997–1005.

Ren, G., Hogg, P.J. & Woolstencraft, D.H., 2012. Mechanical properties of glass silicate based composites - effects of varying fibre volume fractions. *Advances in Applied Ceramics*, 111(3), pp.113–119.

Rezwan, K. et al., 2006. Biodegradable and bioactive porous polymer/inorganic composite scaffolds for bone tissue engineering. *Biomaterials*, 27(18), pp.3413–3431.

Roberts, S. et al., 2011. Prospects of stem cell therapy in osteoarthritis. *Regenerative Medicine*, 6(3), pp.351–366.

Robling, A.G., Castillo, A.B. & Turner, C.H., 2006. Biomechanical and molecular regulation of bone remodeling. *Annual review of biomedical engineering*, 8, pp.455–498.

Rodrigues, A. & Jr., S., 2011. Bioresorbable polymers for tissue engineering. *Tissue Engineering*, 18(18), pp.225–246.

Roman, J. et al., 2001. Role of acid attack in the in vitro bioactivity of a glass-ceramic of the 3CaO.P2O5-CaO.SiO2-CaO.MgO.2SiO2 system. *Biomaterials*, 22(14), pp.2013–2019.

Saito, N. et al., 2005. Synthetic biodegradable polymers as drug delivery systems for bone morphogenetic proteins. *Advanced drug delivery reviews*, 57(7), pp.1037–48.

Sakaguchi, Y. et al., 2005. Comparison of human stem cells derived from various mesenchymal tissues: Superiority of synovium as a cell source. *Arthritis and Rheumatism*, 52(8), pp.2521–2529.

Salgado, A.J., Coutinho, O.P. & Reis, R.L., 2004. Bone tissue engineering: State of the art and future trends. *Macromolecular Bioscience*, 4(8), pp.743–765.

Samavedi, S., Whittington, A.R. & Goldstein, A.S., 2013. Calcium phosphate ceramics in bone tissue engineering: A review of properties and their influence on cell behavior. *Acta Biomaterialia*, 9(9), pp.8037–8045. Available at: http://dx.doi.org/10.1016/j.actbio.2013.06.014.

Sánchez-navas, A. et al., 2013. Crystal Growth of Inorganic and Biomediated Carbonates and Phosphates. In S. O. Ferreira, ed. *Advanced Topics on Crystal Growth*. INTECH Open Access Publisher, pp. 67–88.

Sarugaser, R. et al., 2009. Human mesenchymal stem cells self-renew and differentiate according to a deterministic hierarchy. *PloS one*, 4(8), p.e6498.

Sautier, J.M. et al., 1994. Bioactive glass-ceramic containing crystalline apatite and wollastonite initiates biomineralization in bone cell cultures. *Calcified Tissue International*, 55(6), pp.458–466.

Schugens, C. et al., 1996. Polylactide macroporous biodegradable implants for cell transplantation . II . Preparation of polylactide foams by liquid-liquid phase separation. *Journal of Biomedical Materials Research*, 30(4), pp.449–461.

Scotti, C. et al., 2010. Recapitulation of endochondral bone formation using human adult mesenchymal stem cells as a paradigm for developmental engineering. *Proceedings of the National Academy of Sciences of the United States of America*, 107(16), pp.7251–7256.

Sen, M.K. & Miclau, T., 2007. Autologous iliac crest bone graft: should it still be the gold standard for treating nonunions? *Injury*, 38 Suppl 1, pp.S75–80.

Seo, C.H. et al., 2014. Micropit surfaces designed for accelerating osteogenic

differentiation of murine mesenchymal stem cells via enhancing focal adhesion and actin polymerization. *Biomaterials*, 35(7), pp.2245–2252.

Steinwachs, M.R., Guggi, T. & Kreuz, P.C., 2008. Marrow stimulation techniques. *Injury*, 39(1 suppl), pp.26–31.

Stevens, M.M., 2008. Biomaterials for bone tissue engineering. *Materials Today*, 11(5), pp.18–25.

Suri, S. & Walsh, D. a, 2012. Osteochondral alterations in osteoarthritis. *Bone*, 51(2), pp.204–11.

Szpalski, C., Wetterau, M., et al., 2012. Bone Tissue Engineering: Current Strategies and Techniques—Part I: Scaffolds. *Tissue Engineering Part B: Reviews*, 18(4), pp.246–257.

Szpalski, C., Barbaro, M., et al., 2012. Bone Tissue Engineering: Current Strategies and Techniques—Part II: Cell Types. *Tissue Engineering Part B: Reviews*, 18(4), pp.258–269.

Teixeira, A.I. et al., 2006. The effect of environmental factors on the response of human corneal epithelial cells to nanoscale substrate topography. *Biomaterials*, 27(21), pp.3945–3954.

Teramoto, H. et al., 2005. Resorption of Apatite-wollastonite containing glass-ceramic and β-tricalcium phosphate in vivo. *Acta Medica Okayama*, 59(5), pp.201–207.

Tsetsekou, A. et al., 2001. Optimization of the rheological properties of alumina slurries for ceramic processing applications Part II: Spray-drying. *Journal of the European Ceramic Society*, 21(4), pp.493–506.

Vitale-Brovarone, C. et al., 2008. Biocompatible glass-ceramic materials for bone substitution. *Journal of Materials Science: Materials in Medicine*, 19(1), pp.471–478.

Vitale-Brovarone, C., Baino, F. & Verné, E., 2010. Feasibility and tailoring of bioactive glass-ceramic scaffolds with gradient of porosity for bone grafting. *Journal of biomaterials applications*, 24(8), pp.693–712.

Vogel, V. & Sheetz, M., 2006. Local force and geometry sensing regulate cell functions. *Nature reviews. Molecular cell biology*, 7(4), pp.265–275.

Wang, X. et al., 2016. Topological Design and Additive Manufacturing of Porous Metals for Bone Scaffolds and Orthopaedic Implants: A Review. *Biomaterials*, 83, pp.127–141.

Weiner, S. & Traub, W., 1992. Bone structure: from angstroms to microns. *The FASEB journal : official publication of the Federation of American Societies for Experimental Biology*, 6(3), pp.879–885.

Weiner, S. & Wagner, H.D., 1998. The material bone: Structure-Mechanical Function Relations. *Annual Review of Materials Science*, 28(1), pp.271–298.

Witte, F. et al., 2007. Biodegradable magnesium scaffolds: Part II: peri-implant bone remodeling. *Journal of biomedical materials research. Part A*, 81(3), pp.757–65.

Wu, C. & Chang, J., 2007. Degradation, bioactivity, and cytocompatibility of diopside, akermanite, and bredigite ceramics. *Journal of biomedical materials research. Part B, Applied biomaterials*, 83B(1), pp.153–160.

Wu, C., Ramaswamy, Y. & Zreiqat, H., 2010. Porous diopside (CaMgSi2O6) scaffold: A promising bioactive material for bone tissue engineering. *Acta Biomaterialia*,

6(6), pp.2237–2245.

Xiao, K. et al., 2008a. Indirect selective laser sintering of apatite–wollostonite glass–ceramic. *Proceedings of the Institution of Mechanical Engineers, Part H: Journal of Engineering in Medicine*, 222(7), pp.1107–1114.

Xiao, K. et al., 2008b. Indirect selective laser sintering of apatite-wollostonite glass-ceramic. *Proceedings of the Institution of Mechanical Engineers. Part H, Journal of engineering in medicine*, 222(7), pp.1107–1114.

Yamada, S. et al., 1994. Osteoclastic resorption of apatite formed on apatite- and wollastonite-containing glass-ceramic by a simulated body fluid. *Journal of biomedical materials research*, 28(11), pp.1357–63. Available at: http://www.ncbi.nlm.nih.gov/pubmed/7829566 [Accessed September 7, 2015].

Yamanaka, K. et al., 2015. Seeding of mesenchymal stem cells into inner part of interconnected porous biodegradable scaffold by a new method with a filter paper. *Dental materials journal*, 34(1), pp.78–85.

Yang, D.-C. et al., 2011. Hypoxia inhibits osteogenesis in human mesenchymal stem cells through direct regulation of RUNX2 by TWIST. *PloS one*, 6(9), p.e23965.

Yook, S.-W. et al., 2012. Reverse freeze casting: a new method for fabricating highly porous titanium scaffolds with aligned large pores. *Acta biomaterialia*, 8(6), pp.2401–10.

You, X.Q. et al., 2005. Effect of grain size on thermal shock resistance of Al2O3–TiC ceramics. *Ceramics International*, 31(1), pp.33–38.

Zhang, D. & Kilian, K. a., 2013. The effect of mesenchymal stem cell shape on the maintenance of multipotency. *Biomaterials*, 34(16), pp.3962–3969.

Zhang, H., Ye, X.-J. & Li, J.-S., 2009. Preparation and biocompatibility evaluation of apatite/wollastonite-derived porous bioactive glass ceramic scaffolds. *Biomedical materials*, 4(4), p.045007.

Zhao, J. et al., 2006. A study on improving mechanical properties of porous HA tissue engineering scaffolds by hot isostatic pressing. *Biomedical materials (Bristol, England)*, 1(4), pp.188–192.

APPENDIX

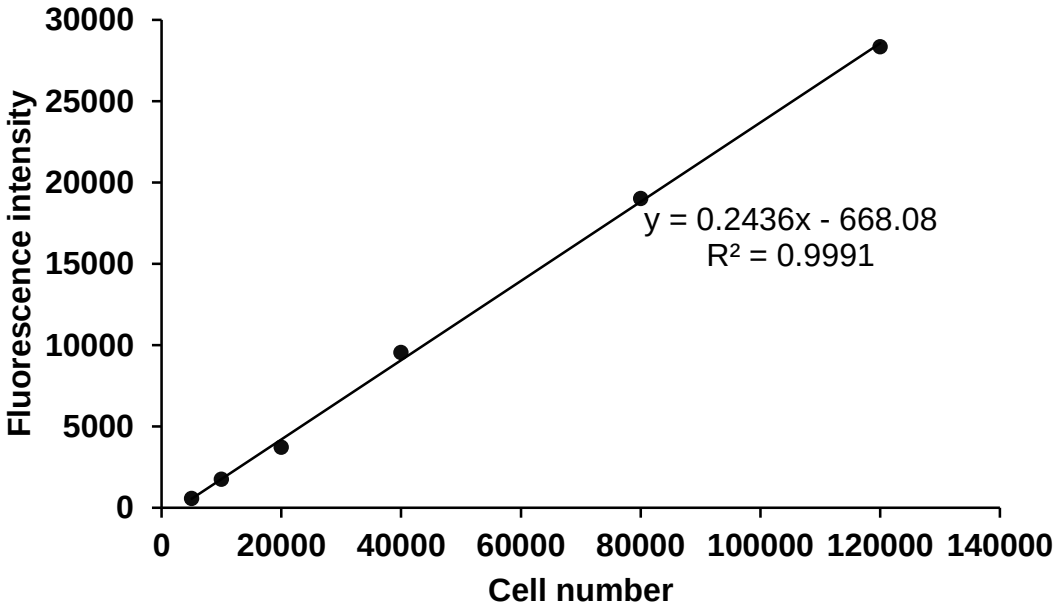

Appendix- Figure 1: Calibration curve for Alamar blue at excitation wavelength 570 nm and emission wavelength at 590 nm.

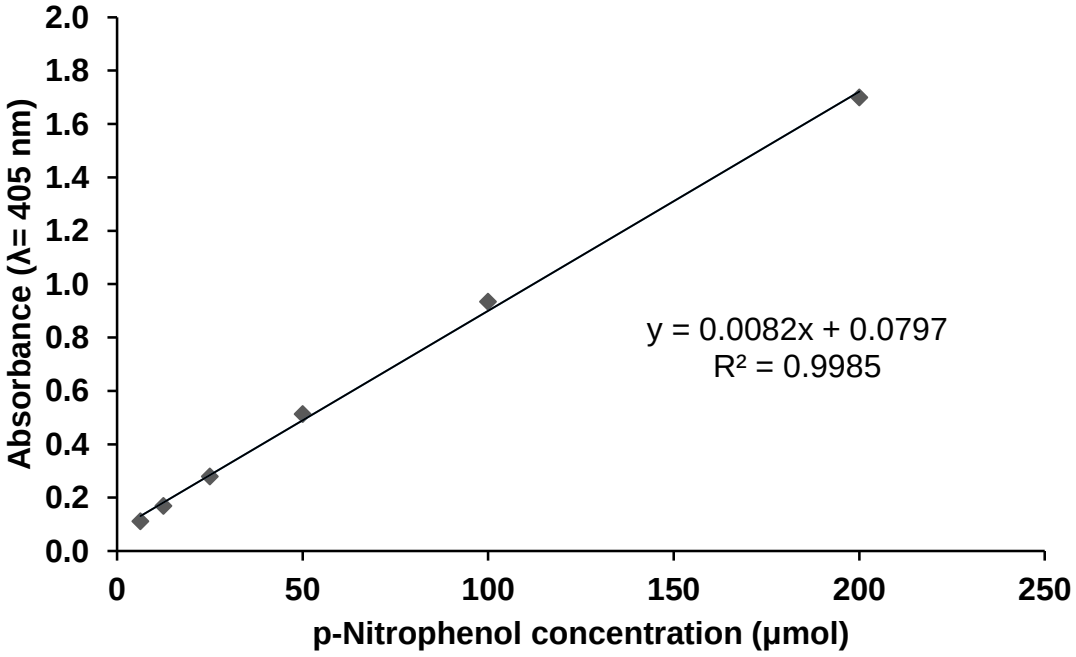

Appendix- Figure 2: Calibration curve of p-nitrophenol absorbance at λ=405 nm.

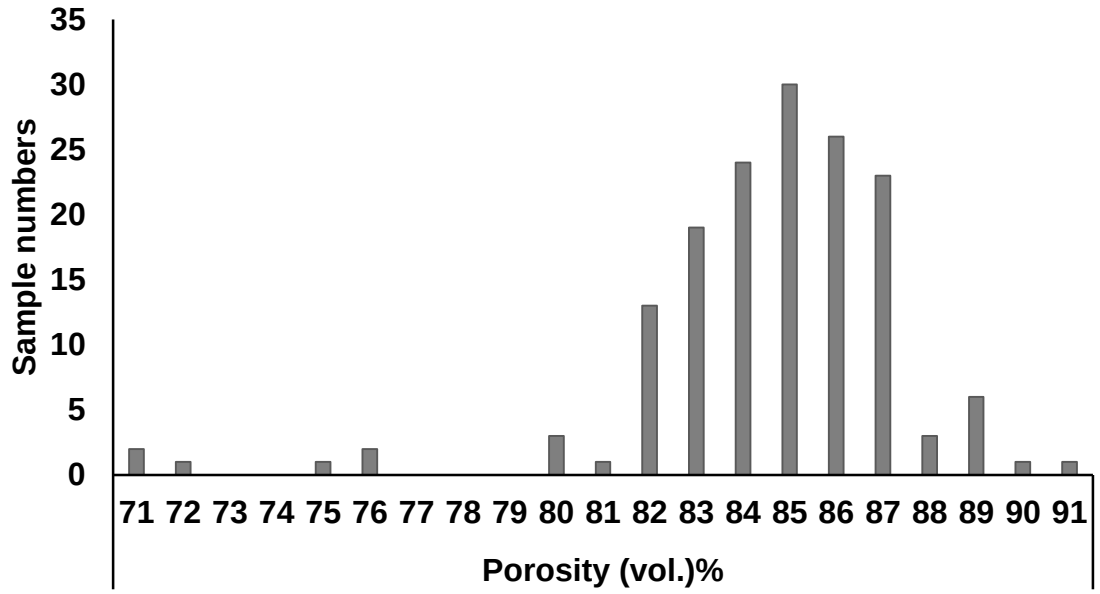

Appendix- Figure 3: Number of sintered A-W TIPS scaffolds that have the corresponding porosity.

Assay	Porosity (vol.) %
Alamar blue, ALP	83, 85, 86
RT-PCR	82, 84, 85, 86, 87
Histology	83, 85, 87
SEM	84, 86
IFA	87, 89

Appendix- Table 1: The porosity of sintered A-W TIPS scaffolds that were used for each assay with Y201 cell line.

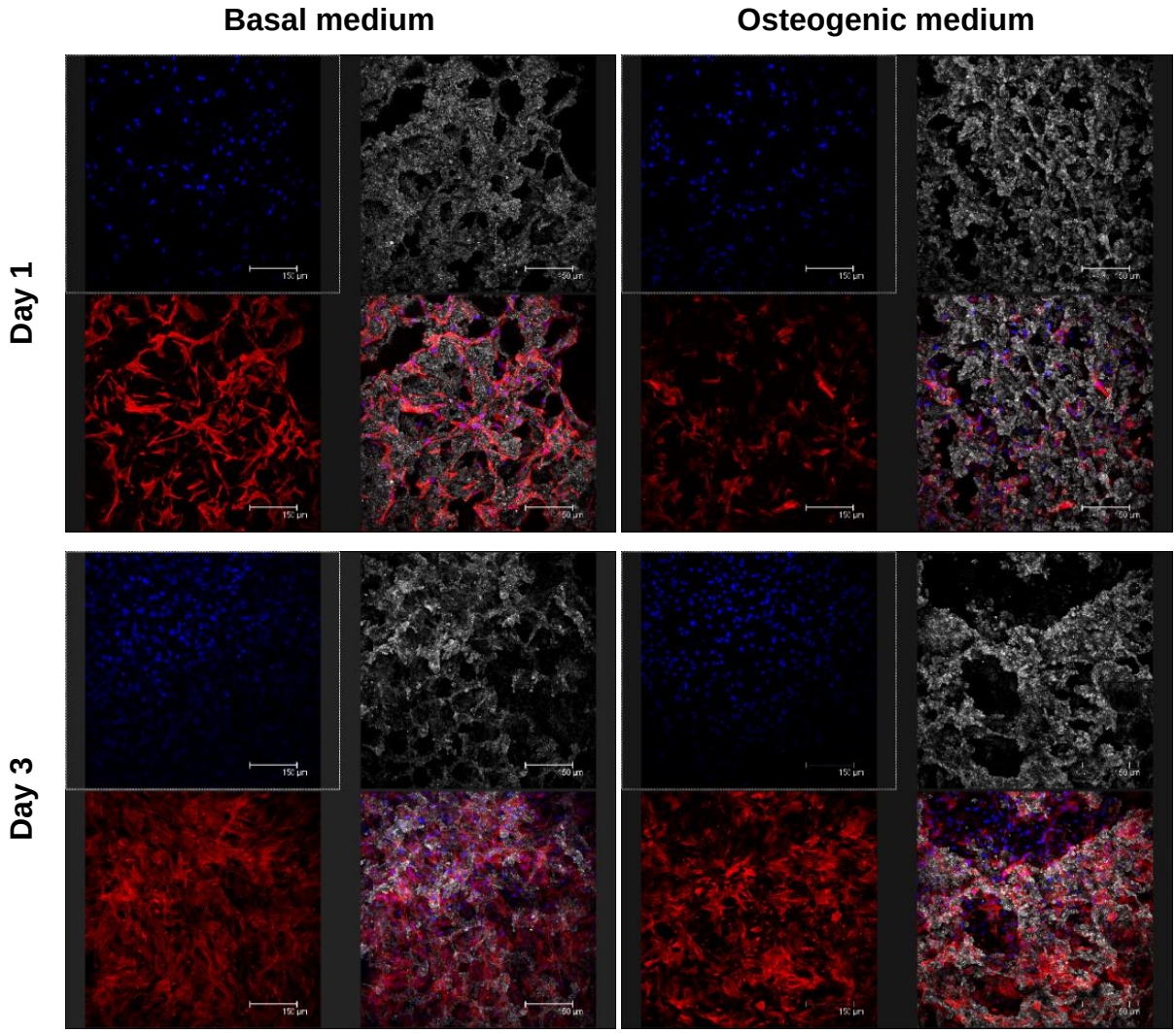

Appendix- Figure 4: Confocal microscopy images of top view of seeded sintered A-W TIPS scaffolds with Y201 after three days of culting in basal and osteogenic media respectively. Red was rhodamine-phalloidin staining for the cytoskeleton and blue was DAPI stained the nuclei of the cells.